

Time-dependent development of Backward Erosion Piping

Pol, J.C.

DOI

[10.4233/uuid:eb5ed3b2-4210-489e-b329-59722a0c50a0](https://doi.org/10.4233/uuid:eb5ed3b2-4210-489e-b329-59722a0c50a0)

Publication date

2022

Document Version

Final published version

Citation (APA)

Pol, J. C. (2022). *Time-dependent development of Backward Erosion Piping*. [Dissertation (TU Delft), Delft University of Technology]. <https://doi.org/10.4233/uuid:eb5ed3b2-4210-489e-b329-59722a0c50a0>

Important note

To cite this publication, please use the final published version (if applicable).
Please check the document version above.

Copyright

Other than for strictly personal use, it is not permitted to download, forward or distribute the text or part of it, without the consent of the author(s) and/or copyright holder(s), unless the work is under an open content license such as Creative Commons.

Takedown policy

Please contact us and provide details if you believe this document breaches copyrights.
We will remove access to the work immediately and investigate your claim.

Time-dependent development of Backward Erosion Piping

Dissertation

for the purpose of obtaining the degree of doctor
at Delft University of Technology
by the authority of the Rector Magnificus, prof. dr. ir. T.H.J.J. van der Hagen,
chair of the Board for Doctorates
to be defended publicly on
Tuesday 6 December 2022 at 12:30 o'clock

by

Johannes Cornelis POL

Master of Science in Civil Engineering, Delft University of Technology, the Netherlands
born in Rijssen, the Netherlands

This dissertation has been approved by the promotor.

Composition of the doctoral committee:

Rector Magnificus	chairperson
prof. dr. ir. S.N. Jonkman	Delft University of Technology, promotor
prof. dr. ir. M. Kok	Delft University of Technology, promotor
dr. ir. W. Kanning	Delft University of Technology, copromotor

Independent members:

prof. dr. ir. P.H.A.J.M. van Gelder	Delft University of Technology
prof. dr. K.G. Gavin	Delft University of Technology
prof. dr. ir. A. Bezuijen	Ghent University
dr. ir. J.D. Rice	Utah State University
prof. dr. ir. M. van Koningsveld	Delft University of Technology, reserve member



Keywords: flood defences, levees, dams, reliability, backward erosion piping, internal erosion, sediment transport, time-dependence, failure mechanism interactions

Printed by: Gildeprint

Cover: Michelle Rudolph

Copyright © 2022 by J.C. Pol

ISBN 978-94-6366-622-0

An electronic version of this dissertation is available at <https://repository.tudelft.nl>

How Much Water Is Inside A Tear

*How much water is inside a tear,
And how long does it take to dry them?
As long as there is misery and fear
In the people who continue to cry them.*

*How much water is inside a flood
And how long does it take to recede?
As long as it takes to restore hope
To the people in desperate need.*

*How much water is inside a storm
And how long does it take to clear?
As long as it takes to rebuild a home
And restore everything that is dear.*

*How much water is inside a city
When a levee suddenly breaks?
As many as are the tears that are cried
When so many million hearts break.*

Rabbi Zoë Klein



Contents

Acknowledgments	ix
Summary	xi
Samenvatting	xv
1 Introduction	1
1.1 Flood risk and levee reliability	2
1.2 Implications of new flood safety standards	2
1.3 Levee failure by backward erosion piping	4
1.4 Knowledge gaps	5
1.5 Research aims and questions	6
1.6 Research outline and methodology	7
1.7 Originality	8
2 Literature review and data analysis	9
2.1 Backward erosion piping: processes and equilibrium	10
2.1.1 Failure process	10
2.1.2 Observations from previous research	11
2.1.3 Equilibrium models	17
2.2 Backward erosion piping: time-dependent development	21
2.2.1 Time-dependent processes	21
2.2.2 Field observations	24
2.2.3 Laboratory experiments	29
2.2.4 Analysis of progression rates from experiments	33
2.2.5 Time-dependent models	36
3 Small-scale Experiments on the Temporal Development of Piping	39
3.1 Introduction	40
3.1.1 Piping process description	40
3.1.2 Piping process in non-equilibrium conditions	41
3.1.3 Modeling of pipe progression	42
3.1.4 Objective	43
3.2 Experimental method	43
3.2.1 Modification of box-type setup	43
3.2.2 Materials and measurement techniques	43
3.2.3 Test procedure	45
3.2.4 Test program	46

3.3	Experimental results	46
3.3.1	General observations on the erosion process	46
3.3.2	Effect of particle detachment on pipe flow resistance	48
3.3.3	Critical head, pipe length and hydraulic gradients	49
3.3.4	Pipe length development	51
3.3.5	Pipe geometry after test	52
3.4	Pipe progression analysis.	55
3.4.1	Critical bed shear stress during equilibrium	55
3.4.2	Drivers of the progression rate	57
3.4.3	Critical bed shear stress during pipe development	59
3.4.4	Sediment transport.	61
3.5	Discussion	65
3.5.1	Comparison with other experiments	65
3.5.2	Reflection on the analysis and experimental setup	66
3.5.3	Erosion process	68
3.5.4	Implications for modelling	68
3.6	Conclusions	68
4	Large-scale Experiments on the Temporal Development of Piping	71
4.1	Introduction	72
4.1.1	Piping process	72
4.1.2	Time-dependent processes in piping	73
4.1.3	Piping experiments including temporal development.	73
4.1.4	Modeling temporal development of piping	74
4.1.5	Research aim.	74
4.2	Experimental setup.	74
4.2.1	Dimensions of the test levee	74
4.2.2	Sand properties	76
4.2.3	Monitoring equipment	76
4.2.4	Construction method.	77
4.2.5	Test procedure	79
4.3	Results and Analysis	79
4.3.1	General observations.	79
4.3.2	Head and hydraulic gradient	79
4.3.3	Progression rates.	82
4.3.4	Erosion volumes and pipe dimensions	84
4.4	Discussion	85
4.4.1	Uncertainties in measurements.	85
4.4.2	Progression rates in other experiments.	86
4.4.3	Pipe dimensions	87
4.4.4	Additional experiment on strength recovery	88
4.5	Conclusions	89

5	Modeling Temporal Development of Backward Erosion Piping	91
5.1	Introduction	92
5.2	Modeling approach.	93
5.2.1	Current DgFlow finite element model	93
5.2.2	Approaches for time-dependent piping erosion modeling	94
5.2.3	Model extension with time-dependent erosion	95
5.3	Simulation of experiments	100
5.3.1	Method.	100
5.3.2	Results	102
5.4	Effect of grain size, scale, and overloading	105
5.4.1	Method: model setup.	105
5.4.2	Results: critical conditions	106
5.4.3	Results: pipe progression.	108
5.4.4	Simplified models for progression rates	111
5.5	Discussion and Conclusions	114
5.5.1	Discussion	114
5.5.2	Conclusions	115
6	Time-dependent Levee Reliability with Cumulative Piping Erosion	119
6.1	Introduction	120
6.1.1	Backward erosion piping failure process	120
6.1.2	Time-variant piping reliability analysis of flood defenses.	121
6.1.3	Objectives and approach	123
6.2	Time-variant reliability analysis method for piping.	123
6.2.1	Piping reliability formulation.	123
6.2.2	Pipe progression model	125
6.2.3	Probabilistic method	127
6.3	Application to coastal and river levees	130
6.3.1	Random variables in base case	130
6.3.2	Base case results	132
6.3.3	Variability in load duration.	135
6.3.4	Sensitivity analysis on base case	136
6.3.5	Influence of levee characteristics	138
6.3.6	Implications for levees in the Netherlands	139
6.4	Conclusions	142
7	Levee reliability with physical interactions between failure mechanisms	145
7.1	Introduction	146
7.2	Interactions in levee failure	148
7.2.1	Levee failure mechanisms and failure paths	148
7.2.2	Physical interactions in levees	149
7.2.3	Approaches to quantify interactions in levees	149
7.3	Quantification method	152
7.3.1	Reliability method	152
7.3.2	Methods for conceptual examples	152
7.3.3	Methods for levee example.	155

7.4	Results	159
7.4.1	Results of conceptual examples.	159
7.4.2	Levee example results	162
7.5	Discussion	169
7.5.1	When are interactions relevant?	169
7.5.2	Limitations of the quantification method.	169
7.6	Conclusions	171
8	Conclusions and recommendations	173
8.1	Conclusions	173
8.2	Recommendations for research.	176
8.3	Recommendations for practice	177
	Bibliography	179
A	Failure case Strijenham	193
B	Progression rates from previous laboratory experiments	201
C	Data of sediment transport in laminar flow	203
D	DgFlow simulation results	209
E	Sensitivity analysis: C_e based on additional tests	213
F	Time-variant reliability: results sensitivity analysis	215
	List of Symbols	219
	Curriculum Vitæ	223
	List of Publications	225

Acknowledgments

It's wonderful to hold a small book that comprises five years of your work. Although there's still a lot unknown, it was satisfying to get a better grip on this mysterious failure process that occurs hidden below the ground surface. But I also strongly hope that the results will be useful for practice, lead to more effective flood protection and hence form a small building block in adapting to climate change. Although some people may think that PhD researchers work for years in isolation, this result would have been impossible without many important contributions.

In the first place, I want to thank my supervisors. Wim, your endless enthusiasm and positive attitude was very important to keep me going. Also thanks for the many discussions, either about the results or any other business; you have shown that PhD supervision is possible from anywhere in the world. Bas, I appreciate the freedom you offered to shape my own research direction and take additional opportunities such as the review for ENW and the fact finding project after the 2021 summer floods. Matthijs, thank you for your confidence and support, and for being the driving force behind the joint activities of the All-risk programs.

It was great to work with national and international experts in the field. Vera and Bryant, it was a pleasure to collaborate on the experiments and their modeling. Thanks for your sharp ideas and comments. Carlo, Gijs, Juan, Lisa and Manuel, I have learned a lot from discussing your alternative approaches to BEP modeling. I bet we haven't cracked the code yet, and I look forward to your advancements. Aron, I was very happy that you could actually code my ideas on time-dependent pipe development in DgFlow. Marieke and Henk, thanks for thinking along, asking important questions, and reflecting on what the results would mean for practice.

Experimental research is hard work, and I am very grateful to everyone who assisted in the experiments. In particular the large-scale experiments were a special experience, building our own test levee and running the tests 24h/day in shifts. Special thanks to Mark and Wouter-Jan for taking over the lead, even during the night, so I could leave it in your hands and have a little sleep. From the observation notes I know you had great nightly discussions on football;-). Deltares is acknowledged for providing the pressure sensors, and Enno for the technical assistance. Jarno and Wouter, thanks for your assistance in the many small-scale experiments that we performed in the GeoHal.

This research was part of the All-risk project, which was funded by NWO and many private and public partners (<https://kbase.ncr-web.org/all-risk/>). It was great to be part of a larger group of researchers studying flood protection from varying perspectives. Within sub-project D, we even managed to create real interaction between the projects of Guido, Mark, Vera and me (resulting in Chapter 7 on interactions). Thanks Paulina for joining the interactions project after your MSc thesis. In the final phase of my project I had to miss the companion of my roommates in room 3.58: Arny, Chris, Mark and Wouter-Jan. Many thanks for the pre-covid chats and coffees.

I am very grateful to HKV for supporting me throughout the project, in particular to Sonja, Saskia and Kees, who encouraged me to start this journey. Wouter, thanks for your support and helping me to balance the lives of PhD researcher, HKV employee, and father. Michelle: thanks for the beautiful cover of this thesis.

Finally, I would probably not have finished this PhD without the support of my family and friends. Mieke, de afgelopen jaren waren soms best taai, maar je hebt me steeds gesteund in het PhD traject. Bedankt voor de ruimte om frustraties te spuien. Voor het relativeren. En voor het inzicht dat de complexiteit van dijken in het niet valt bij die van de menselijke psyche. Jiska, toen ik met dit werk begon, was je nog niet eens geboren, en inmiddels vertel je trots dat je vader onderzoeker is van dijken. Je vraagt vaak hoe iets werkt of waarom iets zo is; daardoor bedenk ik me hoe weinig grote mensen eigenlijk weten. Gelukkig hebben we internet! Femke, jij leeft nog helemaal in het moment, ongecompliceerd. Dat was een goede afleiding van het promotieonderzoek. En eigenlijk vinden wij het allemaal veel leuker om te spelen dan om te werken!

Berkel en Rodenrijs - November 2022

Summary

Structural flood protection systems such as levees are an important component in flood risk reduction strategies. However, living behind levees and dams still comes with risk as these structures can fail and failure can have catastrophic consequences. Key questions in living with this risk are: how large is the risk, and how can this risk be kept at an acceptable level? Answering these questions requires among others knowledge about how these structures fail (*failure mechanisms*) and how likely that is (*failure probabilities*).

This thesis expands such knowledge, focusing on the specific failure mechanism *backward erosion piping* (BEP). Backward erosion piping, or just piping, is a process in which a sandy levee foundation is eroded by groundwater flowing beneath the levee, which can ultimately result in levee collapse. The process becomes visible when the eroded sand settles in the form of *sand boils* behind the levee. Sand boils are observed frequently during high water events, and globally a significant part of levee failures is attributed to piping. Current piping assessment practices in the Netherlands result in unrealistically high failure probabilities (i.e. a low reliability). This may be partly caused by conservative failure model assumptions. This thesis focuses on the conservative assumption of immediate failure once a critical threshold is exceeded, and explores a different approach which considers piping as a time-dependent failure process. This knowledge helps to improve reliability estimates for systems with short high-water events (i.e. in coastal areas) and long-lasting events (along rivers), as well as with emergency response decisions.

Time-dependence in piping failure occurs at two distinct time scales: development of pipe dimensions during an extreme high-water event (hours to days), and long-term development of the reliability over multiple years due to cumulative erosion and possibly strength recovery. Furthermore, time-dependence at the event time scale is present in different components of the failure process: in time-varying water levels, transient groundwater response, timing of blanket rupture, and erosion of the pipe.

Piping requires time to develop into a levee failure as the sand needs to be transported through small voids (pipes) in the sandy foundation. When the high-water duration is shorter than the time required for erosion, or when the process is stopped by timely flood fighting interventions, failure is prevented. Including this time-dependence in the safety assessment of levees results in more realistic reliability estimates and lower levee reinforcement costs. However, time-dependent aspects of the piping erosion process and potential impacts on levee reliability are poorly understood. Therefore, this thesis aims to quantify the time-dependent development of the piping failure process and its impact on levee reliability. This is achieved by literature study, physical model experiments on small and large scales, numerical modeling and probabilistic modeling. These parts are summarized below.

The literature study describes the processes involved in the time-dependent development of backward erosion piping and discusses previous experimental work and predic-

tion models. Analysis of historical levee failures due to BEP in the literature gives a first indication of the time between pipe initiation and breach, which shows a large variation (from less than an hour up to 30 days). The vast majority of cases failed around the flood peak water level (+/- one day), on average 4 hours after the peak. Also laboratory experiments from the literature are analyzed, resulting in a regression model to estimate pipe progression rates based on soil and loading parameters.

Small-scale experiments (0.35 m length) with local measurements of pipe flow conditions were used to study the piping erosion process and how factors like grain size and overloading affect the rate of pipe progression. Progression rates in the small scale tests were in the order of 0.1-1 m/hour. The observations indicate that, in uniform sands, erosion at the pipe tip occurs rather sudden but that the transport of sand in the pipe delays this erosion. The results show that the progression rate can be well explained by the flow conditions (bed shear stress) in the pipe. It was also shown that the relation between sediment transport and shear stress during piping erosion is similar to such relations found in flume experiments with laminar flows of uniform depth. These findings support modeling choices later in this thesis.

A large-scale experiment was conducted to provide a validation test on a realistic levee with a seepage length of 7.2 m and maximum head difference of 1.8 m, a fine sandy aquifer, a clay cover and concentrated outflow. The measured pipe progression rate of 0.3 m/hour is in line with a regression model derived from rates in previous piping experiments. Nine months after the experiment, the levee was re-loaded. This unique strength recovery experiment showed that the levee strength had partially recovered: the erosion process started all over again, albeit with 20% lower critical head and 140% higher progression rate.

To be able to predict time-dependent pipe development for field conditions, a numerical model was developed that simulates time-dependent backward erosion. It is an extension of the finite element equilibrium model *DgFlow*, extended with a sediment balance and a sediment transport equation for laminar flow. This model was calibrated on part of the small-scale and large-scale experiments. Based on these experiments and additional ones from the literature, the calibrated erosion coefficient (C_e) was found to have a mean value of 0.055 and standard deviation of 0.043. A major challenge of the 3D numerical modeling of BEP are scale effects in the computed critical head. At field scales, the simulated critical head in case of 3D concentrated outflows seems to be too low. However, sufficiently detailed large scale experiments for a detailed validation of 3D scale effects are lacking. Finally, a series of model simulations with varying levee properties and hydraulic loads allowed to derive a simplified regression model of the pipe progression rate. Such a simplified model can be efficiently implemented in reliability analyses.

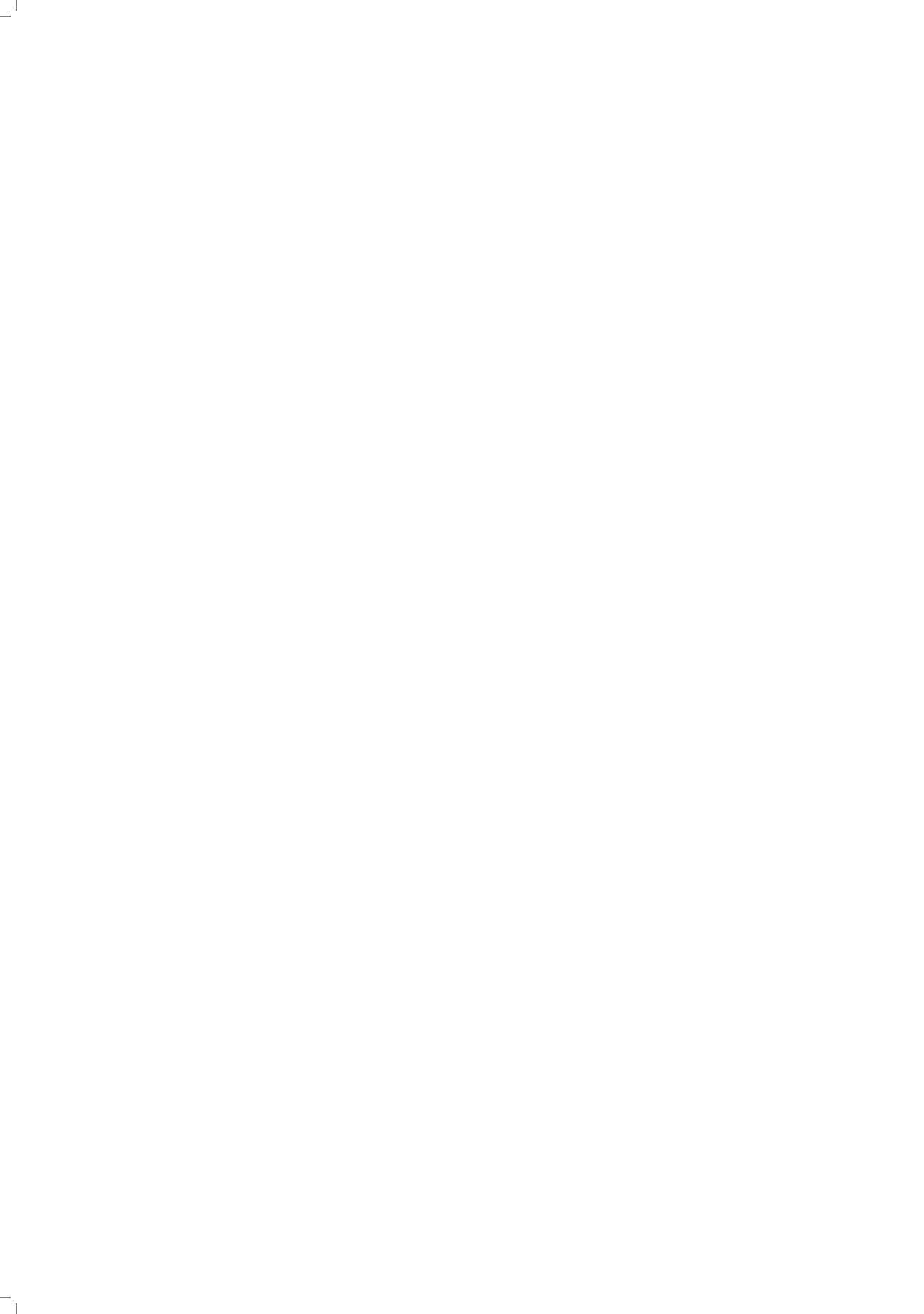
The next step was to quantify how these time-dependent processes affect the failure probability of levees using a time-variant reliability analysis. Therefore, a simplified time-dependent piping failure model was developed including effects of a varying water level, blanket uplift, heave, backward erosion and flood fighting interventions. This model is implemented in a reliability analysis considering cumulative pipe growth over multiple flood events and strength recovery between flood events. Results of the analysis confirm that time-dependent pipe growth has more impact on the reliability in water systems with

a short flood duration (storm-surge). The coastal cases show large reductions in failure probability, ranging from a factor 10 to more than 10^6 for large seepage lengths and fine sand. Reductions are smaller for the river cases, but can still be considerable for particular cases (factor 100 in failure probability). For rivers (long duration), the effectiveness of flood fighting is important in reducing the failure probability, as the longer river floods provide much more time for successful measures than the short coastal surges. The analysis also showed that short pipes formed during past events have only limited effect on the reliability. Based on the results it is concluded that a considerable part of the Dutch levees can benefit from including time-dependent pipe development in the BEP failure model, by reducing or postponing reinforcements. This holds particularly for storm-dominated areas, but to a lesser extent also for areas governed by river discharge.

The last part of the thesis covers a somewhat different but related topic. Physical interactions between failure mechanisms occur if one failure mechanism affects the resistance of another failure mechanism. This can become relevant if a failure mechanism consists of multiple events that need to occur for a breach ('residual resistance after initial failure'). Interactions were defined and described in the context of flood defenses, and analyzed under which conditions such interactions have a large impact on levee reliability. In the studied levee example, interactions between inner slope instability and backward erosion piping increased the failure probability up to a factor 4 compared to an analysis with correlated but non-interacting mechanisms. This can occur when an initial small slope failure is not followed by a major slope failure and flooding, but it decreased the resistance to backward erosion piping.

Time-dependence in backward erosion piping has a significant positive effect on levee reliability. The findings in this thesis can be used to quantify time-dependence in piping analyses and hence to obtain more accurate estimates of the failure probability of flood defenses. In this way, it allows to further optimize the allocation of resources for levee reinforcements to the levee segments where reinforcement is most beneficial. Furthermore, information on failure time scales can be used for emergency response.

Recommendations for further research mainly concern experimental work aligned with numerical analysis, with a focus on scale effects in the critical head and progression rate. The main recommendation for practice (levee managers) is to include the effect of time-dependent pipe growth in levee safety assessments and designs where it is expected to have a large effect on computed reliability and required reinforcements.



Samenvatting

Waterkeringen vormen een belangrijk onderdeel van strategieën om overstromingsrisico's te reduceren. Wonen achter dijken en dammen brengt echter nog steeds risico's met zich mee, want als deze falen (doorbreken of overstromen) kan dat catastrofale gevolgen hebben. Belangrijke vragen hierbij zijn: hoe groot is het risico, en hoe kan dit risico op een aanvaardbaar niveau worden gehouden? Om deze vragen te beantwoorden is onder andere kennis nodig over hoe dijken falen (*faalmechanismen*) en hoe groot de kans daarop is (*faalkansanalyse*).

In dit proefschrift ligt de nadruk op het faalmechanisme terugschrijdende erosie, veelal piping genoemd (Engels: *backward erosion piping*, BEP). Bij dit faalproces erodeert een zandlaag onder een dijk door grondwaterstroming, wat uiteindelijk kan leiden tot een dijkdoorbraak. Het proces wordt zichtbaar wanneer het geërodeerde zand zich achter de dijk afzet in de vorm van zandmeevoerende wellen. Piping is een belangrijk faalmechanisme omdat deze wellen regelmatig worden waargenomen tijdens hoogwater en een aanzienlijk deel van de dijkdoorbraken wordt toegeschreven aan piping. De huidige Nederlandse praktijk van veiligheidsbeoordeling van waterkeringen leidt echter tot (onrealistisch) hoge berekende faalkansen voor piping. Dit kan deels verklaard worden door conservatieve aannames in faalmodellen. Dit proefschrift richt zich op de conservatieve aanname van instantaan falen zodra een kritische waterstand wordt overschreden, en verkent een andere benadering die piping beschouwt als een tijdsafhankelijk faalproces. Deze kennis helpt bij het verbeteren van faalkansinschattingen voor watersystemen met kortdurende belastingen (langs de kust) en langdurige hoogwatergolven (rivieren), en bij het beslissen over noodmaatregelen.

Tijdsafhankelijkheid bij piping vindt plaats op twee tijdschalen: pipegroei tijdens extreem hoogwater (uren tot dagen), en de ontwikkeling van de betrouwbaarheid over meerdere jaren als gevolg van cumulatieve erosie en eventueel herstel van de pipes. Bovendien zijn verschillende onderdelen van het faalproces tijdsafhankelijk: het waterstandsverloop, de transiënte grondwaterrespons, timing van het opbarsten van de deklaag, en het pipegroeiproces zelf. Een pipe heeft tijd nodig om uit te groeien tot een dijkdoorbraak, omdat het zand door kleine holtes (pipes) in de zandlaag moet worden getransporteerd. Als de hoogwaterduur korter is dan de benodigde tijd voor erosie, of het proces stopt door een tijdige noodmaatregel, wordt bezwijken voorkomen. Het meenemen van deze tijdsafhankelijkheid in de veiligheidsbeoordeling van dijken leidt tot realistischere faalkansinschattingen en lagere dijkversterkingskosten. Er is echter weinig bekend over tijdsafhankelijke aspecten van het piping-erosieproces en hun effect op de faalkansen. Daarom heeft dit proefschrift tot doel om deze te kwantificeren. Dit is bereikt met literatuurstudie, experimenten op kleine en grote schaal, en met numerieke en probabilistische modellering. Deze onderdelen zijn hieronder samengevat.

De literatuurstudie beschrijft de processen die een rol spelen bij tijdsafhankelijke pipegroei en bespreekt eerder experimenteel werk en bestaande rekenmodellen. Analyse van historische dijkdoorbraken als gevolg van piping geeft een indicatie van de tijd tussen initiatie en doorbraak, maar deze heeft een zeer grote variatie (van minder dan een uur tot 30 dagen). Verreweg de meeste gevallen bezweken rond de hoogwaterpiek (+/- één dag), gemiddeld 4 uur na de piek. Op basis van laboratoriumproeven uit de literatuur is een eerste regressiemodel afgeleid om de pipegroeisnelheid te schatten op basis van ondergrondparameters en het verval over de dijk.

Nieuwe kleinschalige experimenten (0,35 m lengte) met metingen van de lokale stromingscondities in de pipe geven inzicht in het erosieproces en hoe factoren zoals korrelgrootte en overbelasting de pipegroeisnelheid beïnvloeden. De groeisnelheden in deze proeven zijn in de orde van 0,1-1 m/uur. De observaties laten zien dat erosie aan de pipekop in korte tijd plaatsvindt (in uniform zand), maar dat het beperkte zandtransport in de pipe de pipegroei vertraagt. De resultaten laten zien dat de pipegroeisnelheid goed kan worden verklaard door de stromingscondities (bodemschuifspanning) in de pipe. De relatie tussen sedimenttransport en schuifspanning tijdens pipegroei is vergelijkbaar met dergelijke relaties uit gootexperimenten met laminaire stroming. Deze bevindingen ondersteunen modelkeuzes verderop in dit proefschrift.

Verder is een grootschalige proef uitgevoerd op een realistische dijk met een kwelweglengte van 7,2 m, een verval van 1,8 m, een ondergrond van fijn zand, een kleiafdekking en geconcentreerde uitstroom. De gemeten pipegroeisnelheid van 0,3 m/uur is in overeenstemming met het regressiemodel wat is gefit op laboratoriumproeven uit de literatuur. Negen maanden na het experiment is de dijk opnieuw belast. Dit unieke herstel-experiment laat zien dat de sterkte van de dijk tegen piping gedeeltelijk hersteld was: het erosieproces begon opnieuw, zij het met een 20% lager kritiek verval en 140% hogere groeisnelheid.

Om de tijdsafhankelijke pipegroei in veldomstandigheden te kunnen voorspellen, is een numeriek model ontwikkeld dat tijdsafhankelijke pipegroei simuleert. Het is een uitbreiding van het eindige elementen evenwichtsmodel *DgFlow*, waaraan een sedimentbalans en sedimenttransportformule voor laminaire stroming zijn toegevoegd. Dit model is gekalibreerd aan de hand van een deel van de kleinschalige en grootschalige experimenten. Kalibratie op de experimenten in dit proefschrift en aanvullende experimenten uit de literatuur geeft een erosiecoëfficiënt (C_e) met een gemiddelde van 0,055 en een standaardafwijking van 0,043. Een belangrijke uitdaging bij de 3D numerieke modellering van piping is het schaafeffect in het berekende kritieke verval. Het kritieke verval bij geconcentreerde uitstromingen op veldschaal lijkt onderschat te worden. Voor een grondige validatie van 3D schaafeffecten ontbreken echter voldoende gedetailleerde grootschalige experimenten. Tenslotte is uit een reeks modelsimulaties met variërende dikeigenschappen en hydraulische belastingen een vereenvoudigd regressiemodel van de pipegroeisnelheid afgeleid. Dit vereenvoudigde model kan efficiënt worden toegepast in faalkansanalyses.

De volgende stap is het kwantificeren van de invloed van deze tijdsafhankelijke processen op de faalkans van dijken met behulp van een tijdsafhankelijke betrouwbaarheidsanalyse. Daartoe is een vereenvoudigd tijdsafhankelijk pipingmodel ontwikkeld met ef-

fecten van een variërende waterstand, opbarsten, heave, terugschrijdende erosie en noodmaatregelen. Dit model is geïmplementeerd in een betrouwbaarheidsanalyse waarbij rekening is gehouden met cumulatieve pipegroei gedurende meerdere hoogwaters en herstel van de sterkte tussen hoogwaters. De analyseresultaten bevestigen dat tijdsafhankelijke pipegroei een grote invloed heeft op de betrouwbaarheid in watersystemen met een korte hoogwaterduur (stormgedomineerd). Deze gevallen laten grote reducties in faalkansen zien, variërend van een factor 10 tot meer dan 10^6 voor brede dijken en fijn zand. Bij rivieren (lange hoogwaterduur) is de faalkansreductie kleiner, maar kan voor bepaalde gevallen nog steeds aanzienlijk zijn, tot een factor 100 in faalkans. Voor rivieren is de effectiviteit van noodmaatregelen belangrijk in het reduceren van faalkansen; door de lange hoogwaterduur is veel meer tijd beschikbaar voor geslaagde noodmaatregelen dan langs de kust. Uit de analyse blijkt ook dat korte pipes die zijn gevormd tijdens eerdere hoogwaters beperkte invloed hebben op de faalkans. Op basis van de resultaten wordt geconcludeerd dat het meenemen van tijdsafhankelijke pipegroei in piping-analyses potentie heeft voor een aanzienlijk deel van de Nederlandse dijken, door het beperken of uitstellen van dijkversterkingen. Dit geldt zeker voor storm-gedomineerde gebieden, maar in mindere mate ook voor gebieden waar de belasting wordt bepaald door rivierafvoer.

Het laatste deel van het proefschrift behandelt een enigszins afwijkend maar gerelateerd onderwerp. Fysische interacties tussen faalmechanismen treden op als het ene faalmechanisme de weerstand van een ander faalmechanisme beïnvloedt. Dit kan relevant worden als een faalmechanisme bestaat uit meerdere gebeurtenissen die moeten optreden voor een doorbraak, zogenaamde 'reststerkte na initieel falen'. Dit hoofdstuk beschrijft interacties in de context van dijken, en onderzoekt onder welke omstandigheden interacties invloed hebben op de betrouwbaarheid van waterkeringen. In het beschouwde voorbeeld leidden interacties tussen binnenwaartse macroinstabiliteit en piping tot maximaal een factor 4 hogere faalkans in vergelijking met gecorreleerde maar niet-interacterende mechanismen. Dit kan zich voordoen wanneer een initiële kleine afschuiving niet leidt tot een grote afschuiving en overstroming, maar wel de weerstand tegen piping reduceert.

Tijdsafhankelijkheid bij piping heeft een significant positief effect op de dijkbetrouwbaarheid. De bevindingen in dit proefschrift kunnen worden gebruikt om de tijdsafhankelijkheid in pipinganalyses te kwantificeren en zo faalkansinschattingen van waterkeringen te verbeteren. Op deze manier kunnen investeringen in dijkversterking efficiënter worden verdeeld. Bovendien kan informatie over de pipegroeisnelheid worden gebruikt in crisissituaties.

Aanbevelingen voor verder onderzoek betreffen voornamelijk experimenteel werk in combinatie met numerieke modellering, met de nadruk op schaafeffecten in het kritieke verval en de groeisnelheid. De belangrijkste aanbeveling voor de praktijk (waterkering-beheerders) is om het effect van tijdsafhankelijke pipegroei mee te nemen in veiligheidsbeoordelingen en ontwerpen in gebieden waar een groot effect op de berekende betrouwbaarheid en de vereiste versterkingen verwacht mag worden.



1

Introduction

It is clear why this phenomenon should be studied: society's well-being and the economy are of nationwide interest.

Hans Sellmeijer

1.1 Flood risk and levee reliability

Flooding is a natural hazard with large impacts on societies. According to the EM-DAT disaster database it is the most frequent type of 'natural' disaster [Guha-Sapir, 2016], and it also results in high economic damages [Jonkman, 2005]. The past decades have shown an increase in global flood risk in terms of economic damage, but a decrease in fatalities [Jonkman et al., 2012; Merz et al., 2021; Paprotny et al., 2018]. Without additional risk reduction measures, risks are expected to increase in many regions [Merz et al., 2021]. This increase is driven by socio-economic changes in exposure (land-use, population, economic value) and by climate change (sea level and extreme rainfall). Flood risk reduction strategies are diverse, including protection, insurance, spatial planning and flood-proofing of assets [Green et al., 2000; Poussin et al., 2012]. In highly developed low-lying areas with a high risk level, flood risk reduction strategies commonly depend on structural flood protection measures like levees¹ and dams [Wesselink et al., 2015].

The Netherlands is a typical example of a country depending heavily on structural flood protection measures. Currently, 59% of the land is flood prone, of which 93% is protected by levees, dunes, dams and structures (Fig. 1.1). Three aspects of the Dutch flood safety standards stand out compared to practice in other countries. First of all, they are defined in terms of a maximum allowable yearly probability of flooding, where other countries use design water level approaches. This first aspect is discussed in more detail in section 1.2, as it is an important motivation for the research topics in this thesis. Second, the safety standards are relatively strict, with maximum allowable failure probabilities ranging from 10^{-2} to 10^{-6} per year (Fig. 1.1a). Finally, the safety levels are enforced by law in the Water Act [Kok et al., 2017].

1.2 Implications of new flood safety standards

Recently, there has been a shift in flood safety standards and related practice in The Netherlands. Since the devastating North Sea floods in 1953, the Dutch safety standards were defined in terms of exceedance frequencies of water levels (design water level approach). For instance Central Holland had a design water level with an exceedance frequency of 1/10.000 per year. Levee assessment and design rules were such that levee failure at this design water level is unlikely. This approach is still common practice in other countries. In 2017, new safety standards came into effect, which are defined as a maximum allowable yearly probability of flooding per levee segment (~ 10 km). The level of these standards depends on the potential consequences of a flood. It is derived based on three aspects: optimization of the total costs of protection and potential flood damage, individual fatality risk and group fatality risk [Kok et al., 2017].

The new definition means that the standards now explicitly require to quantify the probability of flooding of the protected area (in most cases a levee breach). For practice, this requires a shift in thinking, because under the old standards it was in line with the safety philosophy to make conservative assumptions (better being on the safe side) to demonstrate that a levee would not fail under design conditions. Now, estimates should be as realistic as possible. This means that all possible failure mechanisms are considered,

¹Levee is used throughout this thesis for earthen flood defense structures; equivalent terms are dikes or flood embankments.

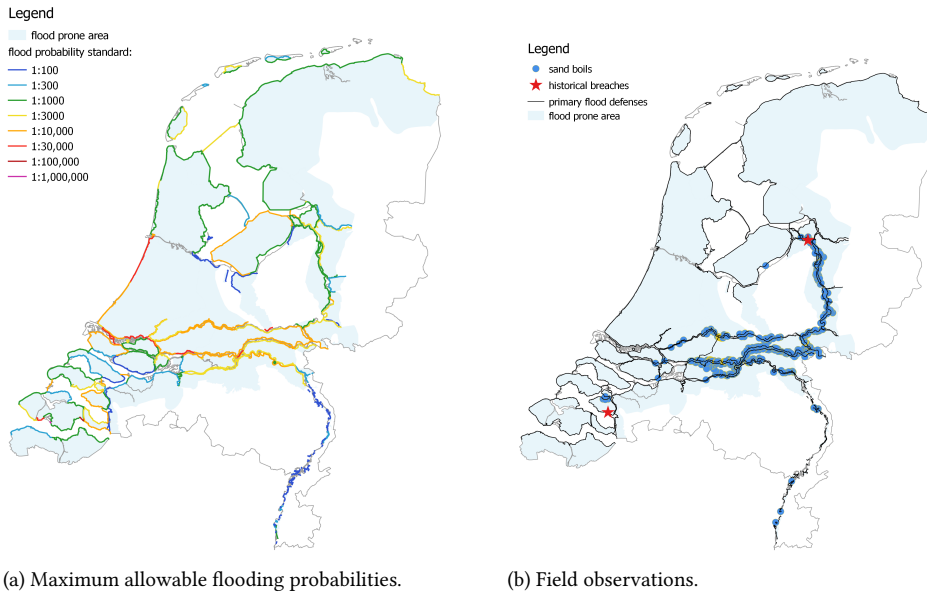


Figure 1.1: Flood prone areas and levee safety standards (a) and piping field observations (b) in the Netherlands. Standards: Georegister [2017]. Sand boil data: <https://wellocaties.app>.

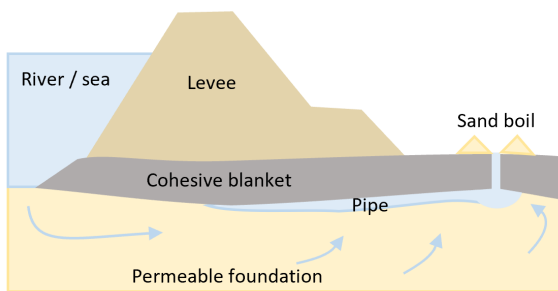
including geotechnical mechanisms which may occur at lower water levels than the design level, and that relevant uncertainties are quantified as much as possible. Part of the assessment and design practices are still based on conservative (i.e. 'safe') assumptions, as these were developed under the old safety standards. That is not striking because replacing safe assumptions by more accurate estimates requires knowledge development and therefore time. One form of conservative assumptions is that that assessment methods generally neglect residual resistance after initiation of the failure process [t Hart et al., 2016], for instance the erosion resistance of the levee core after damage of the revetment. Another conservative assumption is that most failure models implicitly assume that failure occurs instantaneously once a critical level is reached, although some failure processes require time to develop. Due to this time-dependence, combined with the limited duration of a high-water event, the initial failure may not always develop into a breach.

When residual resistance is incorporated in reliability estimates, a new issue emerges which was not relevant in the past. As structures may fail in multiple ways, risk engineers work with a set of different failure mechanisms or failure paths. A failure path is a chain of events leading to failure (i.e. flooding in case of flood defenses), for instance erosion of the levee by overtopping waves. Commonly, first the failure probability of each path is quantified, and subsequently combined to a total failure probability. However, these failure processes may interact: the occurrence of an event in one failure path may change the probability of an event in another failure path. Therefore, the common approach to analyze failure paths separately may be inaccurate in some cases.

1

1.3 Levee failure by backward erosion piping

An important failure mechanism for levees is backward erosion piping (BEP), or just piping. Current BEP assessment practices in the Netherlands result in relatively high failure probabilities (low reliability), which may partly result from conservative failure model assumptions. Backward erosion piping is a form of internal erosion which can lead to failure of levees and dams. It is a failure process by which groundwater flow under a structure erodes the granular foundation that is covered by a cohesive layer. Figure 1.2a illustrates a typical levee configuration prone to piping. The erosion process becomes visible by sand ejections behind the levee, also called *sand boils* (Fig. 1.2b). As more particles erode, the eroded zone, also called *pipe*, progresses in the direction of the river (backwards). This progression requires time. When the pipe reaches the river side, the flow through the pipe increases rapidly, which leads to large deformation of the foundation and likely failure of the structure. If detected, the piping process can be mitigated by timely flood fighting interventions.



(a) Principle of backward erosion piping in a levee cross section.



(b) Sand boil during Meuse floods of summer 2021.

Figure 1.2: Illustrations of backward erosion piping.

There are several reasons to focus on backward erosion piping (BEP) when analyzing residual resistance and time-dependence. Historical failures, field observations and safety assessment illustrate the importance of the failure mechanism. Internationally, a significant part (approximately 15%) of the levee failures were attributed to internal erosion [Danka and Zhang, 2015; Foster et al., 2000; Özer et al., 2020]. Sand boils occur frequently along rivers such as the Rhine (Fig. 1.1b), Mississippi and Danube, but generally do not result in failure. It is unclear to which extent those sand boils indicate a critical situation, and whether it becomes more and more dangerous over the years due to cumulative erosion. Recent safety assessments result in high failure probabilities for BEP and indicate that a large part of the levees in the Netherlands do not comply to backward erosion piping safety requirements [Georegister, 2021; Jorissen et al., 2016; Vergouwe, 2016]. For instance, in the VNK2 project, the flooding probability of 33 out of 58 dike ring areas were dominated by BEP failure [Vergouwe, 2016]. These high failure probabilities may be partly caused by conservative failure model assumptions, such as the assumption of immediate failure once a critical threshold is exceeded instead of a time-dependent failure process.

Finally, research into time aspects of backward erosion piping has been very limited, although several researchers have pointed at the relevance [Calle et al., 1985; Miesel, 1977; Vorogushyn et al., 2009]. Therefore chapter 2-6 of this thesis focuses on the role of time aspects in levee failure by backward erosion piping.

1.4 Knowledge gaps

The previous sections indicate that the current Dutch BEP safety assessment methods contain conservative assumptions, which are not in line with the current safety philosophy based on flooding probabilities. This holds in particular for the time required for the development of a piping failure, which is currently neglected. More accurate assessment methods may yield more realistic flooding probabilities and potentially reduce levee reinforcement costs and societal impact, or lead to more efficient investments in levees. The following paragraphs discuss the knowledge gaps, which prevent the development and application of more accurate assessment methods for time-dependent development of piping. Time-dependent pipe development includes different aspects: (1) high-water duration, (2) transient groundwater response, (3) timing of blanket rupture, (4) time-dependent erosion rate of the pipe, and (5) long-term effects like cumulative erosion. The focus is here on the 4th aspect, but the other aspects are also included in the thesis.

Regarding backward erosion piping, the overarching problem is that there is little knowledge about the time scale of the BEP erosion process as a function of head difference and soil properties, and how that translates into levee reliability. Previous research on BEP has mainly focused on the critical water level leading to failure (e.g., Bligh [1910]; Hanses [1985]; Miesel [1978]; Robbins et al. [2017]; Schmertmann [2000]; Sellmeijer [1988]; Van Beek [2015]; Vandenboer [2019]) instead of how fast that failure develops.

Estimates on time scales of internal erosion from both expert opinions [Barendregt et al., 2005; Brown and Aspinall, 2004] and field cases [Fell et al., 2003] vary by several orders of magnitude. Such a range would result in levees failing either within a few hours or not at all. This large uncertainty hampers practical application. Hence, there is a need for a predictive model of time-dependent BEP development.

Currently, there is no well-validated predictive model available for time-dependent BEP development (more details in section 2.2.5). The earliest analytical model by Kézdi [1979] includes some strong simplifications and is not validated. More recently, several numerical models have been developed [Fujisawa et al., 2010; Rotunno et al., 2017; Wang et al., 2014; Wewer et al., 2021]. However, each of these models was only validated on very few experiments, and some even not on transient parameters. Furthermore, these model validations are performed on an global parameter such as the time to failure, instead of the underlying processes separately. As these models are calibrated and contain many processes, errors in one process can be compensated by errors in other processes. Hence prediction of these models in deviating conditions remains uncertain.

The available BEP experiments reporting time-dependent pipe length development [Allan, 2018; Robbins et al., 2020a, 2017; Van Beek et al., 2010; Vandenboer et al., 2019; Yao, 2014] have insufficiently detailed measurements to allow for a more rigorous model validation. An important missing element in most of these tests are local measurements (i.e. in the pipe) of the seepage flow and pipe flow during critical conditions, instead of just the head difference over the entire structure. Furthermore, it is unknown which processes

govern the time scale of erosion. Is it the seepage at the pipe tip, as hypothesized by Kézdi [1979], or rather the sediment transport capacity of the pipe? This affects which modeling approach is suitable, and therefore understanding these processes is a prerequisite for further model development. Furthermore, an important issue which is also hampered by the lack of local flow measurements, is the translation from small-scale experiments to real-scale levees.

Finally, when such a well-validated model would be available, there are still problems regarding the translation from experiments and model result to failure mechanisms and levee reliability. The first is how to keep the reliability analysis efficient, given that time-dependent models are computationally expensive and required failure probabilities are very small. The second is how to deal with the fact that the reliability is time-variant [Buijs et al., 2009], as pipe development is a function of both hydraulic loading events (peak water level and duration), uncertain soil parameters, and the pipe development in previous events. Furthermore, this time-variant reliability depends on the long-term behavior of pipes after an extreme event: is there cumulative erosion or strength recovery by collapsing pipes? Very little is known about this [Rice et al., 2021]. And for practice, the ultimate question is how much of a difference it makes in the computed reliability of levees depending on factors such as flood duration and subsoil characteristics.

Regarding reliability in case of interactions between failure mechanisms, this is more common in the field of complex mechanical systems [Meango and Ouali, 2019; Sun et al., 2006] but unexplored in the field of flood defenses. Therefore, there is first of all a need to carefully describe such interactions in the context of flood defenses and provide examples. Furthermore, it is unknown in which conditions such interactions have a significant impact on flooding probabilities of levees, so whether this is an issue to worry about. Finally, a practical analysis framework is missing how to perform reliability analysis with interactions.

1.5 Research aims and questions

This thesis aims to improve levee reliability estimates by quantifying the time scale of the piping failure process and its impact on levee reliability. This aim is reflected in the main research question:

How can time-dependent development of backward erosion piping be quantified in levee reliability analyses?

The main question is analyzed with four key research questions, which are addressed in various chapters:

1. What processes determine the rate of pipe progression? (Chapter 3 and 4)
2. How can the time-dependent development of backward erosion piping in field conditions be modeled? (Chapter 5)
3. How is levee reliability impacted by the time-dependent development of backward erosion piping? (Chapter 6)
4. What are interactions between failure mechanisms and how can their impact on levee reliability be quantified? (Chapter 7)

1.6 Research outline and methodology

This section shortly describes the methods used for the different components of the research project and the associated chapters, and how these are related, see also Figure 1.3. The research uses a combination of methods: data collection and analysis of historical failures, analysis of previous experiments, conducting additional experiments on different scales, numerical modeling and probabilistic modeling.

Chapter 2 discusses the most relevant concepts and developments in the fields of backward erosion piping and reliability analysis. Furthermore, it presents some new field data on time-dependent aspects of historical levee failures by piping. These data are collected by literature study and archive research.

The experimental work on time-dependent pipe development includes a series of small-scale experiments (Chapter 3) and large-scale experiments (Chapter 4). The small-scale experiments are aimed at understanding the processes and variables that govern the time scale of the erosion process. The large-scale experiments provide an additional validation, and additionally explore the strength development over multiple flood events (cumulative degradation or strength recovery).

In order to translate the experimental results to field conditions, Chapter 5 develops a finite element model of time-dependent pipe development based on the erosion process observed in the small-scale experiments (Ch. 3). This model is validated on some of the small-scale and large-scale experiments (Ch. 3-4). Based on a large set of simulations with this finite element model, a simplified and efficient model of pipe development for field conditions is derived which can be used for reliability analysis (Ch. 6).

Chapter 6 quantifies the effect of time-dependent pipe development on levee reliability, both in terms of current failure probability and degradation over the years. Therefore, a time-variant reliability analysis approach is applied, which combines Monte Carlo Simulation and Numerical Integration. It uses the simplified pipe growth model from Chapter 5, extreme water level statistics, soil parameters and information on flood fighting interventions. The newly developed method is applied on simplified cases of Dutch levees in different water systems to show how time-dependence affects reliability estimates.

Chapter 7 explores the impact of interactions between failure mechanisms on levee reliability. Like Chapter 5, it uses a reliability analysis framework based on a combination of Monte Carlo Simulation, Numerical Integration and surrogate-modeling. First, the influence of interactions is studied for two simple systems. Then, the method is also applied to a levee example with an interaction between the failure mechanisms slope stability and backward erosion piping.

Finally, Chapter 8 presents the main conclusions and gives recommendations for practice and future research.

All-risk project

This research project is part of the All-risk research program [Kok et al., 2022], which aims to support the Dutch Flood Protection Program (HWBP) in implementing the new risk-based flood protection standards (<https://kbase.ncr-web.org/all-risk/>) This thesis is part of sub-project D, which focuses on the reliability of flood defenses. Other themes in the program are: A) risk framework; B) dynamics in hydraulic loads; C) subsoil heterogeneity; and E) law, governance and implementation.

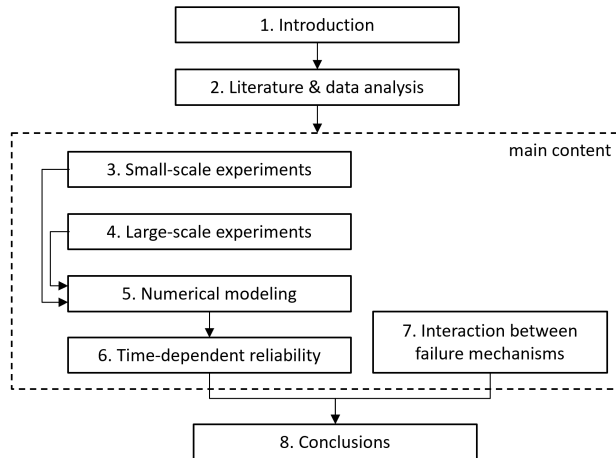


Figure 1.3: Graphical representation of thesis structure.

1.7 Originality

The main contribution of this thesis is that it provides an integral study of the time-dependence of piping failure in the context of levee reliability. It connects different methodologies: data collection of field cases, experimental work, numerical modeling and reliability analysis. Furthermore, it combines knowledge from different disciplines: geotechnical engineering, sediment transport and structural reliability.

The small-scale experiments are the first to show how piping development is related to sediment transport processes in the pipe, through an adapted experimental setup and more extensive measurements than in previous experiments. Although large-scale experiments were done before, the one in this thesis is the first one with concentrated outflow to a small hole (3D groundwater flow), and also the pipe progression can be better inferred from the measurements compared to previous ones. The large-scale recovery experiment is the first to show recovery of pipe resistance after pipe formation. Although time-dependent piping models have been developed before, the implementation in the DgFlow model is the first to use laminar sediment transport equations in a 3D piping model. Based on simulations with this model, a simplified regression model of the pipe progression rate is derived. The presented time-variant reliability analysis method to quantify the impact of time-dependent pipe development on levee safety has a stronger physical basis compared to previous studies. Furthermore, it provides estimates of how strongly time-dependent piping affects the safety of different types of levees and water systems in the Netherlands. The contribution of the analysis of interactions between failure mechanisms, is that it shows in which conditions these are relevant and that it gives guidance on approaches to include such interactions in levee reliability analyses.

2

Literature review and data analysis

Our practical experience can be very misleading unless it combines with it a fairly accurate conception of the mechanics of the phenomena under consideration.

Karl von Terzaghi

This chapter discusses some basic concepts on backward erosion piping, by reviewing the literature and performing additional analyses. The first part describes the failure mechanism, underlying processes, and models to predict the critical head. An analysis is presented on the differences in scale effects between two prediction models, namely the Sellmeijer and Shields-Darcy models. The second part describes the time-dependent development of backward erosion piping, instead of assuming constant equilibrium conditions which are only reached with a sufficiently long flood duration. Time-dependence can be described both at the time scale of extreme events and at the longer time scale of years. The event scale development focuses on the rate of pipe development in relation to the duration of the extreme hydraulic load. Long term development concerns cumulative degradation and potential recovery of pipes between extreme events. An analysis is presented of the time between initiation and breach in historic piping failures. The possibilities of drawing conclusions on cumulative damage or strength recovery from sand boil observations are discussed, and guidance is provided for future observations. Laboratory data which contain information on pipe development rates are described and analyzed, resulting in an empirical regression model to estimate rates of pipe progression based on soil and loading parameters. Finally, the available piping models with time-dependent pipe erosion are discussed. From the findings in this chapter it is concluded that a better understanding and modeling of time-dependent pipe development is needed.

2.1 Backward erosion piping: processes and equilibrium

2.1.1 Failure process

Backward erosion piping (BEP) is a specific form of internal erosion. According to ICOLD Bulletin 164 [ICOLD, 2017] there are four main forms of internal erosion:

1. concentrated leak erosion (enlargement of existing pipes);
2. backward erosion (pipe/void formation by seepage, progressing to upstream side);
 - (a) backward erosion piping (very small pipe developing below a supporting roof);
 - (b) global backward erosion (in case soil is unable to hold a roof, generally a larger void);
3. contact erosion (erosion of fine particles at interface with coarse layer above/below);
4. suffusion (transport of fine particles through the coarser soil fraction).

The general process of backward erosion piping is relatively well known from field observations and laboratory experiments. Backward erosion piping failure occurs when seepage induced by a head difference (H) over the levee leads to erosion of a granular levee foundation which is covered by a cohesive roof, to such extent that a shortcut forms between the upstream and downstream sides. The eroded grains are ejected to the ground surface and settle around the outflow location as a sand boil, which is the main visible sign of BEP.

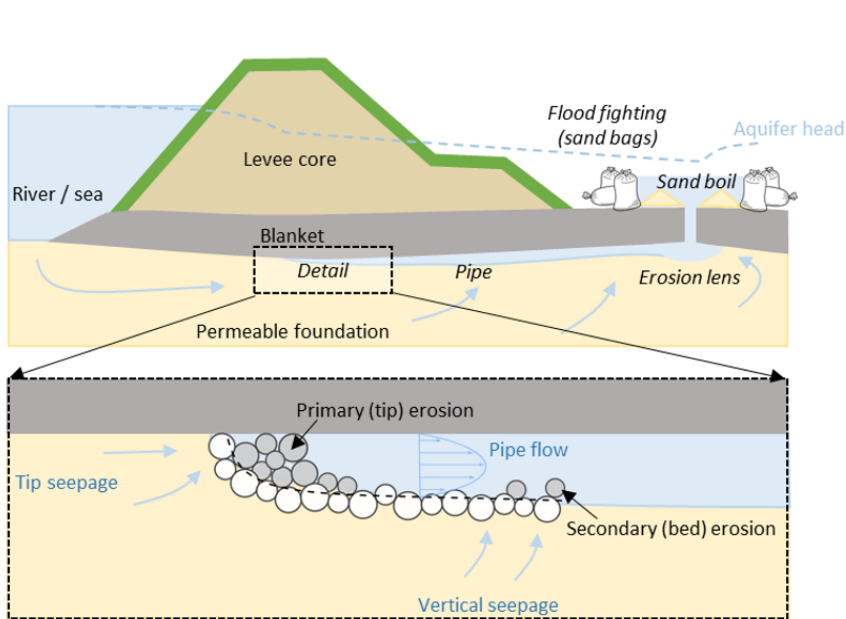


Figure 2.1: Graphical representation of the backward erosion piping process in a levee.

Increased water levels will first induce a seepage flow below the levee which leads to excess water at the land side. Next, for erosion to start there needs to be an unfiltered

exit. In areas with blankets (cohesive top layer on the land side) this generally means either a pre-existing crack through the blanket or rupture of the land side blanket by excess pressure in the aquifer. Then, (vertical) particle erosion will initiate when the local hydraulic gradient near the exit is sufficiently large. Initially, the erosion process will form a small circular erosion lens, which at some point transitions in one or more shallow pipes growing towards the river side. Up to this point, the process can be stopped by flood fighting interventions such as sand bags or filters. When the pipe connects to the river side, the flow rate accelerates and the pipe grows wider. The widening process is followed by gross settlement or slope failures finally resulting in a levee breach.

In specific conditions, some of these stages may not occur, such as rupture or flood fighting. Furthermore, from field observations it may not be evident that it concerns BEP. Other forms of internal erosion may also produce sand boils, for instance suffusion or liquefaction ('fast piping' in Tóth [2004]). To distinguish between BEP and suffusion, more information about the soil characteristics is needed.

2.1.2 Observations from previous research

Research overview

Backward erosion piping has been studied for more than a century. An overview of historical developments is given in Rice et al. [2021]. This section summarizes the main developments. Many of the researchers who studied the piping process in dikes have focused on the critical head H_c as the limit state, and the parameters that determine this critical head.

Based on observed failures, Bligh and Lane [Bligh, 1910; Lane, 1935] determined critical average gradients (H_c/L , where L is the seepage length) over a structure for a range of soil types. Research into the underlying processes started from the 1970's. At the University of Berlin, studies were conducted on factors such as the exit type and hole diameter [Miesel, 1978], multi-layered sands [Muller-Kirchenbauer, 1980] and effects of scale [Hanses, 1985]. Other experiments were conducted at the university of Florida [Townsend et al., 1981], which were used later by Schmertmann [2000] to develop an empirical model for the critical gradient. Following a large-scale experiment in the Netherlands [De Wit et al., 1981], Sellmeijer [1988] developed an analytical equilibrium model based on 2D groundwater flow, laminar pipe flow and stability of grains on the pipe bed (see Section 2.1.3). Later, Van Beek [2015] conducted a large set of new experiments to study factors like exit geometry, scale and sand characteristics. One of the findings is that there is a difference between the initiation of the erosion process and pipe progression. This is discussed below in more detail. Furthermore, the U.S. Army Corps of Engineers [Robbins et al., 2015, 2018] and Allan [2018] also conducted a large set of experiments. Vandenboer et al. [2018a] showed the importance of the 3D character of piping, i.e. the concentration of seepage from a wider area to a small pipe. Both Allan and Vandenboer also studied the effect over overloading, which is discussed in section 2.2.3.

Where most of the researchers mentioned above focus on the critical head of average critical gradient over the structure, some recent experimental work also aims to study local erosion conditions at the exit [Rice and Polanco, 2012], at the progressing pipe tip [Robbins et al., 2017; Xiao et al., 2018] or the pipe bed [Van Beek et al., 2019]. The resistance in a vertical crack through a blanket, caused by the sand-water-mixture, is analyzed

Table 2.1: Overview of experimental research on BEP, grouped by decade. Partly taken from Van Beek [2015]. * contains data on time-dependent pipe development.

Source	Research aims	*
Miesel [1977, 1978]	Erosion mechanism and effect of size of exit diameter.	
Muller-Kirchenbauer [1980]	Erosion mechanism in sand with multiple layers.	
Pietrus [1981]	Effect of artificially created pipe length and radius on critical head.	
De Wit [1984]	Effect of scale, type of exit point and sand properties on the critical head.	
Hanses [1985]	Erosion mechanism, pressure development in pipe and effect of scale on the critical head.	
Townsend et al. [1981]	Effect of sand characteristics on the critical head.	
Silvis [1991]	Investigation of scale effects.	
Yao et al. [2007]	Investigation of effect of configuration on piping process and critical head.	
Ding et al. [2007]	Investigation of piping in sand samples with multiple layers.	
Zhou et al. [2007]	Effect of cutoff wall length and position.	
Van Beek et al. [2008]	Lateral heterogeneity.	
Sellmeijer et al. [2011]	Large-scale experiment (IJKdijk).	
Van Beek et al. [2011]	Effect of scale and sand properties on the critical head.	
Yao [2014]	multi-layer aquifers	*
Van Beek et al. [2014]	initiation in uniform sands	
Van Beek et al. [2015]	3D (hole) experiments at two scales with a range of sand types	
Robbins et al. [2017]	Measuring local gradients in cylindrical setup.	*
Montalvo-Bartolomei et al. [2018]	Initiation of erosion on slope	
Robbins et al. [2018]	Tests on fine gravel	
Allan [2018]	Influence of geometry, exit types, graded soils, cyclic loading and erosion rate.	*
Vandenboer [2019]	3D-effects, pipe geometry, overloading	*
Van Beek et al. [2019]	critical shear stress in cylindrical setup.	
Xiao et al. [2019a,b]	micro-scale observations and analysis of erosion at pipe tip.	
Dirkx et al. [2020]	influence of grain size distribution on initiation	
Akrami et al. [2020]	Medium-scale experiments with Coarse Sand Barrier	
Rosenbrand et al. [2020]	Multi-scale experiments with Coarse Sand Barrier	
Robbins et al. [2020a]	Progression rates in small-scale slope-type experiments	*

theoretically and empirically by Robbins et al. [2020b].

For a more detailed treatment of the BEP process the reader is referred to overviews in Van Beek [2015], Robbins [2016] or Rice et al. [2021]. Two concepts relevant for time-dependence will be explained below: primary vs. secondary erosion, and pipe equilibrium (the difference between initiation, regressive erosion and progressive erosion). Furthermore, some stability criteria for primary and secondary erosion are given.

Primary and secondary erosion

Hanses [1985] observed that backward erosion includes two erosion processes: primary and secondary erosion (Fig. 2.1). Primary erosion is the lengthening of the pipe at the pipe tip. Secondary erosion is the deepening and widening of the pipe. Primary erosion is caused by strong seepage forces that let the soil structure at the tip collapse, resulting in pipe lengthening. Secondary erosion (or lateral erosion) can be caused by the same process along the pipe walls, but also by grains being eroded by the pipe channel flow that exerts a shear stress on the pipe walls and bed. This leads to widening and deepening of the pipe. It is important to note that these two processes are strongly related. In the end, pipe lengthening causes the pipe to progress and ultimately collapse of the structure. But this primary erosion depends on the secondary erosion. Pipe deepening or widening reduces the pipe gradient, which in turn increases the hydraulic gradient in the soil just upstream of the pipe tip, which drives the primary erosion. On the other hand does continuous primary erosion result in a sediment load to be transported by the pipe flow, which reduces the secondary erosion. This is explained and illustrated in more detail in chapter 3, for instance in Fig. 3.1.

Initiation and progression

The critical head can be dominated by initiation or progression [Van Beek, 2015]. Piping initiation is marked by the change from an intact sand bed to a small pipe [Rice and Polanco, 2012]. It occurs when the gradient near the exit exceeds a critical gradient and the sand can be transported out of the sand layer. In some cases that leads to an ongoing erosion process, when flow in and towards the pipe increases with increasing pipe length l . In these cases the critical head is initiation-dominated. In other cases the erosion process reaches an equilibrium at a certain pipe length, and further pipe lengthening only takes place after sufficient head increase. The critical head in this situation is progression-dominated. It occurs when the tip gradient decreases with pipe length.

Both cases are represented in the equilibrium curves shown in Figure 2.2. It plots the equilibrium head H_{eq} as function of pipe length l/L . The critical head H_c is the maximum of H_{eq} and l_c is the corresponding critical pipe length. The part where $l < l_c$ is defined as the regressive erosion phase, and $l > l_c$ as the progressive erosion phase. In the progressive phase, only a head reduction can bring the erosion process back to equilibrium. Initiation-dominated cases have $l_c = 0$, and progression-dominated cases $l_c > 0$. For infinitely deep aquifers the model of Sellmeijer and Koenders [1991] results in $l_c \approx 1/2L$, but it can be more or less depending on the geometry of the aquifer. An alternative expression for l_c as function of aquifer geometry is provided in chapter 6 (Eq. 6.12). The experimental work in this thesis focuses mainly on the progressive erosion phase due to measurement constraints, and the numerical modeling and reliability analysis also include the regressive phase.

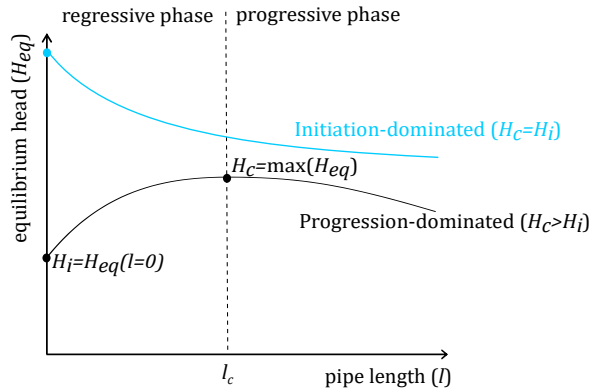


Figure 2.2: Initiation-dominated and progression-dominated equilibrium curves: equilibrium head H_{eq} as function of pipe length l .

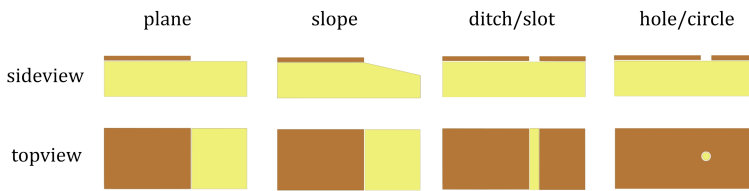


Figure 2.3: Main exit types: plane, slope, ditch, hole. Adapted from Allan [2018]

Which cases are initiation-dominated and which progression-dominated? This largely depends on the type of outflow (see Fig. 2.3). In homogeneous sands, hole-type exits are progression-dominated, whereas ditch-, slope- or plane-type exits tend to be initiation-dominated [Van Beek et al., 2015]. This can be explained by 3-dimensional groundwater flow [Vandenboer et al., 2018a]. In case of hole-type exits, the flow is initially strongly concentrated which easily leads to initiation, but when the pipe develops, the inflow spreads along the entire pipe which can lead to lower tip gradients. In case of the other exit types, the flow is initially spread over the entire width of the seepage domain. This requires a larger head drop to generate high local gradients to initiate erosion. Once the pipe develops, the flow concentrates more, which leads to increasing tip gradients and ongoing erosion.

Note that rupture of the blanket also plays a role: a hole-type exit can still be initiation-dominated if the critical head for uplift or rupture of the blanket is higher than the critical head for pipe progression. Similarly, heterogeneity can make ditch-type exits progression-dominated because a strong layer stops the pipe development at a certain pipe length.

As already noted by Muller-Kirchenbauer [1980], these equilibrium mechanisms can explain why there are much more sand boil observations than breaches. Other explanations why the erosion process is not always completed are flood duration, the presence of stronger layers (heterogeneity) and flood fighting measures.

Primary erosion criteria

Primary erosion is caused by horizontal and vertical seepage forces at the pipe tip. The critical hydraulic gradient of a slope under outward seepage is given by [Kovács, 1981]

$$i_c = -\frac{\gamma_{sat} - \gamma_w}{\gamma_w} \cdot \frac{\tan(\phi) \cos(\alpha_{sl}) - \sin(\alpha_{sl})}{\cos(\alpha_{sl} - \alpha_i) + \tan(\phi) \cos(\alpha_{sl} - \alpha_i)} \quad (2.1)$$

Where γ_{sat} and γ_w denote the bulk weight and the water weight [kN/m³], ϕ denotes the friction angle, α_{sl} the slope angle, α_i is the seepage angle with respect to the line perpendicular to the slope. For $\alpha_{sl} = 0$ and $\alpha_i = 0$, this reduces to the criterion for fluidization due to vertical seepage by Terzaghi [1922]. Such a theoretical approach has a number of drawbacks. For instance, the relevant slope angle at the tip is unknown. It also neglects 3D components of the resistance against primary erosion, such as arching effects [Tran et al., 2017]. Therefore, empirically determined critical gradients are still valuable. However, due to the strong flow concentration near the tip, a difficulty with an empirical approach is that the critical gradient will strongly depend on the distance over which it is measured. To account for this, Robbins [2022] developed the critical secant gradient function (CSGF). It consist of an analytical approximation for the head profile near the pipe tip, and an empirical coefficient C_{CSGF} which is a function of sand properties. The critical gradient i_c evaluated over distance x is given by:

$$i_c(x) = C_{CSGF} \cdot x^{-1/2} \quad (2.2)$$

in which

$$C_{CSGF} = 0.019 \left(\frac{d_{50}}{d_{50,m}} \right) + 0.115 \left(\frac{C_u}{C_{u,m}} \right) + 0.006 \left(\frac{e}{e_m} \right)^{-19.8} \quad (2.3)$$

where C_u is the uniformity coefficient (d_{60}/d_{10}), e void ratio and the regression coefficients are best estimates. In their dataset, $d_{50,m}$, $C_{u,m}$, and e_m were 0.581 mm, 2.02, and 0.581 respectively.

Secondary erosion criteria

Secondary erosion is defined as the widening and deepening of the pipe. Sellmeijer [1988] uses a secondary erosion criterion based on White [1940], who analyzed the equilibrium of a rolling particle under a drag force. This yields the following critical bed shear stress:

$$\tau_c = 1/6\pi\eta(\rho_s - \rho_w)gd \tan \theta \quad (2.4)$$

Where η [-] is a coefficient, θ is the bedding angle and d is a representative grain diameter [m]. Sellmeijer chose $\eta = 0.25$, $\theta = 37^\circ$ and $d = d_{70}$ based on the best fit of his model with large-scale experiments [Silvis, 1991].

The critical Shields number is widely used to describe sediment stability and is defined as:

$$\Theta_c = \frac{\tau_c}{(\rho_s - \rho_w)gd} = f(D_*) \quad (2.5)$$

Where D_* is the dimensionless particle diameter ($D_* = d \cdot (\Delta g / \nu^2)^{1/3}$), $\Delta = \rho_s / \rho_w - 1$ and ν is the kinematic viscosity [m^2/s].

In Eq. 2.4, the critical shear stress is proportional to the grain size, or the critical Shields number is independent of grain size. However, it is known that the critical Shields number varies with grain size, especially in the laminar flow regime [Hoffmans and Van Rijn, 2017], see Figure 2.4. Van Beek [2015] included the effect of grain size in the equation of White (Eq. 2.4) by making the bedding angle (θ) an empirical function of the grain size d_{50} and fitting this to experiments of critical shear stress in laminar flow. This yields Eq. 2.4 in which $\eta = 0.3$, $d = d_{50}$, $\theta = -8.125 \ln d_{50} - 38.777$. This relation is valid for approximately $d_{50} < 0.5$ mm; in coarser sands the flow may become turbulent. Critical shear stresses in pipes were measured in the small-scale experiments (chapter 3). The transition from equilibrium to general grain movement is gradual in turbulent flows or non-uniform sands due to randomness in bed shear stress and grain diameter, but it is sharp in uniform sand in laminar flow [Yalin and Karahan, 1979].

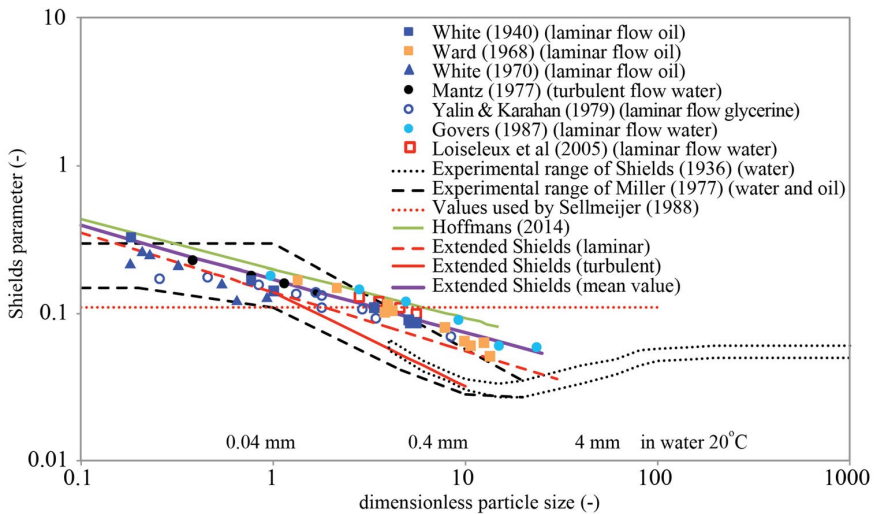


Figure 2.4: Critical Shields number in laminar flow as function of dimensionless particle size [Hoffmans and Van Rijn, 2017].

The classical flume experiments shown in Fig. 2.4 are conducted in flumes with uniform channel depths in lateral direction, so the cross sectional profile is rectangular. In piping experiments, the channel is not rectangular and also meandering. Furthermore, the channel bed in piping experiments is exposed to upward seepage. Upward seepage reduces both the occurring shear stress through a change in velocity profile, as well as the critical bed shear stress through an additional upward force [Cheng and Chiew, 1999; Francalanci et al., 2008; Liu and Chiew, 2012; Lu et al., 2008]. Upward seepage effects on the critical shear stress were included in the model of Sellmeijer [1988] but omitted from a later version of the Sellmeijer model [Sellmeijer, 2006] as he expected that this would not affect the critical grains on top of the bed but only grains deeper in the bed. Above-mentioned studies on upward seepage are conducted for turbulent open channel flow, and

additional experiments in pipes or in laminar flow are needed to confirm whether similar effects can be expected for laminar pipe flow. Preliminary observations in the small-scale experiments (section 3.4.3) suggest that this effect is also present in laminar flow.

2.1.3 Equilibrium models

Backward erosion piping is a complex process in which the processes of seepage, pipe flow, particle equilibrium and particle transport interact. There are several approaches to predict the critical head for a given structure, which can be grouped into three categories:

1. Fully empirical line of creep models [Bligh, 1910; Griffith, 1914; Lane, 1935]
2. Semi-analytical models [Hoffmans and Van Rijn, 2017; Schmertmann, 2000; Sellmeijer et al., 2011; Sellmeijer, 1988]
3. Numerical models [van Esch et al., 2013; Robbins and Griffiths, 2021; Sellmeijer, 2006; Vandenboer et al., 2014; Zhou et al., 2012]

The following sections elaborate on a few of these models.

Empirical line of creep methods

Based on a large number of failures of hydraulic structures and dams, Bligh [1910] and Griffith [1914] suggested that the critical gradient can be given by a single factor (C_{creep}) which depends on the foundation soil type:

$$H_c = L/C_{creep} \quad (2.6)$$

The creep factor C_{creep} [-] for design purposes varies from 4 for coarse gravel to 18 for fine silty sand [Lane, 1935; Richards and Reddy, 2007]. These creep factors implicitly contain a safety margin of approximately a factor 1.5 [Kanning, 2012; Lane, 1935].

Lane [1935], following observations of Griffith [1914], proposed to separate the horizontal and vertical seepage path, where the equivalent seepage length equals the vertical part L_v + 1/3 of the horizontal part L_h . Consequently other creep factors ($C_{creep,Lane}$) are obtained: between 3 (coarse gravel) and 8.5 (fine silty sand). If one would apply Lane's approach to the case without a vertical seepage path ($L_v = 0$) and rewrite to the form of Eq. 2.6, this yields $C_{creep} = 3 \cdot C_{creep,Lane}$, so between 9 (coarse gravel) and 25.5 (fine silty sand). It appears that for cases without a vertical seepage path, Lane's method yields lower critical heads than Bligh's method.

Note that all cases as presented in Lane [1935] have a vertical seepage path, see Fig. 2.5. Their strength may be determined by heave behind the cutoff walls instead of backward erosion. Although more detailed analysis is needed, the data in Fig. 2.5 suggest that the creep ratio tends to be lower when there is less vertical seepage path. Also note that many of these cases are hydraulic structures such as weirs. Stiff (concrete) structures are more prone to unequal settlements and a consequent void between structure and foundation, compared to soft levees. Finally, many factors which are currently known to be important (e.g. aquifer thickness, downstream blankets or exit types), are unknown for these cases. Given these unknowns and the differences with typical levees, caution is needed in the application of these design rules for levees.

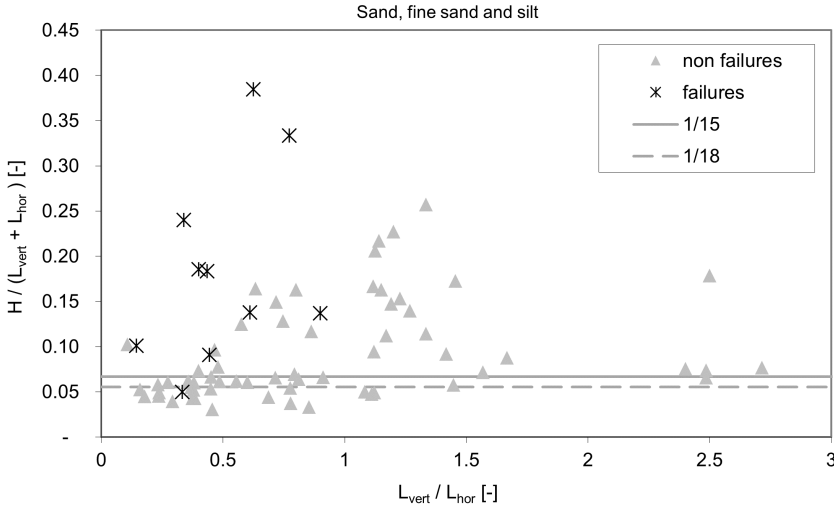


Figure 2.5: Ratio between horizontal (L_{hor}) and vertical (L_{vert}) seepage length in cases used by Bligh and Lane. Based on data from Kanning [2012]; only cases with foundations of sand, fine sand and silt.

Sellmeijer

The Sellmeijer model is the default pipe progression model in The Netherlands, and also internationally recognized as one of the most advanced BEP models [CIRIA, 2013]. The original model is published in Sellmeijer [1988]. It is a semi-analytical equilibrium model based on 2D groundwater flow, laminar pipe flow and stability of grains on the pipe bottom (secondary erosion). For a range of pipe lengths (l), it calculates the head at which the grains in the pipe are just in equilibrium (H_{eq}), resulting in an equilibrium curve like figure 2.2. The critical head H_c (and associated critical length l_c) is then defined as the maximum head on that curve. Curve-fitting of H_c for different parameter combinations leads to an engineering formula for a standard levee (impermeable levee, no cutoff structures, a single homogeneous horizontal aquifer, no blanket on the landward side). Later, the model was implemented in a finite element seepage model (MSeep) to include more complex geometries such as aquifers with a finite depth, which led to an adjusted design formula [Sellmeijer, 2006]. In 2011, the model was adjusted empirically to correspond better with experiments, mainly for courser sands [Sellmeijer et al., 2011]. The adjusted formula for H_c reads:

$$H_c = F_r \cdot F_s \cdot F_g \cdot L \quad (2.7)$$

$$F_r = \eta \frac{\rho_s - \rho_w}{\rho_w} \tan \theta \cdot \left(\frac{D_r}{D_{r,m}} \right)^{0.35} \cdot \left(\frac{C_u}{C_{u,m}} \right)^{0.13} \cdot \left(\frac{KAS}{KAS_m} \right)^{-0.02} \quad (2.8)$$

$$F_s = \frac{d_{70}}{\sqrt[3]{\kappa L}} \cdot \left(\frac{d_{70,m}}{d_{70}} \right)^{0.6} \quad (2.9)$$

$$F_g = 0.91 \left(\frac{D}{L} \right)^{0.28 / [(D/L)^{2.8} - 1] + 0.04} \quad (2.10)$$

In which ρ_s and ρ_w denote the sediment and water density [kg/m^3], η the coefficient of White [-], θ the angle of repose [deg], D_r the relative density [-], C_u the uniformity coefficient [-], KAS the angularity [-], d_{70} the grain size [m], κ intrinsic permeability [m^2], L seepage length [m], D aquifer thickness [m]. $D_{r,m} = 0.725$, $d_{70,m} = 2.08 \cdot 10^{-4}$ m, $C_{u,m} = 1.81$ and $KAS_m = 0.498$ are mean values in the experiments used for the multivariate regression.

Shields-Darcy

The Shields-Darcy (SD) model [Hoffmans and Van Rijn, 2017] describes the same piping process (BEP), but has a different approach and different assumptions. It represents the total critical head drop as the sum of the pipe head drop and the head drop in the aquifer upstream of the pipe. The model is given by Eqs. 2.11 - 2.14:

$$\frac{\Delta H_c}{L} = S_{pipe,c} + \left(1 - \frac{l_c}{L}\right) (S_{sand,c} - S_{pipe,c}) \quad (2.11)$$

$$S_{pipe,c} = \frac{\sqrt{g} (\Theta_c (\rho_s / \rho_w - 1) d_{15})^{3/2}}{\nu \sqrt{\alpha_R}} \quad (2.12)$$

$$S_{sand,c} - S_{pipe,c} = \frac{d_{50} \nu}{l_R k D} \quad (2.13)$$

$$\frac{l_c}{L} = \exp\left(-\left(\frac{\alpha_f D}{L}\right)^2 S_{pipe,c}\right) \quad (2.14)$$

Where l_c denotes the critical pipe length [m], $S_{pipe,c}$ and $S_{sand,c}$ the critical average hydraulic gradient in the pipe and the upstream sand [-], Θ_c the critical Shields parameter [-], ν kinematic viscosity [m^2/s], k hydraulic conductivity [m/s], and $\alpha_R = 6$, $\alpha_f = 5$, $l_R = 18 \cdot 10^{-6}$ m are calibration parameters. According to Hoffmans and Van Rijn [2017], $S_{dike,c} \approx S_{pipe,c}$ for field scales, so the critical gradient is governed by the pipe gradient. Then the pipe gradient can be expressed as:

$$S_{pipe,c} = \sqrt[3]{g(\rho_s/\rho_w - 1)^4 \nu^{-2}} \cdot \sqrt{\frac{(0.2d_{15})^3}{\alpha_R d_{50}}} \approx 1260 d_{15} \sqrt{\frac{d_{15}}{d_{50}}} \quad (2.15)$$

Discussion of Sellmeijer and Shields-Darcy

Differences and similarities between Shields-Darcy and Sellmeijer are discussed in Van Beek and Hoffmans [2017], who note that both model similar processes such as 2D groundwater flow, 1D laminar pipe flow and bed particle equilibrium, but the model outcomes can be very different. These differences were further analyzed during this PhD project in terms of model assumptions, calibration data sets, model results for varying conditions and scale effects [Pol, 2020, 2022]. This section summarizes the findings from the latter two studies.

Particle equilibrium in the original Sellmeijer [1988] model is based on White [1940], which implies a critical Shields number Θ_c which is constant with particle size. The SD model derives Θ_c from laminar flow experiments, where it appears to be a function of grain size. This approach has a better physical basis than the recalibrated effect of grain size ($d_{70,m}/d_{70}$)^{0.6} in Sellmeijer et al. [2011]. However, the difference in critical shear stress

is small for fine, uniform sands, which are often susceptible to BEP. Furthermore, the predicted effect of soil grading (higher strength for more uniform sand) in the SD model is not supported by experiments.

In the Sellmeijer [1988] model, the groundwater flow is solved analytically for an aquifer of infinite depth without blanket. The Sellmeijer et al. [2011] update includes the geometry factor F_g to account for different D/L ratios with impermeable blanket. F_g is derived from simulations with the finite element seepage - piping model MSeep [Sellmeijer, 2006], so this factor is not empirical. Groundwater flow in the SD model is simplified by horizontal flow through the upper part of the aquifer, and assumptions are being made for the distribution of groundwater flow between the pipe and the landward aquifer.

Pipe flow in SD is based on Poiseuille flow: laminar flow in a circular pipe. To translate the critical Shields number to a critical pipe gradient, one needs a hydraulic radius R . This R is unknown, and replaced in the SD model with a calibration parameter α_R (Eq. 2.12). Furthermore, the SD model assumes that the critical pipe discharge $q_{p,c}$ at the land side is equal to $\frac{d_{50}v}{l_R}$, as reflected in Eq. 2.13. Based on analyses with the 2D finite element model D-GeoFlow [Deltares, 2020], Pol [2022] argued that both parameters should be a function of d_{50} and scale (L or D). Large grains and larger aquifers generate a higher discharge and a larger pipe; consequently the gradients are lower to obtain the same critical shear stress (Fig. 2.7). These two assumptions in the SD model can explain why the SD model shows a negligible scale effect in the critical gradient (Fig. 2.6) and why the computed critical head at large scales is much larger than in the Sellmeijer model. The scale effects in D-GeoFlow results are present in all model simulations, regardless of the assumed type of polder boundary conditions (Fig. 2.6). Results of Sellmeijer et al. [2011] and D-GeoFlow (with boundary A) are very close, hence the scale effect in the Sellmeijer model are better supported by numerical modeling than those in the SD model.

Furthermore it is noted that both models are only calibrated on initiation-dominated experiments (slope and plane exits in Fig. 2.3). This is striking, because the stability criterion in both models is based on equilibrium of particles on the pipe bed, whereas in initiation-dominated experiments this equilibrium is never obtained. It was also found in Pol [2022] that the calibrated parameters in both models are sensitive for the choice of calibration dataset, which indicates that the processes are not sufficiently represented by the calibrated models.

Numerical equilibrium models

Empirical and semi-analytical models are not suitable to include a high level of complexity, such as multiple layers, soil heterogeneity or different groundwater boundary conditions. Therefore numerical models have been developed to simulate BEP. MSeep is a stationary finite element groundwater flow model with an implementation of Sellmeijer's piping model [Sellmeijer, 2006]. For a range of pipe lengths $0 < l/L < 1$, it computes the equilibrium head H_{eq} for which particle equilibrium is satisfied in the entire pipe. This yields H_c and l_c . DgFlow [van Esch et al., 2013] is an implementation of Sellmeijer's model in a three-dimensional transient seepage model. This model is still under development at Deltares, and currently also includes a primary erosion criterion, specified as critical hydraulic gradient [van Esch, 2015]. The BEP model by Robbins and Griffiths [2021] includes both laminar and turbulent pipe flow, primary and secondary erosion, and a searching pipe

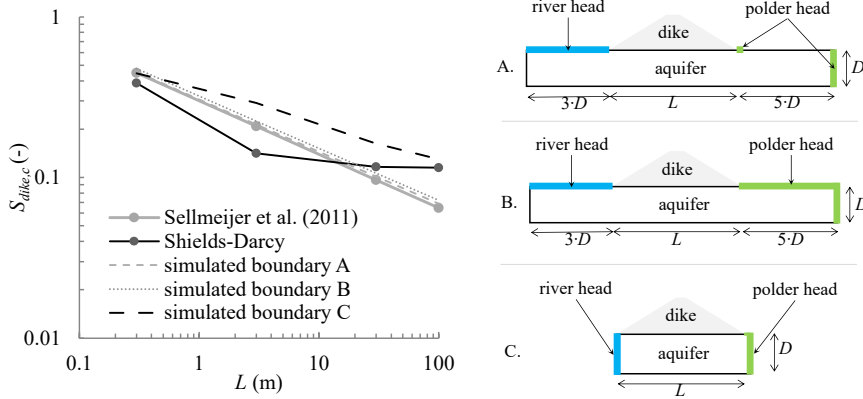


Figure 2.6: Effect of scale on critical gradient of Sellmeijer, Shields-Darcy, and D-GeoFlow models. For $d_{50}=0.180$ mm, $D/L=1/3$. Boundaries: A=impermeable blanket, B=no blanket, C=constant head across depth.

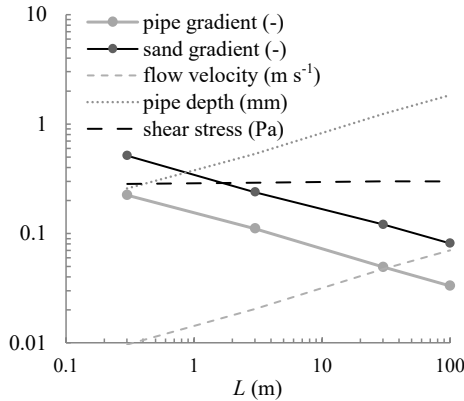


Figure 2.7: Effect of scale on aquifer and pipe flow conditions in D-GeoFlow simulations. For $d_{50}=0.180$ mm, $D/L=1/3$, impermeable polder blanket.

path with adaptive meshing. However, it is in 2D (plane view) and the effect of aquifer depth is incorporated by a correction factor. Other examples of equilibrium models are Zhou et al. [2012] and Vandenboer et al. [2014]. Time-dependent numerical models are discussed in section 2.2.5, including discrete element and multi-phase models. An extensive overview and classification of numerical piping models is given in Robbins [2022].

2.2 Backward erosion piping: time-dependent development

2.2.1 Time-dependent processes

With respect to time-dependent processes, it is useful to make a distinction between event scale behaviour (processes varying during a flood event) and long term behaviour occurring over multiple years, such as deterioration. The next sections discuss both types of behaviour for BEP.

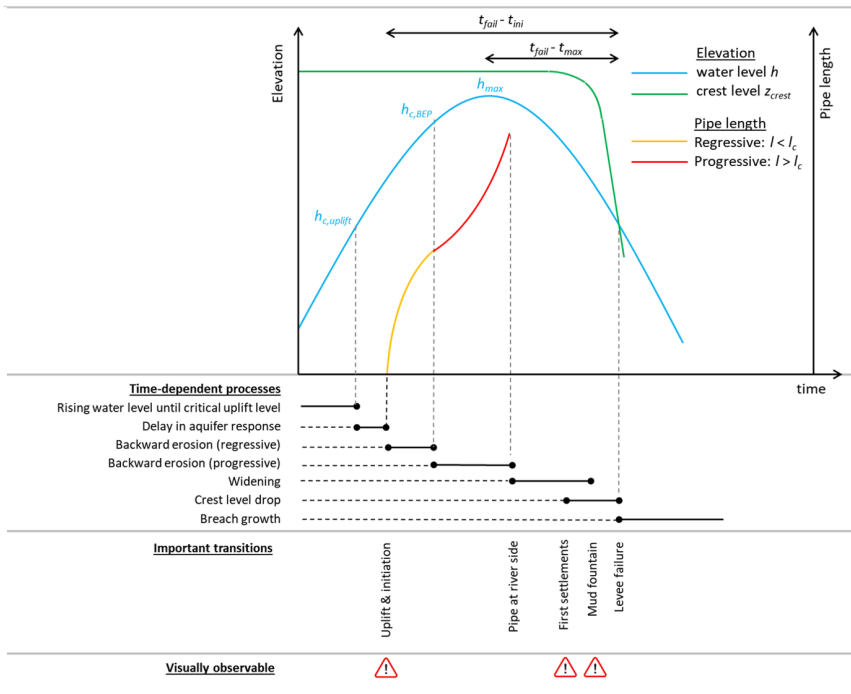


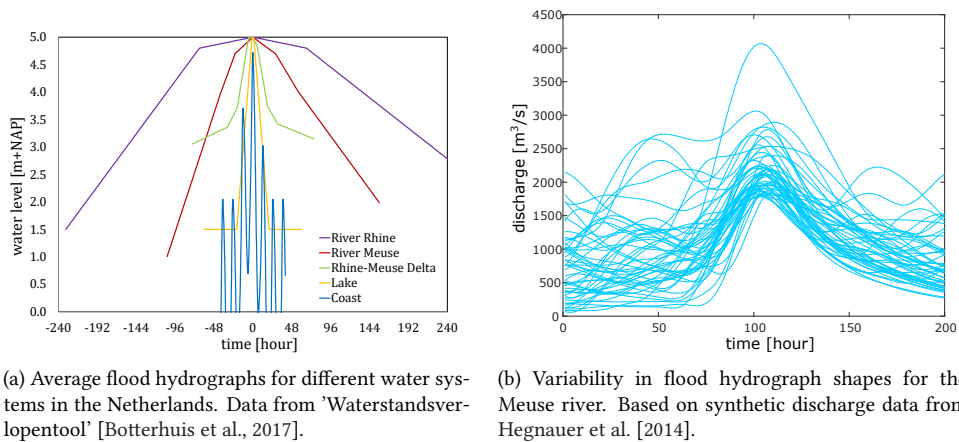
Figure 2.8: Conceptual figure of development of piping in time during a flood event: processes and (observable) transitions in levee state.

Event scale processes

Figure 2.8 visualizes the relevant processes for the development of backward erosion over time, including (observable) changes in the levee geometry. The time-dependent components can broadly be classified in (A) hydraulic loading, (B) transient groundwater flow and (C) soil erosion processes.

(A) Hydraulic loads for piping are high water levels. The longer the high water duration, the more pipes can erode. The characteristic development of the high water level over time, the *hydrograph*, is region-specific and depends on the origin of the flood event, mostly extreme river discharge or storm surge. In the Netherlands, extreme discharges last typically for weeks, while storm surges last between hours to a few days. Figure 2.9a shows average flood durations for the Rhine and Meuse rivers and for the storm surge in coastal areas in the Netherlands. In estuaries and tidal rivers, floods can be compound events of river discharge and storm surge. Hydrograph shapes or flood durations can show a high natural variability [Pol et al., 2015; Vorogushyn et al., 2010], as Figure 2.9b illustrates for hydrographs on the Meuse river.

(B) The aquifer pressure responds with some delay and damping to a water level increase in the river or sea, depending on the flood duration and the geohydrological aquifer and blanket characteristics. A stronger damping is obtained for relatively short floods, low aquifer transmissivity, high conductivity of the polder blanket and wider foreshores. Sev-



(a) Average flood hydrographs for different water systems in the Netherlands. Data from 'Waterstandsverlooptool' [Botterhuis et al., 2017].

(b) Variability in flood hydrograph shapes for the Meuse river. Based on synthetic discharge data from Hegnauer et al. [2014].

Figure 2.9: Hydrographs (flood duration): averages (left) and example of variability (right).

eral models for transient groundwater flow under dikes are available, examples include both analytical [Moench and Barlow, 2000; Ozkan et al., 2008; TAW, 2004] and numerical models [van Esch et al., 2013].

(C) In case the aquifer pressure leads to uplift and rupture of the cohesive layer, the backward **erosion** process is initiated. The progression rate of backward erosion depends on several factors including the soil characteristics and head difference, which is discussed in more detail in section 2.2.4 and is an important subject of chapter 3-6. Once the pipe is connected to the upstream side, the small pipe widens from upstream to downstream. The enlargement or widening process can take significant time due to temporary clogging and clearing of the pipe [Van Beek et al., 2010]. When the pipe widened sufficiently, the process accelerates strongly, resulting in a mud fountain and levee failure.

Long term behaviour

Rivers in the Netherlands (Rhine), the USA (Mississippi) and Italy (Po) frequently experience sand boils but very few levee breaches [Aielli et al., 2018; Glynn et al., 2012; Van Beek et al., 2018]. Piping erosion can develop gradually over the years without levee failure and without clear sign how far erosion has progressed. This raises the question whether these sand boils are a gradually increasing threat to the levee safety due to cumulative erosion. Three aspects related to this long term behaviour are:

1. decrease or increase in piping initiation level over the years;
2. cumulative strength degradation or strength recovery;
3. changes in hydraulic load (subsidence, sea level rise and changing river discharges).

Equilibrium curves (Fig. 2.2) can help to understand long term behavior from the perspective of backward erosion. If pipes developed in the regressive regime, piping may reactivate in a subsequent flood at a higher water level. On the other hand, if a pipe is in the progressive regime, each sand boil leads to a reduction of the strength and piping

reactivates at lower water levels during subsequent floods. In practice, the behavior is more complicated due to sand which settles in the sand boil after an event and is easily ejected by the concentrated upward flow (heave).

Piping is defined to have a fully cumulative character if there is no strength recovery between two flood events. This means that during a subsequent flood, the pipe continues to grow from the state at the end of the previous flood. This is also called the memory-effect, as the resistance depends on flood events in previous years. Alternatively, pipes may recover fully or partly to their original strength. Possible recovery mechanisms are settlement of the cohesive roof into the pipe or filling of the pipe by fine material. Settlement could be accelerated by traffic loads and fluctuations in groundwater level or temperature. Filling could be enhanced by rainfall and runoff and biological activity. Both mechanisms reduce the pipe depth, but in case of filling the grain size in the pipe may also change. These processes are still poorly understood due to a lack of laboratory and field measurements. Section 2.2.2 discusses the use of field observations to study strength recovery. Section 4.4.4 describes a strength recovery experiment.

Finally, the hydraulic drivers of the process also change over the years. Important factors are climate change (sea level rise or changes in extreme river discharge), land subsidence, and human interventions in water systems (excavations, sand mining).

2.2.2 Field observations

Field data on BEP was collected for two goals: (1) to obtain an indication of the time between initiation and breach in historical failures, and (2) to obtain an indication of long term trends in the critical head based on sand boil observations (cumulative erosion). Cases have been limited to piping in levees, so cases in large dams have not been included.

BEP levee failures in The Netherlands

Internationally, many levee or dam breaches have been attributed to BEP [Danka and Zhang, 2015; Foster et al., 2000; Fry, 2016; Özer et al., 2020]. Although many sand boils have been observed during high water events, only two levee breaches of primary flood defenses in The Netherlands can be attributed to backward erosion piping. One was located along the river IJssel near Zalk in 1926 and one along the Eastern Scheldt estuary at Strijenham (near Tholen) in 1894. Previous authors include a third case along the river Meuse near Nieuwkuijk [Van Beek et al., 2018] in 1880. However, the report of the chief engineer Bake [Johanson, 1981] describes that a rod could be pushed horizontally in the erosion hole halfway at the inner slope. This demonstrates that this breach is likely caused by internal erosion through the sandy levee core, and not by backward erosion piping in the foundation. It is likely that there have been more piping failures in the past, but cases may be under-reported because the mechanism was not well known and with the breach often the evidence is gone.

The case of Strijenham is of particular interest because (a) it is in a coastal area with short storm surges and few sand boil observations, and (b) it failed during a moderate high water event one week after an extreme storm. This example illustrates that levees in tidal areas subject to a short flood duration can also fail by BEP; that the mechanism does not only occur in river levees. Although the short flood duration and additional strength of tidal deposits can increase the resistance against piping significantly, there is also little

time for detection and emergency measures compared to riverine systems. Appendix A presents a reconstruction of the historical situation of the levee and historical water levels based on archive research.

Timing of piping failure in levees

Although historical levee failures attributed to BEP provide no direct evidence about the rate of backward erosion, these cases may provide information on the order of magnitude of the duration of the failure process, and variation therein. Table 2.2 summarizes the BEP cases in levees for which information is available regarding the time of failure (breach observed), the time of initiation (sand boil observed) and the time of the flood peak. t_1 is the time between initiation (sand transport) and failure (breach). t_2 is the time between flood peak and failure; negative numbers indicate failure before the peak. L is the seepage length.

The table immediately makes clear that there is a huge range in the estimated time between initiation and breach (t_1), from a few minutes up to a month. If one would interpret the ratio L/t_1 as a rough approximation of the progression rate, these values range from 0.1 to 100 m/hour, or approximately 10^{-5} to 10^{-2} m/s (Fig. 2.10a).

A direct translation of these numbers to piping assessments of levees is difficult, for a number of reasons. First, in practice it is often unclear whether failure is of the classical backward erosion type, or that it may be uplift or liquefaction followed by slope failure, because of the lack of accurate eyewitness reports. Second, there may have been erosion before sand boiling was reported, in which case t_1 is an underestimate. Third, during the period t_1 the erosion process may have stopped, either naturally or by flood fighting, in which case t_1 is overestimated and L/t_1 underestimates the progression rate. Fourth, there may have been pipes or weakened zones present before the flood event, in which case L/t_1 overestimates the progression rate. These uncertainties make it hard to draw strong quantitative conclusions from these field cases, but it is clear that the variation is large and that the erosion process requires substantial time in some cases.

Regarding the timing of failure with respect to the flood peak (t_2), 2/3 failed after the peak (Fig. 2.10a). The median value of t_2 is 2.3 hours after the peak, the mean 3.8 hours, and the standard deviation 68 hours. The large range originates mainly from the Paizhou, Jiujiang and Strijenham cases which failed several days from the peak. In case of an instantaneous failure process, one expects that all failures occur before the peak. So these observations show that there is a delay involved in piping failure, for instance through time lags in ground water response or time required for the erosion process.

Field observations on cumulative erosion or recovery

As discussed in section 2.2.1, it is poorly understood how the resistance of pipes develops over longer time scales (years). This section first discusses conceptually how sand boil observations could be used to learn about cumulative erosion or pipe recovery, and then discusses to which extent the available field observations in Table 2.3 provide evidence for cumulative erosion or recovery.

The equilibrium curve and the regressive vs. progressive erosion regime (Fig. 2.2), are useful concepts to think about pipe recovery. Based on these theoretical curves, changes in H_{eq} during an extreme event show an increasing trend (regressive regime) or decreasing trend (progressive regime) in case there is no recovery, as depicted in Fig. 2.11. Although

Table 2.2: Timing of breach in piping failures. WS=water system: C=coast, R=river. t_1 =time between initiation and breach. t_2 =time of breach w.r.t. flood peak. Remarks: ⁽¹⁾=higher flood a week before. ⁽²⁾= possibly interaction with I-wall.

Location	WS	Failure date	t_1	t_2	L [m]
China					
Changkai levee [Peng and Zhang, 2011]	R	2010.06.21, 18:30	1-2 d	0-14 h	40
Mengxi levee [Van Beek et al., 2013]	R	1998.08.07	14-30 d	0 d	63
Paizhou levee [Van Beek et al., 2013]	R	1998.08.01	2 h - 2 d	-9 d	63
Jiujiang City levee [Danka and Zhang, 2015; Li et al., 2003]	R	1998.08.07, 13:30	'quickly'	+5 d	19
Hungary [Nagy and Toth, 2005]					
Duna Right, 5+396	R	June 1954	-	2.5 h	-
Duna Right, 35+021	R	June 1954	-	4.5 h	-
Duna Right, 54+684	R	June 1954	-	20 h	-
Duna Left, 25+770	R	1956.03.08. 11:00	-	-3 d	-
Duna Left, 11 locations	R	1956.03.14. 07.50	-	20-23 h	-
Duna Right, 39+750	R	1956.03.10. 21:20	-	+1.5 h	-
Duna Right, 39+112	R	1956.03.11. 4:45	-	+6 h	-
Kettős-Körös [Nagy and Toth, 2005; Tóth, 2004]	R	1980.07.28, 6:35	5 min	+26h	-
Italy [IRPI, 2021]					
Caselle Landi	R	1917.06.01, 5:00	-	+1 h	-
Castelnuovo	R	1917.06.01, 17:00	-	+13 h	-
Mezzani	R	1951.11.14, 7:30	-	-4 h	-
Colorno	R	1951.11.14, 14:30	-	2 h	-
Netherlands					
Strijhenham ⁽¹⁾ [Buijs, 2013; Wilderom, 1964]	C	1894.12.30, evening	3-6 h	7 d	40-60
Zalk [Buijs, 2013; van Dam and Beijersbergen, 1981]	R	1926.01.08, 9.15	1-2 h	0 d	40
USA					
Arboga [Meehan, 2018]	R	1997.01.03, evening	1 d	+6 h	40-60
Sutter Bypass [Risher and Gibson, 2016]	R	1997.01.04, 18:30	1-2 h	0 d	35-60
London Avenue South ⁽²⁾ [IPET, 2007; Kanning et al., 2008]	C	2005.08.29, 6:00-8:00	0-3 h	1-3 h	23
Vietnam					
Van Coc [Tu, 2014]	R	1986.07.28, 1:25	0-11 h	-17 h	58
Cong Thon [Tu, 2014]	R	1971.08.23, 20:00	-	+18 h	> 25

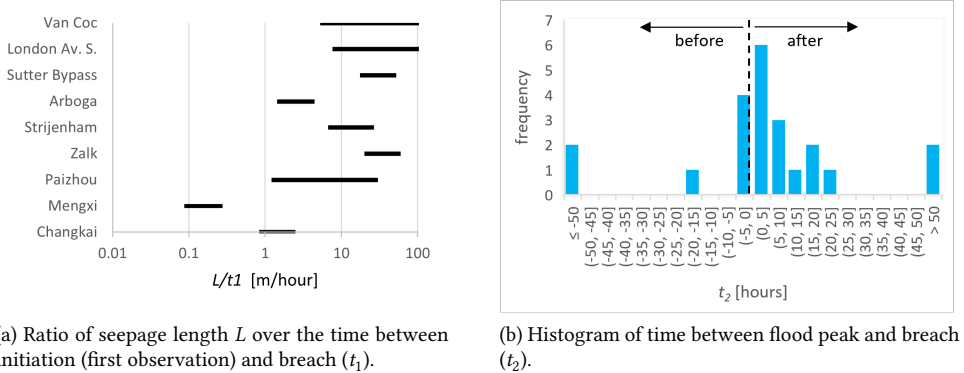


Figure 2.10: Estimates of the time to failure (t_1 and t_2) in field cases.

recovery mechanisms are not fully understood, it is plausible that it results in a decrease of the pipe depth or deposition of finer particles in the pipe. If there is still a pipe present (i.e. partial recovery), both mechanisms reduce the head at which particles start to erode due to respectively the higher pipe flow velocity or higher erodability of the inwashed fine particles. However, if the old pipe is completely filled (i.e. complete recovery), the pipe length becomes 0 and the equilibrium head equals the original initiation head $H_{eq}(0)$. And depending on the regressive or progressive regime, this yields a higher or lower H_{eq} . This results in the different trends between flood events (Fig. 2.11). Hence strength recovery can be inferred from a series of measurements of the equilibrium head H_{eq} during high water events over a period of many years. However, a long-term trend in initiation head only is not a sufficient indicator of recovery. Additionally, changes in equilibrium head *between* extreme events are needed. This requires measurements of H_{eq} in each flood event both when the erosion starts and when it stops.

None of the reviewed datasets on sand boil observations [Aielli et al., 2018; Tu, 2014; Van Beek et al., 2018] satisfies this requirement, so currently there is no quantitative evidence of strength recovery from field cases. The equilibrium head can be measured relatively simple if there is a frequent levee inspection or a monitoring program for selected sand boils. The start of erosion can be estimated from the time of the first sand boil ejections. In case of sand bagging, the height required to stop the sand boil provides an additional equilibrium head. And flood levels are falling one can remove sandbags temporarily until sand transport just starts again. Such a time series of equilibrium head over the years can also indicate whether the strength is gradually decreasing over the years, and hence help identifying critical situations.

The paragraph below shortly discuss the sources in Table 2.3, which may provide indirect evidence of recovery or have been referred to in this context. Glynn and Kuszmaul [2004] were likely the first to discuss cumulative effects of piping. They describe that more reaches with sand boils were registered along the Mississippi during the lower 1995 flood (86 locations) compared to the significantly higher (and longer) 1993 flood (42 locations). From this they conclude: "This observation and others support the hypothesis

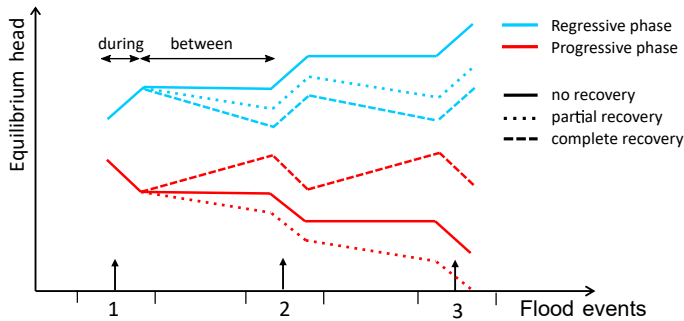


Figure 2.11: Hypothetical trends in long-term development of the equilibrium head during and between flood events, depending on erosion phase and recovery.



(a) Frequently reactivating sand boil near Guardia Ferrarese along the Po river, Italy [Martínez et al., 2020].



(b) Settlement due to collapsed pipe along the Mississippi, Ensley levee [USBR and USACE, 2019].

Figure 2.12: Field observations of sand boil reactivation and pipe collapse (potential recovery mechanism).

that an increase in piping incidence at lower than design flood levels indicates progressive (cumulative) erosion of the levee foundation” [Glynn et al., 2012]. However, this decrease in critical head for initiation is no evidence that pipes stayed intact and erosion is fully cumulative. It can also be the case that the erosion was initiation-dominated or in the progressive regime and also (partly) recovered. Or that the cracks formed in 1993 were still open and filled with sand which could be easily eroded. Furthermore, it is remarkable that only 37% (32 locations) of the 1995 piping locations were also documented in 1993 [Glynn et al., 2012], so 63 % were new locations which indicates this is not related to cumulative erosion. Therefore there must be another explanation for the increased observations; for instance physical changes in the levee or river system or more awareness of the inspectors after the great 1993 flood. Another example reported by Sills in Rice et al. [2021] concerns a Mississippi levee at Buckshoot Reach, where the initiation water level has dropped several feet over a few decades. Also this case does not contain direct evidence for recovery or cumulative erosion; the reduction in initiation head can also be caused by a progressive erosion regime, with and without recovery. USBR and USACE [2019] report a direct obser-

Table 2.3: Potential sources on long-term effects of piping (cumulative erosion or recovery).

Location	Indication of cumulative effect
St. Louis district Mississippi R., USA [Glynn and Kuszmaul, 2004; Glynn et al., 2012]	More sand boils in 1995 compared to more extreme 1993 flood.
Buckshoot Reach, Mississippi R., USA [Rice et al., 2021]	Initiation water level is reported to decrease over years.
Ensley, Memphis, Mississippi R., USA [USBR and USACE, 2019]	Several pipe collapses identified early 2012 after spring 2011 floods.
Field test IJzendoorn, Rhine River, NL [van den Ham, 2019; Rice et al., 2021]	Open pipe found in clayey transition layer, two years after field test.
Guarda Ferrarese, Po River, Italy [Marchi et al., 2021; Martínez et al., 2020]	Sand boil reactivated in 2018 at lower level than in 2014.

vation of pipe recovery at Ensley Levee, Memphis, along the Mississippi. Approximately a year after the 2011 spring floods, several pipe collapses were observed (Fig. 2.12b). Two years after a field test at IJzendoorn, the Netherlands, the site was excavated [van den Ham, 2019; Rice et al., 2021]. No pipe or open void was observed in the top of the sand layer, but in the transition layer of clayey sand to sandy clay. Although this layer is less erodible, cracks seem to have created hydraulic shortcuts through this layer which transported sand to the surface. It is uncertain whether a pipe that formed in the sand layer was closed over the two years or was difficult to detect, or that the pipe only developed in the transition layer. In Italy, a sand boil at Guarda Ferrarese, Po River (Fig. 2.12a), reactivated in 2018 at a lower water level than in 2014 [Marchi et al., 2021; Martínez et al., 2020]. However, Martínez et al. [2020] conclude that the lower reactivation level was facilitated by a significant ditch deepening.

This review on long-term effects shows that field observations in the literature provide no clear evidence whether strength recovery occurs between flood events, and to what extent. Reductions in initiation head have been reported, but are no evidence of recovery or cumulative erosion. There is one direct observation of pipe collapse (Ensley), and one of an open pipe (IJzendoorn). It is recommended to start long-term measurements of equilibrium head. These are currently unavailable but can provide more (quantitative) information on strength recovery and are relatively simple to execute.

2.2.3 Laboratory experiments

Some researchers reported information on the rate of pipe progression, or the pipe length development over time [Allan, 2018; Miesel, 1977, 1978; Muller-Kirchenbauer, 1980; Robbins et al., 2017; Vandenboer et al., 2019; Yao, 2014; Yao et al., 2013]. These experiments are discussed below, and Table 2.4 summarizes the main characteristics. Then, section 2.2.4 describes a regression analysis performed on part of these experiments to obtain an approximate prediction of progression rates. Therefore, the experiment descriptions in the current section also explain how the data were used in the regression.

Before proceeding, first some basic concepts are clarified. Figure 2.13 shows a cross section of a common setup. In most experiments, the head is increased step-wise until no equilibrium is reached anymore (Figure 2.13, right). This head is the critical head H_c . The

Table 2.4: Experiments with data on pipe length development over time. N=number of tests.

* included in regression of section 2.2.4.

multi-layered

^o instantaneous progression rates, 14 points in 9 tests^v only tests with max. factor 1.4 overloading used

Source	Setup, exit	L [m]	d_{70} [mm]	N	remark
Miesel [1977, 1978]	box, hole	0.71-1.36	Sand F	3	
Muller-Kirchenbauer [1980]	box, hole	0.7	?	1	
IJkdijk [Parekh et al., 2016; Sellmeijer et al., 2011]	levee, plane (Fig. 2.17c)	15	0.18-0.26	3	*
Van Beek et al. [2011]	box, slope (Fig. 2.17a & 2.17b)	0.3-1.45	0.15-0.43	19	*
Yao [2014; 2013]	box, hole & slope	0.35	0.15	7	*,#
Robbins et al. [2017]	cylinder, slope (Fig. 2.17d)	0.95	0.33	14	*, ^o
Vandenboer et al. [2019]	box, hole	0.3	0.19	2	*, ^v
Allan [2018]	box, hole (Fig. 2.17e)	1.3	0.30	16	
Robbins et al. [2020b]	box, slope	0.65	0.39-2.8	55	

pipe length at that moment is the critical length l_c . The (instantaneous) pipe progression rate v is defined as the increase in straight pipe length l over a given period of time t . This analysis uses the average rate over the period between the time at which the critical length is reached and at which the pipe length is equal to the seepage length L : $v_{c,avg} = (L - l_c)/(t_{end} - t_c)$.

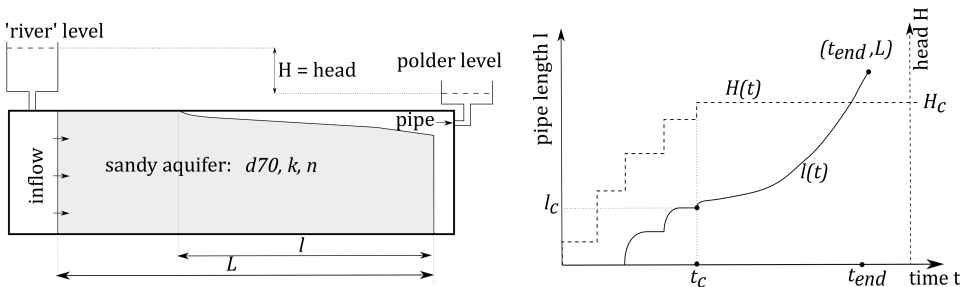


Figure 2.13: Definitions used in progression rate analysis [Pol et al., 2019]. Left: cross-section of experimental setup (slope type box). Right: typical development of head and pipe length.

Miesel and Muller-Kirchenbauer

The studies of Miesel and Müller-Kirchenbauer [Miesel, 1977, 1978; Muller-Kirchenbauer, 1980] are the first to report in more detail on the piping erosion process, including some results in terms of the development over time. However, the presented data are very limited, and give more an impression of the time scales than that they allow for a quantitative analysis.

Miesel presents the pipe length development in three experiments: test 7 and test 72 in Miesel [1977] and test 81 in Miesel [1978]. All experiments are hole-type exits with Sand F, of which the grain size is not reported. Test 7 includes a graph of the pipe length as function of time (Fig. 2.14). It shows that the progression rate first slows down up to $t \approx 50$ min, probably near the critical pipe length, and subsequently accelerates. The progression rate is $2 \cdot 10^{-4}$ m/s. Test 72 only includes the length and erosion time in the progressive phase ('kritischer Bereich'), which yields an average progression rate of $1.4 \cdot 10^{-4}$ m/s. The results presented of test 81 only include the relative pipe length development in the progressive phase (Fig. 2.15). Therefore no progression rates are available, but the result shows that in this test the pipe develops at a rather constant rate, and does not accelerate as strongly as predicted by the model of Kézdi [1979] as given in Eq. 2.18.

Muller-Kirchenbauer [1980] reports a progression rate of $2.8 \cdot 10^{-3}$ m/s in a 2D setup (ditch-type exit, Bild 13), but the soil properties are unknown.

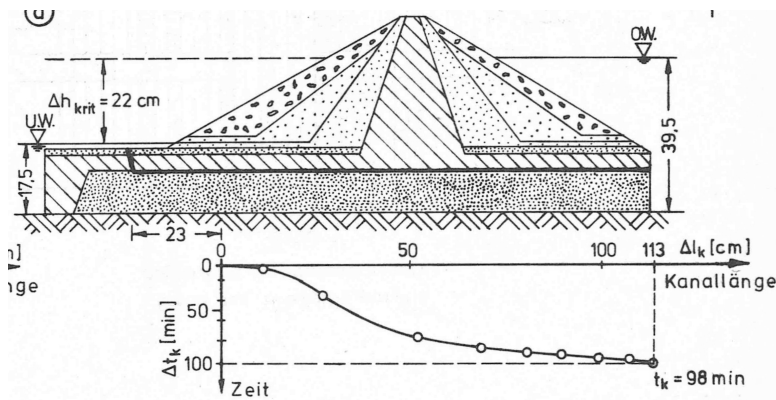


Figure 2.14: Pipe development in experiment 7 under the critical head drop [Miesel, 1978].

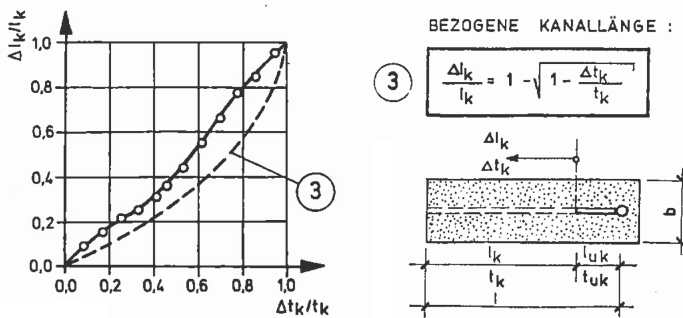


Figure 2.15: Pipe development in test 81, including pipe length development based on Kézdi's progression model indicated with (3) [Miesel, 1978].

IJkdijk & Van Beek

The IJkdijk experiments are large scale ($L=15$ m) tests on newly constructed clay levees, two on fine sand and one on coarse sand, with a plane type exit (Fig. 2.17c). Pipe pro-

gression could not be observed directly due to the clay cover, but was estimated from the response of a grid of pore pressure sensors and other observations [Parekh et al., 2016; Sellmeijer et al., 2011]. This method is quite uncertain; for instance the estimated pipe length in tests 1 and 3 shown in Sellmeijer et al. [2011] does not exceed half of the seepage length in the entire test, and progression rates based on the pressure stabilization (ps) time in Parekh et al. [2016] are a factor 2-3 higher. A reinterpretation of the measurements in Sellmeijer et al. [2011] and Parekh et al. [2016] yields progression rates of $5 - 7 \cdot 10^{-5}$ m/s for the fine sand and $1 \cdot 10^{-4}$ m/s for the coarse sand.

Van Beek et al. [2011] conducted a large series of experiments but does not report pipe development over time. The data was re-analyzed to obtain progression rates from a selection of small-scale and medium-scale slope-type experiments (Fig. 2.17a and 2.17b) with a clear pipe path [Pol et al., 2019].

Yao

The experiments by Yao [2014; 2013] are small-scale hole and slope experiments with two layers of sand (fine on top of coarse). The progression rates are derived visually from figures of pipe length vs. time in the PhD thesis [Yao, 2014]. Hole type tests used are B115, B118, BC116 and BC117 (all). Slope type tests used are BC109, BC110 and BC111 (tests BC112 and E114 are not included as results were considered less reliable). In the regression analysis in Pol et al. [2019], k and d_{70} in case of multi-layer tests are based on the top layer properties.

Robbins

Robbins et al. [2017] developed a cylindrical setup to be able to measure local pressure gradients in the pipe and at the tip (Fig. 2.17d). These local (critical) gradients are assumed to be independent of scale and setup, and therefore of interest to model pipe progression. The curved roof restricts pipe meandering and ensures that the pipe passes below a row of pore pressure sensors. Dye can be injected to measure pipe flow velocity. They measured the pipe length development, which allows to relate progression rates to the local gradients at the tip. Two sand types and three cylinder diameters were tested. Progression rates are up to 1 cm/s (for the coarsest sand). The progression rate is related to the average Darcy velocity 10 cm upstream of the pipe tip. Robbins et al. [2017] also suggest that it is related to the local tip gradient, but the presented relation is weak, especially for higher void ratios. A disadvantage of this setup is that the seepage is strongly 1-dimensional (small D/L); therefore results are difficult to translate to field situations with hole-type exits.

The regression analysis only includes data from tests on 40/70 sand in tube B and C, as the smallest tube A did not produce a representative erosion process. Because the applied head was not constant throughout the tests (sometimes the erosion process was stopped temporarily), average progression rates could not be used. Therefore, from these tests we selected intervals where the average gradient was constant and the progression continuous (not intermittent), and calculated progression rates and average gradients in each interval. This resulted in 14 datapoints from 9 tests. The corresponding progression rates vary between $4 \cdot 10^{-4}$ to $2 \cdot 10^{-3}$ m/s.

Vandenboer

Vandenboer et al. [2019] conducted small-scale hole-type experiments with a constant head which is larger than the critical head H_c (they call it supercritical load) and with detailed pipe length measurements. The ratio of H/H_c varies between 1 and 5. Like Miesel's experiments, the tests with $H/H_c = 1$ and gradual head increase show a slight acceleration when the pipe approaches the upstream side. At higher degrees of overloading, the progression rate is almost constant. At $H/H_c = 1.4$ the erosion develops still as (a few) channels. But at higher degrees of overloading, the erosion also develops in sideward direction. It seems the pipe has no time to increase in length and thereby concentrate the seepage to the pipe tip. The results illustrate that the progression rate strongly depends on the degree of overloading. Tests with $H/H_c = 1.4$ yield an average progression rate of $7.7 \cdot 10^{-5}$ m/s, while $H/H_c = 1.4$ yields $2.9 \cdot 10^{-4}$ m/s, a factor 3 increase. Given the different erosion process, and the fact that a water level $H > 1.4 \cdot H_c$ is unlikely to occur at levees, only tests with $1 < H/H_c < 1.4$ are included in the regression analysis.

Allan

Allan [2018] performed a large set of experiments investigating several factors of the piping process. Part of the tests focus on the effect of overloading ('above critical loading'). These tests are conducted on Sydney Sand ($d_{50}=0.30$ mm, $C_u=1.3$), have a geometry of $L=1.3$ m, $D=0.31$ m, $W=0.45$ m, and a circular exit. In the normal loading tests, progression rates varied between 1.6-7.4 mm/minute ($2.7 - 12 \cdot 10^{-5}$ m/s). Allan notes that similar values occur in tests by Townsend et al. [1981]. Under overloading, the progression rate increased with approximately a factor 3 for each 10% overloading above the critical head (Fig. 2.16). These data is not included in the ISGSR regression, as it was not available at that time.

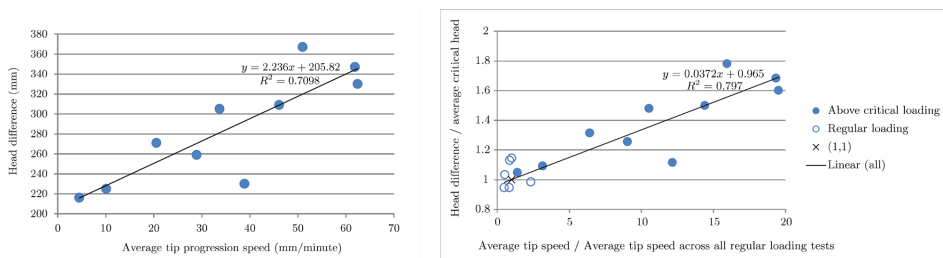


Figure 2.16: Effect of overloading on the progression rate [Allan, 2018]. Left: absolute values. Right: relative to the regular loading tests.

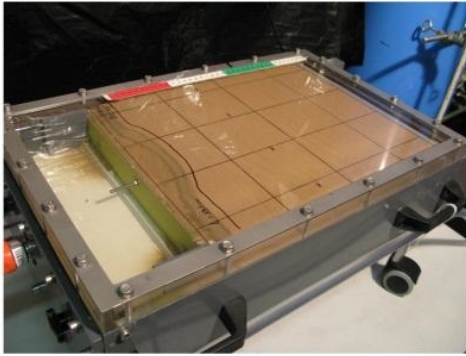
2.2.4 Analysis of progression rates from experiments

This section describes a regression analysis to obtain an empirical estimate of the pipe progression rate based on laboratory experiments¹.

The experimental data used for the regression analysis is composed of 45 tests from six test series with different setups (indicated by * in Table 2.4). The entire dataset is

¹This analysis is published in Pol et al. [2019].

2



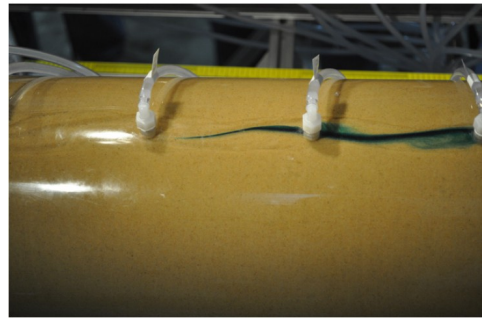
(a) Small-scale box [Van Beek, 2015].



(b) Medium-scale box [Van Beek, 2015].



(c) Large-scale levee (IJkdijk) [Van Beek, 2015].



(d) Cylinder [Robbins et al., 2017].



(e) Medium-scale box [Allan, 2018].

Figure 2.17: Experiments with progression rates are conducted in different types of setups.

included in Appendix B. The older experiments are not included due to insufficient information Miesel [1977, 1978]; Muller-Kirchenbauer [1980], and the data from Allan [2018] and Robbins et al. [2020b] was not yet available when the analysis was performed.

To identify important factors that predict the progression rates, correlations between the average progression rate in an experiment ($v_{c,avg}$) and several predictors (H_c/L , L , d_{70} , n , D_r , k) were established; visually using scatterplots and quantitatively using the Kendall rank correlation coefficient τ_K . The critical gradient, the hydraulic conductivity and the grain size have a significant ($p < 0.05$) correlation with the progression rate (Kendall's τ_K between 0.25 and 0.39). No significant relation with porosity or relative density was found.

The predictors are correlated (e.g., d_{70} and k) and may not all be needed as predictors. Therefore, a multivariate linear regression model (Eq. 2.16) was created by stepwise addition of the predictors. First, the variables $v_{c,avg}$, k and d_{70} were made dimensionless by scaling with their mean value across all tests, denoted by overbars: $\overline{v_{c,avg}} = 6.5 \cdot 10^{-4}$ m/s, $\overline{k} = 3.4 \cdot 10^{-4}$ m/s, $\overline{d_{70}} = 2.4 \cdot 10^{-4}$ m. After that, a logarithmic transformation of v , H_c/L and k was applied because the scatterplots indicated a logarithmic relation. This results in:

$$\log\left(\frac{v_{c,avg}}{\overline{v_{c,avg}}}\right) = a_1 + a_2 \cdot \log\left(\frac{H_c}{L}\right) + a_3 \cdot \log\left(\frac{k}{\overline{k}}\right) + a_4 \cdot \frac{d_{70}}{\overline{d_{70}}} + a_5 \cdot n \quad (2.16)$$

Indeed it appears that d_{70} and n do not significantly improve the regression model. Therefore, only H_c/L and k are used as predictors. Omitting d_{70} and n from Eq. 2.16 yields:

$$v_{c,avg} = \overline{v_{c,avg}} \cdot 10^{a_1} \cdot \left(\frac{H_c}{L}\right)^{a_2} \cdot \left(\frac{k}{\overline{k}}\right)^{a_3} \quad (2.17)$$

The best fit ($R^2=0.66$) for Eq. 2.17 is found for coefficients $a_1=0.79$, $a_2=1.4$, $a_3=0.57$ (with standard deviations on coefficients of 0.14, 0.22 and 0.081 respectively).

In addition to this purely statistical model, Kezdi's analytical model was applied to the data. This model is based on the assumption of proportionality between the instantaneous progression rate and the pore velocity at the pipe tip [Kézdi, 1979]:

$$v_c(t) = \frac{dl}{dt} = \frac{C_k \cdot k \cdot H(t)}{(L - l(t)) \cdot n} \quad (2.18)$$

In which C_k is the proportionality constant. Note that this model assumes a linear decrease in head between upstream level and pipe tip and no head drop in the pipe, although the actual head drop is nonlinear due to flow concentration and there will also be a pipe head drop. By solving the differential equation in Eq. 2.18 for a constant head $H(t) = H_c$, this model leads to the following average progression rate:

$$v_{c,avg} = \frac{2 \cdot C_k \cdot k \cdot H_c}{L \cdot n} \quad (2.19)$$

The best fit of Eq. 2.19 is found for $C_k=1.6$ ($\sigma=0.1819$, 95% conf. interval 1.28-1.99). This results in a R^2 values of 0.66 and 0.40 respectively (see Figure 2.18). Figure 2.18 shows that the order of magnitude is predicted well for a wide range of experimental setups. The lower panels show the model uncertainty factor ($m_v = v_{exp}/v_{model}$) including a fit of a lognormal

distribution. In terms of the R^2 values, the multivariate regression model performs better than the calibrated Kézdi model on these experiments. However, this indicator may be too positive, as the data was not split in a calibration and validation set due to the limited number of tests.

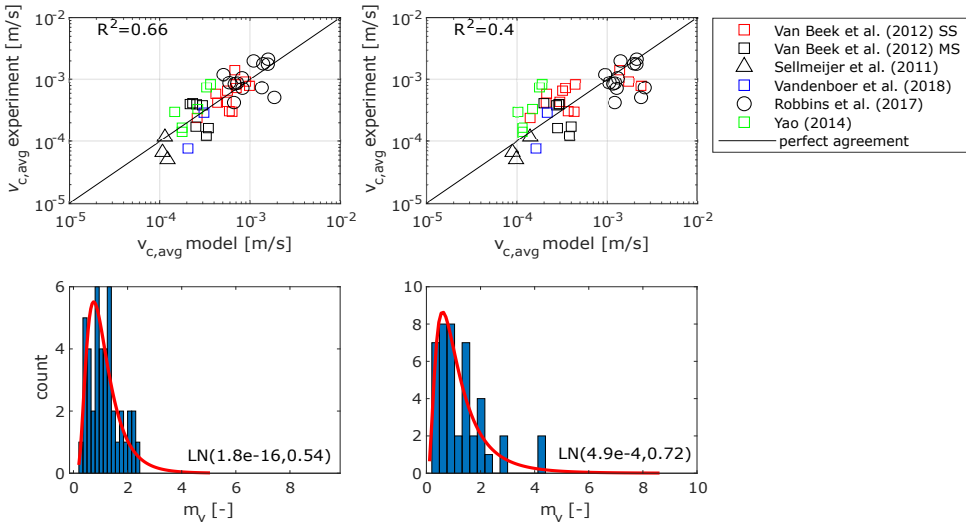


Figure 2.18: Progression rates in previous experiments, and predictions of Eq. 2.17 (Multivariate, left) and Eq. 2.19 (Kézdi-fit, right).

Discussion of laboratory experiments

The studies in section 2.2.3 show that the progression rate is related to hydraulic gradient, grain size and degree of compaction. Measured progression rates vary several orders of magnitude between different setups (e.g., slope or hole), sand types and degree of overloading. A challenge in interpreting these results is that most experiments were performed on much smaller scales than typical levee dimensions (seepage length and aquifer depth in the order of 10-100 m). Since the progression rate appears to be a function of the applied and critical head, which do not scale linearly with seepage length, extrapolation to field conditions introduces a large uncertainty in predicted progression rates. Scaling requires relating the progression rate to local, scale-independent conditions. Only Robbins et al. [2017] evaluated local hydraulic gradients at the pipe tip, which are considered scale independent erosion criteria. The other studies only present global hydraulic gradients.

2.2.5 Time-dependent models

The literature presents different approaches to model the pipe advancement process, from analytical to different types of numerical models.

Analytical

A simple analytical model has been used by Kézdi [1979], assuming that the advancement rate is proportional to the average seepage velocity upstream of the pipe tip and that there

is no head loss in the pipe (Eq. 2.18). Such analytical models can be easily integrated in a reliability analysis, and may provide a first estimate of progression rates, but lack some important features of the piping process. For instance, it lacks a stability criterion such as critical gradient, so pipe progression only stops at zero head difference, which is not in agreement with the equilibrium that is observed in experiments. Furthermore, both the head loss in the pipe and (2D or 3D) flow concentration to the tip can have a significant influence on the head profile and the local seepage velocity at the tip.

Numerical

On the other hand there are several transient numerical models coupling groundwater flow, pipe flow and particle transport. Numerical piping models can be grouped in the following categories [Wang et al., 2014]:

1. Seepage models with increased permeability to represent the pipe zone [Rahimi et al., 2020; Wewer et al., 2021].
2. Discrete Element models (DEM) solving the fluid flow and individual particle movement [El Shamy and Aydin, 2008; Froiio et al., 2017; Tran et al., 2017].
3. Multi-phase (fluid, soil) models [Rotunno et al., 2019; Wang et al., 2014]

Discrete Element models are not discussed further, as these are not feasible for modeling at field scales because of their computational time. However, these type of models can be used to study micro-scale processes, and findings can be used in the FEM modeling approaches.

Wang et al. [2014] modeled pipe progression using a 2D FEM model with steady seepage flow, turbulent pipe flow and a primary erosion criterion. Progression is determined by a critical pore shear stress at the tip and the rate of progression by an erosion coefficient depending on excess pore shear stress (following Fox et al. [2007]). First, the smallest particle fraction is eroded, until the critical porosity is reached and the tip is switched to pipe element. Therefore the progression rate represents the required time for removal of fines from the coarse matrix at the tip. This process is more applicable to graded soils than uniform soils. Secondary erosion (widening) and additional pipe resistance due to the eroded sediment load is not included in the model. The direction of progression is free. The model is validated on H_c in one test; the time-dependent development is not validated.

The multi-phase model by Rotunno et al. [2019] includes 3D transient seepage flow, turbulent pipe flow, and a primary and secondary erosion criterion. Primary erosion is modelled using the approach in Fujisawa et al. [2010], secondary erosion by a critical Shields parameter and empirical excess shear stress relation. Eroded sediment is transported as fluidized sand (3rd phase besides soil and water). The model is validated on the large-scale Deltaflume [De Rijke, 1991] and IJkdijk [Sellmeijer et al., 2011] experiments. Deltaflume allows only for validation of the critical conditions (H_c), IJkdijk also for the time-dependent development. This is the only model accounting for the rate of primary and secondary erosion.

A different approach is to use a seepage model and represent the pipe by an increased permeability, depending on the size of the pipe. This can be applied if the pipe flow is laminar, due to the linear relation between pipe discharge and gradient, similar to Darcy seepage flow. It is often applied in the equilibrium models (section 2.1.3), where the pipe

depth is iterated so that the shear stress equals its critical value. Recently, the method has been used to model time-dependent development.

Rahimi et al. [2020] use a 3D seepage model with permeability amplification to simulate time-dependent pipe development. The progression is based on a primary erosion criterion like Wang et al. [2014]: the porosity increases by removing the particle fraction smaller than a critical particle diameter. Every time step, the porosity is updated, resulting in an increase in permeability. The model does not contain a pipe depth equilibrium. More important, the model does not include any erosion laws. The model is validated on three medium-scale slope experiments from Robbins [2016]. Although the permeability evolves during a simulation, actually this is not time-dependent development but length-dependent. It is expected that changing the time step will change the progression rate with the same amount.

Wewer et al. [2021] modeled the time-dependent pipe progression in a 2D transient seepage model, where the erosion rate (at the exit) is prescribed by laminar sediment transport equations. Using an assumption of the relation between pipe length and pipe depth, the eroded volume per time step is translated to a pipe length increase. The main strength of the approach is the limited computational time and the explicit modeling of laminar sediment transport. Main limitations are the 2D approach and the required assumption for the pipe depth as function of length.

Hybrid approaches

The analytical models lack important features of the erosion process, and are poorly validated. The numerical models allow for more complex modeling with complex geometries, heterogeneity or transient flow. A drawback is that complex models are computationally expensive and the fundamental erosion processes in these models have been poorly validated. From a reliability point of view there is a need for computationally efficient models that still capture the main factors of influence, so something in between the two groups described above. Kramer [2014] used such a hybrid approach combining critical conditions from the Sellmeijer equilibrium model (actually a neural network of MSeep simulations) and progression rates based on erosion function according to Wang et al. [2014]. This allows to compute the pipe length development under a time-varying water level. However, the model describes only the regressive phase and it is not integrated with the timing of uplift and heave. It also requires assumptions regarding pipe geometry. Furthermore, as noted before, the approach of Wang et al. [2014] is not validated for piping and seems to be more suited to erosion in graded material. Hence the physical basis of this hybrid approach can be improved, but chapter 6 will use the concept of combining the Sellmeijer equilibrium model with estimates of the progression rate.

3

3

Small-scale Experiments on the Temporal Development of Piping

At present, advances are limited more by our lack of understanding of the processes, which prevents the selection of the best modeling approach, and by the lack of field and laboratory data to test such models.

Wilson et al. [2018] on soil erosion

Most research on backward erosion piping focused on the critical head difference at which piping failure occurs. Two aspects have received less attention, namely (1) the temporal evolution of piping and (2) the local hydraulic conditions in the pipe and at the pipe tip. This chapter describes a series of small-scale experiments with local pressure measurements in the pipe during equilibrium and pipe progression for different sands and degrees of hydraulic loading. The experiments confirm a positive relation between progression rate and grain size as well as the degree of hydraulic overloading. Furthermore, an analysis of pressures in and upstream of the pipe shows that the rate of BEP progression can be better explained by the bed shear stress and sediment transport in the pipe than by the seepage velocity at the pipe tip. It is also shown that a detachment of sediment from the tip increases the pipe resistance and pauses the primary erosion, hence the rate of progression depends on the rate at which the sediment is transported through the pipe. These insights provide a first empirical basis for modeling pipe development using a coupled seepage - pipe flow - sediment transport model.

This chapter is based on Pol, J.C., Kanning, W., van Beek, V.M., Robbins, B.A., and Jonkman, S.N. (2022). Temporal evolution of backward erosion piping in small-scale experiments. *Acta Geotechnica*. <https://doi.org/10.1007/s11440-022-01545-1>, except for section 3.3.2 which is based on Pol, J.C., Van Klaveren, W., Kanning, W., Van Beek, V.M., Robbins, B.A., and Jonkman, S.N. (2021). Progression Rate of Backward Erosion Piping: Small Scale Experiments. Proceedings of the 10th international conference on scour and erosion (ICSE-10), pp 93–102. Data link: <https://doi.org/10.4121/20805451.v1>

3.1 Introduction

Internal erosion is a significant threat to levees and dams [Danka and Zhang, 2015; Foster et al., 2000; Fry, 2016; Özer et al., 2020], but time scales of the failure process are hard to quantify [Fell et al., 2003]. Different types of internal erosion can be distinguished: concentrated leak erosion, suffusion, contact erosion, and backward erosion piping. Backward erosion piping (BEP) can be defined as the failure process by which seepage under a structure erodes the granular foundation that is covered by a cohesive roof, forming a hydraulic shortcut. For many levees, backward erosion piping is the most common form of internal erosion because of the cohesive deposits which form a roof above sandy aquifers.

3.1.1 Piping process description

The BEP failure process starts with high external water levels that cause excess water pressure at the landward toe of the structure. When a cohesive blanket is present at the landward side, erosion can occur through either pre-existing defects in the blanket or cracks caused by uplift and rupture. If the vertical pressure gradient over the exit through the confining layer is sufficiently high to initiate vertical transport of sand, a cavity forms below the exit hole and the sand settles around the exit hole as a sand boil. At some point, a small pipe starts to develop from the cavity in the upstream direction. When the head difference (H) over the levee is sufficiently high and prolonged, the erosion continues in the upstream (backward) direction until a hydraulic shortcut forms, which likely results in a levee breach. However, if the head difference is too low or drops too quickly, an equilibrium occurs with a partially developed pipe.

The head drop at which equilibrium occurs (H_{eq}) varies with pipe length l [Hanses, 1985; Sellmeijer, 1988]. The maximum H for which an equilibrium exists in stationary conditions is defined as the critical head difference H_c , and l_c is the corresponding pipe length. This point (H_c, l_c) marks the transition from the regressive phase ($l < l_c$) to the progressive phase ($l > l_c$). Exceeding H_c long enough ultimately leads to a levee breach.

Most previous BEP research focused on this critical head difference H_c and the influence of aquifer geometry and sand properties on this critical condition, for example [Bligh, 1910; Hanses, 1985; Sellmeijer, 1988; Van Beek, 2015]. Such a stationary approach, which neglects the development over time, may be sufficient in many cases such as rivers with relatively long floods or dams with permanent pools. However, when the flood duration is short compared to the time scale of backward erosion, a dike may survive a short duration flood, whereas it would fail under a long duration flood [Hanses, 1985]. These insights are important for levee safety assessments and for emergency response.

This raises the question of how to predict the temporal development of the backward erosion process. The 20th century studies of Miesel [1977], Muller-Kirchenbauer [1980] and Hanses [1985] report very limited data on the development over time. More recently, several researchers studied pipe progression rates (dl/dt) experimentally [Allan, 2018; Pol et al., 2019, 2021a; Robbins et al., 2020b, 2017; Vandenboer et al., 2019]. Robbins et al. [2017] used cylindrical flumes and correlated progression rates to seepage velocity and void ratio. Allan [2018] studied progression rates under overloading ($H > H_c$) in a rectangular setup with hole-type exit (seepage length $L=1.3$ m). Vandenboer et al. [2019] also studied the effect of overloading, but in a small-scale ($L=0.3$ m) rectangular flume with hole-type exit. Pol et al. [2019] derived progression rates from various available BEP experiments, and

correlated these to hydraulic conductivity and the global horizontal hydraulic gradient. Robbins et al. [2020b] analyzed progression rates in small-scale flumes with a slope-type exit, for a wide range of grain sizes. Finally, Pol et al. [2021a] report pipe progression rates in a large-scale experiment (chapter 4). These studies show that the progression rate is related to head difference, grain size and degree of compaction. Measured progression rates vary several orders of magnitude between different setups (e.g., slope or hole), sand types and degree of overloading.

A challenge in interpreting these results is that most experiments were performed on much smaller scales than typical levee dimensions (seepage length and aquifer depth in the order of 10-100 m). Since the progression rate appears to be a function of the applied and critical head, which do not scale linearly with seepage length, extrapolation to field conditions introduces a large uncertainty in predicted progression rates. Scaling requires relating the progression rate to local, scale-independent conditions. Only Robbins et al. [2017] and Pol et al. [2021a] evaluated local hydraulic gradients at the pipe tip, which are considered scale independent erosion criteria. The other studies only present global hydraulic gradients.

3.1.2 Piping process in non-equilibrium conditions

BEP consists of two distinct types of erosion [Hanses, 1985]: lengthening of the pipe by detachment of grains from the soil skeleton at the pipe tip (primary erosion) and enlargement of the pipe cross section (secondary erosion). The primary erosion mechanism can be considered as successive slope failures which occur if the forces exerted on the grains by the seepage flow exceed the resistance [Howard and McLane, 1988; Schmertmann, 2000]. Particles slide in the pipe, may rest temporarily on the bed, and are gradually transported by the flow. When detached grains rest temporarily on the bed or roll through the pipe, the shallower pipe results in a temporarily higher flow velocity, higher pipe gradient, and therefore a lower tip gradient (Fig. 3.1). That delays or stops the pipe lengthening. The tip gradient will increase due to the removal of grains in the pipe and the next slope failure occurs when the tip gradient has recovered to the critical value [Pol et al., 2021b]. This intermittent pipe lengthening has been observed for example by Hanses [1985]. The description above is based on observations when the pipe is close to equilibrium. In case of high progression rates, there will be continuously a layer of moving grains because the critical gradient at the pipe tip has been exceeded by such an amount that the influence of the sediment load in the pipe is not sufficient to reduce the pipe tip gradient below the critical value. In the case of internally unstable soils, the tip failures may also be delayed by erosion of the finer fraction from the coarser soil matrix [Kenney and Lau, 1985]. In case of very fine dense sand, the rate of slope failures may be limited by dilatancy effects. Soil matrix expansion up to the critical porosity requires an inflow of water. The lower the permeability, the more time is needed to supply this water. Therefore it can pose a limit on the rate of primary erosion, similar to breaching flow slides described by van Rhee [2015]. At the same time, the pipe downstream deepens by secondary erosion if the bed shear stress exceeds its critical value [Van Beek, 2015]. Deepening reduces the gradient in the pipe and hence increases the tip gradient, so the two types of erosion are coupled.

Given these two erosion processes, the time scale of erosion can be considered as the combination of (1) time needed for erosion of grains in the pipe until the local tip gradient

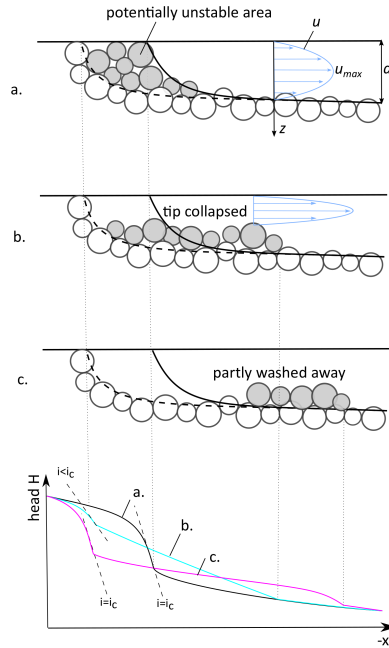


Figure 3.1: Conceptual description of primary and secondary erosion near the pipe tip. The lower panel indicates the head profile and tip gradients (i) during stages a-c.

recovers to the critical value, (2) time needed for erosion of a finer fraction at the tip, and (3) time needed for dilation of soil matrix at the tip. For the sands considered in this chapter, we assume that the second and third component can be neglected.

3.1.3 Modeling of pipe progression

Several methods have been proposed to model the development of the pipe length over time for engineering purposes, which are summarized here. Kézdi [1979] hypothesized that the progression rate of BEP is proportional to the pore flow velocity at the pipe tip. However, his model of pipe progression neglects pipe resistance, seepage concentration at the pipe tip, and includes no critical pore velocity. Furthermore, there is hardly any experimental data to test this hypothesis. Some empirical relations between erosion rate and seepage gradient were developed in the context of streambank erosion of cohesive soils due to seepage [Chu-Agor et al., 2009; Fox et al., 2007]. Robbins et al. [2020a] determined such a relation for BEP experiments based on modelled seepage gradients and measured progression rates, and included this in a quasi-stationary BEP model. Additionally, several numerical models have been developed to predict BEP by coupling seepage, pipe flow and sediment transport relations [Rotunno et al., 2019; Wewer et al., 2021]. However, the pipe length development as predicted by these models has not been validated on different types of BEP experiments, as experiments with suitable measurements are very limited.

3.1.4 Objective

The goal of this study is to better understand and model the development of piping erosion over time. To achieve this, we measured local, scale-independent, conditions that explain the temporal development of piping (i.e., the progression rate). We modified a commonly used BEP laboratory setup to measure pore pressures and pipe pressures during the piping process with a high spatial and temporal resolution. The experimental program included different sand types with varying degree of compaction to explore the effects of grain size and compaction. The chapter is structured as follows: section 3.2 describes the experimental method, section 3.3 the primary experimental results, section 3.4 an analysis of local flow conditions, pipe development and sediment transport, and sections 3.5 and 3.6 contain the discussion and conclusions, respectively.

3.2 Experimental method

3.2.1 Modification of box-type setup

Previous research into BEP progression rates has either used a rectangular box-type setup [Allan, 2018; Robbins et al., 2020b; Vandenboer et al., 2019] or a cylinder-type setup [Robbins et al., 2017]. The box-type setup poses less restrictions on flow from the sides and results in flow concentration toward the exit. On the other hand, a cylinder forces the pipe to grow right below a row of sensors to measure pipe pressures. To combine the advantages of both types, we modified the box-type setup used by Van Beek [2015] and Vandenboer et al. [2019] so that pipe pressures can be measured.

The sample dimensions are 0.48 x 0.30 x 0.1 m (Fig. 3.2). The box has a 10 mm thick acrylate cover with a 6 mm diameter exit hole. The seepage length L equals 0.352 m, between upstream filter and the exit. The modification is twofold. First, two permeable barriers of filter fabric (0.05 mm aperture) were placed longitudinally and 35 mm apart to prevent sideways pipe growth but allow flow to pass. Second, silicon strips (0.3 mm high, 3 mm wide, 10 mm long) were placed diagonally with 20 mm spacing between the rows, and sand was sprinkled over them while the silicon dried (grey strips in Fig. 3.2). These two steps restrict the pipe path to the middle 35 mm of the box, without significantly influencing the flow. Hereby, the pipe can meander slightly, while also being close to the sensors and not significantly influencing the piping process. At the interface with the guides, the porosity may be slightly higher as the grains do not interlock. However, as will be demonstrated in section 3.3.3, this does not have a significant effect on the results, as the pipe tip generally propagates at some distance from the guides. Finally, 20 mm spaced pressure ports were added in the center axis of the box and connected to pressure sensors at the side of the box (Fig. 3.3). Influence of the ports on progression is expected to be negligible, given their limited volume and not extruding into the sand.

3.2.2 Materials and measurement techniques

The experiments include three fine, uniform sands with characteristics as shown in Table 3.1. The FPH sand was also used in Pol et al. [2021a]; the Baskarp B25 sand was used in Akrami et al. [2020] and Rosenbrand et al. [2020]. Grain sizes were determined by dry sieving. Porosity n_{min} is based on the method in ASTM4253 (dry method, vibrating needle instead of vibrating table) and n_{max} on ASTM4254 (funnel method). The porosity n_{sb} and

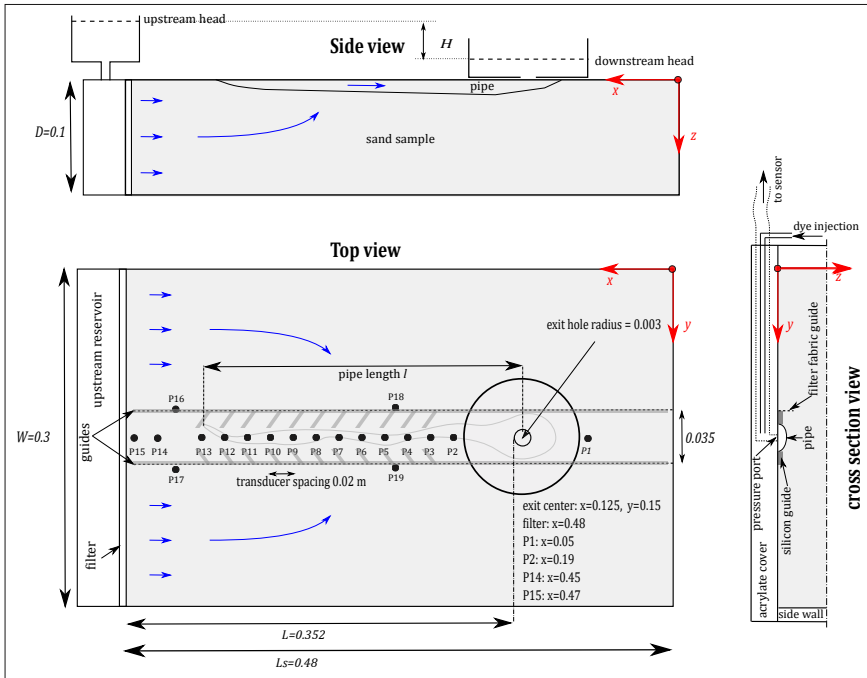


Figure 3.2: Drawing of experimental setup.

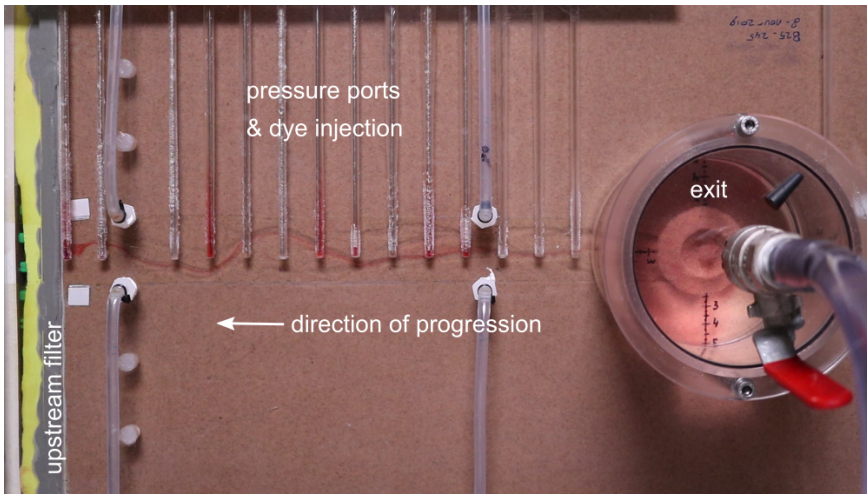


Figure 3.3: Top view of the setup at the end of experiment B25-245.

Table 3.1: Characteristics of sands used in small-scale experiments. B25 grain sizes, n_{min} and n_{max} are from Akrami et al. [2020].

Sand type	d_{10} [mm]	d_{50} [mm]	d_{60} [mm]	d_{70} [mm]	C_u [-]	n_{min} [-]	n_{max} [-]	ρ_s [kg/m ³]	n_{sb} [-]	θ_{sb} [°]
FPH	0.127	0.185	0.202	0.223	1.6	0.361	0.485	2610	0.419	38.6
B25	0.150	0.228	0.246	0.260	1.6	0.352	0.459	2650	0.410	37.6
FS35	0.328	0.422	0.442	0.462	1.35	0.344	0.444	2650	0.386	36.7

slope angle θ_{sb} of the sand boil per sand type were determined by measuring its height, diameter, and dry mass at the end of each test. The water temperature was between 20 and 22°C.

Water levels at the upstream and downstream sides were measured using riser tubes at least every five minutes, up to every minute during progression. The flow rate was measured at the same frequency using a digital scale. Pore pressures were measured by differential pressure transducers (Sensortech RPOP001D6A), through the ports P1-P19 (Fig. 3.2), at a sampling frequency of 10 Hz.

Three cameras recorded the erosion development. The main camera above the setup provides a top view of the sand sample, every 10 seconds. In some tests, we recorded short close-up videos of the erosion process using a second camera, which was placed temporarily on top of the cover. The last camera recorded the volume of the eroded sand, every minute. Pipe length and sand boil diameter were estimated visually at least every five minutes, up to every minute during progression.

Pipe depth in equilibrium conditions was measured using a laser device (DSE ODS 120) mounted on a movable frame to create transects perpendicular to the pipe. Pipe depth measurements during pipe progression were not feasible as the laser device would limit observation of the pipe by blocking the view from top and moving particles would affect the depth measurement.

Pipe flow velocities in equilibrium conditions were extracted from videos of dye tracer injections. A red dye was injected under low pressure through one of the pressure ports (usually P14 or P15) for approximately 2 seconds. The propagation velocity of the dye in the x-direction is obtained by tracking the change in color intensity relative to a video frame before injection [Ghilardi et al., 2014]. Usually, we injected 5-7 times in the same equilibrium conditions, from which we take the median propagation velocity. We assume that this represents the maximum flow velocity over the velocity profile in a cross section (u_{max}).

3.2.3 Test procedure

The test procedure consists of sample preparation, loading, and measurement cycles. First, the sample is prepared with the box in the vertical position by sprinkling dry sand in deaired water, and the sample is compacted by tapping the box with a hammer. Then, the box is closed and placed in the horizontal position, and the head at both sides of the sample is leveled. The loading procedure is as follows: keep the head difference constant if there is still erosion after 5 minutes, or increase it otherwise. The head difference is increased by reducing the downstream head, and the upstream head is kept constant. When the pipe

reached the upstream filter, the downstream head was raised (suddenly) to stop erosion. Then, the head difference was increased in small steps of 2 mm until grains started moving somewhere in the pipe. If the movement continued, the head difference was decreased by 2 mm. This procedure was iterated until the bed was just in equilibrium. In those conditions, the head drop was kept constant and the pipe depth, local hydraulic gradients in the pipe, and local maximum flow velocity u_{max} were measured to determine the critical bed shear stress. During the test, measurements of pipe length, sand boil radius, flow rate and total head drop were taken every five minutes, up to every minute during progression. After the test, the sand boil was collected, dried and weighed.

3

3.2.4 Test program

The test program consists of two phases as shown in Table 3.2. First, tests 217-222 are reference tests without guides to verify that the changes in experimental setup do not influence the critical head difference and average progression rate. Note that tests 218 and 219 are not representative as the pipe initially developed towards the side of the box, affecting the critical head. Tests 223-231 were not included in Table 3.2 since these involved iterative improvements of the guides to obtain stable results. Phase 2 consists of tests 232-250 with the adapted setup and varying sand type, degree of compaction and hydraulic loading. Densely packed samples have a relative density (D_r) of 0.7-0.8 and loose samples of 0.5-0.55. The standard loading scenario L1 is to gradually increase the head difference to the critical head difference (H_c) and then keep it constant. L3 and L4 are overloading scenarios, which means that after a stable pipe developed with pipe length $l \approx 0.14$ m (Table 3.2), the head is suddenly increased to $1.2 \cdot H_c$ (L3) and $1.1 \cdot H_c$ (L4) respectively and then kept constant. Note that the effective head drop over the sample (H_{corr}) is not always constant after H_c is reached, due to filter and exit losses changing with flow rate. Correction for filter and exit losses is described in section 3.3.3. Furthermore, the hydraulic conductivity k is estimated from flow rate and pressure gradient near the upstream filter, so it may be less reliable for tests 217-222 (marked with #). The results in Table 3.2 are discussed in section 3.3.3.

3.3 Experimental results

This section reports the experimental observations and the basic measurements of hydraulic head and pipe geometry. Analyses of progression rates, shear stresses and sediment transport require more interpretation and are therefore described separately in section 3.4.

3.3.1 General observations on the erosion process

This section describes the observed phases of the BEP process and (visual) observations of the erosion process at the grain scale. Like in other hole-type experiments [Miesel, 1977; Van Beek, 2015; Vandenboer et al., 2019], each test showed several phases for an increasing head drop: fluidization of sand in the exit hole, formation of a circular void (lens) around the exit hole, pipe growth towards an equilibrium (regressive) and progressive pipe growth until the pipe forms a hydraulic shortcut. Figure 3.4 indicates these phases in a plot of the head at each transducer. Before the erosion phases, the heads respond almost instanta-

Table 3.2: Overview of experiments and primary results. D_r is Relative density, Load is type of loading, k is hydraulic conductivity, $H_{c,corr}$ is corrected critical head, l_c is critical pipe length, $i_{c,tip}$ is critical pipe tip gradient, $v_{c,avg}$ is average progression rate after critical point.

* in case of overloading tests, the maximum applied head drop.

in case of overloading tests, the pipe length at which the head was raised to the maximum.

local pressure measurements not reliable

° test configuration without guides

Test nr.	configuration			results				remarks
	D_r [-]	Load	k [m/s]	$H_{c,corr}$ [cm]	l_c [cm]	$i_{c,tip}$ [-]	$v_{c,avg}$ [m/s]	
B25_217	0.802	L1	$3.0 \cdot 10^{-4}$	6.7	20.0	-	$6.80 \cdot 10^{-5}$	#, °
B25_218	0.798	L1	$2.8 \cdot 10^{-4}$	7.1	12.5	-	$7.37 \cdot 10^{-5}$	#, °, sideward growth
B25_219	0.806	L1	$3.0 \cdot 10^{-4}$	7.2	9.5	-	$1.53 \cdot 10^{-4}$	#, °, sideward growth
B25_220	0.803	L1	$2.8 \cdot 10^{-4}$	6.3	15.5	-	$7.10 \cdot 10^{-5}$	#, °
B25_221	0.792	L1	$2.7 \cdot 10^{-4}$	6.8	19.5	-	$9.20 \cdot 10^{-5}$	#, °
B25_222	0.807	L1	$2.7 \cdot 10^{-4}$	6.4	10.0	-	$5.42 \cdot 10^{-5}$	#, °
B25_232	0.796	L1	$2.7 \cdot 10^{-4}$	6.2	15.6	0.64	$1.02 \cdot 10^{-4}$	air bubbles in sample
B25_233	0.545	L1	$3.6 \cdot 10^{-4}$	6.2	12.7	0.49	$1.68 \cdot 10^{-4}$	
B25_234	0.545	L1	$3.7 \cdot 10^{-4}$	4.7	17.4	-	$9.46 \cdot 10^{-5}$	
FPH_235	0.738	L1	$1.1 \cdot 10^{-4}$	6.6	11.8	0.69	$3.00 \cdot 10^{-5}$	
B25_236	0.777	L1	$2.5 \cdot 10^{-4}$	6.1	18.6	0.66	$9.14 \cdot 10^{-5}$	
FPH_237	0.791	L1	$1.1 \cdot 10^{-4}$	6.5	19.0	0.50	$6.35 \cdot 10^{-5}$	
FS35_238	0.671	L1	$1.0 \cdot 10^{-3}$	6.2	18.9	0.50	$3.21 \cdot 10^{-4}$	
FS35_239	0.768	L1	$9.0 \cdot 10^{-4}$	5.6	13.9	0.73	$8.53 \cdot 10^{-5}$	
FS35_240	0.490	L1	$1.2 \cdot 10^{-3}$	5.6	21.3	0.57	$1.39 \cdot 10^{-4}$	
FS35_241	0.492	L1	$1.2 \cdot 10^{-3}$	5.5	18.6	-	$1.44 \cdot 10^{-4}$	
FS35_242	0.708	L3	$8.7 \cdot 10^{-4}$	7.5*	13.0	0.76	$6.67 \cdot 10^{-4}$	
B25_243	0.792	L1	$2.6 \cdot 10^{-4}$	5.9	16.8	0.69	$5.17 \cdot 10^{-5}$	sample badly connected to cover; not used
B25_244	0.558	L1	$3.3 \cdot 10^{-4}$	10.9				
B25_245	0.577	L1	$3.1 \cdot 10^{-4}$	5.4	19.7	0.43	$6.14 \cdot 10^{-5}$	
FS35_246	0.718	L1	$9.0 \cdot 10^{-4}$	6.1	17.9	0.83	$4.19 \cdot 10^{-4}$	
B25_247	0.797	L3	$2.4 \cdot 10^{-4}$	8.1*	14.9	-	$5.58 \cdot 10^{-4}$	
B25_248	0.799	L3	$2.5 \cdot 10^{-4}$	8.2*	12.5	0.68	$4.69 \cdot 10^{-4}$	
B25_249	0.804	L4	$2.5 \cdot 10^{-4}$	7.3*	15.0	0.71	$3.03 \cdot 10^{-4}$	
B25_250	0.799	L4	$2.5 \cdot 10^{-4}$	7.1*	16.0	0.68	$2.58 \cdot 10^{-4}$	

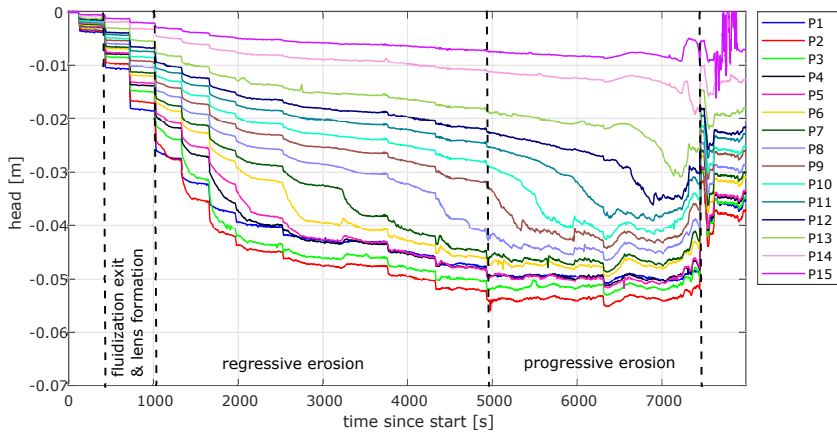


Figure 3.4: Head development in sensor P1-P15 and erosion phases in experiment B25-245.

neously to an increasing head drop. During erosion, the heads decrease also gradually under a constant head drop due to the pipe lengthening. It was also observed that after a head increase, the location in the pipe where grains started eroding was not always the same. Visual observations during the head increase indicate that erosion sometimes starts in the bed, sometimes at the tip. This suggests that both the bed and the tip are close to critical conditions, at least in the regressive phase.

At a few instances during the test program, the erosion process at the pipe tip was visualized using close-up videos. Grain detachment at the tip generally occurred in cycles. Sometimes, first a small displacement of particles in the zone upstream of the tip was observed, which increased the porosity locally. Sometimes, there was rearrangement of a few small particles in the sand upstream of the tip without the other grains moving. Quickly after the small displacement, a group of grains detached and moved into the pipe. Part of the grains washed away directly, while another part settled close to the tip. These settled grains were transported gradually until the cycle repeated. Between the group detachments, also individual particles detach. At higher progression rates, it was more difficult to distinguish separate cycles and the erosion process is more continuous. There is much variation between and within tests regarding the occurrence and duration of these steps in the erosion cycle, but the process generally followed this cycle.

3.3.2 Effect of particle detachment on pipe flow resistance

One test (B25_245) includes a close-up video of the tip during a transition from equilibrium to erosion with some particle detachment in groups. In this case, the pipe tip also grows closely under the pressure sensors. At the start of the video, the tip is right under P8, and the shortest distance from the other sensors to the pipe during its development is approximately 1 mm (P2,P3,P7), 2 mm (P6) and 7 mm (P4,P5). So the pipe is below or almost below most of the sensors. This allows to observe the effect of group detachment on the pipe pressure response. During the video, the tip progressed by 18 mm. Figure 3.6 shows a screenshot of the video, including pipe contours (drawn manually).

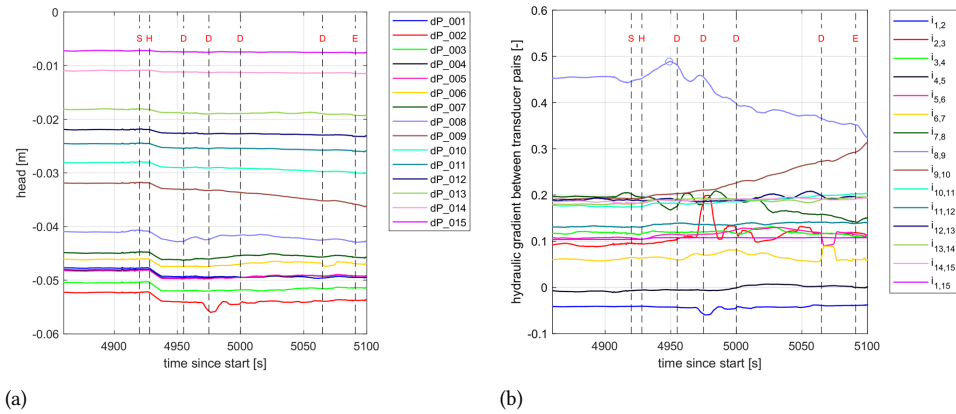


Figure 3.5: Pipe pressures (a) and gradients (b) during head increase and grain detachment. In red: S=start video, H=head increase, D=group detachment, E=end video. Right figure subscripts refer to the same “dP” sensors, downstream to upstream, on the left.

Figure 3.5 shows the pipe pressure of, and the gradient between, different sensors at that time ($4900 < t < 5100$) together with an indication of the time of group detachment (D). The time of group detachment is observed from the video. At the start of the video (S), the pipe tip is stable. After the increase in head difference of 2 mm (H), the gradient upstream of the tip between P8 and P9 ($i_{8,9}$) increases to its maximum value, and then decreases towards the pipe gradient as the tip propagates upstream (and now $i_{9,10}$ increases). However, it can be seen that the decrease in $i_{8,9}$ is not gradual, but temporarily drops by approximately 0.02-0.03 after the first group detachment. The effect of the first group detachment on the pressures is also seen in the downstream gradient $i_{7,8}$ (temporary gradient increase) and to a lesser extent in $i_{6,7}$ (temporary gradient increases several seconds later). Similar pressure fluctuations were observed in tests on FPH and FS35 sand, but these could not be related to group detachment because of lacking close-up videos. Note that the head drop in P2 around $t=4975$ s is caused by local erosion of the pipe wall and not directly by group detachment. The fluctuations in gradient are larger than the measurement uncertainty in pipe gradient (approx. 0.01), and its downstream propagation confirms that it is no sensor noise.

These effects of group detachment on the tip gradient seem small, but are approximately as large as the increase needed to start the erosion. This means that the tip gradient temporarily drops below the critical tip gradient and temporarily stops the tip erosion. These observations indicate that the transport of particles from the pipe tip affects the progression rate.

3.3.3 Critical head, pipe length and hydraulic gradients

The main results of the experiments are given in Table 3.2. The measured critical head drop H_c is the sum of the head drop over the sample $H_{c,corr}$, the upstream filter loss, and the exit losses. The filter loss was estimated by a linear regression of the head profile



Figure 3.6: Zone around pipe tip in test B25_245 s just before ($t=4975$ s) and during ($t=4976$ s) second group detachment.

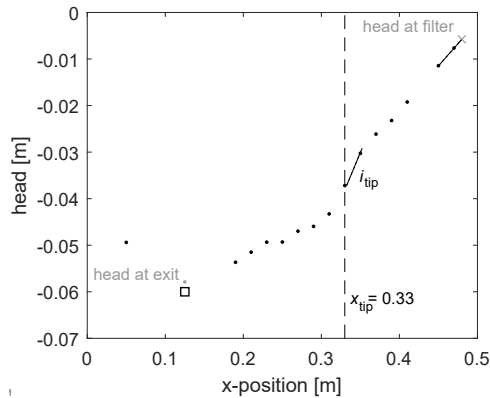


Figure 3.7: Example of the head profile close to critical conditions in test B25_245. \square = downstream head. x = head at filter. Estimates based on regression are indicated by the grey dot and cross.

through sensors P14-P15. The exit loss is estimated from regression on sensors P2-P5, but due to nonlinearities in the head profile around the tip this is only reliable when the tip has passed P5 ($x > 0.25$ m, $l > 0.115$ m). Therefore, for $l > 0.115$ m, the exit loss from regression was related to the flow rate Q for each test. Ultimately, the estimated exit loss throughout the test is based on this relation between exit loss and measured flow rate. At the critical pipe length, the average estimated filter and exit losses were 6.1 and 5.6 mm, respectively. The critical pipe length $l_c = x_{tip,c} - x_{exit}$ is the pipe length when the head reaches H_c . The average progression rate after the critical head has been reached $v_{c,avg} = (L - l_c)/(t_{end} - t_c)$ is based on visual observations of the pipe tip position. Hydraulic gradients between transducer pairs were derived from the pressure measurements, mostly having a 0.02 m spacing (Fig. 3.7). Critical tip gradients $i_{c,tip}$ are defined as the maximum gradient of the transducer pairs passed during the regressive phase (so pipe is close to equilibrium). These values are not available for all tests, as the pipe tip sometimes passed besides all pressure ports in the regressive phase. If multiple values were obtained for one test, Table 3.2 gives the maximum.

Modification of the setup (guides and pressure ports) did not lead to significant differences between the control group of dense B25 sand (tests 217 and 220-222, see Table 3.2) and modified group (tests 232, 236, 243), in terms of critical head $H_{c,corr}$ (6.3 – 6.8 cm before, 5.9 – 6.2 cm after), critical length l_c (10 - 19.5 cm before, 15.6 - 18.6 cm after) and progression rate $v_{c,avg}$ (0.05 - 0.09 mm/s before, 0.05 - 0.10 mm/s after). The slightly lower H_c (9%) after modification may be the result of a locally lower compaction and hence higher conductivity at the guides. In case of the coarse FS35 sand however, the pipe width may have been limited by the guide distance of 35 mm (see section 3.2.1), resulting in slightly deeper pipes compared to a situation without guides.

Both the net head drop over the sample $H_{c,corr}$ (Table 3.2) and the local critical tip gradient $i_{c,tip}$ have a positive relation with D_r for both the B25 and FS35 sands (Fig. 3.8), which confirms findings by Robbins et al. [2017]. The critical pipe length l_c varied between 30% and 60% of the seepage length. Given the large variability in l_c , it is not possible to infer significant effects of grain size or compaction.

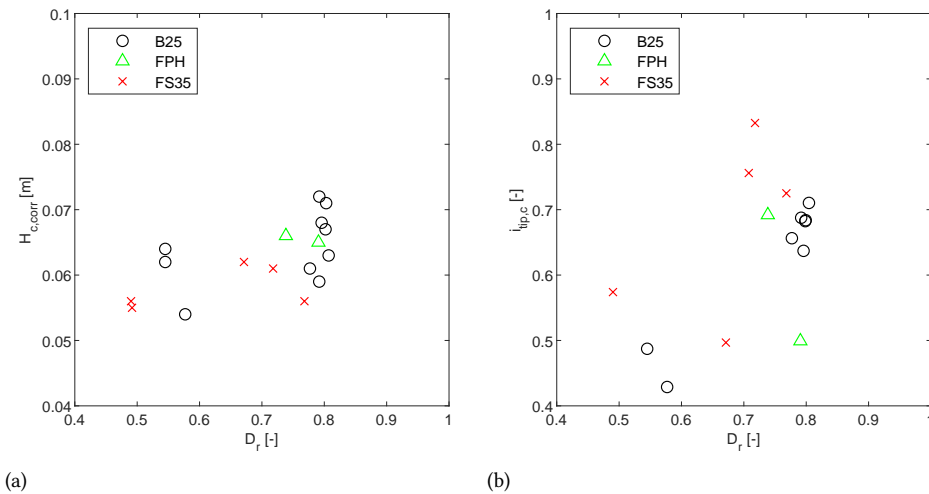


Figure 3.8: Critical head drop (a) and local critical tip gradient (b) as function of relative density D_r .

3.3.4 Pipe length development

Kézdi [1979] expected acceleration of the pipe development because of the increasing upstream secant (average) gradient with increasing pipe length. Figure 3.9 shows the pipe length development between the critical length $l = l_c$ and when the upstream filter is reached ($l = L$). Pipe length and time are normalized. The normalized pipe length becomes $l_n = (l - l_c)/(L - l_c)$ and the normalized time $t_n = (t - t_c)/(t_{end} - t_c)$, in which t_c is the time when $l = l_c$ and t_{end} is the time when $l = L$. On average, there is some acceleration in normal loading tests, which are closer to equilibrium. However, there is hardly acceleration in the B25 overloading tests as indicated by the nearly linear curve (note that absolute progression rates are higher).

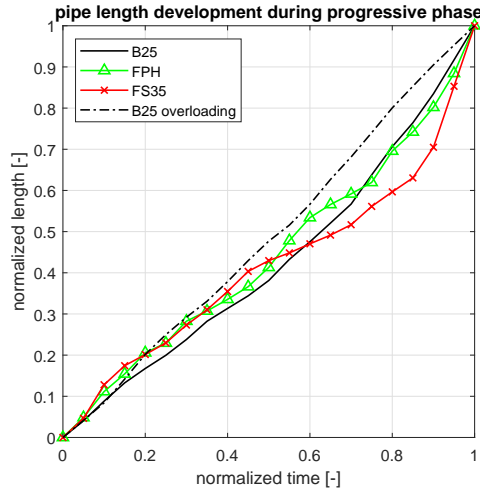


Figure 3.9: Normalized pipe length development in normal loading and overloading tests, average of tests per sand type.

This confirms experiments by Vandenoer et al. [2019] using the same setup, and another hole-type experiment by Miesel [1978]. However, slope-type experiments by Robbins et al. [2020b] showed very rapid progression and did not accelerate. Slope-type tests are initiation-dominated [Van Beek, 2015] and therefore overloaded more severely under a constant head. Apparently, the progression rate does not increase with pipe length in those overloading conditions, despite the increasing upstream secant gradient. That indicates that the progression rate is limited by the transport of sediment down the pipe rather than the limited supply of water to the pipe tip in severely overloaded conditions. The observation of acceleration shows that the progression rate (load effect) is not constant for a constant load. Here it is noted that the upstream filter resistance increased slightly with pipe length in several tests, resulting in a decreasing head drop over the sample. Without that resistance, the acceleration is expected to be even more pronounced.

3.3.5 Pipe geometry after test

The pipe geometry was analyzed to estimate the shear stress acting on the pipe bottom during equilibrium in a fully formed pipe. When a pipe had fully developed to the upstream filter and the head drop was lowered to bring the grains in equilibrium (see section 3.2.3), the pipe geometry was measured at several transects between $x=0.22$ m and $x=0.46$ m (approx. 2 cm spacing) using a laser scanner. From these cross sections, longitudinal profiles of the average pipe depth (a_{avg}), maximum pipe depth (a_{max}), area (A), hydraulic radius (R) and pipe width ($w_{avg} = A/a_{avg}$) were determined for the situation that the pipe reached the upstream filter. Note that several tests showed some erosion between the pipe reaching the filter and the laser measurement, as shown by the photos and sand boil dimensions. Based on the sand boil dimensions at these two moments in B25 and FS35 tests 232-250 and an assumed total pipe width of 25 mm (B25) or 30 mm (FS35), this resulted in an average depth increase of 0.1 mm.

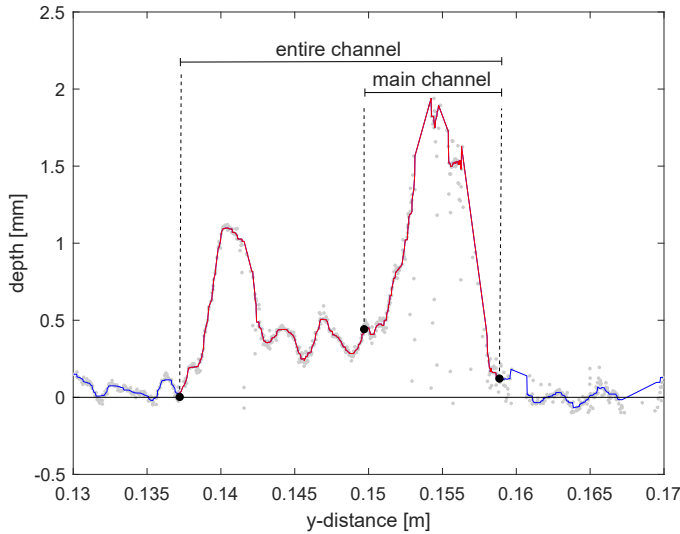


Figure 3.10: Example of cross section at $x=0.22$ m at the end of test B25-245.

When the pipes progressed, the channels were often migrating sideways, especially in the downstream parts of the finer sands B25 and FPH. This results in inactive channels without sediment transport and presumably a low flow rate. As we assume that the main flow conveying channel is representative for the pipe flow conditions such as shear stress, using the entire channel would lead to an incorrect bed shear stress τ (as a_{avg} is underestimated). This channel migration is not the result of the setup modification as it also occurs in Vandenoer et al. [2018b], though it is expected to occur less due to the application of the guides, see Fig. 3.2. The definition of the boundaries of the main channel is based on visual interpretation of the depth profile (Fig. 3.10). If one channel is clearly larger than the other, the largest is selected as main channel. If both are equally large or there is only one, the main channel equals the entire channel. Figure 3.11 shows pipe geometry based on the entire channel and the main channel. The main channel approach yields higher a_{avg} , lower w_{avg} and more consistent geometries across the three sands. In section 3.4.1 (Fig. 3.12) we show that the main channel approach yields more consistent shear stresses. Therefore, the main channel geometry is a better representation of the pipe flow than the entire cross section and we use it to estimate pipe flow conditions.

Figure 3.11b shows the resulting depth profile (a_{avg}) per sand type. The solid lines indicate the average of tests 232-250, the error bars indicate \pm one standard deviation. The pipe depth scales with the permeability as $a \propto \sqrt[3]{\kappa}$ [Vandenoer et al., 2018b]. Scaling with d_{50} gives reasonable results too for these sands; which one scales better can only be assessed with a wider range of grain size and uniformity. The depth profile can be approximated with a power function as:

$$a = 6.0 \sqrt[3]{\kappa(x_{tip} - x)} \quad (3.1)$$

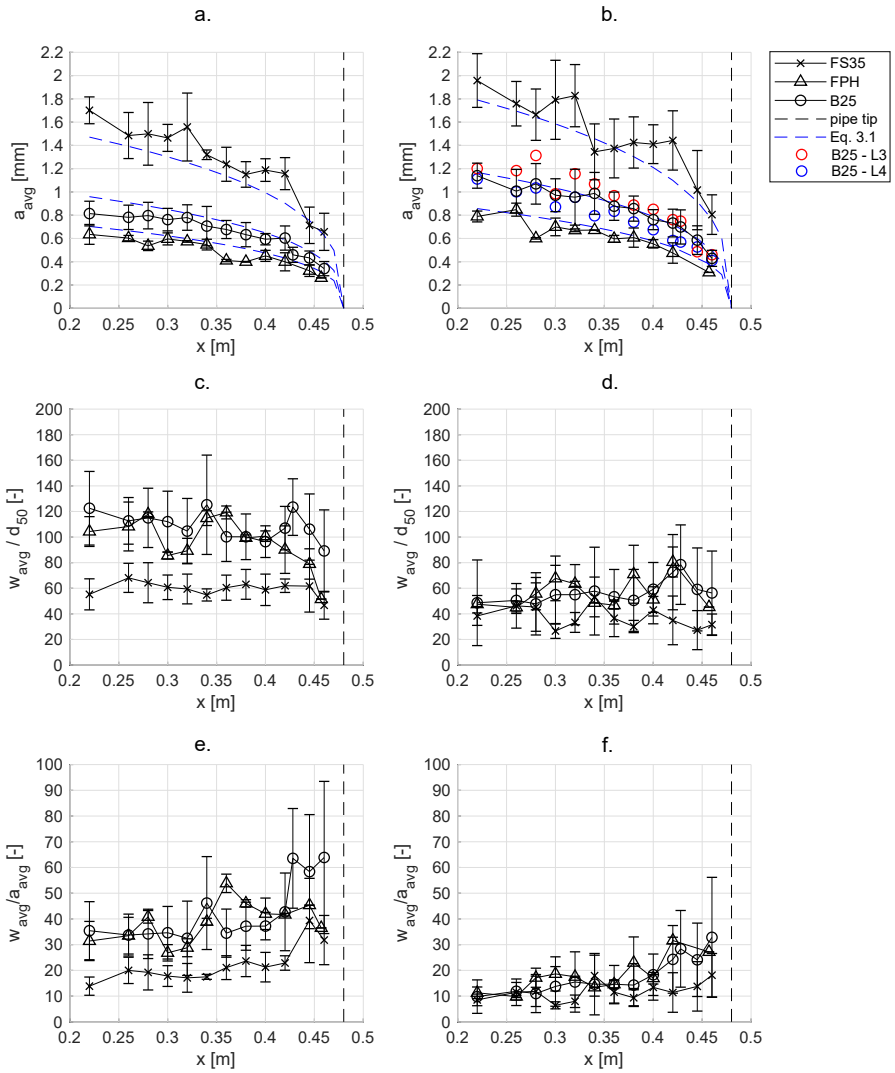


Figure 3.11: Pipe geometry during equilibrium with fully developed pipe in tests 232-250, excluding B25-244. Based on entire channel (left) and main channel (right). Error bars indicate \pm one standard deviation. $x=0.48$ is the upstream boundary.

The profiles of a_{max} and R (not shown in Fig. 3.11) have a similar form with coefficients 10 and 2.8, respectively. The shape of the depth profile will depend on the spatial distribution of seepage towards the pipe, so on aquifer geometry. As this relation is purely empirical, it is only to be used to analyze the current experiments. Three B25 tests (230, 236 and 245) include depth measurements when the pipe was partially developed ($l < L$). From the depth data (not shown here) it follows that the partially developed depth profile is similar to Eq. 3.1. Therefore, we assume that Eq. 3.1 also holds during progression. Figure 3.11b indicates that there was no significant difference in equilibrium depth profiles between the average of all tests and the ones with overloading (L3 and L4). Therefore, we assume that overloading does not lead to significant differences in depth.

The average pipe width w_{avg} is rather constant along the pipe (Fig. 3.11d) and in the order of 60 times d_{50} for B25 and FPH sands. This results in a main channel w_{avg}/a_{avg} ratio of 10 at the downstream side to 25 near the pipe tip. Furthermore, based on the photos taken from top, we found the tip width to be approximately 30 times d_{50} , confirming Van Beek [2015]; Xiao et al. [2019a]. However, the tip width increases with the degree of overloading, up to $45 \cdot d_{50}$ at $1.2 \cdot H_c$. The pipe width in FS35 sand is lower than in B25 and FPH sand, with $w_{avg} = 40 \cdot d_{50}$. This may be caused by the limited space (35 mm) between the filter fabric guides. This restriction may have caused narrower and deeper cross sections, which could explain the underestimated FS35 depth using Eq. 3.1.

3.4 Pipe progression analysis

This section analyzes the pipe progression rates and its relationship with tip seepage velocity and pipe shear stress. First, the bed shear stress in equilibrium conditions with a fully developed pipe is computed with different approaches and compared to existing data of critical bed shear stress. This information is subsequently used to determine the bed shear stress during pipe progression. The tip seepage velocity is calculated from the measured tip gradient i_{tip} , conductivity k and porosity n , and both parameters are related to the pipe progression rate. Finally, the sediment transport is compared to sediment transport relations from classical, laminar flume experiments conducted for studies of sediment transport in open channels.

3.4.1 Critical bed shear stress during equilibrium

The critical bed shear stress for incipient motion is an important parameter to predict piping and was determined from measurements at the end of each test, for the situation of a fully developed pipe. The pipe geometry is based on the main channel (see section 3.3.5). The local hydraulic gradients between transducer pairs are only calculated for those pairs below which the pipe progressed. The maximum flow velocity in the pipe was measured by injection of a dye in one of the pressure ports close to the filter (P14 or P15).

Bed shear stress can be calculated based on either pressure gradient and pipe depth, pressure gradient and flow velocity or flow velocity and pipe depth. First, we present the three equations to calculate shear stress. Later, we show the resulting shear stresses for the piping experiments. In the equations below, the subscript of τ indicates on which quantities it is based, for example τ_{ai} is based on pipe depth a and hydraulic gradient i . First, from a balance of forces it follows that the average shear stress along the wetted

perimeter is the product of hydraulic radius $R = a/2$ and local pressure gradient in the pipe dp/dx , which gives for parallel plates [Sellmeijer, 1988]:

$$\tau_{ai} = R \frac{dp}{dx} = \rho_w g \frac{a}{2} i \quad (3.2)$$

Alternatively, one can use the relation between depth-averaged flow velocity, pressure gradient and pipe depth from the Poiseuille equation for laminar flow between parallel plates [Sellmeijer, 1988]:

$$\frac{dp}{dx} a^3 w = 12U w a \mu \quad (3.3)$$

in which $U = 2/3 u_{max}$ [Spiga and Morino, 1994]. Substitution of a in the shear stress equation 3.2 by Eq. 3.3 gives:

$$\tau_{ui} = \sqrt{3\mu U \frac{dp}{dx}} \quad (3.4)$$

Alternatively, substitution of dp/dx in the shear stress equation 3.2 by Eq. 3.3 gives:

$$\tau_{ua} = \frac{6\mu U}{a} \quad (3.5)$$

Note that the Reynolds number ($Re = 4RU/\nu$) during equilibrium at the end of the tests was in the order of 40 for FPH sand, 80 for B25 sand and 280 for FS35 sand, which confirms that the flow was laminar ($Re < 2100$). As the main channel w/a ratio lies in the range of 10 to 25, the assumption of parallel plates is a reasonable approximation [Spiga and Morino, 1994; Van Beek, 2015].

These three expressions (Eqs. 3.2, 3.4 and 3.5) for the shear stress are equivalent under the assumption of laminar flow between parallel plates but require different input. During equilibrium conditions, all three inputs (pipe depth a_{avg} , local gradient between transducer pairs i , and flow velocity u_{max}) were measured along the pipe to be able to compare Eqs. 3.2, 3.4 and 3.5. Finally, the measured shear stress $\tau(x)$ is averaged over the length of the pipe. In the analysis we assume that water density $\rho_w = 1000 \text{ kg}\cdot\text{m}^{-3}$, and dynamic viscosity $\mu = 1 \text{ mPa}\cdot\text{s}$ (20 degrees C). Figure 3.12 shows the resulting critical bed shear stress from Eqs. 3.2, 3.4 and 3.5 during equilibrium (average of all tests with equal d_{50}), plotted as critical Shields number $\Theta_c = \tau_c / (\rho_s - \rho_w) g d$ against dimensionless particle diameter $D_* = (\Delta g / \nu^2)^{1/3} d_{50}$. Results of Eq. 3.2 and 3.5 are plotted for both the average depth a_{avg} of the main channel and of the entire channel. With the entire channel, Eqs. 3.2, 3.4 and 3.5 yield different results, especially in case of the finer sands. With the main channel approach, the results are much closer, supporting the assumption of parallel plates and the use of the main channel depth. The main channel results are in good agreement with classical flume experiments on a plane bed [Govers, 1987; Loiseleux et al., 2005; Mantz, 1977; Pilotti and Menduni, 2001; Ward, 1968; White, 1940, 1970; Yalin and Karahan, 1979], piping experiments in cylinders [Van Beek et al., 2019] and predictions of critical shear stress by Van Beek [2015] and Cheng [2004]. In terms of τ_c , the main channel results are in the range of 0.314 – 0.360 Pa for FPH, 0.368 – 0.385 Pa for B25, and 0.417 – 0.564 Pa for FS35. So, the observed critical shear stresses as calculated using Eqs. 3.2, 3.4 and 3.5 are

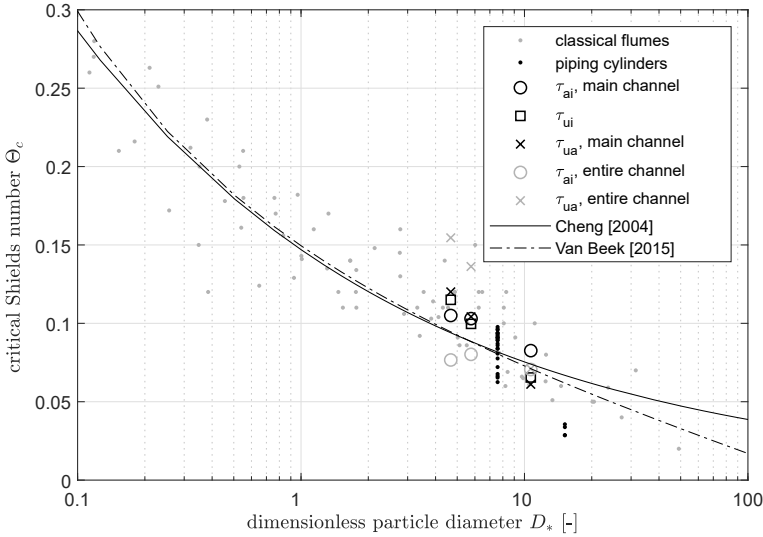


Figure 3.12: Critical Shields number during equilibrium with fully developed pipe in tests 232-250, average value per sand type, plotted with empirical relations [Cheng, 2004; Van Beek, 2015] and experiments in laminar flow in piping cylinders [Van Beek et al., 2019] and classical flumes [Govers, 1987; Loiseleux et al., 2005; Mantz, 1977; Pilotti and Menduni, 2001; Ward, 1968; White, 1940, 1970; Yalin and Karahan, 1979].

in line with other experiments, and therefore these equations are also applied to calculate shear stress during progression in section 3.4.2.

3.4.2 Drivers of the progression rate

The progression rate $v = dl/dt$ is a practical engineering metric for the temporal development of the piping process. This section correlates the observed progression rate during the progressive erosion phase to two variables: (1) seepage velocities upstream of the pipe tip following Kézdi [1979], and (2) bed shear stresses in the pipe.

The seepage velocity just upstream of the pipe tip is derived from measured tip gradients:

$$u_p = \frac{k \cdot i_{tip}}{n} \quad (3.6)$$

In which i_{tip} is the local hydraulic gradient measured over a distance of 2 cm (transducer spacing) upstream of the pipe tip, and k and n are the initial hydraulic conductivity and porosity. While Kézdi [1979] neglects head loss in the pipe and assumed that i_{tip} equals the average upstream gradient, this section applies the same concept, but using measured local gradients. In contrast, Robbins et al. [2020b] used back-calculated tip gradients from a FEM model.

The bed shear stress is calculated with Eq. 3.2 during the progressive erosion phase, since no flow velocity measurements during progression are available:

$$\tau(x, t) = 0.5\rho_w g a(x, t) i(x, t) \quad (3.7)$$

The pipe gradient i is calculated as the hydraulic gradient between the transducers downstream of the pipe tip. Shear stress is calculated both based on the average of all transducer pairs downstream of the tip ($\tau_{\text{bed,average,all}}$) and based on the average of the transducer pairs where the pipe passed right under both ports ($\tau_{\text{bed,average,passed}}$). The first may include more scatter from transducers pairs which are partly above and partly besides the pipe but contain more datapoints to be included in the averaging.

Due to a lack of depth measurements during progression, we assume that the depth profile has the same shape as during equilibrium at the end of the tests (Eq. 3.1):

$$a(x, t) = 6.0 \cdot \sqrt[3]{\kappa(x_{\text{tip}}(t) - x) - 0.0001} \quad (3.8)$$

The depth of 0.0001 m is subtracted to account for the residual erosion after reaching the upstream filter (see section 3.3.5). We believe this provides a reasonable estimate of the depth profile as it is similar to some depth measurements made for partially developed pipes in three B25 tests (see section 3.3.5). Furthermore, Eq. 3.8 was verified for test B25-247 (at $l=0.14$ m) using the Poiseuille relation (Eq. 3.3) and measured gradient near the exit ($i=0.153$ between transducers P2-P4), flow rate ($Q_w = Uwa=1.12$ mL/s), and pipe width ($w=0.01$ m). Eq. 3.3 yields a calculated depth of $a=0.96$ mm, whereas Eq. 3.8 yields $a=1.1$ mm.

We calculated seepage velocity (Eq. 3.6) and pipe shear stress (Eq. 3.7) for each time that the tip passed a pressure port in the progressive phase ($l > l_c$). However, we omit seepage velocity and tip gradient data if the pipe tip passed besides that transducer, as this data is unreliable. And we omit shear stress data if no value is measured for either $\tau_{\text{bed,average,all}}$ or $\tau_{\text{bed,average,passed}}$. This results in 75 datapoints from test 232-250 for seepage velocity and 103 datapoints from test 233-250 for shear stresses, which are from different sand types and degrees of overloading and measured at different pipe lengths. Note that using an equal number of data points for all parameters in Fig. 3.13 would not affect the trends in Fig. 3.13, but the lesser datapoints would make the analysis in Table 3.3 unreliable. Finally, the corresponding progression rate at these passing moments is calculated using a moving average (over 3 datapoints; usually 3 minutes) of the visually observed tip position.

Figure 3.13 shows the relations between progression rate and several parameters related to seepage velocity and pipe shear stress. Values of ρ_p indicate Pearson correlations. Figure 3.13a shows that the progression rate is proportional to the tip seepage velocity up for tests with normal loading (L1) on different sand types. However, the overloading tests (L3 and L4) on B25 sand show higher progression rates which cannot be explained by the seepage velocity as the seepage velocity hardly changes under overloading. Figure 3.13 (a-c) show how the effect of up is composed of k and i_{tip} and that the hydraulic conductivity explains most of the variation in progression rate observed in normal loading tests, not the tip gradient. Furthermore, the measured local tip gradient i_{tip} does not seem to increase with the degree of overloading, although there is substantial variability in these measurements. This can be caused by a higher porosity at the tip, or by higher resistance in the pipe (due to high sediment load). Furthermore, it is likely that the tip gradient cannot exceed its critical value much, as the tip material will collapse (see Fig. 3.13). Figure 3.13(e-f) shows that the bed shear stress is a better predictor, see also section 3.4.3 for more discussion. Compared to the seepage velocity it predicts the overloading tests reasonably well and explains part of the variation within groups (e.g. group FS35,L1). $\tau_{\text{bed,average,all}}$

Table 3.3: Estimated critical bed shear stress [Pa] during progression. Based on linear regression on the data of progression rate vs. shear stress (Fig. 3.13).

* less significant ($0.01 < p\text{-value} < 0.05$)

° not significant ($p\text{-value} > 0.05$): τ_{crit} estimated visually

	transducer pair	FPH	B25	FS35
<i>During progression</i>	first pair near tip	0.10°	0.11	0.15°
	average of passed	0.13*	0.18°	0.25
	average of all	0.19*	0.2	0.4
	average near exit	0.22°	0.26	0.42
<i>During equilibrium (end of test)</i>	average of passed	0.339	0.377	0.476

gives an even stronger relation (Fig. 3.13f), probably due to the averaging of noise caused by some pressure ports being besides the pipe and that generally a larger part of the pipe is included in the averaging due to less strict criteria. Finally, the data show no relation between D_r and progression rate in normal loading tests (Fig. 3.13d).

3.4.3 Critical bed shear stress during pipe development

Section 3.4.1 shows measured critical bed shear stresses τ_c during equilibrium at the end of the tests. However, τ_c during progression can also be estimated from the plots in Fig. 3.13f, as the point where the progression rate reaches 0. We fitted a linear regression line through the same data as in Fig. 3.13e-f, of which the intercept is a proxy of the critical bed shear stress during progression. The same procedure was followed for the shear stress at the first transducer pair downstream of the tip and for the average shear stress between the 5 transducers (P2-P6) closest to the exit. Table 3.3 shows the obtained results, including the values with fully developed pipes at the end of the tests. It appears that the estimated τ_c during progression is lower than during equilibrium in fully developed pipes. The estimated τ_c near the exit is similar to the average τ_c in the pipe, but the estimated τ_c near the pipe tip is clearly lower.

There is a general consensus that upward seepage reduces both the occurring shear stress due to a change in velocity profile as well as the critical shear stress [Cheng and Chiew, 1999; Francalanci et al., 2008; Lu et al., 2008]. Regarding the impact on sediment transport rates, these studies show diverging results. Upward seepage effects were omitted from the Sellmeijer model [Sellmeijer, 2006] as they expected that this would not affect the eroding grains on top of the bed. As upward seepage is most severe at the pipe tip, this effect could explain the lower critical shear stress near the tip in Table 3.3. The critical bed shear stress under upward seepage is equal to $\tau_c = \tau_{c,0} \left(1 - \frac{i_u}{i_f}\right)$ where $\tau_{c,0}$ is the critical bed shear stress without seepage, i_u is the upward hydraulic gradient in the bed, and i_f is the critical gradient for fluidization [Cheng and Chiew, 1999]. Finite element simulations of test B25-245 (for $l=0.185$ m) [Robbins et al., 2022] show that the upward seepage gradient below the pipe varies from approximately 0.35 at the tip to 0.2 at a distance of 3 cm from the tip. The fluidization gradient is $i_f = (1 - n)(\rho_s/\rho_w - 1)$ [Terzaghi, 1922], which equals 1 for B25 sand with $n=0.4$. The resulting 20-35% reduction in τ_c partly explains the lower experimentally obtained critical shear stress ‘during progression’ as compared to

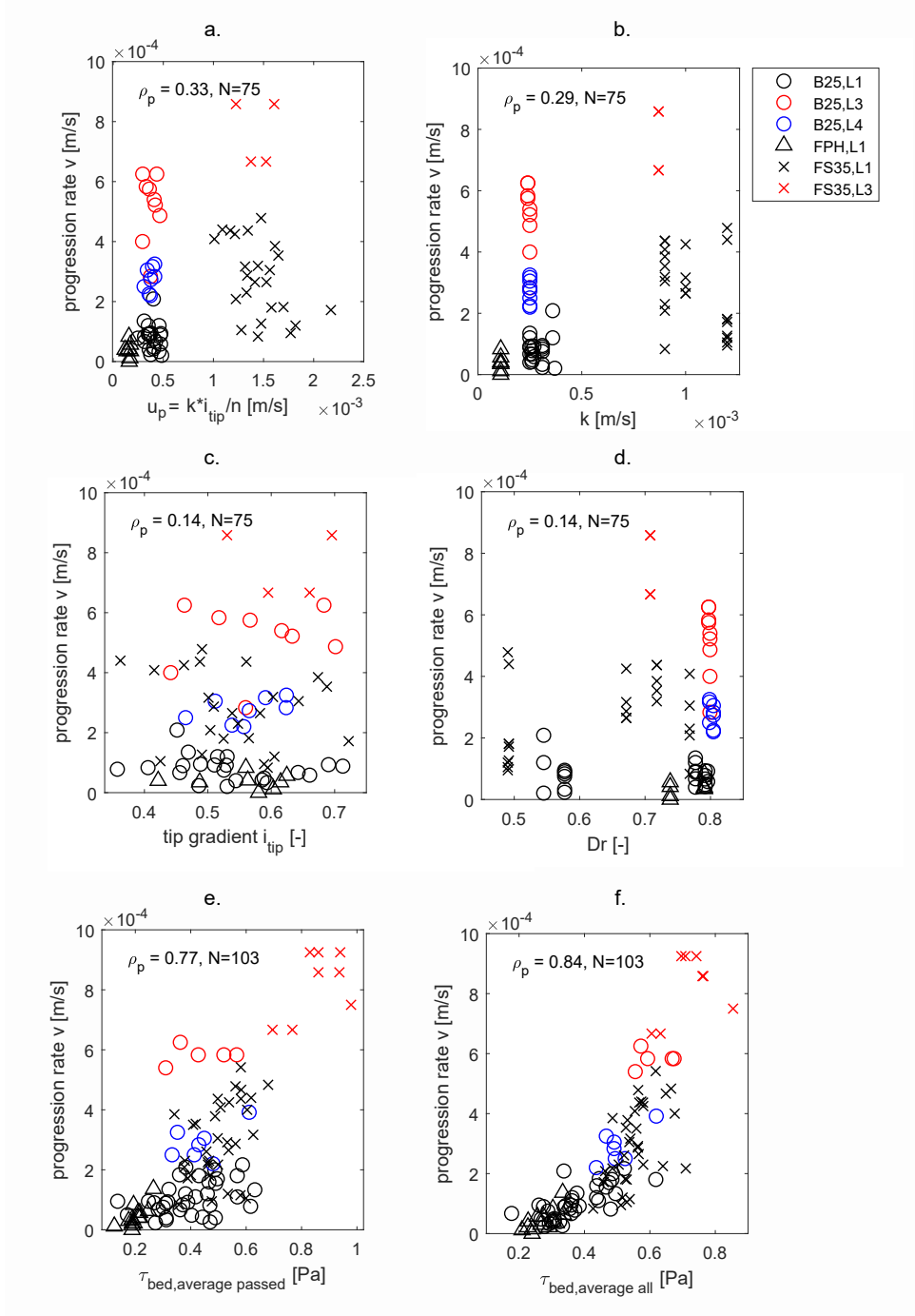


Figure 3.13: Relation between progression rate and seepage velocity, bed shear stress, tip gradient, conductivity, and compaction. Color indicates loading type; marker indicates sand type.

‘during equilibrium’ (Table 3.3). These findings indicate that upward seepage may have a significant effect on τ_c in BEP. Upward seepage affects the acting shear stress τ through a change in the near-bed velocity profile [Cheng and Chiew, 1999]. A full quantification of these effects for the case of laminar flow in rectangular ducts is beyond the scope of this research and needs to be verified with modelling or future experiments with more detailed information on pipe depth, pipe velocity profile, and upward seepage gradients in case of partially developed pipes. Omitting the upward seepage effect from BEP models may be acceptable if the effect on the acting shear stress τ balances the effect on the critical shear stress τ_c .

3.4.4 Sediment transport

The dependence on the bed shear stress raises the question whether the piping erosion rate can be predicted using sediment transport equations. Sediment transport (bed load) in turbulent flow is typically related to the bed shear stress through:

$$q_{*E} = \alpha_1(\Theta - \Theta_c)^{\alpha_2} \quad (3.9)$$

in which the Einstein number $q_{*E} = q_v/(d\sqrt{\Delta g d})$, q_v a volumetric sediment flux per unit width, Θ the Shields number, the critical Shields number $\Theta_c = f(\text{Re}_*)$, and the coefficients for turbulent flow are $\alpha_1 \approx 4$, $\alpha_2 \approx 1.5$ [Wong and Parker, 2006]. Similar equations exist for laminar flow [Charru et al., 2004; Cheng, 2004; Malverti et al., 2008; Ouriemi et al., 2007; Yalin, 1963], see Table 3.5. The sediment transport rate in laminar flow scales better by a viscous scaling rather than the inertial scaling of the Einstein number [Charru et al., 2004; Ouriemi et al., 2007]:

$$q_{*v} = \frac{q_v}{(\rho_s - \rho_w)g d^3/\mu} \quad (3.10)$$

Although our experiments were not specifically designed for this purpose, we complemented the available experimental data on sediment transport rates in laminar flow [Abramian et al., 2019; Charru et al., 2004; Delorme et al., 2018, 2017; Grass and Ayoub, 1982; Malverti et al., 2008; Seizilles et al., 2014] with estimated sediment transport rates from the piping experiments in this chapter. Table 3.4 summarizes the materials and flow conditions in the classical flume experiments. More details of the original data are given in Appendix C. The sediment transport rate q_v (volume per unit width) in the piping experiments is estimated from the growth rate of the sand boil radius (Fig. 3.3) and an average main channel width near the exit of $40 \cdot d_{50}$ (Fig. 3.11). Assuming a cone-shaped sand boil with equal inner and outer slopes, its sediment volume is given by:

$$V_{sb} = (1 - n_{sb}) \frac{\pi}{4} \cdot \tan \theta_{sb} [r_b^3 + r_e^3 - r_e r_b^2 - r_b r_e^2] \quad (3.11)$$

In which n_{sb} the porosity in the sand boil, θ_{sb} the slope angle, r_b the radius of the sand boil (observed during the tests), and r_e the exit hole radius (0.003 m). Values of n_{sb} and θ_{sb} given in Table 3.1 are based on sand boil dimensions and dry sand mass measured at the end of tests 224-250. The Shields number Θ at the downstream end of the pipe is based on Eq. 3.7 using the average pipe gradient over the 5 transducers near the exit (P2-P6) and pipe depth a_{avg} at the exit ($x=0.125$ m) from Eq. 3.8, which increases with pipe

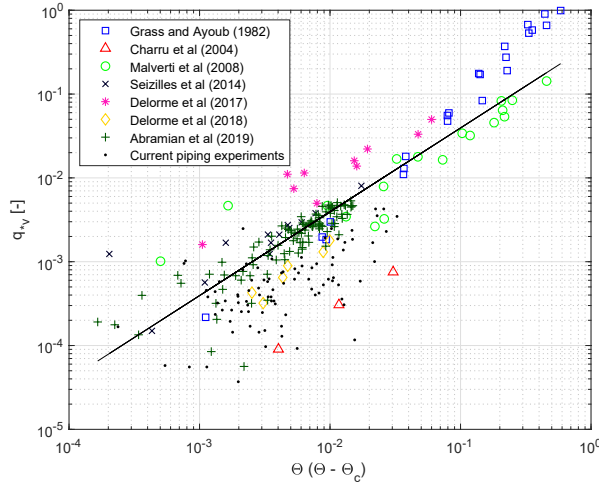


Figure 3.14: Sediment transport rate as function of $\Theta(\Theta - \Theta_c)$ in classical flume experiments from literature and the piping experiments in this chapter.

length. The critical Shields numbers Θ_c at the downstream end of the pipe are calculated as 0.0736 (FPH), 0.0705 (B25) and 0.0615 (FS35) from τ_{exit} in Table 3.3, so from extrapolating the shear stress to $v = 0$. Note that this estimate of Θ_c during progression is relatively low compared to the value at the end of the tests (Fig. 3.12), which is possibly due to upward seepage during the piping experiments.

Figure 3.14 shows the sediment transport rate q_{*v} as function of $\Theta(\Theta - \Theta_c)$, for both the classical flume experiments and the piping experiments. The experimental data mostly follows the same trend. Only the data of Charru et al. [2004] is below the range of other data, and Grass and Ayoub [1982] shows a higher exponent. The transport rate in the piping experiments is approximately a factor 5 below the average trend, but falls within the experimental range, and shows a similar trend with increasing Shields number. As can be expected, the scatter in the piping experiments is larger than in classical flume experiments because there is intermittent erosion, no wide uniform bed and flow profile, and no depth profile measurements during progression.

Least square fitting of the flume data alone results in the following empirical relation with $R^2 = 0.90$ and a median absolute percentage error ($|q_{predict} - q_{exp}|/q_{exp}$) of 0.373, drawn in Fig. 3.14:

$$q_{*v} = 0.39\Theta(\Theta - \Theta_c) \quad (3.12)$$

Figure 3.15 shows the ability of Eq. 3.12 and the models by Yalin [1963], Charru et al. [2004], Cheng [2004] and Ouriemi et al. [2007] to predict the classical flume experiments from the literature [Abramian et al., 2019; Charru et al., 2004; Delorme et al., 2018, 2017; Grass and Ayoub, 1982; Malverti et al., 2008; Seizilles et al., 2014] Cheng [2004] and Ouriemi et al. [2007] fit well to the higher transport rates, but overestimate the transport for flow conditions close to critical. Yalin [1963] generally performs well but shows some underestimation closer to critical. The empirical model by Charru is about one order of

Table 3.4: Characteristics of classical flume experiments on sediment transport in laminar flow.

authors	grain type	d [mm]	ρ_s [kg/m ³]	ρ_w [kg/m ³]	D_* [-]	a/d [-]
Grass and Ayoub [1982]	sand	0.14	2650	995- 1000	2.62- 4.11	14
Charru et al. [2004]	acrylic	0.58	1180	950	1.03	10-12
Malverti et al. [2008]	glass	0.075	2500	1000	1.84	13-40
Seizilles et al. [2014]	plastic	0.344	1520	1000	5.92	<10
Delorme et al. [2017]	silica & coal	0.130- 0.400	1500- 2650	1000	3.29- 6.79	-
Delorme et al. [2018]	corundum	0.416	3900	1150	3.25	-
Abramian et al. [2019]	resin	0.827	1540	1160	2.9	4-6
Current experiments	sand	0.185- 0.422	2610- 2650	1000	5-10	2-5

Table 3.5: Empirical and semi-empirical models for the sediment transport rate in laminar flow. Partly based on Ouriemi et al. [2009] and Wewer et al. [2021].

Reference	Type	transport rate $q_{sv} = \frac{q_v}{(\rho_s - \rho_w)gd^3/\mu}$
Yalin [1963]	semi-empirical	$\frac{\mu}{\sqrt{(\rho_s - \rho_w)gd^3\rho_w}} 0.635s \sqrt{\Theta} \left[1 - \frac{\ln(1+as)}{as} \right]$ $a = 2.45 \frac{\sqrt{\Theta}}{\rho_s/\rho_w^{0.4}}, s = \frac{\Theta - \Theta_c}{\Theta_c}$
Charru et al. [2004]	empirical	$0.025\Theta(\Theta - \Theta_c)$
Cheng [2004]	semi-empirical	$\frac{\mu}{\sqrt{(\rho_s - \rho_w)gd^3\rho_w}} 41\Theta^{-0.5} \text{Re}_* \left[\sinh 0.139\Theta^{1.181} \text{Re}_*^{0.39} \right]^2$
Malverti et al. [2008]	empirical	$\frac{\mu}{\sqrt{(\rho_s - \rho_w)gd^3\rho_w}} 0.67\Theta(\Theta - \Theta_c)^{1.5}$
Ouriemi et al. [2009]	semi-empirical	$n \frac{\Theta_c}{12} \left[\frac{\Theta}{2\Theta_c} \left(\frac{\Theta^2}{\Theta_c^2} + 1 \right) - \frac{1}{5} \right] \approx n \frac{\Theta_c}{24} \left(\frac{\Theta}{\Theta_c} \right)^3$
New fit	empirical	$0.39\Theta(\Theta - \Theta_c)$

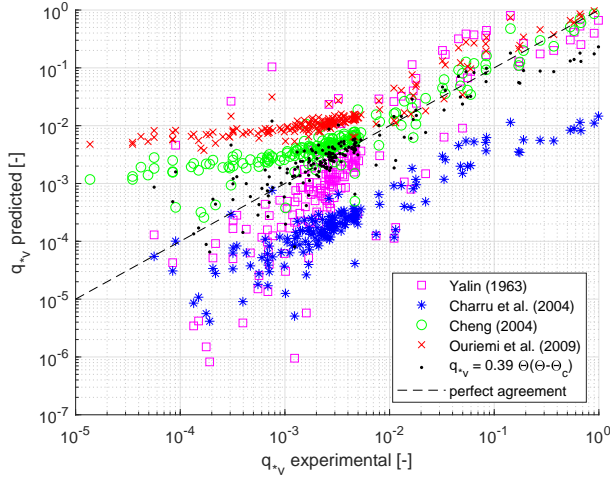


Figure 3.15: Experimental data in classical flume experiments (see Fig. 3.14) as predicted by several sediment transport equations including Eq. 3.12.

magnitude below the average trend of the flume data, which is in line with findings of Wewer et al. [2021] that Charru underestimates the pipe progression. However, it is a lower bound for the piping data. The simple empirical regression from Eq. 3.12 performs well over a wide range of measurements but underestimates the highest transport rates. As in the piping experiments $q_{s,v} < 10^{-2}$, Eq. 3.12 is a suitable empirical model.

So far, the analysis focused on the relation between transport rate and shear stress in the classical flume experiments and piping experiments. The measured transport rate can also be used for an additional cross-check on the assumptions on the pipe geometry during progression. For a progressing pipe, the sediment mass balance states that the increase in pipe volume per unit time ($dl \cdot (1-n) \cdot A_{exit}$) is equal to the total sediment transport at the downstream end of that pipe ($Q_s \cdot dt$). Assuming a rectangular cross-section ($A_{exit} = w_{exit} \cdot a_{exit}$), this relates the progression rate dl/dt to the sediment transport rate as:

$$v_{predict,V} = \frac{dl}{dt} = \frac{q_v}{(1-n)a_{exit}} \quad (3.13)$$

Combining Eq 3.12 and 3.13 results in a progression rate as function of the measured shear stress near the exit:

$$v_{predict,\Theta} = \frac{(\rho_s - \rho_w)gd^3}{\mu} \cdot \frac{0.39\Theta(\Theta - \Theta_c)}{(1-n)a_{exit}} \quad (3.14)$$

For the same data as in Fig. 3.13 and using a_{exit} from Eq. 3.8 and assuming $w_{exit} = 40 \cdot d_{50}$, Eq 3.13 and 3.14 were evaluated and compared to the measured progression rate. Figure 3.16a shows that $v_{predict,V}$ yields a correct magnitude of dl/dt , providing a cross-check that reasonable assumptions were made regarding a_{exit} and w_{exit} . Figure 3.16b

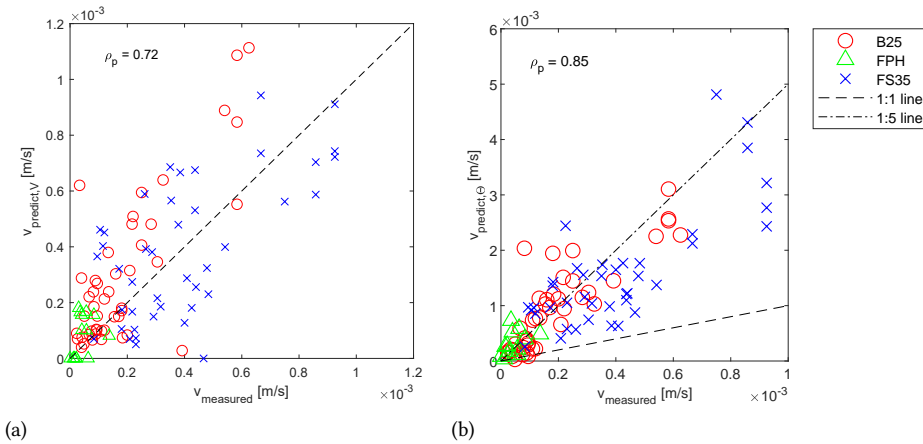


Figure 3.16: Measured progression rate in piping experiments and predictions using Eq. 3.13 (a) and Eq. 3.14 (b).

shows that Eq. 3.14 results in an overprediction of the progression rate by a factor 5, which agrees with the difference between piping tests and classical flume experiments in Fig. 3.14. Therefore, we recommend using a coefficient of 0.08 instead of 0.39 in Eq. 3.12 when modelling BEP using sediment transport relations, until more is known about the applicability of these sediment transport relations for BEP.

3.5 Discussion

This discussion section compares the results to previous experiments, reflects on the experimental setup and finally discusses the erosion process and some implications for modelling the temporal development of BEP.

3.5.1 Comparison with other experiments

First, we compare our results with previous BEP experiments. No experiments with progression rates on these specific sands and with the same setup have been reported, but there are several experiments with a similar setup and sand of a similar size. The critical head of B25 is similar to tests on M32 sand ($d_{50}=0.251$ mm) by Vandenoer et al. [2018b], but is lower than small-scale tests on Itterbeck 125-250 sand ($d_{50}=0.219$ mm) by Van Beek [2015] due to lower permeability. We find a slightly larger pipe depth at the end of the tests compared to Vandenoer et al. [2018b], but this can be explained by differences in test procedure, as Vandenoer stopped the experiment immediately when reaching the filter, whereas we brought the pipe in equilibrium conditions.

In terms of progression rates, the closest comparison can be made between the tests on FPH sand and tests on M34 sand ($d_{50}=0.155$ mm) by Vandenoer et al. [2019], which were both conducted in small-scale setups with hole-type exit. For loading conditions of $H/H_c = 1$, Vandenoer reports an average progression rate of $7.3 \cdot 10^{-5}$ m/s which is comparable to our rate of $4.7 \cdot 10^{-5}$ m/s for FPH sand. Comparing with small-scale slope

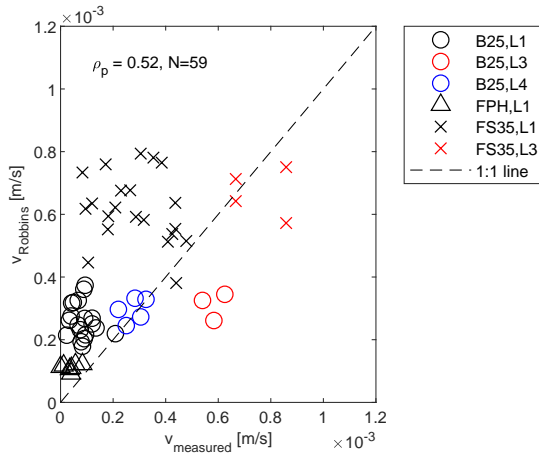


Figure 3.17: Measured progression rate in piping experiments and prediction using Eq. 3.15 [Robbins et al., 2020b].

exit experiments [Pol et al., 2019; Robbins et al., 2020b; Van Beek et al., 2011], we find almost one order of magnitude lower progression rates. As explained in section 3.3.4, this is likely due to fact that slope setups are generally initiation-dominated and therefore are more severely overloaded when the pipe length increases. This indicates that a model with local parameters can be more accurate compared to one using average gradients and average progression rates. Robbins et al. [2020b] proposed a relation with the local tip gradient:

$$v_{Robbins} = 0.15 \left(\frac{d_{50}}{1.27 \cdot 10^{-3}} \right)^{-0.84} \left(\frac{e}{0.647} \right)^{-3.1} \left(\frac{k \cdot i_{tip}}{n} \right) \quad (3.15)$$

In which $e = n/(1 - n)$ is the void ratio. Figure 3.17 shows that Eq. 3.15 cannot predict our measurements accurately for both normal loading and overloading based on measured gradients.

3.5.2 Reflection on the analysis and experimental setup

In this section, we discuss several assumptions in our analysis which may influence the results.

First, this research focuses on the internal erosion mechanism of backward erosion piping, which can occur when there is a supporting cohesive roof above the cohesionless soil. In this case, erosion takes place predominantly in the sand, resulting in relatively wide pipes which can be approximated by flow in wide rectangular ducts. In case of other forms of internal erosion, such as concentrated leak erosion, the erodible surface is all around, resulting in circular pipes. Findings in this chapter cannot be applied directly to other forms of internal erosion. Due to the assumption of laminar flow, the sediment transport equations may also not apply to the process of pipe widening (enlargement) after a hydraulic shortcut formed, which likely results in turbulent pipe flow.

Second, the critical local tip gradient (Fig. 3.8b) can serve as a local criterion for pipe progression. Like a cylindrical setup [Robbins et al., 2017], our adapted setup is very suitable to measure these criteria. However, it is important to note that its value depends on the sensor spacing, and when applied in numerical modelling this should match with the grid size for instance.

Third, as we have no frequent pipe depth measurements during progression, we assume that the shape of the equilibrium depth profile at the end of the tests also applies to partially developed pipes. This assumption affects the computed bed shear stresses. Yet, we expect this provides a reasonable estimate of the depth profile as it matches depth measurements made for partially developed pipes in three B25 tests 230, 236 and 245.

Fourth, based on a preliminary analysis we found a difference between the critical bed shear stress in equilibrium conditions at the end of the tests and during progression. Furthermore, during progression, the estimated critical shear stress near the pipe tip is lower than near the exit. A possible explanation for this finding is the effect of upward seepage on the grain stability, which is absent the end of the tests. Upward seepage also affects the pipe flow velocity profile, and thus the relation between pipe flow rate and bed shear stress. For modelling purposes, it is important to apply a critical shear stress that is consistent with the applied pipe flow equations. It is recommended to investigate whether computations with and without upward seepage give a significant difference in critical pipe gradient.

Finally, we find that the sediment transport rate in our experiments is approximately a factor five below what is expected based on most classical flume experiments, although still above data of Charru et al. [2004]. The reason for the lower transport rate in piping tests is not clear, as there are several possible explanations. First, the ratio of the flow depth to the particle diameter (a_{avg}/d_{50}) is relatively low, which may restrict the transport. Second, the intermittent erosion in BEP may result in a lower transport rate as the change in sand boil size is measured over a longer interval (typically 5 minutes). Furthermore, values of Θ and Θ_c during progression depend on the assumed depth profile, but this cannot explain a factor 5. Finally, the grains may be transported over a smaller width than $40d_{50}$, concentrated in the channel center, which would increase q_{*v} , but also cannot explain a factor 5. Given the uncertainties in the determination of Θ , Θ_c and q_{*v} during progression, we recommend testing whether this difference can be confirmed by BEP experiments with more detailed measurements of sediment transport rate and both acting and critical shear stress.

The adapted setup allows to force the pipe development in the vicinity of the pore pressure sensors, and thus allows to measure local pipe gradients and flow velocities. This in turn, allows to determine local hydraulic gradients and bed shear stresses during equilibrium and pipe development. We see some further improvements of the setup to obtain better measurements. First, additional pressure sensors to measure the exit head loss and vertical gradients below the pipe. Pressure ports using wider slots instead of small holes would allow for a more accurate measurement of tip gradients, as it reduces the scatter from the pipe passing at some distance from the center line. Second, to reduce uncertainties in the pipe depth development during progression, more geometry measurements should be taken during the regressive and progressive erosion phase. This will yield more reliable estimates of acting and critical shear stress during pipe development.

3.5.3 Erosion process

Pipe lengthening occurs if the stability criterion at the pipe tip (e.g., local gradient) is exceeded [Hanses, 1985]. On the other hand this often requires pipe deepening which is governed by the critical bed shear stress in the pipe [Sellmeijer, 1988]. As conceptualized in the introduction, the time scale of the BEP erosion process (time between successive tip failures) can be dominated by gradual removal of finer material from the soil matrix at the tip, by gradual soil matrix expansion due to limited inflow (dilatancy), or by the sediment transport capacity of the pipe. In these uniform sands and in near-critical conditions, our experiments show no gradual removal of fines from the tip, as assumed by Fujisawa et al. [2010] among others, but instead a stable soil at the tip between successive tip failures. If the process would be driven by gradual removal of fines or by dilatancy, one would expect a strong relation between progression rate and tip gradient, which was not found in both normal and overloading conditions. It was also observed in near-critical conditions that grain detachment leads to a temporary increase in pipe gradient and corresponding decrease in tip gradient (section 3.3.2), indicating that the time between tip failures depends on the time needed for clearing the pipe. This importance of the sediment transport capacity is supported by the strong correlation between progression rate and bed shear stress in our experiments, in both normal and overloading conditions. We expect that in practice the pipe sediment transport capacity dominates the BEP time scale, because most river levees susceptible to piping are built on uniform sand and are only moderately overloaded in terms of critical head. Removal of finer particles may be important for graded material, and dilatancy may start to play a role in case of strong overloading of dense sand.

3.5.4 Implications for modelling

The results indicate that the progression rate is more complex than just a function of the seepage velocity or gradient at the tip. During overloading, for example, the progression rate increases much more than is expected based on the seepage velocity only. Because the sediment transport rate in the piping experiments shows a similar relation with the bed shear stress as in classical flume experiments in laminar flow, we propose to use a transport relation like Eq. 3.12 for BEP modelling, similar to the recent work by Wewer et al. [2021]. However, as progression occurs on exceedance of a critical condition at the pipe tip [Robbins and Griffiths, 2021], such a condition would further improve the model. Therefore we propose to implement a sediment balance (Exner), a transport relation like Eq. 3.12 and a critical tip gradient in a 3-dimensional BEP model [van Esch et al., 2013]. Such a coupled model may still need calibration on experiments like the ones presented here. Finally, we note that values assumed for Θ_c must be consistent with the modelling of Θ , in terms of whether is accounted for effects of vertical seepage on the velocity profile and the bed shear stress.

3.6 Conclusions

To better understand the processes determining the temporal development of backward erosion piping, we performed a series of small-scale experiments. Our experimental setup guides the eroding pipe along a densely spaced row of pressure transducers, which allows local pressure measurements right in the pipe during equilibrium and progression. This is

an advantage compared to most previous experiments [Allan, 2018; Robbins et al., 2020b; Vandenboer et al., 2019]. Pipe geometry and flow velocity measurements allow for calculating bed shear stresses. The guiding of the pipe did not significantly influence the progression rate. We used three fine uniform sands ($0.185 < d_{50} < 0.422$ mm), compacted to a relative density between approximately 50% and 80%. In addition to the regular loading up to the critical head, some experiments were overloaded at 10-20% above the critical head.

The results confirm the positive relation between progression rate and grain size or permeability [Allan, 2018; Pol et al., 2019; Robbins et al., 2017], as well as the distinct effect of even a small degree of overloading [Vandenboer et al., 2019]. The finding that the progression rate depends on the loading introduces an important problem. For a given head drop H , the loading effect which drives progression (e.g., tip gradient or bed shear stress) depends on both the scale of the problem (i.e., seepage length) and the length of the pipe. Therefore, the progression rate will be time- and scale-dependent. Kézdi [1979] and Robbins et al. [2020b] proposed to relate the progression rate to the local hydraulic gradient or seepage velocity at the pipe tip, which is modelled as function of time and scale. However, the current experiments indicate that the sediment transport in the pipe is a stronger predictor than the seepage velocity at the tip. First, the tip gradient does not increase significantly with the degree of overloading. Second, groups of detached sediment create extra pipe flow resistance and temporarily reduce the tip gradient, and thus control the time scale of tip erosion. Third, the estimated bed shear stress during pipe progression correlates well ($\rho = 0.84$) with the progression rate, compared to $\rho = 0.33$ for seepage velocity. Especially the overloading situations are predicted better by bed shear stress than by seepage velocity. This suggests that the sediment transport capacity is a main, limiting factor in BEP progression rates of uniform sands.

The critical bed shear stress has been determined for the first time in a rectangular piping setup. The values after the tests (complete pipe) are in good agreement with piping tests in a cylindrical setup [Van Beek et al., 2019] and classical flume tests in laminar flows. However, estimated critical shear stresses for a partially developed pipe are much lower and seem to decrease in the vicinity of the pipe tip. This reduction can be partly explained by the effect of strong upward seepage [Xiao et al., 2019a]. Seepage is known to decrease both the exerted and critical shear stress in turbulent flows [Cheng and Chiew, 1999], but this has not been fully quantified for laminar pipe flow, and requires further study.

The relation between sediment transport rate and Shields number in the BEP experiments follows a similar trend as in classical, laminar flume experiments such as Grass and Ayoub [1982]. We fitted an empirical relation (Eq. 3.12) to describe the sediment transport as function of the Shields number. Since there is a large scatter in the data from both the piping experiments and flume experiments at low transport rates, this should be studied further with more accurate measurements. If these relations indeed apply to backward erosion piping, time-dependent pipe progression can be modelled by coupling a BEP model [van Esch et al., 2013] with sediment transport relations (Eq. 3.12) and a sediment mass balance [Wewer et al., 2021] and a local critical tip gradient as primary erosion criterion Robbins and Griffiths [2021]. Such a model would contribute to more accurate assessments of the risk of piping failure in case of a limited duration of the hydraulic load, and therefore support more efficient designs of flood defenses.



4

Large-scale Experiments on the Temporal Development of Piping

4

Unfortunately a given field case rarely permits a conclusive evaluation of any prediction technique because it is unusual to find a case where the field situation and the mechanisms involved have been fully identified.

T.W. Lambe

This chapter presents a large-scale backward erosion piping experiment primarily aimed at studying the pipe development over time. In addition, it presents preliminary findings on the strength recovery after a flood event in which a pipe has formed. To study the pipe progression in realistic conditions, we built a 1.8 m high levee with a cohesive blanket and hole-type exit on a sandy foundation. The pipe was guided along a row of pore pressure transducers in order to derive its temporal development from pore pressure changes. The experiment showed an average progression rate of 8 m/day during the progressive erosion phase. The recovery test shows partial strength recovery after nine months of rest: the erosion process had to start all over again, albeit with 20% lower critical head and 140% higher progression rate.

The majority of this chapter is based on Pol, J.C., Kanning, W., & Jonkman, S.N. (2021). Temporal Development of Backward Erosion Piping in a Large-Scale Experiment. *Journal of Geotechnical and Geoenvironmental Engineering*, 147(2), 04020168, [https://doi.org/10.1061/\(ASCE\)GT.1943-5606.0002415](https://doi.org/10.1061/(ASCE)GT.1943-5606.0002415). The recovery experiment (section 4.4.4) is published as Pol, J.C., Kanning, W., and Jonkman, S.N. (2022). Strength Recovery in a Large-Scale Backward Erosion Piping Experiment. Proceedings of the 28th Annual Meeting of the European Working Group on Internal Erosion, Sheffield, UK. Data link: <https://doi.org/10.4121/uuid:3b44f87b-cc0f-4c03-a192-e81078dec53d>

4.1 Introduction

Flooding is one of the most significant natural disasters worldwide [Jonkman, 2005]. The past decades have shown an increase in flood risk [Jongman et al., 2012; Paprotny et al., 2018], and without counter-measures, this is expected to further increase due to climatic and socio-economic changes. A common strategy to reduce flood risk is using structural flood protection measures like levees and dams. Levee failure may occur due to a range of failure mechanisms such as overflow, slope instability or internal erosion [Morris et al., 2008]. This study focuses on the mechanism of backward erosion piping (in short piping), which is a form of internal erosion. After overtopping, piping is considered one of the most hazardous failure mechanisms in dams [Foster et al., 2000] and river levees [Danka and Zhang, 2015; Tóth and Nagy, 2006; Özer et al., 2020].

4

4.1.1 Piping process

Piping occurs when seepage induced by a head difference (H) over the levee leads to erosion of a granular levee foundation which is covered by a cohesive roof, to such extent that a hydraulic shortcut forms. The eroded grains settle around the outflow location as a sand boil. In areas with blankets (cohesive top layer on the land side) there are three necessary conditions to induce piping failure: (1) rupture of the land side blanket, (2) transport of the granular material through the fault in the blanket and (3) formation of a continuous pipe below the structure [Schweckendiek et al., 2014]. This chapter focuses on the third condition.

From the beginning of the 20th century, extensive research has been done on the factors that determine the critical head difference (H_c) at which piping occurs (i.e. a fully developed erosion channel creating a full hydraulic shortcut resulting finally in a breach), for example Bligh [1910], Miesel [1978], Hanses [1985], Sellmeijer [1988], Schmertmann [2000], Van Beek [2015], Robbins et al. [2017] and Vandenboer [2019]. The findings which are most relevant for this chapter are discussed below.

Based on a dataset of dam and levee failures, Bligh [1910] observed that piping occurs if the global hydraulic gradient (head difference H divided by seepage length L) was larger than a critical creep value which depends on the type of soil.

Based on laboratory studies, Hanses [1985] noted that the erosion process includes both primary erosion (lengthening of the pipe) and secondary erosion (widening and deepening of the pipe). Both processes occur in conjunction: pipe lengthening results in higher flow rates and subsequent pipe deepening and widening. Miesel [1977] and Muller-Kirchenbauer [1980] observed that after initiation of erosion, the erosion often stopped and progressed only after a head increase. This equilibrium can be explained by several factors such as the convergence of flow to the exit.

An equilibrium curve (Fig. 2.2) shows pipe length (l) versus the head at which all grains are just in equilibrium (H_{eq}). The critical head H_c is the highest head at which equilibrium is possible. When the pipe grows longer than the corresponding critical length l_c , equilibrium can only exist when the head is lowered sufficiently. A configuration is *progression-dominated* if an equilibrium develops after an initial formation of a pipe and *initiation-dominated* if this is not the case [Van Beek, 2015], see Fig. 2.2. Levees with cohesive blankets are often progression dominated due to the concentrated outflow. The phases before and after the critical point are in this chapter referred to as regressive and progres-

sive, respectively. Regressive means that an equilibrium is reached given a constant head; while progressive means that the pipe growth continues given a constant head.

In the Netherlands, levees are assessed and designed using the model of Sellmeijer [1988] or a simplified formula [Sellmeijer et al., 2011]. Sellmeijer's model combines 2D groundwater flow, pipe flow and stability of grains on the pipe bed. As such, this stability criterion is based on secondary erosion. The model predicts an equilibrium curve like Fig. 2.2, which is also observed in experiments.

4.1.2 Time-dependent processes in piping

Current steady piping models are focused on the critical head, but in some cases time-dependent processes can be relevant. Time-dependence in the piping failure process includes three main components: (1) hydraulic load, (2) groundwater flow and (3) pipe growth. The duration of the extreme hydraulic load (first component) is the driver: the shorter the load duration, the less time is available for the piping process to develop. A flood with limited duration, such as a storm surge, induces non-stationary seepage flow, which leads to delay and damping in the response of the aquifer pore pressure at the downstream side of the levee (second component). This reduces the potential for rupture of the blanket and initiation of piping, but also delays these events. This chapter focuses on the third component: pipe growth. Once piping has initiated, it takes time to progress towards the upstream side and create a shortcut. If the load has reduced sufficiently in the meantime, the erosion process stops and failure is prevented. The pipe progression rate v , either in the progressive or regressive phase, is defined as the increase in pipe length l over a given period of time t .

4.1.3 Piping experiments including temporal development

A number of experiments include information about the development of the pipe over time. Experiments of the progression rate of piping at small and medium scale were recently carried out by Robbins et al. [2017], Vandenboer et al. [2019] and Allan [2018]. Progression rates were also obtained by Pol et al. [2019] from a selection of small and medium scale tests by Van Beek [2015]. Apart from scale effects, these laboratory experiments differ from field conditions in having a smooth, rigid roof above the sandy layer.

Two large scale piping experiments relevant to levees are: (1) Large scale tests in the Delta Flume at Deltares [De Rijke, 1991; Silvis, 1991]. However, these tests were stopped just after the critical head was reached, so these include only a small part of the progressive phase. (2) Development of the pipe length in the IJkdijk large scale tests [Van Beek et al., 2010] is shown in Sellmeijer et al. [2011] and Parekh et al. [2016], based on pore pressure changes. The pipe pattern in these tests is 2-dimensional with multiple sand boils and pipes, caused by the plane type exit configuration. In combination with limited sampling, this gives substantial difficulties in determining the pipe length development. For instance, in Sellmeijer et al. [2011] the derived maximum pipe length in test 1 and test 3 is far less than the seepage length of 15 m. And in test 2, which is shown in both publications, a pipe length of 1.5 m is reached after almost 80 hours according to Parekh et al. [2016] and after 50-65 hours according to Sellmeijer et al. [2011].

4.1.4 Modeling temporal development of piping

Several authors have modeled aspects of the temporal development of piping, such as an equilibrium condition in a transient groundwater flow model [van Esch et al., 2013], secondary erosion rates in Hole Erosion Tests [Bonelli and Benahmed, 2010] and in laminar flow [Cheng, 2004], and primary erosion rates [Fujisawa et al., 2010; Kézdi, 1979; Rotunno et al., 2019; Wang et al., 2014]. Although significant advancements were made in recent years, no model is known to the authors which includes both primary and secondary erosion mechanisms and which is validated on a wide range of sands and test configurations. The model of Rotunno et al. [2019] contains both mechanisms and was applied to the IJkdijk and Delta Flume experiments, but requires calibration of the primary erosion coefficients.

4

4.1.5 Research aim

Most piping research focuses on the critical head. Recent work also describes the temporal development in laboratory experiments, but there is still a need for a coherent predictive model of temporal development. To support the validation and development of such a model, this chapter aims to study the temporal development of piping in terms of pipe progression rates during the progressive phase of a progression dominated configuration. This is achieved by a large scale experiment that reflects realistic conditions including a blanket and a hole-type exit, while monitoring the main parameters (pore water pressure, sand discharge, flow rate). The resulting data set is publicly available for other researchers to validate their models [Pol et al., 2020].

4.2 Experimental setup

4.2.1 Dimensions of the test levee

The Flood Proof Holland test facility [Kreijns et al., 2018] was used to conduct the piping experiments on a large scale (i.e. representative of a real levee) but in a controlled environment. The design of the test levee was constrained by the test facility dimensions to a maximum levee height of 1.8 m, a minimum levee base length of 10 m and a maximum aquifer depth of 1 m. Initial calculations with the model of Sellmeijer [2006] predicted no failure at the maximum head of 1.8 m and a seepage length of 10 m, regardless of sand type (fine or coarse). Therefore the seepage length was shortened by installing a pipe and infiltration boxes (Fig. 4.1). Undesired seepage to and from the sand bed was prevented by a HDPE geomembrane at the bottom and sides and a 0.35 m cohesive (clay) blanket that extends below the levee body, separating the levee body from the aquifer. This setup with blanket was chosen since this is the most common levee configuration in the Netherlands. The cohesive blanket allows for realistic sand/blanket interaction, as well as for deformation; both of which are not incorporated in laboratory experiments with a rigid transparent boundary.

The sand bed was rectangular with length $L_s=9.5$ m, depth $D=1$ m and width $W=1.2$ m. The seepage length L , between exit and downstream side of the infiltration box, was 7.2 m. The exit was a hole with a diameter of 13 mm. The fine sand (grain size $d_{50}=185$ μm) was based on the lowest expected critical head. See Table 4.1 for more details.

In order to measure water pressures in the pipe accurately, the pipe needs to grow

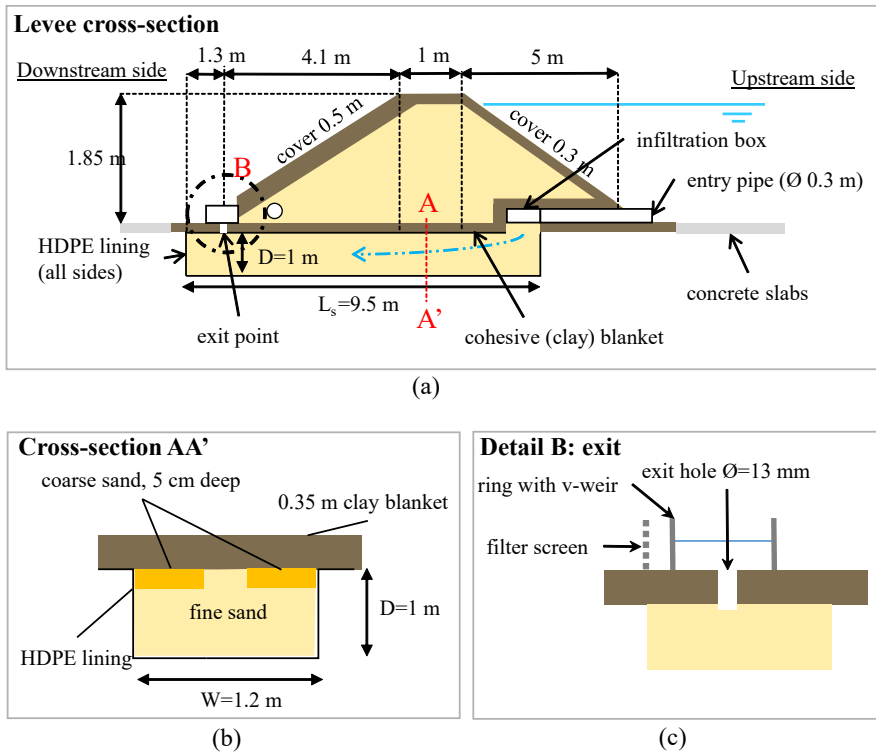


Figure 4.1: Sketch of test levee design: cross section of levee (a), sand bed (b), and detail of exit hole (c). Not to scale.

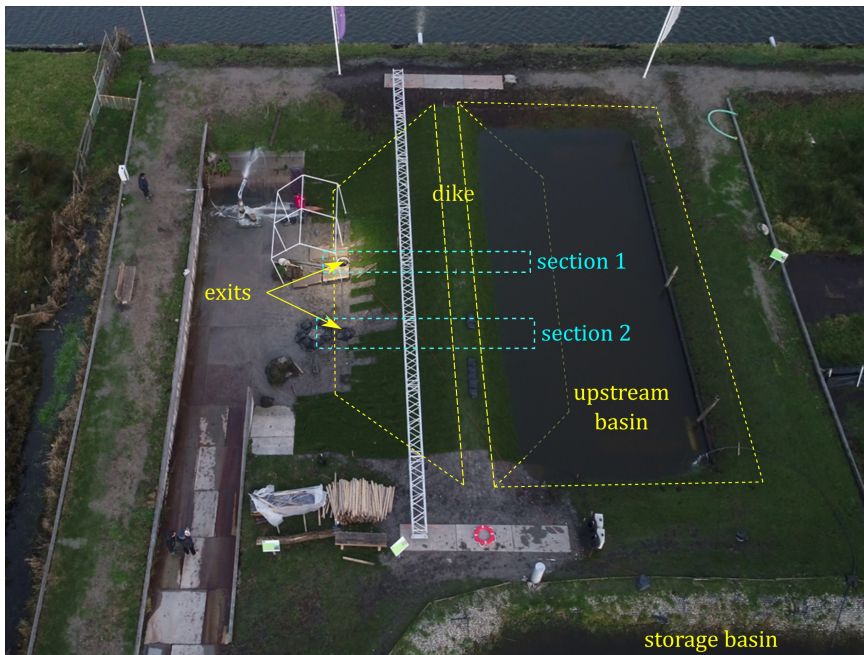


Figure 4.2: Aerial view of test basin. (Photo by B. Strijker.)

under the pressure transducers. To prevent side-wards pipe development, strips of coarse sand were included in the upper 0.05 m of the sand bed (Fig. 4.3). The shape of the strips minimizes disturbance of the process. First, the alternating pattern of coarse and fine sand prevents a strong preferential flow through the coarse sand. Second, the diagonal positioning prevents the pipes to grow to the edges. Finally, the strips were relatively thin: 0.05 m compared to an aquifer thickness of 1.0 m. Uncertainties related to the coarse sand strips are discussed further in section 4.4.

The sandy levee had a clay cover at the upstream side and crest as well as at the interface between sand bed and levee body. It had clayey, loamy and sandy covers at the downstream side for overflow erosion tests (outside the scope of this chapter [Yagisawa et al., 2019]). The tested cross section was at the interface of a loamy and sandy downstream slope. The entire levee was covered with grass sods. Due to the clay lining, the composition of the levee body has no significant influence on the piping process. See Fig. 4.2 for an overview of the levee and test basin.

4

4.2.2 Sand properties

Table 4.1 shows the properties of the fine and coarse sands. For some parameters, multiple samples were tested, in which case also the standard deviation σ and number of tests N are given. Some properties of the coarse sand were not relevant for the test and therefore not measured. Grain sizes ($d_{10} - d_{70}$) were obtained by sieving. The in-situ porosity (n) was determined by pushing five thin walled steel cylinders horizontally into the upper layer of the sand bed, measuring their volume and weighing the oven-dried sand. Minimum and maximum porosity was estimated by compacting oven-dried sand in a cylinder. Particle density (ρ_s) was determined by a pycnometer. Intrinsic permeability (κ_{lab}) was determined in the lab using a constant head test, and converted to hydraulic conductivity for the field test temperature of 5°C (k_{lab}). The in-situ hydraulic conductivity (k_{levee}) was determined using measured head, discharge and Darcy's law. The coefficient of uniformity (C_u) and relative density (D_r) were calculated from the values above.

4.2.3 Monitoring equipment

The main monitoring equipment consisted of 14 atmospheric pressure corrected pore pressure transducers placed on the interface of the sand bed and clay blanket, plus one in the upstream basin and one in the levee core. Fig. 4.3 shows their numbering. Their signal (1/10 Hz) was monitored in real time in the control room. Styrofoam beads (1-2 mm) with different colors were placed in the top of the sand bed at different distances along the expected pipe path (Fig. 4.3). The beads are used as a visual monitoring aid, where beads of a certain color appearing at the outflow point show that the pipe has at least passed the location associated with the bead color. Flow rate and sand discharge were measured at the exit hole location each 30-60 minutes, depending on the rate of erosion. A $\varnothing 0.6$ m bucket with cut out bottom and a V-notch weir with an angle of $\theta_w = 55^\circ$ was placed around the exit (Fig. 4.4). The flow rate Q_w [m^3/s] was calculated from the water level h_k [m] above the V-notch weir using Shen [1981]:

$$Q_w = 2.36 \cdot 0.577 \cdot \tan(\theta_w/2) \cdot (h_k + 0.00123)^{5/2} \quad (4.1)$$

Table 4.1: Properties of test materials.

Parameter	Units	Fine sand	Coarse sand
		$\mu (\sigma, N)$	$\mu (\sigma, N)$
d_{10}	μm	127 (3,3)	190 (-)
d_{50}	μm	185 (9,3)	400 (-)
d_{60}	μm	201 (3,3)	450 (-)
d_{70}	μm	223 (15,3)	500 (-)
ρ_s	kg/m^3	2610 (5,2)	-
n	-	0.383 (0.005,4)	-
n_{min}	-	0.361 (-)	-
n_{max}	-	0.485 (-)	-
κ_{lab}	m^2	$1.2 \cdot 10^{-11} (5.6 \cdot 10^{-12}, 6)$	$4.1 \cdot 10^{-11} (8.3 \cdot 10^{-13}, 3)$
k_{lab} at 5°C	m/s	$8.0 \cdot 10^{-5} (3.6 \cdot 10^{-5}, 6)$	$2.6 \cdot 10^{-4} (5.4 \cdot 10^{-6}, 3)$
k_{levee}	m/s	$9 \cdot 10^{-5}$	-
C_u	-	1.59 (0.01,3)	2.4 (-)
D_r	-	0.823	-

Eroded sand deposited around the exit hole was collected using a spoon. First, a small part (approximately 50 g) was stored for grain size analysis. The residual sand was supplemented with water up to a fixed volume (usually 400 ml) and the sand-water mixture was weighed. The dry sand mass (M) follows from the mass of the mixture and the water and sand densities. The mass of the small part and the residual were combined in one time series. This in-situ method was validated in the lab against oven-drying, which confirmed its suitability.

4.2.4 Construction method

After excavation of a trench in the clay-peat subsoil, the HDPE geomembrane was placed in the trench and the moist fine sand was added and compacted in 0.20 m layers using a vibrating plate. Then, the sand was saturated from below by infiltration through a vertically placed pipe at the downstream end of the sand bed. It is likely that some air was trapped in the sand and no 100% saturation was achieved. This is supported by a delay in the measured pore pressure response. After leveling the sand, the diagonal strips were carefully excavated using a trowel to a depth of 0.05 m, filled with coarse sand and compacted by tamping. The styrofoam beads were pushed in the sand bed and directly covered by clay. Then, the clay blanket was carefully placed on the sand by an excavator and compacted with a vibrating plate. Transducers were packed in a filter sleeve, installed in holes through the clay layer extending 10 mm into the sand bed, and sealed with bentonite. Finally, the levee was constructed on top of the blanket. There were four weeks between the installation of the transducers and the start of the experiment.

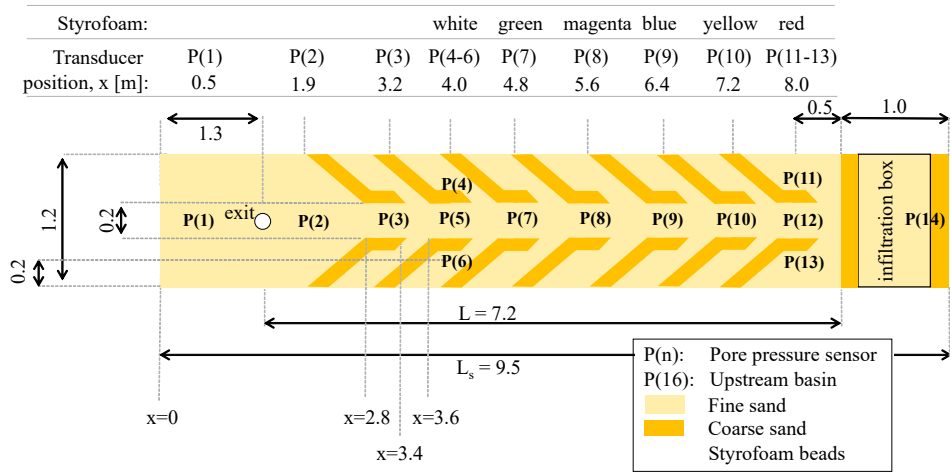


Figure 4.3: Top view of sand bed showing exit, coarse sand strips, transducer position and styrofoam bead colors. Dimensions in meters. Not to scale.



Figure 4.4: Exit point in the center of a bucket with V-notch weir.

4.2.5 Test procedure

At the start of the test, the pressures were constant and the pressure readings were set to a zero level. Then, the exit hole was created by piercing the cohesive blanket. The upstream basin level was initially raised in 0.3 m steps, which was reduced to 0.1 m steps at a basin level of 0.9 m. The level was only raised if no sand transport was observed for 30 minutes. Each 30-60 minutes, the exit location was inspected, discharge measured and sand samples taken. The inspection interval was based on the rate of development of the process. The development of pore pressures was checked continuously for signs of erosion near one of the transducers, which is visible as pressure drop or peak in local gradient [Parekh et al., 2016; Robbins et al., 2017]. The test was stopped by pumping the water out of the upstream basin when the pipe tip reached the upstream side of the sand bed ($x=8$ m), which could be seen in the pressure measurements.

4.3 Results and Analysis

4.3.1 General observations

The piping process went through the several phases described in literature [Van Beek, 2015]: seepage without sand transport, fluidization of sand in the exit hole, crater formation, equilibrium (regressive phase) and ongoing erosion (progressive phase), see Fig. 4.5. It was observed visually that the sand deposition at the exit is not continuous but intermittent. This may be caused by groups of grains being detached from the pipe tip which has been observed by many researchers, e.g. Van Beek et al. [2015] and Xiao et al. [2019a].

The effects of piping erosion were clearly visible in the pore pressure measurements, which is the primary source of information in this experiment. Styrofoam beads from the pink, green and white strips were only observed at the end of the test, during the widening phase. Because the pipe must have passed the beads much earlier, it is suggested that the beads got stuck in the shallower parts of the pipe. However, it is unlikely that this influenced the flow or erosion process, since the pipe can easily grow around it. Due to the large delay, this method was not used to estimate pipe tip position. The method may only be successful in case of finer beads, with a diameter similar to the grain size. Furthermore, the discharge readings were not accurate enough to measure small changes. Therefore only the order of magnitude is known, but it is not possible to detect significant changes during the test. These measurements should be more sensitive in future tests. The mass of the sand collected with a spoon shows a consistent trend (Fig. 4.10a). As the eroded sand cannot leave the bucket, the error in the cumulative mass will be small.

4.3.2 Head and hydraulic gradient

Pore pressure development

This section describes the measured pore pressures and hydraulic gradients, which form the basis for the analysis of progression rates. The following pre-processing steps were taken. The transducers were zeroed just before the test during no-flow conditions at an upstream level of 0.065 m, to ensure that all pressures are relative to the same reference level. Therefore, all measurements were increased by 0.065 m head. Furthermore, sensors P2 and P3 showed some sudden drops in pressure which could not be explained by physical behavior. These jumps of 2 kPa at the maximum were removed from the signal. It is noted

that P2 and P3 do not affect the conclusions on the progression rates, as these transducers were passed when the flow was not yet in the progressive phase. Finally, the 0.1 Hz signal is smoothed using a 600-second moving average.

Fig. 4.5 shows the resulting head time series of each transducer in the central row. All heads are relative to the upstream basin floor. P16 is the upstream head, P1 is the most downstream transducer in the aquifer (Fig. 4.3). When the upstream head increases step-wise, the sensors respond depending on the position. Due to seepage through the levee, the upstream head tends to decrease slowly but a constant basin level is attempted by periodic filling. When the pipe tip approaches a transducer, the graph shows a drop in head. This behavior is also observed in Parekh et al. [2016]. When the tip passes, the head stabilizes because it shows the (relatively constant) pipe head. The circles are not relevant at this point; these are used in section 4.3.3 to derive the tip position. Vertical lines indicate the phases of regressive erosion, progressive erosion and widening. The transition from regressive to progressive is chosen at the time that the erosion no longer stabilizes. The maximum upstream head is slightly higher.

Note that the head at P9 is not consistent with the other locations. The transducers spacing is 0.80 m from P3 to P12, so the head difference between those sensors should be similar. The head of P9 is about 0.05-0.10 m too close to P10 during the progressive phase. Possible causes are a poorly compacted zone, preferential flow through coarse sand or an error in the position of the sensor. In the rest of the analysis, the original values of P9 are used.

The average hydraulic gradient i between transducer pairs as shown in Fig. 4.6 follows from the head difference and the distance between transducers. In the rest of this chapter, 'gradient' indicates the horizontal hydraulic gradient: $i = dh/dx$ (positive for flow towards the exit). Initially, the gradients increase with increasing upstream head. Pipe erosion leads to a decrease in head in the transducer just upstream of the pipe tip and an increase in gradient between the two transducers upstream of the pipe. A clear example is the gradient between P7 and P8 (gradient $i_{7,8}$), which peaks at the moment the pipe reaches P7.

Figs. 4.8a and 4.8b show longitudinal head profiles at several points in time, which could be useful for the validation of the gradient in the pipe and upstream of the pipe tip. The pipe gradient is approximately 0.12, and the gradient over the first 0.8 m upstream of the pipe tip varies between 0.31 and 0.41.

Exit loss

The head loss over the exit hole is estimated as the difference between the downstream water level (0.18 m) and the head at transducer P1. This is an underestimation of the exit loss, because the head at P1 may be slightly higher than the head below the exit, but expected to be small because there will be little flow from P1 to the exit. The exit loss is approximately 0.1 m during the regressive phase. During the progressive phase, it increases gradually to 0.13 m at the transition to the widening phase and 0.20 m just before the end of the test. This increase may be explained by the increasing sand transport, which leads to more exit resistance [Robbins et al., 2020b]. As the cover thickness is 0.35 m, the vertical gradient over the exit hole varies between 0.3 and 0.6.

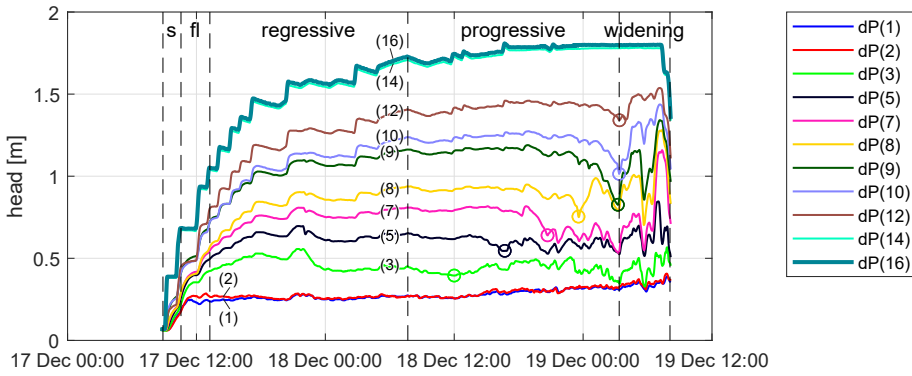


Figure 4.5: Head at central row of transducers. Circles indicate assumed pressure stabilization point. P(16) is upstream basin level. 's'=seepage, 'fl'=fluidization.

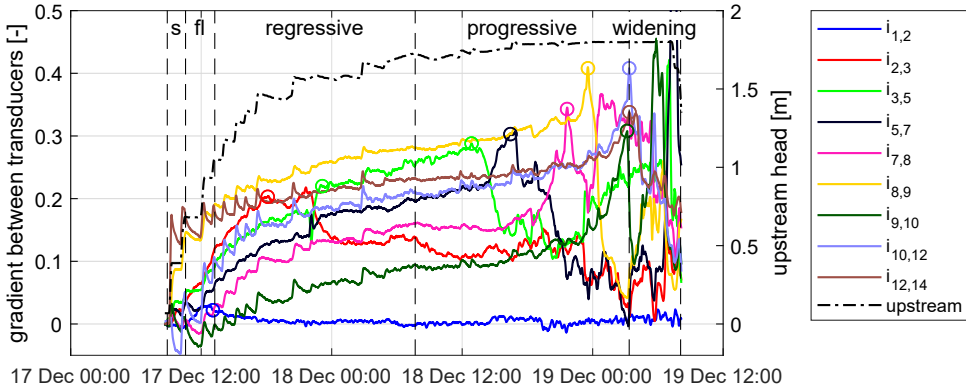


Figure 4.6: Average hydraulic gradient between all transducer pairs in the central row. Circles indicate assumed peak in gradient. 's'=seepage, 'fl'=fluidization.

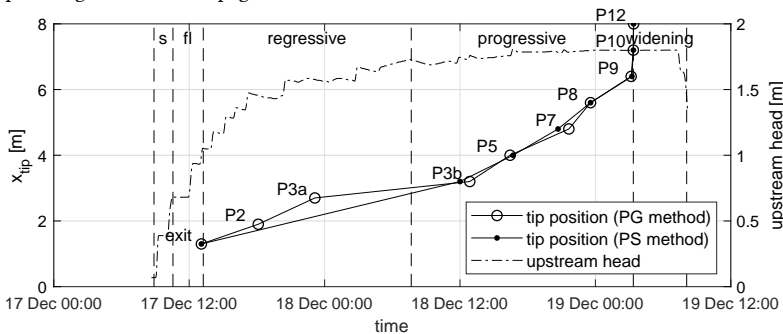
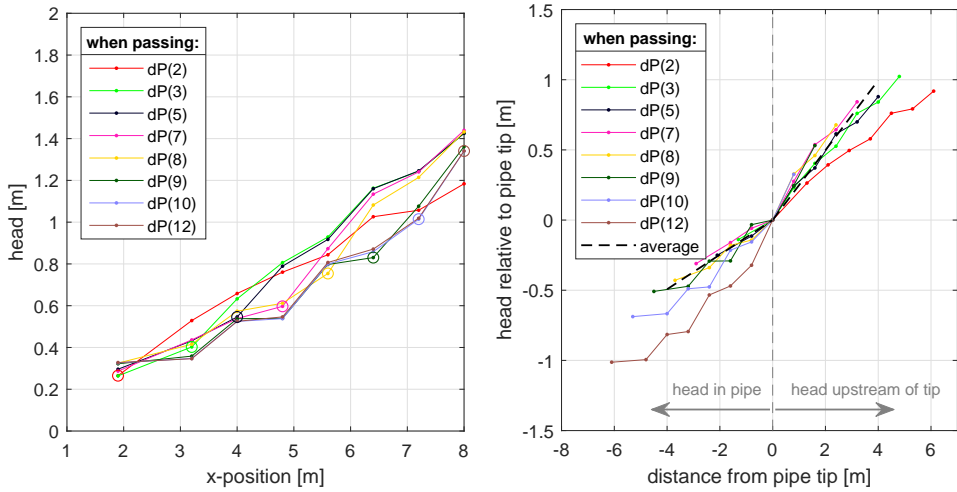


Figure 4.7: Development of pipe tip position using peak gradient (PG) and pressure stabilization (PS) methods. 's'=seepage, 'fl'=fluidization.



(a) Absolute head profile. Circles indicate transducer positions. Right of this circle shows the upstream head, left of it shows the pipe head.

(b) Head profile relative to pipe tip. "average" is based on the average of the gradients of sensor P3-P12.

Figure 4.8: Head profiles during moment of passing of each transducer.

Critical head

The exit hole fills with fluidized sand at a head difference of 0.5 m. First sand boil formation is observed at a head difference of 0.85 m. The critical head difference (H_c) at which erosion does not stop anymore, is estimated at 1.52 m (1.7 m upstream, 0.18 m downstream head). Correction for 0.10 m exit head loss reduces H_c further to 1.42 m. This observed value is compared to numerical model predictions of MSeep [Sellmeijer, 2006], as well as the analytical models of Sellmeijer et al. [2011], Bligh [1910] and Hoffmans and Van Rijn [2017], using the mean soil properties from Table 4.1. Bligh's creep factor of 15 for moderate fine sand is corrected for the implicit safety factor in Bligh's design rule [Kanning, 2012], which yields a creep factor of 10. The predicted critical head differences are 1.80 m (MSeep), 1.60 m [Sellmeijer et al., 2011], 0.72 m [Bligh, 1910] and 1.30 m [Hoffmans and Van Rijn, 2017]. All predictions are without 0.10 m exit resistance. Note that larger difference between predicted and observed values do not necessarily indicate that these models perform less in field situations. Some of these models were derived or calibrated for situations which differ from this test in terms of aquifer geometry and exit type. So the results should be viewed primarily as indication how robust the prediction is in different configurations.

4.3.3 Progression rates

Derivation of pipe tip position

Because a pipe causes a drop in pore pressure, the pipe tip position can be derived from changes in head and gradient in time. This only applies in case the pipe is sufficiently close to the sensor, which was ensured by the guides. The moment that the pipe reaches

a transducer can be based on pressure stabilization [Parekh et al., 2016] or peak gradients [Robbins et al., 2017]. In the pressure stabilization method, the pipe passes the n^{th} transducer when the head h_n stabilizes after a pronounced decrease. In the peak gradient method, the pipe passes the n^{th} transducer when the gradient $i_{n,n+1}$ peaks after a gradual increase and before a pronounced decrease.

The passing times of the pressure stabilization and peak gradient methods are determined visually from Fig. 4.5 and Fig. 4.6 respectively, and are indicated by circles in those figures. After the passing time, the pressure fluctuates more strongly, which may be caused by temporal clogging or pipe meandering. Fig. 4.7 shows the development of the pipe tip position, by plotting the sensor positions against the passing times (x is distance from downstream end of the sand bed, see Fig. 4.3). The moment of initiation is plotted with the exit location ($x=1.3$ m). P1 has no pipe passing because it is located behind the exit. The passing time of the two most downstream transducers, P2 and P3, was more difficult to identify. During the assumed passing of P2 the flow is not stationary yet and therefore a pressure stabilization is hardly identifiable. During the assumed passing of P3 the erosion process is very slow (confirmed by erosion volumes), which gives a prolonged increase in gradient instead of a sharp peak. Therefore it is chosen to assign a point P3a at the moment that the pressure starts to increase strongly (17 Dec 22:00) in addition to point P3b at the peak before the gradient drops (18 Dec 12:00). Since these two transducers mostly reflect the regressive phase, these do not influence the analysis for the progressive phase.

Fig. 4.7 shows that both methods (peak gradient and pressure stabilization) give very consistent results, and passing times are increasing with x -position as expected. The results are more consistent than the earlier IJkdijk-experiment [Parekh et al., 2016], probably because the pipe is closer to the transducers and there is a single pipe instead of a network. For further analysis, the results of the peak gradient method are used.

Progression rates can be determined from the slope of the lines in Fig. 4.7. The average progression rate after P3b is passed is approximately 0.1 mm/s, with a maximum of 2 mm/s in the last 1.6 m. Note that the progression rates during the regressive phase are not representative because the time of the transducer passing is relatively uncertain and the rate depends on the head increase interval.

The critical pipe length is the length corresponding to H_c , when the erosion process is just in equilibrium. This results in a slow progression rate, and is the case during the approach of P3: an almost horizontal line between $x_{tip}=2.7$ m and $x_{tip}=3.2$ m in Fig. 4.7. In further analysis, the average is used: $x_{tip}=2.95$ m. The pipe length l is the difference between x_{tip} and x_{exit} (1.3 m), so the observed critical pipe length $l_c=2.95-1.3=1.65$ m. MSep predicts $l_c=1.55$ m, which is close to the observed value. Both Sellmeijer's and Bligh's design rules predict no critical pipe length. The observed l_c is smaller than the commonly assumed $1/3L - 1/2L$ [Sellmeijer and Koenders, 1991] due to the low ratio of aquifer depth to seepage length (D/L).

Progression rate as function of local gradient

Some authors expect that the progression rate is governed by primary erosion and depends on the local hydraulic gradient or pore velocity just upstream of the pipe tip [Kézdi, 1979; Robbins et al., 2017]. Fig. 4.9 shows these relationships for the transducers that were

passed during the progressive phase (P3-P10). The right axis indicates the pore velocity just upstream of the pipe tip, which equals $u_{p,tip} = k \cdot i_{tip}/n$. The line indicated by $v_{c,avg}$ is the average progression rate during the progressive phase. This value is relatively high because of the high progression rate at the end of the test.

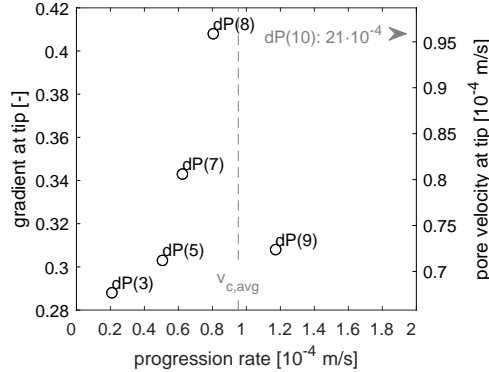


Figure 4.9: Progression rate as function of gradient and pore velocity just upstream of the pipe tip, calculated over 0.8 m (transducer spacing).

The data seems to confirm a relationship between tip gradient and progression rate for transducers P3-P9, but there are also some outliers. Probably the tip gradients for P8 and P9 in Fig. 4.9 are overestimated and underestimated, respectively, because of the bias in sensor P9 (noted in section 4.3.2). Furthermore, the peak gradients are expected to increase monotonously with x-position (and thus transducer number) because the seepage path becomes shorter. The deviation of P8 and P9 from this trend supports the hypothesis that these values should be more in line with P3-P7. P10 shows a much higher rate, but this outlier is likely due to the near breach conditions. The overall pattern shows an increase in progression rate with tip gradient, but without sufficient data to fit a reliable relation. Because of the uncertainty, this relationship should be tested in a more controlled laboratory experiment.

4.3.4 Erosion volumes and pipe dimensions

This section aims to estimate the pipe geometry based on the measurements of pipe length and mass of eroded sand. The measured dry sand mass M [kg] is converted to initial soil volume V_{exp} [m^3] by:

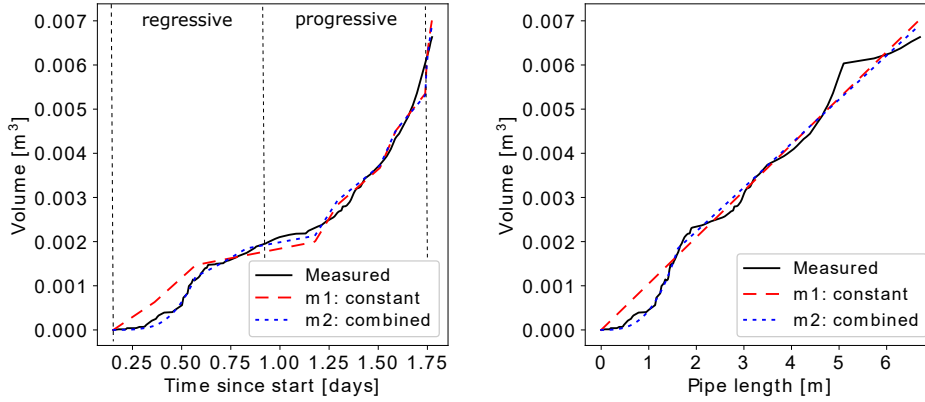
$$V_{exp} = \frac{M}{\rho_s(1-n)} \quad (4.2)$$

The black line in Fig. 4.10a shows the measured erosion volume. Initially, the erosion accelerates, after 15 hours after the start it slows down, and during the progressive phase it accelerates again. Note that, in the regressive phase, the volume increase depends on the applied head increments. Fig. 4.10b shows the volume against pipe length.

Two simple models 'm1' and 'm2' are defined for the pipe volume as function of pipe length. Eq. 4.3 represents a pipe with constant cross sectional area A_0 . Eq. 4.4 represents a combination of an ellipsoid when the pipe length $l \leq l_t$, which transitions to a pipe with

Table 4.2: Applied pipe geometry models.

Geometry	Best fit coefficients	RMSE [m ³]
Eq. 4.3: constant	$A_0=0.001 \text{ m}^2$	$2.5 \cdot 10^{-4}$
Eq. 4.4: combined	$A_0=0.001 \text{ m}^2, A_d = 2.7 \cdot 10^{-5}, l_t=1.60 \text{ m}$	$1.5 \cdot 10^{-4}$



(a) Volume as function of time.

(b) Volume as function of pipe length.

Figure 4.10: Measured and modeled erosion volume.

a constant area A_0 for $l > l_t$. A_d is a coefficient representing the length-width-depth ratio of the ellipsoid.

$$V_{m1}(l) = A_0 l \quad (4.3)$$

$$V_{m2}(l) = \begin{cases} \frac{16}{3} \pi A_d l^3, & \text{if } l \leq l_t \\ \frac{16}{3} \pi A_d l_t^3 + A_0(l - l_t), & \text{if } l > l_t \end{cases} \quad (4.4)$$

The coefficients in Eq. 4.3 and Eq. 4.4 result from minimizing the RMSE between measured $V_{exp}(t)$ and modeled $V_{m1}(t)$ or $V_{m2}(t)$. Table 4.2 and Fig. 4.10a show the best fit of each model. The fitted value of $l_t=1.60$ corresponds to the critical length of 1.65 m which was based on the pressure response. The combined model (Eq. 4.4) fits the measurements slightly better than the constant model (Eq. 4.3), but especially after the transition to the progressive phase (1.60 m) the difference is negligible. So after an initial increase, the ratio of volume over length or the average cross sectional area is relatively constant.

4.4 Discussion

4.4.1 Uncertainties in measurements

Important results such as progression rates and tip gradients are based on the pore pressure measurements. There are some uncertainties in these data which also affect the results to some extent. First, as discussed in section 4.3.2, the head at P9 is probably too

high, so gradient $i_{8,9}$ will be too high and $i_{9,10}$ too low. Without this uncertainty, the relation between progression rate and local tip gradient in Fig. 4.9 is expected to be stronger. Second, the actual pipe head can be lower than the measured pipe head if the pipe passed the sensor at some distance. This does not affect the (average) progression rate, but can be an explanation for the spatial variation in gradients after the pipe passed (Fig. 4.6). Third, it should be noted that the calculated gradient is affected by the transducer spacing (0.8 m and thus averaged over this distance) so the actual gradients close to the tip will be larger. Furthermore, the pressure data smoothing (window size) slightly reduces the peak gradients (e.g. in Fig. 4.9, up to 6%), but it has no effect on the progression rate or the conclusions. Finally, the gradients between the most upstream transducers (9,10,12,14) peak almost instantaneously. The resulting high progression rate (2 mm/s) is considered less reliable, but the true development over this last 1.6 m is unclear. If this part is omitted, the average rate will be 0.06 mm/s instead of 0.1 mm/s. These uncertainties in pressure can be reduced by performing similar (laboratory) experiments with more densely spaced pressure transducers and in which the pipe development can be observed visually.

4

The pattern of coarse sand strips (Fig. 4.3) gives rise to the following points of attention. First, if the pipe tip touches a coarse strip with higher permeability, the pore pressure on the upstream side of that strip drops too. This increases the uncertainty in tip position. However, the effect on the progression rate is expected to be small as the error is similar at all transducers P3-P12. Second, it is expected that the pipe tends to grow along the coarse strips. In the area between two consecutive strips, it may grow temporarily sideways, which may reduce the progression rate and increase the pipe volume. Finally, the strips with higher permeability may change the groundwater flow field. Because they are thin (0.05 m compared to an aquifer depth of 1.0 m) and volume (0.07 m³ compared to an aquifer volume of 11.4 m³), they will have no significant influence on the bulk conductivity. This is also reflected by the similarity between bulk conductivity (k_{levee}) and fine sand conductivity (k_{lab}), see Table 4.1. Hence, there may be some local disturbance of the flow field by the strips, but the effect on piping progression is limited since piping progression is mainly determined by the bulk conductivity of the sand aquifer. It is recommended to confirm this limited influence using a detailed 3D piping erosion model, and to search for an experimental setup or measurement technique that allows sufficiently detailed measurements without disturbance of the sample.

4.4.2 Progression rates in other experiments

Based on a compilation of laboratory tests [Robbins et al., 2017; Sellmeijer et al., 2011; Van Beek et al., 2011; Vandenboer et al., 2019; Yao, 2014], we proposed two equations in section 2.2.4 for the average progression rate during the progressive phase ($v_{c,avg}$). The rate is a function of loading (global hydraulic gradient), soil properties (hydraulic conductivity, porosity) and empirical coefficients: The average rate of 0.1 mm/s found in this large scale test (see section 4.3.3) is in good agreement with both empirical formulas. Eq. 2.17 and Eq. 2.18 yield 0.19 mm/s and 0.14 mm/s respectively, and 0.1 mm/s was observed (see red dot in Fig. 4.11). These rates are relatively close to the 0.05-0.06 mm/s obtained in the IJkdijk large scale tests on fine sand [Sellmeijer et al., 2011; Van Beek et al., 2010].

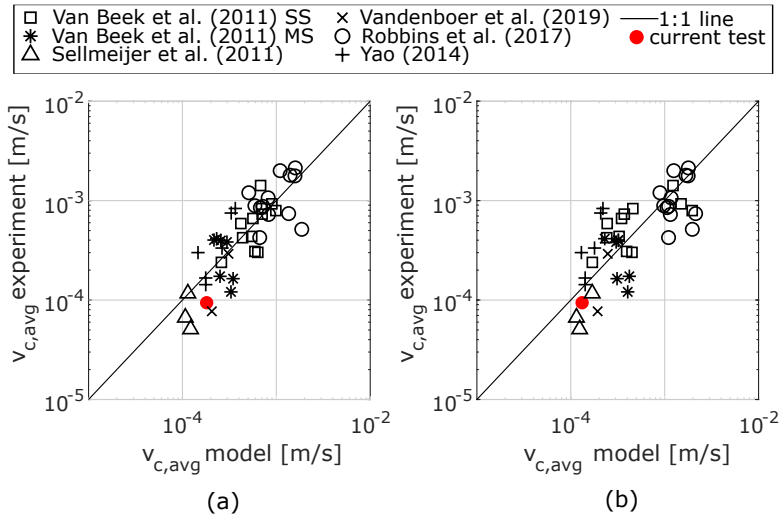


Figure 4.11: Average progression rate during the progressive phase compared to other experiments. The progression rate is modeled using Eq. 2.17 (a) and Eq. 2.18 (b). SS=small scale, MS=medium scale.

4.4.3 Pipe dimensions

During the progressive phase, the pipe area A_0 is approximately 0.001 m^2 . Assuming that the pipe is not wider than 0.2 m (width of the middle strip of fine sand), the pipe depth is at least 5 mm , which is about $30 \cdot d_{50}$. This is larger than values found in laboratory experiments with rigid covers [Allan, 2018; Hanses, 1985; Van Beek et al., 2015; Vandenkoer et al., 2018b]. Pipe depth in these experiments varies approximately from $2 - 20 \cdot d_{50}$, and the pipe width is $20 - 100 \cdot d_{50}$, which yields an area of $40 - 2000 \cdot d_{50}$ ($7-360 \text{ mm}^2$ for the grain size in this test). In contrast to these lab experiments, IJkdijk tests had a clay cover. At the start of the widening phase of IJkdijk test 3, the eroded sand mass was 80 kg [Van Beek et al., 2010]. Based on a $l=15 \text{ m}$ and $n=0.398$, this equals an estimated average cross sectional area of 3300 mm^2 . Note that the IJkdijk test had several active sand boils over the aquifer width of 12 m , whereas our test has only one. Given these differences, the erosion volumes of the two large scale tests are similar. It is not entirely clear whether the larger average cross sectional area compared to lab experiments is only due to scale or also due to the cohesive blanket. A larger aquifer width and depth results in a higher discharge, so it may be expected that pipes are larger as well. The effect of a cohesive blanket could be caused by the blanket roughness or the deformation of the blanket during the test, which leads to more erosion while the pipe dimensions are not increasing. Because of the large differences in pipe volumes between laboratory tests with rigid cover and field experiments with cohesive blanket, practitioners should be careful to estimate pipe lengths from observed sand boil volumes in field conditions combined with cross sectional areas in laboratory tests.

4.4.4 Additional experiment on strength recovery

Assessments of backward erosion piping in dams and levees usually assume an undisturbed soil: i.e. initially there is no pipe present. However, field observations show that sand boils occur more often than failures, so there will likely be small pipes or voids present after a flood. Reasons that these pipes did not lead to failure can be that (1) the head was sufficient for initiation but not for progression; or (2) the head was high enough, but the flood event was too short for the pipe to progress completely backwards [Hanses, 1985]. A partially present pipe can weaken a levee. From a stationary point of view because the presence of a pipe leads to a lower critical head in the progressive phase (Fig. 2.2). From a time-dependent point of view also because there is less time required for piping to progress completely. Over time, this can lead to cumulative damage and a decreasing safety level if the pipe is not repaired or recovers by natural processes (Fig. 2.11)¹. Therefore, it is of interest to what extent and how fast pipes recover after they occurred.

4

This section describes a pipe recovery experiment on the same test section as the large-scale levee experiment in this chapter [Pol et al., 2022b]. The objective of the recovery experiment was to explore whether some form of strength recovery takes place in a previously formed pipe that progressed completely through the foundation.

In the test of 17-19 December 2018, a pipe formed from downstream to upstream. After the hydraulic shortcut occurred according to the analysis of the pressure response, the erosion process continued for 4-5 hours. So there has been some pipe widening too. We reloaded this test section on 3-4 September 2019, with the same procedure. Local hydraulic gradients, measured by pressure sensors at the sand-clay interface, indicate the development of the pipe over time.

Both tests are compared in terms of critical head and progression rate (Fig. 4.12). The critical head difference between the sensor furthest upstream in the aquifer (nr. 12) and sensor furthest downstream (nr. 2) decreased from 1.15 m in 2018 to 0.90 m in 2019, so up to 80% of strength was recovered. As the distance between these sensors is 6.1 m, the critical average horizontal gradient in the latter test was 0.15. This is more than the critical gradient one would expect with a hydraulic shortcut; in that case the critical horizontal gradient of a 2 mm deep pipe with the given grain size would be approximately 0.03 ($i_c = \tau_c / (\rho g 1/2a)$).

Figure 4.12 also shows the pipe length development. The average progression rate dl/dt in the progressive stage, was 19 m/day in the recovery test of 2019 compared to 7.8 m/day in 2018, hence, the progression rate more than doubled. It is interesting that the progression in the recovery test develops again from downstream to upstream, i.e. it starts over again albeit quicker and with a lower critical head. In case of a hydraulic shortcut being present, instead of this gradual development one expects a quick response of the pressures at the upstream side, which is not observed.

Together, these observations show that there was partial recovery over a period of nine months: the levee was weaker than originally but not as weak as expected with a hydraulic shortcut. The relatively short time since construction (one year) in combination with a thin clay cover may have contributed to the recovery as new levees can be expected to settle significantly, potentially closing pipes and cavities. On the other hand, in field conditions there are additional factors that may enhance recovery, such as traffic

¹A review of field evidence regarding long-term trends and pipe recovery is given in section 2.2

loads, siltation, biological activity and fluctuations in temperature and ground water level. Further research should focus on the effect of e.g. cover properties and pipe size on the degree and rate of recovery, and estimate time scales of recovery.

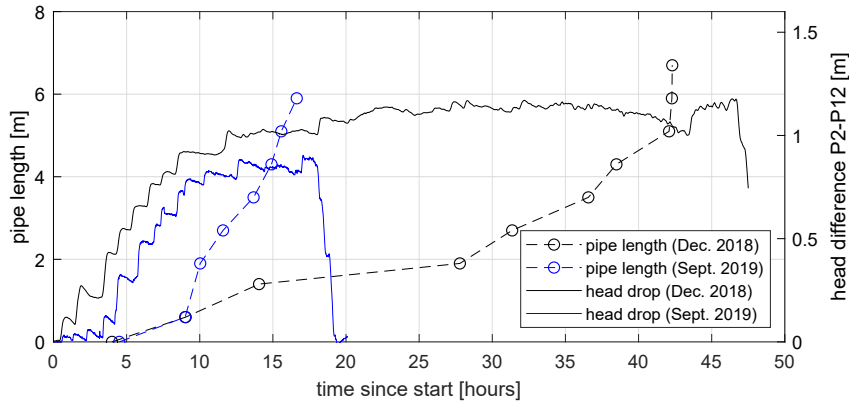


Figure 4.12: Comparison of head and pipe length development in the original experiment (black) and recovery experiment (blue).

4.5 Conclusions

The large scale backward erosion piping experiment described in this chapter was designed to study the temporal development of piping in terms of pipe progression rates. The test levee had a 1 m deep sandy aquifer with a seepage length of 7.2 m. Compared to previous large-scale experiments [De Rijke, 1991; Silvis, 1991; Van Beek et al., 2010], there are two main improvements. First, it had a large scale configuration with clay blanket and hole-type exit. Second, the pipe growth was focused along a row of pore pressure transducers using coarse sand strips, which allows more accurate monitoring of the progression rate.

The performed experiment delivered a useful data set for BEP model validation [Pol et al., 2020]. First, the experiment confirmed several stages of the piping process described in other research, such as the existence of an equilibrium after initiation (regressive phase) which turns into progressive erosion after a critical head is exceeded. Second, the pipe length development was successfully derived from pore pressure data and shows a consistent trend in the sense that pipe length increases monotonically with time. The average progression rate during the progressive phase (at constant head) was approximately $1 \cdot 10^{-4}$ m/s (8 m/day). This value is in line with a multivariate regression on previous experiments [Pol et al., 2019].

The observed critical head difference H_c , corrected for exit loss, was 1.42 m. The critical pipe length l_c was approximately 1.65 m, which is 23% of the seepage length. It was found that the pipe volume increases linearly with pipe length, after an initial cubic increase. However, the derived average cross sectional area (approx. 1000 mm^2) was significantly larger than in small scale experiments.

An important question for modeling is whether the progression rate is governed by

primary erosion or secondary erosion. The results show a relation between tip gradient and progression rate. However, this does not show that the progression rate is governed only by primary erosion, because secondary erosion is also related to the tip gradient. For a better understanding of the dominant drivers, these mechanisms should be studied in more controlled laboratory experiments².

Information on the temporal development can be applied to, for example, levee safety assessments, emergency response planning and prioritization of monitoring in the most critical levee sections. The relatively slow progression observed in this experiment indicates the importance of the temporal aspects. If similar rates occur in the field, it takes approximately one week for a pipe to develop through 50 m seepage length of a levee. In areas with shorter flood duration, this has a significant positive impact on the calculated safety against piping and thus on reinforcement costs. On the other hand, factors such as overloading ($H > H_c$) are expected to speed up the erosion rate [Vandenboer et al., 2019], and soil heterogeneity may either increase or decrease the progression rate.

The recovery experiment, in which the levee was reloaded after 9 months, showed partial recovery of the pipe strength. The erosion process started all over again, albeit with lower critical head and higher progression rate. This is a promising finding for concerns regarding cumulative degradation in the long term [Glynn et al., 2012], and needs further study to quantify recovery for field conditions.

Current piping models should be extended with temporal development, based on further laboratory experiments that show dependence on hydraulic loading, scale and sand properties. Although the dimensions of this test (mainly the aquifer) are still smaller than in many field situations, the experiment provides a novel data set to validate or benchmark piping models.

²This was done in the small-scale experiments in chapter 3, which were performed after the large-scale experiment in this chapter.

5

Modeling Temporal Development of Backward Erosion Piping

Ceci n'est pas une pipe

René Margritte

5

Abstract

This chapter investigates how the time-dependent development of backward erosion piping (BEP) can be simulated using numerical simulation of the erosion process. Therefore, a 3D finite element equilibrium BEP model is extended with a formulation for the sediment transport rate. The model is compared to and calibrated with several experiments. Finally, a large set of simulations is analyzed to study the effects of factors such as grain size, scale (seepage length) and overloading on the rate of pipe progression. The results show that the development of BEP in the small-scale experiments is predicted well. Challenges remain for the prediction of the critical hydraulic load on larger scales, primarily due to limited large-scale experiments with sufficiently accurate measurements. The results show that the progression rate increases with grain size and degree of overloading and decreases with seepage length, which is consistent with experimental observations. For practical applications, a simple regression model is derived to predict the progression rate as function of grain size, hydraulic gradient and degree of overloading.

5.1 Introduction

Research over the past decades had led to an increased understanding of the processes involved in backward erosion piping (BEP) [Hanses, 1985; Miesel, 1977; Schmertmann, 2000; Sellmeijer, 1988; Van Beek, 2015]. This involves among others the interplay between groundwater flow in an aquifer, flow in micro-scale channels or pipes, primary erosion of the soil at the pipe tip (pipe lengthening) and secondary erosion (pipe deepening and widening), see Fig. 5.1. This research, and the resulting predictive models, focused primarily on the critical conditions for BEP to develop. More recently, there is an increasing amount of research into time-dependent aspects of the erosion process, both experimentally [Allan, 2018; Pol et al., 2022a; Robbins et al., 2017; Vandenkoer et al., 2019] and using numerical modeling [Rotunno et al., 2019; Wewer et al., 2021]. This is especially relevant for BEP risk assessments of hydraulic structures when the hydraulic load is shorter than the time scale of the erosion process from initiation to catastrophic failure. Furthermore, insights in the time scale of the failure process, and how that depends on local factors, may inform emergency response decisions when initiation of failure is observed. Such applications need a predictive model to translate experimental results to field conditions. These models can be empirical [Pol et al., 2019], semi-analytical [Kézdi, 1979], based on finite elements [Rotunno et al., 2019] or discrete elements [Tran et al., 2017]. This chapter describes a 3D finite element model (FEM) to simulate the time-dependent development of BEP based on a sediment mass balance and an empirical sediment transport relation. Secondly, the model outcomes are compared to several experiments. Thirdly, effects of grain size, scale, and overloading on the progression rate are analyzed and translated to simplified regression models for the progression rate in field conditions.

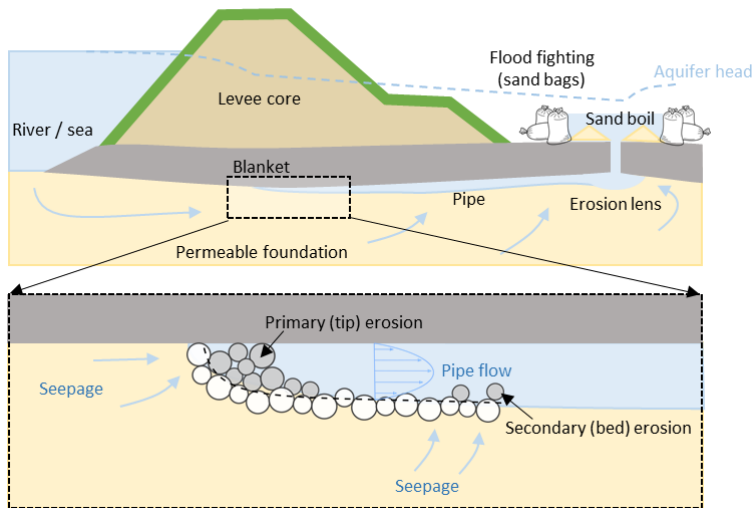


Figure 5.1: Visualization of the main processes of backward erosion piping.

5.2 Modeling approach

The basis for the developed numerical model is the DgFlow finite element model, which was developed by van Esch et al. [2013] to simulate backward erosion piping. The 2D-version of the model (D-GeoFlow) is also being used in levee safety analyses in the Netherlands [Deltares, 2020] and yields similar critical heads as the Sellmeijer et al. [2011] model. Later, DgFlow has been extended to a 3-dimensional domain and includes a strength criterion for primary erosion [van Esch, 2015]. In this chapter, "DgFlow" refers to the version including 3D flow and primary erosion, unless stated otherwise. DgFlow is an equilibrium model: for a given head difference it computes whether grain equilibrium can be satisfied and what the corresponding pipe dimensions are, but it does not model how that equilibrium state is reached in time. So this model can compute the critical head for BEP but not the time-dependent development. This time-dependent erosion is added in this chapter. Section 5.2.1 summarizes the most important features of the current DgFlow model; for further details we refer to van Esch et al. [2013] and van Esch [2015]. Section 5.2.2 discusses different potential modeling approaches to extend the model with time-dependent erosion, and section 5.2.3 describes the approach chosen in this thesis for the time-dependent modeling of piping.

5.2.1 Current DgFlow finite element model

The DgFlow model couples 3 dimensional transient seepage flow, steady 1 dimensional laminar pipe flow and a grain stability criterion to simulate the development of the pipe length for an imposed head difference.

The pore pressure p is computed with transient groundwater flow equations considering mass conservation and Darcy's law:

$$(\alpha + n\beta)S \frac{\partial p}{\partial t} + n \frac{dS}{dp} \frac{\partial p}{\partial t} + \frac{\partial q_i}{\partial x_i} = 0, \quad q_i = - \frac{k_r \kappa_{ij}}{\mu} \left(\frac{\partial p}{\partial x_j} - \rho_w g_j \right) \quad (5.1)$$

where α [m²/N] is the compressibility of the soil skeleton, β [m²/N] the compressibility of the pore water, n [-] porosity and S [-] the degree of saturation. Specific discharge q_i [m/s] relates to relative permeability k_r [-], intrinsic permeability κ_{ij} [m²], μ dynamic viscosity [N/m²s] and density ρ [kg/m³]. The groundwater flow simulations in this chapter are simplified to quasi-steady saturated flow ($\frac{\partial p}{\partial t} = 0$ and $k_r = 1$).

Pipe flow is based on laminar Poiseuille flow between parallel plates, which provides the relation between pipe discharge, depth and hydraulic gradient:

$$\frac{dp}{dx} a^3 w = 12U w a \mu \quad (5.2)$$

in which a denotes pipe depth [m], w pipe width [m], p pore pressure [N/m²], U cross-sectional average flow velocity [m/s] and x horizontal distance [m]. In DgFlow, w is related to a using a specified w/a ratio. The acting bed shear stress τ_{bed} for parallel plates ($w \gg a$) is given by:

$$\tau = R \frac{dp}{dx} = \frac{a}{2} \frac{dp}{dx} \quad (5.3)$$

in which R is the hydraulic radius [m]. The grain stability is modeled following White [1940] and Sellmeijer [1988] in which the critical bed shear stress is given by:

$$\tau_c = \eta \frac{\pi}{6} (\rho_s - \rho_w) g d \tan(\theta) \quad (5.4)$$

in which η is White's coefficient [-], ρ_s sediment density [kg/m^3], d grain size [m] and θ bedding angle [deg]. Equating Eq. 5.3 and 5.4 yields the pipe equilibrium condition. Based on experimental data, Van Beek [2015] proposed to use $d = d_{50}$, $\eta=0.3$ and $\theta = -8.125 \cdot \ln(d_{50}) - 38.777$. This is also known as the Calibrated White approach.

The Poiseuille pipe flow and Darcy groundwater flow equations have a similar form: in both cases the discharge is proportional to the pressure gradient. Therefore, the pipe flow can be solved as part of the groundwater computation, using an equivalent permeability κ_p which corresponds to a rectangular pipe with depth a and width w . For 1D pipe elements in a 3D model, this relation becomes [van Esch, 2015]:

$$\kappa_p = \frac{wa^3}{12} \quad (5.5)$$

Note that κ_p [m^4] is not equal to the intrinsic permeability κ [m^2].

In a given time step, the equilibrium depth of all pipe elements is solved iteratively by step-wise increasing a (and hence w and κ_p) and updating the groundwater flow accordingly, until the equilibrium condition is met. The depth iteration step is given by $\Delta a = 100d/(\text{mPicard} - 1)$, where mPicard is a numerical model setting. See Fig. 1 in van Esch et al. [2013] for a graphical explanation of this iterative scheme. The pipe length increases if the primary erosion criterion is exceeded. The strength criterion for primary erosion is defined in terms of critical local hydraulic gradient over the first element upstream of the pipe tip $i_{tip,c}$ [van Esch, 2015; Robbins and Griffiths, 2021; Rosenbrand et al., 2021]:

$$i_{tip} = \rho_w g \frac{dp}{dx} > i_{tip,c} \quad (5.6)$$

Although the groundwater flow can be modeled as transient in DgFlow, the increase in pipe depth and length in response to that flow is instantaneous. The following sections present the proposed method to extend the current model with a time-dependent development of the pipe.

5.2.2 Approaches for time-dependent piping erosion modeling

Based on observations in small-scale experiments (chapter 3), the pipe progression in poorly graded sand can be described as follows. The erosion mechanism at the tip can be described as micro-scale slope failures which occur rather sudden if the seepage flow forces at the tip exceed the resistance of the packed grains (Fig. 3.1). The sand is detached in groups of grains, although also individual particle movement occurs. Part of the sand keeps moving; another part settles on the bed in front of the pipe tip and are gradually transported by the flow (secondary erosion). Pipe pressure measurements showed that the sediment load in the pipe results in a temporarily higher flow resistance (pressure drop) in the pipe. Consequently this gives temporarily a lower tip gradient which delays the

pipe lengthening. When a sufficient amount of sand is transported so that the tip gradient has recovered to its critical value, the next slope failure occurs (Fig. 3.5). These observations indicate that the sediment transport capacity of the pipe is an important factor in the progression rate.

Such processes can be modeled using different approaches which represent the dynamics of the erosion process with different levels of detail.

1. The first method is to solve a sediment mass balance in space and time with a sufficiently small time step to capture the dynamics of the sediment movement in the pipe. So, one could simulate the above-mentioned temporary increase and decrease in flow resistance due to sediment moving through the pipe, either represented as a lower depth or a higher sediment concentration. The sediment from the collapsing tip element is added as a source term to the upstream pipe element once the primary erosion criterion is exceeded. This approach is used by Rotunno et al. [2019] and reflects the above-mentioned observations well. However, a major drawback is the small time step needed to simulate the dynamic sediment wave propagation through the pipe.

2. The second method is to solve the sediment balance in space and time as well, but the tip element is gradually deepened by the same secondary erosion laws as the rest of the pipe, instead of an instantaneous sediment mass transfer from soil to the pipe. Here the progression rate is still driven by the sediment transport capacity, but the dynamics of the moving sediment wave are not solved. This allows for larger time steps and hence more efficient simulations. To our best knowledge, this approach has not been used yet.

3. The third method is to solve the sediment balance in time, but integrated over the pipe length. Here the increase in pipe volume equals the sediment transported at the downstream end, and the spatial distribution of the erosion (lengthening and deepening) is forced by an assumed relation between pipe depth and pipe length [Wewer et al., 2021]. As this approach also does not simulate the dynamics of sediment movement and multiple elements can switch to pipe elements within a time step, the time step can be relatively large. However, this approach is not compatible with the model approach of DgFlow in which each pipe element is deepened based on the local acting and critical shear stresses.

To keep the simulation time step relatively large and to avoid any assumption of a pipe depth profile, we adopt the second method as explained further in section 5.2.3.

5.2.3 Model extension with time-dependent erosion

We extend the current 3D DgFlow model [van Esch, 2015] with a time-dependent formulation of the backward erosion process. First, we describe here the main features of the employed method, which is based on the second approach in the previous section. As DgFlow is an equilibrium model, it computes the pipe depth at which the pipe bed is in equilibrium ($\tau = \tau_c$). Based on the experiments in chapter 3, we assume that the rate of pipe progression (dl/dt) depends on the sediment transport capacity of the pipe flow, which is a function of the degree to which the critical shear stress is exceeded ($\tau - \tau_c$). To model this time-dependent process in DgFlow, we compute the pipe depth increase based on a sediment mass balance and sediment transport equations for laminar flow. In this way, the computed pipe depth can be temporarily smaller than the equilibrium depth that is computed using the current DgFlow model. The lower the shear stress, the more time it takes to reach the equilibrium depth. This pipe deepening (secondary erosion) affects the

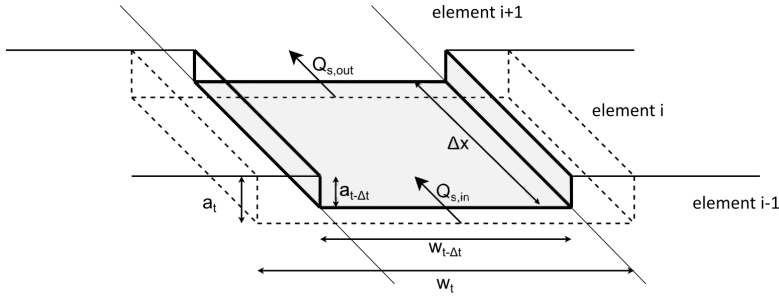


Figure 5.2: Sediment balance of an element: increase in pipe volume (depth a , width w) equals change in sediment transport capacity ($Q_{s,out} - Q_{s,in}$).

hydraulic gradient at the pipe tip, and therefore the rate of pipe deepening affects the rate of pipe progression (primary erosion).

5

Secondary erosion

Pipe deepening by secondary erosion is governed by a sediment balance (Fig. 5.2). The sediment balance of an element i with fixed length Δx_i but variable depth a and width w , subject to a volumetric sediment transport rate Q_s [m^3/s] over the time interval Δt is given by:

$$a_{t,i} w_{t,i} \Delta x_i = a_{t-\Delta t,i} w_{t-\Delta t,i} \Delta x_i + \frac{(Q_{s,out} - Q_{s,in}) \Delta t}{(1-n)} \quad (5.7)$$

This can be written in terms of the volumetric sediment transport rate per unit width q_v [m^2/s] as:

$$a_{t,i} w_{t,i} \Delta x_i = a_{t-\Delta t,i} w_{t-\Delta t,i} \Delta x_i + \frac{(q_{v,t-\Delta t,i} w_{t-\Delta t,i} - q_{v,t-\Delta t,i-1} w_{t-\Delta t,i-1}) \Delta t}{(1-n)} \quad (5.8)$$

This balance is similar to the Exner equation which is widely used for sediment transport in rivers:

$$(1-n) \frac{\partial a w}{\partial t} = \frac{\partial q_v w}{\partial x} \quad (5.9)$$

Assuming a fixed depth-width ratio N and only an increase in depth, substitution of $w = N \cdot a$ into Eq. 5.8 and division by $N \cdot \Delta x$ gives:

$$a_{t,i}^2 = a_{t-\Delta t,i}^2 + \frac{\langle q_{v,t-\Delta t,i} a_{t-\Delta t,i} - q_{v,t-\Delta t,i-1} a_{t-\Delta t,i-1} \rangle \Delta t}{(1-n) \Delta x_i} \quad (5.10)$$

Here $\langle \cdot \rangle$ denotes the positive part (only depth increase). Preventing the model to simulate a decrease in pipe depth may introduce an error in the sediment balance in case $dq_v/dx < 0$. However, we motivate this choice by the fact the the pipe flow rate always increases with distance from the pipe tip. Eq. 5.10 is used to compute the pipe depth in each pipe element based on the pipe depth in the previous time step and sediment transport rate in the current and upstream elements in the previous time step. The computed sediment flux q_v [$\text{m}^3/\text{s}/\text{m}$] is based on an empirical relation with the excess bed shear stress in laminar flows:

$$q_v = C_{e,\tau} \cdot \tau \langle \tau - \tau_c \rangle \quad (5.11)$$

Other excess shear stress equations have been considered, but this form is simple and matches sufficiently well with experiments (section 3.4.4). The factor $C_{e,\tau}$ [$\text{m}^2\text{Pa}^{-2}\text{s}^{-1}$] is a model input, the acting bed shear stress is based on parallel plates (Eq. 5.3) and the critical bed shear stress is determined with Eq. 5.4. $C_{e,\tau}$ is in fact the combination of two scaling terms and an empirical coefficient, because Eq. 5.11 was originally written in dimensionless form as [Pol et al., 2022a]:

$$\frac{q_v}{(\rho_s - \rho_w)gd^3/\mu} = C_e \cdot \Theta(\Theta - \Theta_c) \quad (5.12)$$

where $\Theta = \tau/(\rho_s - \rho_w)gd$ is the Shields number and $C_e = 0.08$ is an empirical dimensionless coefficient. In Eq. 5.12 there is a sediment transport scaling term $C_1 = (\rho_s - \rho_w)gd^3/\mu$ and a scaling term $C_2 = 1/(\rho_s - \rho_w)gd$ which is the scaling between shear stress and Shields number. So $C_{e,\tau}$ can be written as:

$$C_{e,\tau} = C_e C_1 (C_2)^2 = \frac{C_e d}{(\rho_s - \rho_w)g\mu} [\text{m}^2\text{Pa}^{-2}\text{s}^{-1}] \quad (5.13)$$

As the coefficient $C_e = 0.08$ was derived in section 3.4.4 using d_{50} , the d_{50} should be used as representative diameter in this calculation. So, the pipe deepening (secondary erosion) is controlled by Eq. 5.10, 5.11, 5.3 and 5.4.

Primary erosion

In the current DgFlow model, pipe lengthening (primary erosion) is controlled by the following criterion [van Esch, 2015; Rosenbrand et al., 2021]: the first soil element upstream of the pipe switches to a pipe element if the local hydraulic gradient over that soil element exceeds a critical value $i_{tip,c}$ (Eq. 5.6). Upon opening, a pipe element gets an initial depth a_{ini} to avoid an unrealistically low equivalent permeability κ_p and corresponding high hydraulic gradient which could stop the pipe from further progression. a_{ini} is a model input, and typically chosen in the order of d_{50} . In our time-dependent model, this initial volume ($a_{ini}^2 \cdot N$) is created instantaneously and not part of the sediment balance, and therefore introduces an error in the rate of pipe deepening. When the pipe depth is much larger than a_{ini} , this error is small.

Note that the model includes no explicit time-dependency in the primary erosion rate, unlike for instance Fujisawa et al. [2010] or Rotunno et al. [2019] who employ also a transport law for primary erosion. Instead, in our approach the primary erosion of an element occurs instantaneously but the rate of progression is limited by the sediment transport rate in the pipe. A low transport rate results in slowly increasing pipe depths, which lead to higher flow resistance and therefore indirectly controls the rate of primary erosion. This approach can be justified if the primary erosion occurs in relative short timescales, for instance in poorly graded sands (chapter 3).

Integration in DgFlow simulation procedure

The flow chart of Fig. 5.3 presents where the time-dependent erosion is integrated in the current DgFlow model simulation procedure.

In each time step, the model performs two analyses, indicated by the green boxes: first secondary erosion (box 4) and then primary erosion (box 5). In the secondary erosion analysis, for each pipe depth increment Δa , first a groundwater flow calculation is performed

(box 6), followed by a check whether the depth in each element is larger than the equilibrium depth (box 7b, 7e). If so, secondary erosion occurs and the depth is increased by Δa . Then the obtained pipe depth is translated to equivalent permeability (box 7g), which is used in the flow calculation for the next depth increment.

When the equilibrium pipe depth has been determined for each pipe element, the primary erosion criterion is checked at the first element upstream of the pipe (box 5). If this criterion is exceeded, that element switches to pipe element and the depth iteration procedure of box 4 is repeated. If it is not exceeded, the next time step is calculated.

The time-dependence is included in box 7c and 7d, where the pipe depth may only increase up to the depth a_{max} which follows from Eq. 5.10 and 5.11.

Numerical step sizes

Relevant numerical step sizes related to the secondary erosion are pipe grid size Δx , time step Δt and depth increment Δa .

To avoid the progression rate to depend directly on the time step or grid size, opening of an element should take multiple time steps. In that way, the depth of the first pipe element can increase gradually. This requires the $\Delta x/\Delta t \gg dl/dt$. So for a given pipe element size, the maximum time step can be estimated if the order of magnitude of the progression rate is known.

Secondly, the depth iteration step Δa must be smaller than the depth increase during one time step ($\Delta a/\Delta t < da/dt$). The reason is that when the sediment transport becomes too low, so that $da < \Delta a$, the pipe depth will not increase anymore. Δa is controlled by the numerical model parameter mPicard and the grain size d (see section 5.2.1). As the smallest amount of pipe deepening that must be simulated is difficult to estimate beforehand, one can evaluate the sensitivity of the model results for mPicard. For the small-scale simulations in which $\Delta t=10$ s (section 5.3), mPicard=2000 is sufficiently stable.

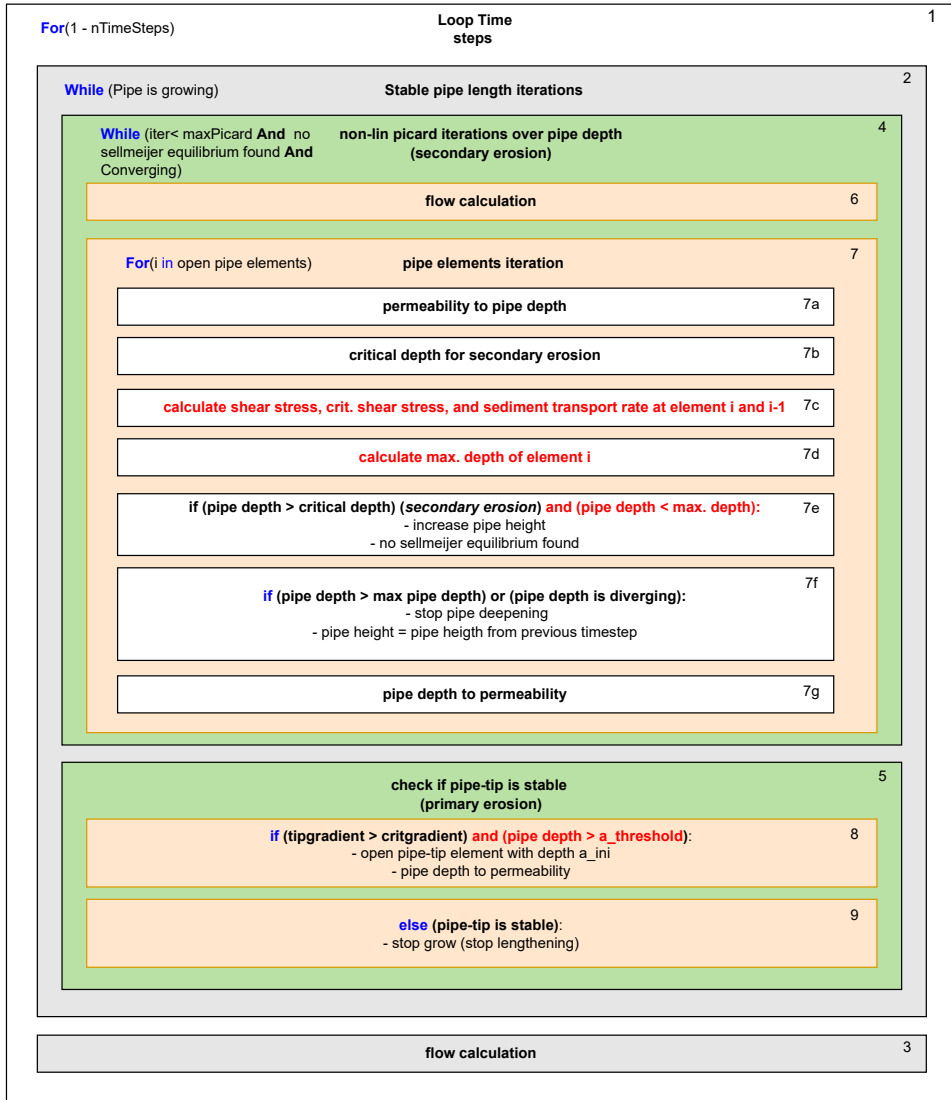


Figure 5.3: Flow chart DgFlow simulation. Additions for time-dependent erosion indicated in red.

5.3 Simulation of experiments

In order to test the developed model, several experiments with detailed measurements of pressure and pipe development from chapter 3 and 4 are simulated.

5.3.1 Method

For the simulation of experiments, we use selected small-scale experiments from from chapter 3 as these contain densely spaced measurements of the head in the sample as well as the pipe length development over time. For two sand types (B25 and FS35), we selected experiments with dense and loose sand and one with overloading ($H > H_c$). This resulted in the following six tests: B25-232 (dense), B25-245 (loose), B25-248 (dense, 20% overloading), FS35-238 (dense), FS35-240 (loose) and FS35-242 (dense, 20% overloading). Additionally, the large-scale experiment in chapter 4 is simulated. Material parameters and other model inputs are shown in Table 5.1. For the small-scale tests, four parameters were calibrated to resemble the results of these experiments. η , w/a , $i_{tip,c}$ are calibrated to resemble the critical head, although these variables were also measured. The erosion coefficient C_e is calibrated to resemble the pipe length development over time. For the large-scale test, only w/a and C_e are calibrated. The two small-scale overloading experiments are only used for the calibration of C_e , as equilibrium was not reached in these experiments.

5

Small-scale experiments

The computational grid has 1D linear pipe elements with length $\Delta x = 0.01$ and tetrahedral soil elements of 0.02 m (Fig. 5.4a). Boundary conditions are located on the surfaces as indicated in Fig. 5.4b. These are head boundaries based on the measured head difference over the sample, corrected for head loss in the upstream filter and the exit hole. Other boundaries are no-flow. The time step Δt is chosen based on the expected progression rate and grid size. In these experiments, the progression rate is in the order of $10^{-4} - 10^{-3}$ m/s. To satisfy $\Delta x/\Delta t > 10^{-3}$ with $\Delta x = 0.01$, this requires $\Delta t < 10$ s.

Calibration is performed in two steps: first we calibrate η , w/a , $i_{tip,c}$ on the conditions during the time step in which the critical head is reached, then we calibrate C_e on the pipe length development over time.

Four goodness of fit criteria are used for the critical conditions:

1. critical head $\frac{|H_{c,exp} - H_{c,model}|}{H_{c,exp}}$;
2. critical pipe length $|l_{c,exp} - l_{c,model}|$;
3. head profile in the pipe: $\text{RMSE}(h_{c,exp}(x) - h_{c,model}(x))$;
4. head profile along the entire center axis: $\text{RMSE}(h_{c,exp}(x) - h_{c,model}(x))$.

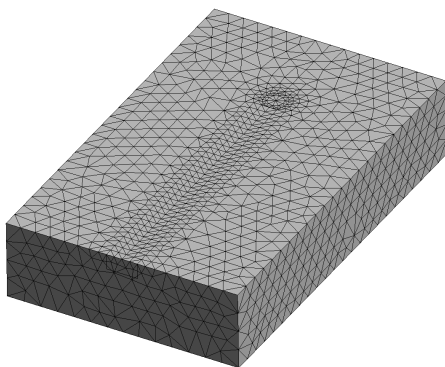
All simulations with different parameter combinations are ranked on each criterion, and the product of these four ranks determines the total rank. The total rank is minimized, so the four criteria are equally important in the calibration.

Two goodness of fit criteria are used for the pipe length development over time:

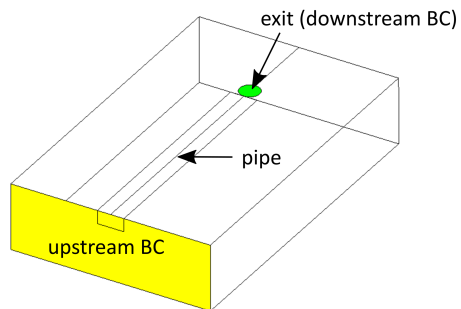
1. total pipe length development $\text{RMSE}(l_{exp}(t) - l_{model}(t))$;

Table 5.1: Model input used for simulation of experiments.

	small-scale						large-scale FPH
	B25-232	B25-245	B25-248	FS35-238	FS35-240	FS35-242	
Input parameters							
d_{50} mm	0.228	0.228	0.228	0.422	0.422	0.422	0.185
ρ_s kg/m ³	2650	2650	2650	2650	2650	2650	2610
ρ_w kg/m ³	1000	1000	1000	1000	1000	1000	1000
κ 10 ⁻¹¹ m ²	2.75	3.16	2.55	10.2	12.2	8.87	1.2
n -	0.377	0.402	0.377	0.381	0.399	0.377	0.383
θ °	29.36	29.36	29.36	24.36	24.36	24.36	31.06
μ Pa s	0.001	0.001	0.001	0.001	0.001	0.001	0.00133
η -							0.4
$i_{tip,c}$ (5 cm)							1.1
Calibrated							
η -	0.35	0.3		0.35	0.3		
$i_{tip,c}$ (1 cm)	1.1	0.9		1.1	0.9		
w/a -	20	25		25	25		700
C_e -	0.012	0.010	0.030	0.018	0.007	0.018	0.014



(a) Grid.



(b) Boundary conditions.

Figure 5.4: Small-scale model grid and head boundary conditions. For dimensions see Fig. 3.2.

2. average progression rate $v = dl/dt$ in the progressive phase $\frac{|v_{exp} - v_{model}|}{v_{exp}}$. The progressive phase is for the experiment $l_{c,exp} < l_{exp} < 0.30$, and for the model assumed to be $0.20 < l_{model} < 0.30$).

Again the simulations with different parameter combinations are ranked on each criterion, and the product of these two ranks determines the total rank, which is minimized.

Large-scale experiment

For the simulation of the large scale experiment, η and $i_{tip,c}$ are not calibrated but $\eta = 0.4$ is chosen based on critical shear stress measured on this sand (section 3.4.1) and $i_{tip,c}$ is chosen as 1.1. This value follows from the measured critical gradient of 0.28 over 80 cm spacing (section 4.3.3), which is translated to an average gradient over 5 cm using Eq. 5.14. As no pipe geometry measurements are available, w/a is calibrated on the critical head profile. C_e is calibrated on the pipe length development. The pipe grid size is 5 cm and the time step is 100 s.

5

5.3.2 Results

Small-scale experiments

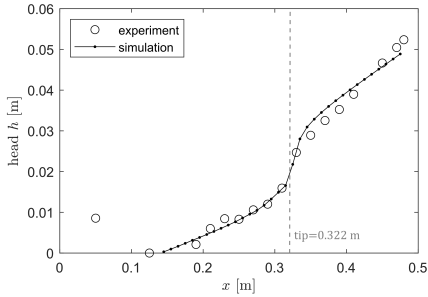
The best-fit values for the calibrated parameters are given in Table 5.1. The obtained values for η are close to the 0.3 found by Van Beek [2015] and measured critical shear stresses in these experiments (section 3.4.1). The obtained w/a -ratios are also within the range of 10-30 measured in the experiments (section 3.3.5). These two parameters affect the hydraulic gradient in the pipe. The obtained critical tip gradients over the model grid spacing of $\Delta x = 1$ cm (0.9 for loose and 1.1 for dense sands) are translated to gradients over $\Delta x = 2$ cm as the spacing in the measurements was 2 cm. This was done using the critical secant gradient function from Robbins [2022], which can be rewritten as Eq. 5.14:

$$i_c(\Delta x) = i_0 \sqrt{\frac{\Delta x_0}{\Delta x}} \quad (5.14)$$

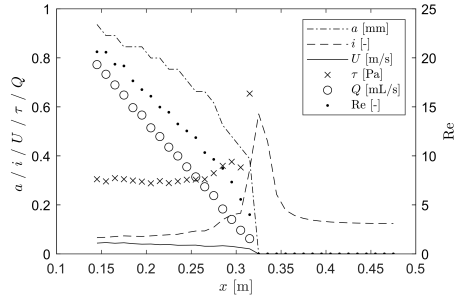
where i_0 is the measured gradient, Δx_0 the measurement spacing and Δx the desired spacing. This yields gradients of 0.64 and 0.78 respectively. The measured $i_{tip,c}$ for the loose sand in section 3.3.3 was lower (range 0.4-0.6), but for the dense sand this was similar to the calibrated value (range 0.6-0.8).

The calibrated values for C_e are consistent between the two sands but approximately a factor 3 to 10 lower than the 0.08 expected from Eq. 5.13. This may be the partly caused by the representation of the pipe as a straight rectangular channel, which requires less transport to obtain a given pipe length compared to a meandering channel. Furthermore, it is noted that sediment transport rates are typically associated with large uncertainties: variations of one order of magnitude are commonly observed in sediment transport relations based on lab tests.

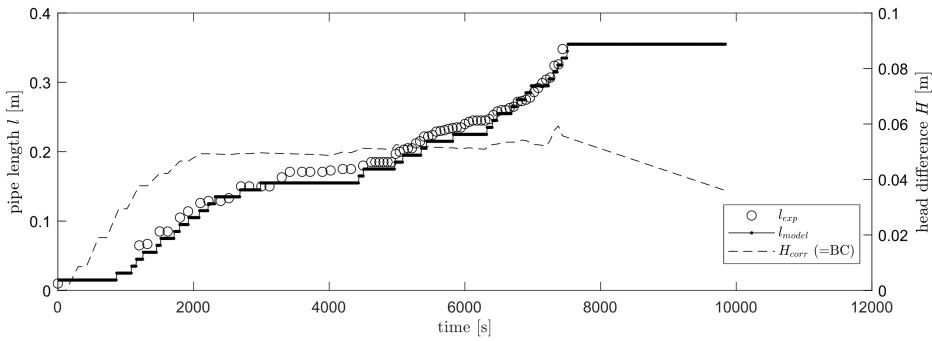
Figure 5.5 shows the best-fit result for test B25-245. The simulated head profile (Fig. 5.5a) and pipe length development (Fig. 5.5c) agree well with the measurements. Computed pipe flow conditions are shown in Fig. 5.5b. The computed pipe depth of 1 mm is slightly larger than the measured 0.8 mm, and the flow is clearly laminar ($Re \approx 20$).



(a) Head profile in critical conditions.

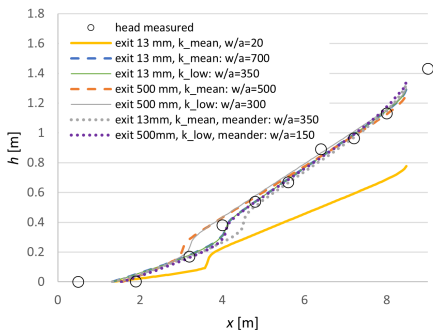


(b) Modelled pipe flow variables in critical conditions.

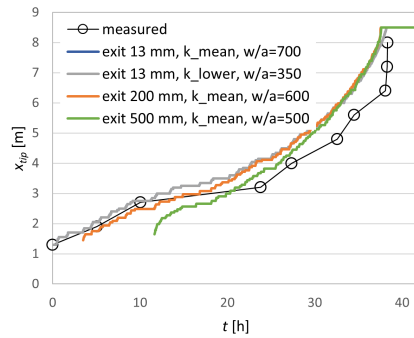


(c) Pipe length development and imposed head.

Figure 5.5: Calibrated model results for small-scale experiment B25-245 ($i_{tip,c} = 0.9$, $\eta = 0.3$, $C_e = 0.014$).



(a) Head profile in critical conditions.



(b) Development of pipe tip position x_{tip} .

Figure 5.6: Calibrated model results for the large-scale experiment ($i_{tip,c} = 1.1$, $\eta = 0.4$, $C_e = 0.014$) compared with measurements.

Large-scale experiment

When using the same $w/a = 20$ as in the small-scale experiments, the critical head profile is strongly underestimated by the model (yellow line in Fig. 5.6a). Apparently, there is more resistance present than what is modeled with parameters based on the small-scale experiments. This can be something in the execution of the experiment, or a physical process which is not represented well in the model. Here we increased the w/a ratio to match the measured head profile, although other model parameters could be adjusted (e.g. η).

A w/a ratio of 700 was needed to obtain a reasonable head profile. As the w/a ratio of 700 is far higher than found in small-scale tests, we simulated a few slightly different model configurations with more resistance to investigate how this changes the required w/a . First, the diameter of the circular downstream boundary was increased from 13 mm to 200 mm and 500 mm to simulate the influence of lens formation around the exit hole. Second, the soil permeability of $1.2 \cdot 10^{-11} \text{ m}^2$ was decreased to $6 \cdot 10^{-12} \text{ m}^2$, which is the expected value minus one standard deviation (lower bound). Third, a meandering pipe was implemented such that the actual pipe length was $\sqrt{2}$ times the straight pipe length of 7.2 m. This tortuosity can be around 1.5-2 in piping experiments [Wewer et al., 2021].

The required w/a ratio decreases with all changes, but even in the lowest case with exit diameter of 500 mm, lower bound permeability and meandering pipe, a value of 150 is still required (Fig. 5.6a). Note that this value does not necessarily reflect the physical geometry of the pipe cross section, but through calibration it became a general pipe resistance factor. The source of this additional resistance is not entirely clear, but potential explanations include wider and shallower pipes, pipe meandering, clay cover roughness, reduced permeability due to fines or a leaky aquifer. Hence it remains also uncertain how this resistance depends on the scale of the experiment. Because the scale-dependence potentially has a large impact on model results on field scale, this needs further study. For instance by simulating multi-scale hole-type experiments that include information on pipe geometry and pipe flow conditions. It is noted that a recent study with the 3D DgFlow model without primary erosion also indicates that the critical head is underestimated [Van Beek et al., 2022], and that $w/a \approx 100$ is needed to reproduce medium scale laboratory experiments.

For the analysis of the pipe development over time, we calibrated C_e for different scenarios of the permeability (expected and lower bound) and different exit diameters. The numerical simulations show a temporary decrease in progression rate around the critical length ($x_{tip} \approx 2.95 \text{ m}$), which was also observed in the measurements. In all simulated cases, the obtained C_e to match the measured total erosion time is close to 0.014. So similar to the small-scale experiments, the calibrated value is a factor 5-6 below that in Eq. 5.13, possibly due to the representation of the pipe as straight rectangular channel.

Concluding remarks

The comparison with experiments shows that the DgFlow model with instantaneous erosion is well able to reproduce the measured critical head and critical pipe length in the small-scale tests. This is illustrated by the result that all calibrated parameters (w/a , η , $i_{tip,c}$) take values which are close to the measured ones. Only for the loose sand tests, the critical tip gradient found by calibration is slightly higher than measured. The critical conditions of the large-scale experiment could only be reproduced with a much higher

pipe flow resistance than used for the small-scale experiments. Calibration of w/a yields $w/a = 700$ compared to $w/a = 20$ in the small scale experiments. The reason for this additional resistance could not be demonstrated and needs to be studied in more depth.

With respect to the time-dependent pipe development, the modified DgFlow model can reproduce this reasonably well, although the erosion coefficient C_e needs to be calibrated. Calibration on the different small-scale experiments yields $0.007 < C_e < 0.030$ (average: 0.016). Calibration of the large-scale experiment yields $C_e = 0.014$, which is in close agreement with the small-scale results.

5.4 Effect of grain size, scale, and overloading

In section 5.3, the developed model was tested and calibrated on several experiments. This section uses the model to study how factors such as grain size, scale and overloading affect the simulated pipe development, and ultimately to derive relations between pipe growth rate and above-mentioned factors.

5.4.1 Method: model setup

To study the effect of grain size, scale, and overloading on the pipe development over time, we have set up a series of simulations in which those properties vary. In addition, the sensitivity of the computed development for several model assumption and parameters is investigated.

The simulations include six sand types as indicated in Table 5.2. Grain sizes range from 0.200-0.400 mm. For each grain size, two intrinsic permeabilities are used which correspond to a uniformity coefficient $C_u = d_{60}/d_{10}$ of 2 and 3. The bedding angle θ is based on Van Beek [2015]. The erosion coefficient C_e is assumed to be 0.08, the value in Eq. 5.13 prior to calibration, but varied in some cases to 0.008, 0.016 and 0.16 to investigate the sensitivity for C_e . Other parameters assumed to be constant are: $\rho_s = 2650$ [kg/m³], $\rho_w = 1000$ [kg/m³], $\mu = 0.00133$ [Pa s], $n = 0.4$, $\eta = 0.3$, $w/a = 20$, $a_{ini} = d_{50}$, $a_{thr} = d_{50}$.

The critical gradient $i_{tip,c}$ depends on the sand properties such as compaction [Robbins et al., 2017] and pipe grid size. As the grid size increases with scale, the modeled value of $i_{tip,c}$ will vary with scale. For the purpose of illustration, we assume that $i_{tip,c} = 0.7$ (over 2 cm). This value is based on the dense ($D_r = 0.8$) experiments in Pol et al. [2022a]. To obtain $i_{tip,c}$ for larger grid sizes than 2 cm, the critical head H_c as calculated with the finest grid is reproduced using coarser grids by reducing $i_{tip,c}$. So the tip gradient over 5 cm is found by matching the critical head with the 2 cm grid simulation. This is repeated with 5, 10 and 20 cm grids, and the resulting critical gradients are given in Table 5.3.

Simulations are ran at five scales, represented by the seepage length L of 0.9, 3, 9, 30 and 90 m. The aquifer geometry is constant across scales: aquifer depth $D = L/3$, aquifer width $W = L$ and the distance between exit point and polder boundary equals $2\bar{D}$.

For each combination of scale and grain size, we first determine the critical head H_c using a simulation with gradually increasing head difference and instantaneous erosion (very high C_e). Then, we run time-dependent simulations (normal C_e) with different degrees of overloading. The applied constant head drop $H(t)$ equals $1.05 \cdot H_c$, $1.1 \cdot H_c$, $1.2 \cdot H_c$, $1.3 \cdot H_c$ and $1.4 \cdot H_c$.

The model grid is similar to the one used for simulating the small-scale experiments

Table 5.2: Sand characteristics used for simulation.

sand	d_{50} [mm]	C_u [-]	κ [m ²]	θ [°]
S2-2	0.200	2	$2.2 \cdot 10^{-11}$	30.4
S2-3	0.200	3	$9.7 \cdot 10^{-12}$	30.4
S3-2	0.300	2	$5.0 \cdot 10^{-11}$	27.1
S3-3	0.300	3	$2.2 \cdot 10^{-11}$	27.1
S4-2	0.400	2	$9.0 \cdot 10^{-11}$	24.8
S4-3	0.400	3	$3.9 \cdot 10^{-11}$	24.8

Table 5.3: Model settings and parameters used for simulation at different scales (L).

L [m]	pipe mesh [m]	soil mesh [m]	time step [s]	$i_{tip,c}$ [-]
0.9	0.02	0.05	10	0.7
3	0.02	0.2	10	0.7
9	0.1	0.5	200	0.2
30	0.1	2	200	0.2
90	0.2	5	500	0.15

(Fig. 5.4), but the vertical boundary at the polderside (downstream) is a constant head boundary with head equal to the exit point instead of a no-flow boundary. This is assumed to be a more realistic representation of field conditions. The soil and pipe grid sizes used for the analysis of the progression rates are indicated in Table 5.3, as well as the typical time step in these simulations.

So the main variations are: 5 scales (L), 6 sand types, 4 erosion coefficients (C_e) and 5 degrees of overloading (H/H_c). Not all 600 possible combinations have been simulated because of limitations in computational time, but a total of 74 (see Appendix D). For instance, other sands than S2-2 and variations in C_e were only simulated on the scales $L = 3$ and $L = 30$ m. The set of 74 includes 59 hole-exit simulations, 7 plane-exit simulations and 8 simulations for sensitivity analyses.

5

5.4.2 Results: critical conditions

First we discuss the computed critical head H_c as these results directly affect the computed temporal development of BEP. The critical head is computed by applying a stepwise increasing head difference and setting C_e to a sufficiently high value to yield an instantaneous response of the pipe depth to the applied head.

Equilibrium curve

First, we focus on the equilibrium curve: the equilibrium head H_{eq} as function of pipe length. For 3D hole-type configurations, H_{eq} initially increases with pipe length until the critical head H_c is reached (Fig. 5.7). After the critical point is reached, H_{eq} decreases but relatively little. For 3D plane-type configurations, which are strongly initiation-dominated and hence do not reach equilibrium once erosion starts, the computed H_{eq} decreases steadily with pipe length (Fig. 5.7). These trends were also observed in experiments by Van Beek [2015]. This can be explained by the concentration of groundwater flow to the pipe tip in the initiation stage and when the pipe grows towards the upstream side.

The finding for hole-type exits that H_{eq} decreases relatively little after the critical length is reached, has implications for the long-term development of pipes under multiple short flood events. Then, the strength (H_c) does not decrease much in each flood event, and the degradation over the years is mainly due to the decrease in the required time for the pipe to progress through the remaining soil.

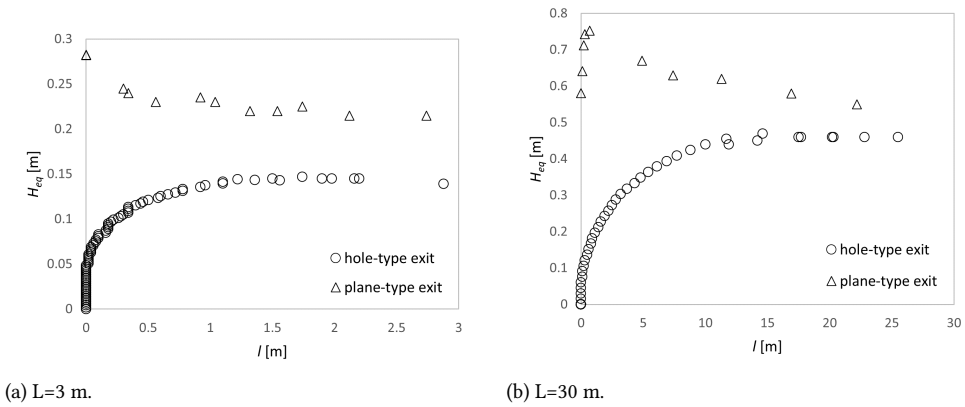


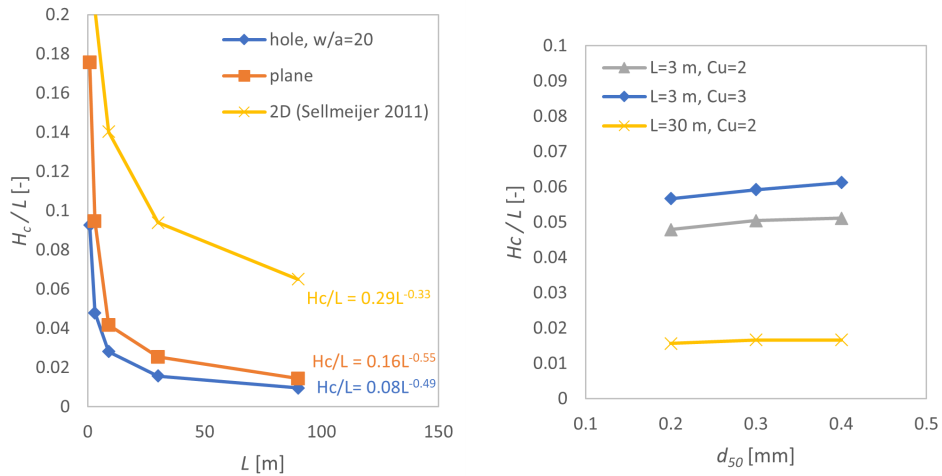
Figure 5.7: Equilibrium curve: equilibrium head drop H_{eq} as function of pipe length l . Results for S2-2 sand and $L = 3 - 30$ m modeled with adapted DgFlow model.

Critical head

Now, we focus on the critical head H_c and three factors of influence: scale, exit type and grain size (see Fig. 5.8). Coarser sand has a higher critical shear stress, but this is counteracted by a higher permeability. The net effect of grain size on the critical head appears to be small (Fig. 5.8b). Scale, here expressed in terms of the seepage length L , and exit type have a significant effect on the computed critical head as shown in Fig. 5.8a. The critical gradient H_c/L decreases with L , although the critical head H_c still increases with L .

The critical head in case of 3D flow towards a hole-type exit is lower compared to 2D flow with a plane-type exit or the critical head predicted by the 2D Sellmeijer model. This was also found experimentally by Vandenboer et al. [2018a] and Van Beek [2015]. Furthermore, the model results (using $w/a = 20$) show a different scale effect: $H_c/L \propto L^{-1/2}$ instead of $H_c/L \propto L^{-1/3}$ as obtained for 2D [Sellmeijer, 1988]. This results in even lower critical heads at large scales. Available hole-exit experiments at different scales show scale effects between $L^{-0.3}$ and $L^{-0.45}$ [Van Beek, 2015]. Additional experiments by Allan [2018] could not clearly confirm whether scaling follows $L^{-1/3}$ [Sellmeijer, 1988] or $L^{-0.2}$ [Schmertmann, 2000]. Despite the significant uncertainties, these experiments suggest somewhat lower scaling exponents than the $-1/2$ that results from DgFlow with $w/a = 20$. This can be obtained by modeling an increasing pipe resistance with scale (e.g., through w/a). For instance, in case of $w/a \propto L^{1/2}$ the simulated critical gradient scales as $H_c/L \propto L^{-0.4}$. Since the available experiments are insufficient for a validation of the predicted underlying processes such as head profile and pipe dimensions, and the cause of the additional resistance in the large-scale experiment (section 5.3.2) remains unclear, currently it remains uncertain which scale effect is correct.

Simulation of a plane-type exit yields a 50-100% higher critical head (strongly initiation-dominated) but a similar scale effect ($\propto L^{-0.55}$), see Fig. 5.8a. A theoretical scale effect of $L^{-0.5}$ for initiation was found by Bezuijen and Steedman [2010] and Van Beek [2015].



(a) Effect of scale and exit configuration for S2-2 sand ($d_{50} = 0.200$ mm). (b) Effect of grain size (hole exit, $w/a=20$).

Figure 5.8: Modelled critical head difference H_c .

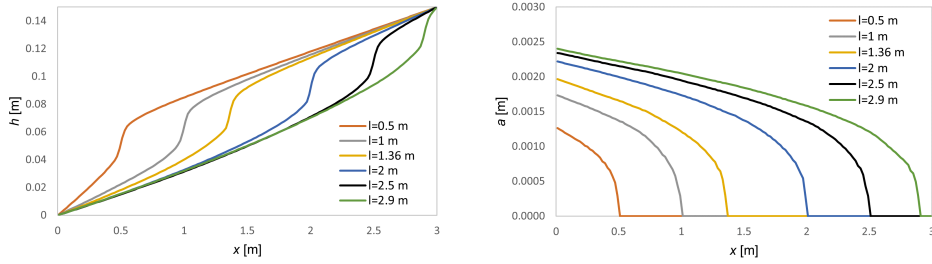
5.4.3 Results: pipe progression

The simulated head profile and pipe depth profile at different stages of the process under a constant head ($H/H_c = 1.1$) for a hole-type exit are shown in Fig. 5.9. Initially, the pipe is relatively shallow, which gives a high gradient in the pipe. When it gets longer, the pipe deepens gradually and the pipe gradient decreases. For larger pipe lengths, the deepening mainly takes place near the upstream end of the pipe. Here the inflow into the pipe is largest, which leads to the largest spatial gradient in sediment transport and hence most deepening. Fig. 5.10 shows the typical pipe length development over time under a constant head. In the initial erosion phase, the progression rate dl/dt is highest. Later, it decreases to a fairly constant rate. When the pipe length approaches the seepage length, there is some acceleration, which appears most clearly on smaller scales and with little overloading.

Average progression rates

The rest of this section focuses on the average progression rate in the part $L/2 < l < L$, which is approximately the progressive erosion phase ($l > l_c$). Three main factors of influence on the average progression rate are shown here: scale, grain size and degree of overloading. Additionally, we analyze the sensitivity of the progression rate for other factors such as the erosion coefficient C_e , exit type, the presence of local stronger layers, and model time step.

The results indicate that the progression rate increases with grain size and degree of overloading, and decreases with scale (Fig. 5.11). Simulated pipe progression rates at field scale (90 m) are almost an order of magnitude slower than on the laboratory scale (0.9 m). The increasing progression rate at higher degree of overloading is in qualitative agreement with findings by Allan [2018] and Vandenboer et al. [2019] but the magnitude



(a) Head profiles.

(b) Pipe depth profiles.

Figure 5.9: Modeled head and depth profiles at different pipe lengths, for $L = 3$ m, S2-2 sand ($d_{50} = 0.200$ mm), $H = 0.157$ m. $l = 1.36$ m is the critical length.

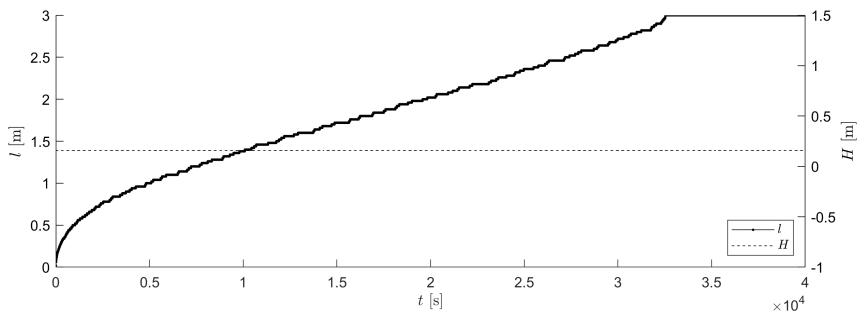
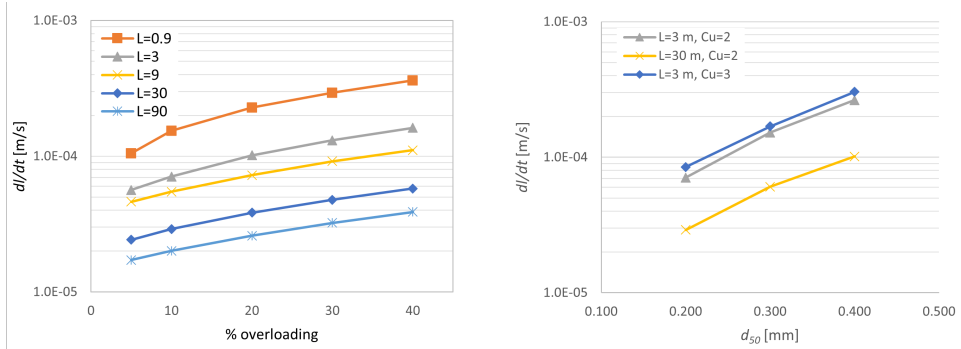


Figure 5.10: Modeled pipe length development, for $L = 3$ m, S2-2 sand ($d_{50} = 0.200$ mm), $H = 0.157$ m, $H_c = 0.143$ m.



(a) Effect of scale and overloading for S2-2 sand ($d_{50} = 0.200$ mm). (b) Effect of grain size for 10% overloading.

Figure 5.11: Average progression rate for the pipe length interval $L/2 < l < L$.

5

of the effect differs. The small-scale experiments ($L = 0.34$ m) by Vandenboer et al. [2019] show a factor 3 increase in progression rate for 40% overloading, the medium-scale ($L = 1.3$ m) experiments by Allan [2018] a factor 10, and our simulations show a factor 4 increase at the smallest scale ($L = 0.9$ m)

The influence of grain size and permeability, for $L = 3 - 30$ m and at 10% overloading, is shown in Fig 5.11b. Although the critical gradient is not strongly dependent on grain size (Fig. 5.8b), the progression rate is; so the progression rate cannot be explained solely by critical gradient.

Sensitivity for model assumptions

We investigated the sensitivity of the simulated average progression rate to several model assumptions, both physical (erosion coefficient) and numerical (time step).

The simulated progression rate relates linearly to the erosion coefficient C_e . Hence, uncertainties in C_e can be easily translated in terms of progression rate. This relation was observed for the hole-exit cases with $L=3$ m and 30 m, $d_{50}=0.200$ mm and 0.400 mm, all at 10% overloading.

Secondly, the influence of time step Δt was checked for the case with $L=3$ m, S2-2 sand and 10% overloading. For this case we find only a 2% increase in average progression rate when doubling the time step from $\Delta t = 5$ s to $\Delta t = 10$ s.

Finally, the sediment balance was checked by comparing the simulated increase in pipe volume per unit time (dV/dt) with the total sediment transport at the exit (Q_s). The difference between these terms was typically in the order of 10%, and are related to the sources of errors as mentioned in section 5.2.3.

To investigate potential effects of heterogeneity, we added a stronger sand barrier ($i_{tip,c} = 1.4$) in the pipe path at $2.8 < x < 3.2$ m. The progression rate at 10% overloading with barrier ($H=0.200$ m) is a factor two higher than without barrier ($H=0.157$ m), and equals the progression rate in a model without barrier loaded at $H=0.200$ m. So a locally stronger sand layer gives a higher critical head, but once exceeded this corresponds to an overloading situation with higher progression rate.

5.4.4 Simplified models for progression rates

Numerical models like the one developed in section 5.2.3 are impractical to apply directly in reliability analyses of levees because of the significant computation time (several hours). In order to translate the model results to explicit formulas which can be easily evaluated, we develop regression models for (1) the average progression rate in the progressive phase and (2) the instantaneous progression rate in both the regressive and progressive phases. The relations between the different regression models and the numerical simulations and experiments on which these are based, are shown in Fig. 5.12.

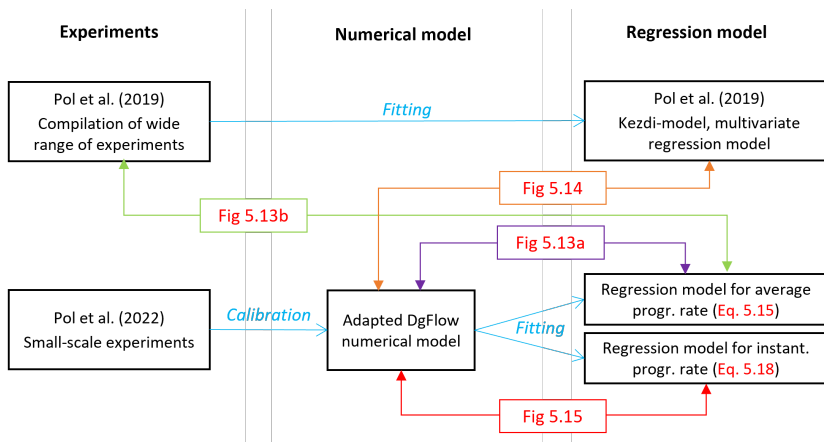


Figure 5.12: Relation between experiments, numerical simulations and regression models, including the figures in which these are compared.

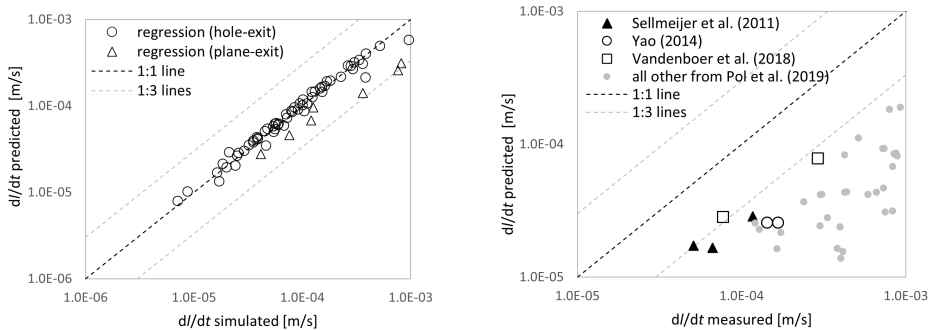
Average progression rate

For the average progression rate during the progressive phase, we fitted the following regression model on the 59 hole-exit simulations mentioned in section 5.4.1:

$$v_{c,avg} = 6.61 \cdot 10^4 \cdot C_e (d_{50})^{1.65} \left(\frac{H_c}{L} \right)^{0.89} \left(\frac{H}{H_c} - 1 \right)^{0.53} \quad (5.15)$$

This model is derived using 80% of the dataset; the other 20% is predicted with $R^2 = 0.97$. Given the underlying simulations, this equation applies to situations with localized out-flow (hole-exit), homogeneous aquifers with $D/L \approx 1/3$, $0.2 < d_{50} < 0.4$ mm and $2 < C_u < 3$, and up to 40% overloading ($H/H_c < 1.4$).

Figure 5.13a compares the simulated progression rate with the prediction by Eq. 5.15. The hole-exit configurations are predicted very well. Deviating configurations (plane-exit) are under-predicted by a factor 1.5-3, as these are more severely overloaded with respect to the equilibrium head H_{eq} . Figure 5.13b compares the measured progression rates in the set of experiments compiled in Pol et al. [2019] with the prediction by Eq. 5.15 using the calibrated $C_e = 0.016$. The small-scale homogeneous hole-exit experiments by Yao [2014] and Vandenboer et al. [2019], and the large-scale IJkdijk experiment by Sellmeijer et al. [2011] are most representative, as these are progression-dominated. Note that the



(a) Comparison with simulations in section 5.4.3.

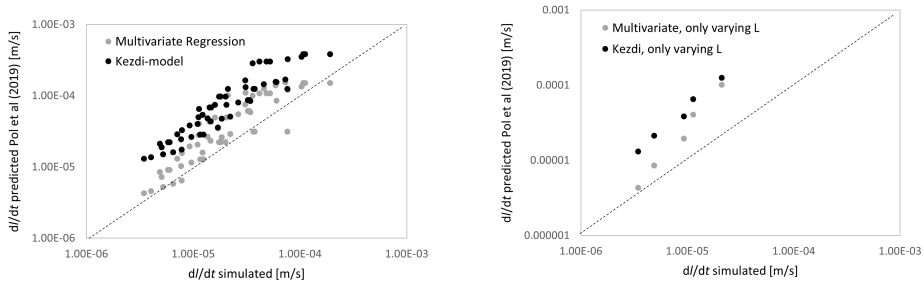
(b) Comparison with experiments compiled in Pol et al. [2019].

Figure 5.13: Predicted average progression rate with Eq. 5.15 compared to simulations (Fig. 5.13a) and experiments (Fig. 5.13b).

5

other experiments (plane-exit, cylindrical, multi-layer) are plotted for reference, but these are outside the conditions for which Eq. 5.15 was derived. The measured rates in the 7 progression-dominated tests are a factor 3-5 higher than predicted with Eq. 5.15 with $C_e = 0.016$ as found in our experiments. Hence, a higher C_e is required to reproduce the progression rate. The required C_e to predict those experiments and the selected small-scale and large-scale tests from this thesis, can be described by a lognormal distribution with mean of 0.044 and standard deviation of 0.048. This distribution is used in the reliability analysis of chapter 6. Later, it was investigated how the distribution changes when all experiments from chapter 3 and 4 are added to this comparison and how that affects the reliability analyses (Appendix E). That changes the mean to 0.055 and the standard deviation to 0.043. Although this updated distribution is considered more representative, the reliability analyses in chapter 6 are based on the original distribution because it has no major impact on the results.

Pol et al. [2019] fitted two empirical models on a set of average progression rates in small-, medium- and large-scale experiments with different configurations (hole, plane, slope and multi-layer). Although three large-scale ($L = 15$ m) tests are included, this set still lacks sufficient experiments on field scale. Hence, extrapolation to field scale remains uncertain. Therefore, we compare the two empirical models to the numerical simulations, with special focus on the effect of scale. Figure 5.14a compares the progression rate of all hole-exit cases using the calibrated $C_e = 0.016$ with the rates predicted by those two empirical models. The multivariate model gives on average similar progression rates compared to the numerical simulations. However, in the lower range (often larger scale) the multivariate model gives lower progression rates. The Kézdi model gives a factor 3-4 higher progression rates compared to the simulations. As this point cloud of simulations on a wide range of scales lies approximately parallel to the 1:1 line (Fig. 5.14b), this supports the conclusion that effects of scale in the Kézdi-model correspond better to the numerical simulations than those effects in the multivariate model.



(a) All simulated hole-exit cases.

(b) Cases where only L varies (S2-2 sand, 5% overloading).

Figure 5.14: Average progression rate of numerical simulations compared with the prediction by the two empirical models (Multivariate Regression, Kézdi-model) in Pol et al. [2019].

Instantaneous progression rate

Although the simulated progression rate for hole-exits under a constant head is rather constant, it can be higher during the beginning of the regressive phase. This section seeks to find a more generalized prediction model that includes both the progressive and regressive phase, and also covers both progression-dominated and initiation-dominated cases (i.e. hole and plane exits). Similar to the average progression rates (Eq. 5.15), we relate the instantaneous progression rate $v(t)$ to the erosion coefficient C_e , grain size d_{50} , average gradient $H(t)/L$ and overloading $H(t)/H_{eq}(t)$. Note that overloading is here defined with respect to H_{eq} and not to H_c . To obtain $v(t)$ and $H_{eq}(t)$, we divided the seepage length in 100 equal segments with position l . For each segment, we determine when the pipe tip passes the segment in the time-dependent simulation and the corresponding progression rate $v(l)$. From the equilibrium curve, we obtain $H_{eq}(l)$.

We included the following cases for which we derived an equilibrium curve: S22 sand with hole and plane exit and seepage lengths of 3 and 30 m; and S42 sand with hole exit and seepage lengths of 3 and 30 m. It appeared that the hole and plane configurations show different trends, and could not be fully represented in one simple regression model. The main difference is that the progression rate in the plane simulations remains rather constant with increasing pipe length, while the overloading (H/H_{eq}) increases. Therefore we fit the regression model only on the hole configurations, and show how that model predicts the plane simulations.

If we assume the same form as the regression model for the average progression rate (Eq. 5.15), we obtain:

$$v(t) = 1.3 \cdot 10^5 \cdot C_e \cdot (d_{50})^{1.65} \left(\frac{H_{eq}(t)}{L} \right)^{0.87} \left(\frac{H(t)}{H_{eq}(t)} - 1 \right)^{0.84} \quad (5.16)$$

The exponents are similar to those in Eq. 5.15, only the influence of overloading is slightly

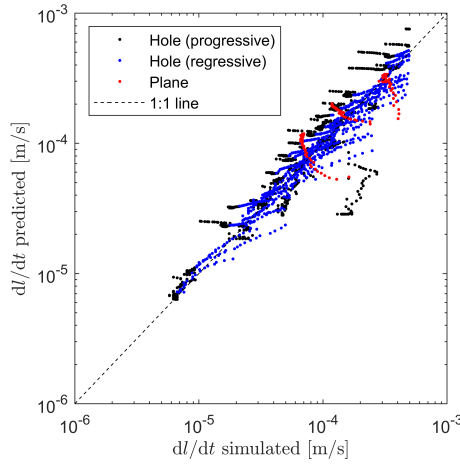


Figure 5.15: Instantaneous progression rate in simulations compared with the prediction of Eq. 5.18.

5

larger. Due the similarity of the exponents 0.87 and 0.84, this can be simplified to:

$$v(t) = 1.3 \cdot 10^5 \cdot C_e \cdot (d_{50})^{1.65} \left(\frac{H(t) - H_{eq}(t)}{L} \right)^{0.85} \quad (5.17)$$

Also this model is derived using 80% of the dataset; the other 20% is predicted with $R^2 = 0.94$. The equation can also be derived using k instead of d_{50} . This gives an equations similar to Kézdi [1979], but extended with an overloading term and an exponent on the seepage velocity:

$$v(t) = 89 \cdot C_e \left(k \frac{H(t) - H_{eq}(t)}{L} \right)^{0.81} \quad (5.18)$$

This equation has the same performance ($R^2=0.94$) and gives virtually the same result for the tested simulations. Additional simulations with varying combinations of k and d_{50} are needed to conclude which is a better predictor. Figure 5.15 visualizes how Eq. 5.18 compares to the simulated progression rates. The regressive phase of the hole-exits, on which Eq. 5.18 is derived, agrees well as expected. The plane-exit simulations and the progressive phase of the hole-exit simulations show some more deviation but the order of magnitude is still captured. Eq. 5.18 is also applied in the reliability analyses in chapter 6.

5.5 Discussion and Conclusions

5.5.1 Discussion

This discussion focuses on three aspects of the numerical model: (1) the model's advancements compared to current engineering models, (2) model limitations, (3) differences between the model and field conditions.

For the comparison with engineering models, we focus here on the model by Sellmeijer et al. [2011] which is used in routine safety assessments and design of levees in

the Netherlands. The FEM implementation in DgFlow provides much more freedom in analyzing deviating aquifer characteristics, groundwater boundary conditions, and in particular the step to a 3D domain. Furthermore, the model of Sellmeijer et al. [2011] does not include a primary erosion criterion and the critical bed shear stress τ_c from White [1940] was modified in the 2011 re-calibration with small-scale experiments. In the FEM model we used a different τ_c formulation by Van Beek [2015] which corresponds better to experiments. Finally, the main advancement of this work is the time-dependent secondary erosion formulation which allows to simulation the rate of pipe progression.

A first limitation of the model is that the pipe is represented as a straight rectangular channel, while lens formation, channel shape and channel meandering will affect both the predicted critical head and the progression rate. Secondly, the numerical formulation introduces two errors in the sediment balance (section 5.2.3). These errors are limited but can be reduced by an improved numerical implementation. Finally, a general limitation of any BEP model is the uncertainty around the translation from small to large scales and the lack of multi-scale experiments with detailed measurements of the pipe flow and geometry. The importance of these scale effects is illustrated by the difference in scale effect between 2D and 3D simulations (Fig. 5.8a), and the fact that prediction of H_c for the large-scale experiment proved difficult when using the a priori estimate of $w/a = 20$ (Fig. 5.6a). The very low critical head that is obtained with the 3D model for field scale situations (Fig. 5.8a) seems unrealistic based on the past performance of levees. Therefore this modeled scale effect requires further analysis, in particular into the effect of using 1D line elements to model the pipe [Robbins et al., 2022] combined with the element size on different scales.

Field conditions can deviate in several aspects from the simulations performed in this chapter, and hence result in different behavior. For instance, soil heterogeneity causes pipes to meander and form multiple branches when searching for the weakest path [Kanning, 2012]. This has different effects on the rate of pipe progression. Meandering pipes result in more head drop in the pipe [Wewer et al., 2021]. Furthermore, the development of multiple or meandering pipe branches requires more sediment to be transported which will reduce the progression rate. On the other hand, a locally higher erosion resistance along the pipe path may result in a higher progression rate once this local barrier is exceeded (like overloading).

Furthermore, some aquifer properties such as depth/width/length ratio and leakage length were not varied and are not explicitly included in the regression functions. The $D/W/L$ ratio of the simulations in section 5.4.1 was kept constant at 1/3/3. Leakage only varies between the plane and hole exits, both allowing flow to the polder. Hence, the regression functions may be less accurate in case of strongly deviating conditions such as very narrow aquifers or a seepage block on the polder side. Although not incorporated in the regression functions, the model on which the regression is based can be easily adapted to incorporate leakage length and aquifer shape.

5.5.2 Conclusions

This chapter develops a numerical model to simulate time-dependent development of backward erosion piping in a 3-dimensional domain. This model is based on the DgFlow numerical equilibrium model [van Esch, 2015; van Esch et al., 2013] which includes simulation of piping in a 3D-domain and with both a primary and secondary erosion criterion. We

added a sediment transport formulation for secondary erosion (pipe deepening), instead of the search for an equilibrium depth as in van Esch et al. [2013]. In this way, the time required for pipe deepening limits the rate of pipe progression, and hence introduces the time-dependence in the backward erosion process. First, the model was tested on small-scale and large-scale experiments. Second, in a parametric study a variety of situations were simulated to explore how the critical head and pipe progression rate depends on grain size, scale and degree of overloading. Finally, we fit a simple regression formula for the average progression rate as function of the above-mentioned factors.

With respect to the predicted critical head, we draw the following conclusions. The model was calibrated on the critical head profile in the small-scale experiments, by calibrating three input parameters which are also measured (η , w/a , $i_{tip,c}$). The model can reproduce the critical head profile including critical pipe length reasonably well, and calibrated values closely match the measured ones, which gives confidence in the model performance on this scale. In the large-scale experiment, the input parameter w/a (pipe width to depth ratio) could not be measured accurately. Using $w/a = 20$ (as measured on small scale), the critical head of the large-scale test is significantly under-predicted. A much higher flow resistance is required to reproduce the measured critical head profile, e.g. by using $w/a = 700$. Although we identified potential causes of this difference (meandering, lens formation, lower permeability), a full explanation is still lacking, and further study is required due to its implications for predicting BEP on larger scales.

An important question for practical application is the scale effect: how does the critical gradient H_c/L depend on scale (e.g. seepage length L). According to the 2D analysis by Sellmeijer [1988] and 2D simulations with D-GeoFlow [Pol, 2020], this scales as $H_c/L \propto L^{-1/3}$. A 3D analysis without primary erosion [Van Beek et al., 2022] indicated a scaling of $H_c/L \propto L^{-1/4}$. In this study we found a scaling of $H_c/L \propto L^{-1/2}$ for 3-dimensional domains (both with hole-exit and plane-exit) assuming a scale-independent pipe geometry (w/a ratio). At small scale, 3D experiments and simulations already give a lower critical head compared to the current 2D prediction by Sellmeijer et al. [2011]. With a stronger scale effect, this difference between 2D and 3D increases even more at larger scale (field scale). However, this result depends on the assumed constant w/a ratio, which may need to be higher at larger scales. Hence it is essential to better understand the processes behind this scale effect and verify predictions with multi-scale experiments.

With respect to the predicted pipe length development over time, we conclude the following. The developed model can reproduce the measured pipe length development reasonably well when the erosion coefficient C_e is calibrated. Calibration of the small-scale and large-scale experiments yields consistent values of 0.016 and 0.014, respectively. This is a factor 25 lower than the average value of 0.39 from rectangular flume experiments and a factor 5 lower than the 0.08 estimated from the small-scale experiments. It may be partly explained by the simplification of the pipe as straight rectangular channel in the model, which underestimates the volume of sediment to be transported. However, we recognize that much is still unknown about the details of the erosion process in BEP and C_e partly functions as calibration factor. When also measured progression rates from additional experiments [Sellmeijer et al., 2011; Vandenboer et al., 2019; Yao, 2014] and all experiments from chapter 3 and 4 are considered, C_e can be described by a lognormal distribution with mean of 0.055 and standard deviation of 0.043.

The results indicate that the average progression rate, after exceeding the critical pipe length, increases with grain size and degree of overloading and decreases with scale, which is consistent with experimental observations. For practical applications, the simulated average and instantaneous progression rates have been simplified to regression functions of grain size, critical gradient and degree of overloading (Eqs. 5.15 and 5.18). These regression functions are suitable to predict the progression rate in case of hole-type exits (concentrated outflow) but can also provide an order of magnitude for plane configurations. The functions are not derived for cases with heterogeneous aquifers or levees with structural elements. Furthermore, the computed progression rates can be used to inform emergency interventions about the order of magnitude of the time to breaching, but it should be recognized that local factors and anomalies can lead to strongly different breaching times for a specific location.

Although the simulated small-scale experiments can be predicted well by the model, we recommend to validate the model more thoroughly on a larger set of experiments, especially those on larger scales and with measurements of the pipe geometry. Secondly, to make the derived simplified models for average and instantaneous progression rate more robust, these can be based on a more diverse set of simulations.



6

Time-dependent Levee Reliability with Cumulative Piping Erosion

One doesn't have to understand the details of a key parameter in a problem to make use of it.

John Schmertmann

6

Abstract

Chapters 3, 4 and 5 describe the time scales of the backward erosion process using experiments and numerical modeling. This chapter quantifies how this time-dependence affects the failure probability of levees. Therefore this chapter develops a time-dependent piping failure model including effects of a varying water level, blanket uplift, heave, backward erosion and flood fighting interventions. Next, this model is included in a time-variant reliability analyses which quantifies how the reliability evolves over the years due to cumulative pipe growth over multiple flood events and strength recovery between flood events. Analysis results indicate the importance of the characteristic flood duration (which differs between type of water system). The coastal cases show large reductions in failure probability, ranging from a factor 10 to more than 10^6 for large seepage lengths and fine sand. Reductions are smaller for the river cases, but can still be considerable (factor 100-1000) for particular cases. For rivers (with long flood duration), the effectiveness of flood fighting is important. The reliability analysis shows that a relatively short pipe (i.e. much shorter than the critical pipe length) that formed during past events does not have a significant impact on the reliability. Based on the results it is concluded that a considerable part of the Dutch levees can benefit from including time-dependent pipe development in the BEP failure model and reliability analysis, and thereby contribute to avoiding or postponing unnecessary reinforcements.

6.1 Introduction

This chapter focuses on the translation of the results from the experiments and numerical modeling to an estimate of the levee reliability or failure probability. First the piping failure process and available piping reliability analyses are discussed in sections 6.1.1 and 6.1.2.

6.1.1 Backward erosion piping failure process

Levee failures are frequently attributed to piping, see for example the cases listed in Table 2.2. The failure mechanism of piping can be described by a series of processes, as illustrated in Fig. 6.1 and 6.2. A more extensive treatment of the mechanisms is found in Rice et al. [2021] or ICOLD [2017]. The description in Fig. 6.1 is similar to a failure path [Van et al., 2022], but in this figure the processes are not defined as discrete events.

As the water level rises, pore pressures in the aquifer increase. Excess pressures behind the levee can lead to uplift and rupture of the blanket, creating an exit point. Depending on the excess pressure, sand can be transported through the vertical crack (this is often called heave in the Netherlands). The transported sand creates a void (pipe) which develops backward, in the direction of the river. When the pipe reaches the river, the flow increases and pipe cross section enlarges (also called widening). When the pipe become sufficiently large it leads to instability and collapse of the levee, by gradual crest level decrease or slope failure. The erosion process stops when successful flood fighting interventions are employed (e.g., sand bags to reduce the hydraulic head) or when the water level decreases sufficiently. For a further description of the erosion process and available prediction models we refer to chapter 2.

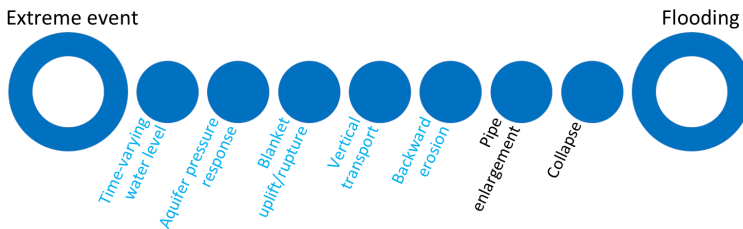


Figure 6.1: Main physical processes involved with failure due to backward erosion piping. This chapter includes the processes with blue labels, and also flood fighting interventions.

Effects of time-dependency are present in most parts of the failure process. The three main factors are identified as: (1) the time-dependent development of the hydraulic load, (2) the time-dependent response of aquifer pressures to this load and associated effects on blanket uplift, and (3) time-dependent pipe development. Most current prediction models assume a constant water level, steady state groundwater flow and instantaneous pipe progression once a critical condition is exceeded. There are practical methods to include transient groundwater flow [Barends, 1982; Ozkan et al., 2008; TAW, 2004], but only as far as it affects the safety against blanket uplift, not integrated with backward erosion. This chapter does not consider transient groundwater flow, although it can have a significant impact on reliability in particular situations. The focus of this chapter is on the interaction

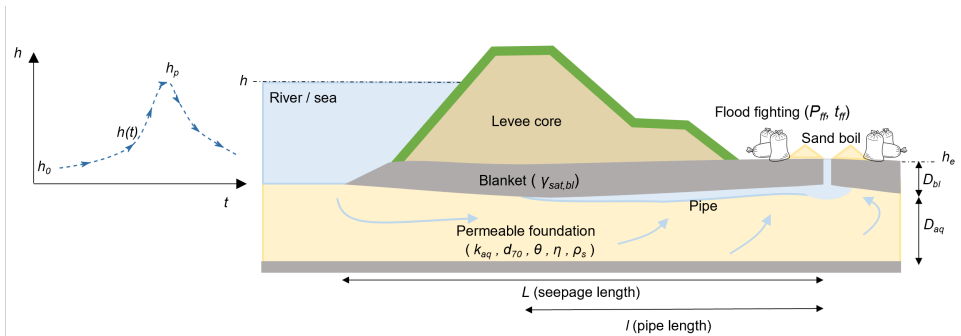


Figure 6.2: Illustration of backward erosion piping in a levee on a sandy foundation and definition of variables used in the analysis.

between factors 1 and 3: if the pipe develops relatively slowly compared to flood duration, water levels may recede before the pipe has fully developed and no failure occurs during a flood.

Besides these time-dependent processes within an event, time-dependence also appears in long-term development of the reliability (i.e. multiple years). If pipes develop only partially during an event, this creates a different situation during the next high water compared to the original situation. A partially present pipe prior to a new flood means that less time is required for pipe progression through the foundation. Hence, the resistance against piping may decrease over the years. However, this may be compensated by a recovery of the pipe resistance in the period between flood events (see section 4.4.4 for a recovery experiment).

6.1.2 Time-variant piping reliability analysis of flood defenses

Reliability analysis is a process to determine the safety level of a structure [e.g., Baecher and Christian, 2005; Melchers and Beck, 2017b]. In the context of flood defenses, this means determining the probability of failure (flooding). In general this includes the definition of a failure limit state function (LSF) and failure model, defining statistical distributions for the model inputs such as soil properties, and performing the actual computation with a suitable probabilistic method. Several time-invariant examples of piping reliability analyses are described in the literature [e.g., Calle et al., 1985; Rice and Polanco, 2012; Vrijling, 2001; Wolff, 2008]. Studying the time scale of the BEP erosion process was already recommended in early works [Calle et al., 1985] but this aspect has received little attention so far. A few works describe a reliability method where BEP is represented as a time-dependent process and are discussed below.

Buijs et al. [2009] provide an approach for analyzing time-dependent flood defense reliability over the structure's lifetime, including an example for piping. They model the evolution of degrading parameters using stochastic (Gamma) processes and using a partly physics-based (hierarchical) process model where the seepage length reduces based on the applied water level. This physics-based model is equivalent to the model of Kézdi [1979] except that porosity is not included. The chosen parameter distributions are given in Buijs

[2008]. Subsequently, the degrading seepage length $L(t)$ is used in the Sellmeijer model to obtain a degrading critical head $H_c(t)$. Modeling deterioration of piping resistance with stochastic processes has several problems. First, the pipe length development is hard to observe, hence the stochastic process parameters cannot be determined. So one needs to rely on a physics-based model instead. Second, the pipe length development is likely not independent between years, but could accelerate.

Vorogushyn et al. [2009] developed levee fragility curves for piping and micro-instability, which describe the failure probability conditional on the hydraulic load (peak and duration). In their physics-based analysis, piping failure is a combination of four processes: transient seepage, blanket uplift, exceedance of a critical head for backward erosion, and the pipe length reaching the outer water side. Although at that time hardly any information on the rate of pipe length development was available, they included also this process in the analysis. The limit state of the critical pipe length is defined as the difference between seepage length (levee base width) and pipe length: $L - l$. They assumed a deterministic progression rate $v = \frac{dl}{dt}$ of 0.158 m per hour ($4.4 \cdot 10^{-5}$ m/s) based on a Deltaflume experiment [Weijers and Sellmeijer, 1993]. The authors stress that more research is needed to quantify this progression rate (effect of sand properties and load) as it has a large effect on the computed failure probability of piping. From the description in the paper, it seems that a time-varying water level is not included in the analysis of pipe progression. The study does not analyze the long-term reliability under multiple storm events.

Chen and Mehrabani [2019] describe a method for time-dependent reliability of coastal flood defenses, and include piping degradation over time in their analysis through seepage length reduction. They apply a semi-Markov deterioration modeling approach. Here the levee can have discrete states (condition grades), and the transition probabilities from state i to j depend on the time that the levee has been in state i . The approach of a seepage length reduction which modifies Sellmeijer's prediction for the critical head, is similar to Buijs et al. [2009]. The difference is that Chen and Mehrabani [2019] assume certain degrees of seepage length reduction given a levee condition grade (based on expert judgment or inspections). Hence, the method is less suitable for a more physics-based description of pipe length development (as function of hydraulic loads and subsoil characteristics).

To summarize, Buijs et al. [2009] and Chen and Mehrabani [2019] focused on the long-term development (lifetime) while Vorogushyn et al. [2009] only included the pipe development within an extreme event. On the other hand, the pipe development in Vorogushyn et al. [2009] is more physics-based. Given the advancements in the time-dependent development of BEP described in this thesis, there are some potential improvements of the above-mentioned three works, in particular in the physics-based description of the BEP failure process.

- include a varying water level within a storm event, instead of a block shape as used in Buijs et al. [2009] and Chen and Mehrabani [2019].
- base the progression rate on physical experiments and numerical modeling, and allow the progression rate to vary within a storm event.
- include a threshold, e.g the equilibrium head $H_{eq}(l)$, below which no backward erosion occurs as the grains on the pipe bed are in equilibrium.
- include blanket uplift, heave (sand transport through vertical crack) and flood fight-

ing interventions, including their timing within an event, as conditions which limit the time available for pipe growth.

- define failure as a pipe progressing entirely through the levee foundation, instead of the head exceeding the critical head.

6.1.3 Objectives and approach

Considering the above-mentioned delay in piping failure due to the time required for pipe erosion from initiation to failure, the objective of this chapter is to quantify how this time-dependence affects the reliability of levees compared to an analysis in which piping is considered as instantaneous failure process. Therefore, a piping failure model is developed which describes the relevant processes (uplift, heave, backward erosion, flood fighting) in an integrated manner, and this model is integrated in a time-variant reliability method. The analyses focus on the contribution of time-dependent erosion to the reliability, and how this depends on the characteristics of hydraulic loads, levee, subsoil and operational aspects.

6.2 Time-variant reliability analysis method for piping

This section explains the methods used in this chapter to analyze the time-variant reliability of levees with respect to the failure mechanism backward erosion piping. This includes both the models which describe pipe development (section 6.2.2) and the probabilistic methods (section 6.2.3).

6.2.1 Piping reliability formulation

General reliability formulation

Levee reliability is defined as the probability that a levee fulfills its function (i.e. non-failure) in a given period of time. Failure is governed by a combination of variables which can be described by time-invariant random variables and time-variant ones (stochastic processes). In case of levees, piping failure is caused by extreme high water levels (hydraulic load) from storms or river floods which lead to strength degradation by increasing the eroded pipe length if a critical water level is exceeded (Fig. 6.3). The time-dependent

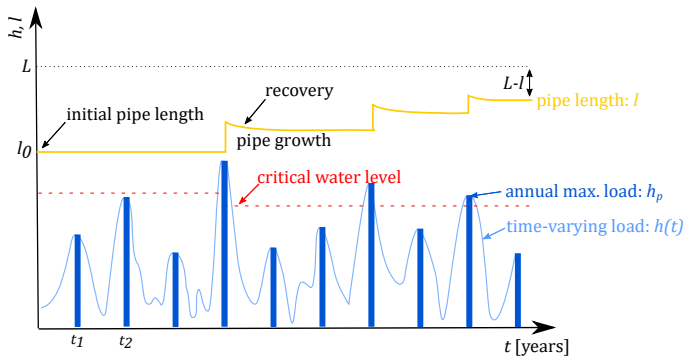


Figure 6.3: Illustration of time-dependent pipe length development over a 10-year period.

reliability problem can be formulated as [e.g., Melchers and Beck, 2017b]:

$$P_f(t) = P(g(\mathbf{X}(t)) \leq 0) = \int_{g(\mathbf{X}(t)) \leq 0} f_{\mathbf{X}(t)}(\mathbf{x}(t)) \cdot d\mathbf{x}(t) \quad (6.1)$$

where P_f denotes the probability of being in the failed state in year t , \mathbf{X} is a vector of random variables, $g(\cdot)$ the limit state function and $f_{\mathbf{X}(t)}(\mathbf{x}(t))$ the joint probability density of the random variables. The reliability index β is defined as: $P_f(t) = \Phi(-\beta(t))$, where Φ is the standard normal distribution.

The probability in Eq. 6.1 can be interpreted as cumulative or lifetime failure probability, i.e. the probability of failure between the start of the analysis and year t . The probability of failure occurring in year t is given by $dP_f(t)/dt$. The conditional failure rate $\lambda(t)$ (also called hazard function) is the probability of failure occurring in year t given no failure occurred in the previous years. It can be computed from Eq. 6.1 by [JCSS, 2001]:

$$\lambda(t) = \frac{dP_f(t)/dt}{1 - P_f(t)} \quad (6.2)$$

Both the cumulative probability and the conditional failure rate are presented in the analyses in this chapter.

Classical approaches to solve this reliability problem are sampling based methods such as Monte Carlo Simulation (MCS) [Rubinstein and Kroese, 2008] and approximation methods such as the first-order reliability method (FORM) [Hasofer and Lind, 1974].

6

Limit state function for piping

Assuming failure when a hydraulic shortcut has formed through the levee foundation, the limit state function (LSF) for backward erosion piping can be formulated as the difference between seepage length L and pipe length l [Vorogushyn et al., 2009]. Here we use the pipe length at the end of a flood event l_e to define failure:

$$g(\mathbf{X}) = L - l_e \quad (6.3)$$

and Eq. 6.1 can be rewritten as:

$$P_f(t) = P(l_e(t) \geq L) \quad (6.4)$$

Although this LSF is very simple, the challenge is to determine the pipe length at the end of a flood event or year, $l_e(t)$. This parameter is a function of many other parameters with different statistical characteristics, for example initial pipe length, hydraulic loads (peak level & duration), time-invariant levee properties and flood fighting interventions. Section 6.2.2 describes the pipe progression model used for computing l_e .

Uncertainties in BEP & implications for reliability

The piping erosion process is driven by extreme high water levels, in combination with levee properties governing the levee resistance against these loads, and sometimes human

actions such as flood fighting interventions. Here we first discuss the statistical characteristics of the different random variables that govern BEP and their implications for the reliability analysis method.

Commonly, two main types of uncertainties are distinguished [Paté-Cornell, 1996; Slijkuis et al., 1999]: (1) aleatory or inherent uncertainty representing random variations in time (or space) and (2) epistemic uncertainty representing a lack of knowledge or data. The difference between those types is relevant for time-variant reliability because it affects the correlation between the structural performance over time [Kiureghian and Ditlevsen, 2009]. For piping reliability, hydraulic loads such as maximum water levels can be considered aleatory uncertainty and independent between years (each year this variable has a new value). Levee properties and model parameters are classified as epistemic and fully dependent between years (each year this variable has the same value). Uncertainties in successful flood fighting may contain both types of uncertainty and are partly dependent between years. Due to this dependence, the structural performance $g(\mathbf{X})$ in year t and $t+1$ is also correlated. The pipe length is not an input variable but is derived from the input variables, hence it is affected by both types of uncertainties.

From a reliability point of view, piping erosion is further characterized by:

- a deterioration process, of which the rate of deterioration is given by the pipe progression rate v which depends on the hydraulic loads, strength properties (L , d_{50} , ...) and on previous pipe growth.
- levee properties and flood fighting interventions are considered constant over time but affect the pipe progression rate.
- extreme loads (yearly max. magnitude, duration) occur independently from both the levee properties and the previous pipe growth.
- extreme loads are uncorrelated in time if assessed with sufficiently large time interval (years).
- loads may change over time due to stresses like sea level rise or changing river discharges.
- levee safety standards require small failure probabilities (10^{-2} to 10^{-6} per year for segments, even higher for individual sections)

Hence, the probabilistic method must to be able to describe the dependencies in time and still be suitable for small probabilities (efficient).

6.2.2 Pipe progression model

The pipe progression model predicts the temporal development of pipe length l under a given hydraulic load event and consists of physical processes (blanket uplift, pipe erosion) and human actions (flood fighting). In this chapter, pipe progression is described by the instantaneous progression rate $v(t)$ as derived from model simulations in chapter 5 (Eq. 5.18) but only if a set of conditions (I_{er}) is satisfied which are specified below:

$$v(t) = \frac{dl}{dt} = \begin{cases} 89 \cdot C_e \left(k \frac{H(t) - H_{eq}(t)}{L} \right)^{0.81} & \text{if } I_{er} = \text{true} \\ 0 & \text{else} \end{cases} \quad (6.5)$$

Here C_e denotes an erosion coefficient [-], k hydraulic conductivity [m/s], H imposed head difference [m], H_{eq} equilibrium head [m] and L seepage length [m]. Note that here

t describes the time within a flood event, so on much shorter time scales than in section 6.2.3 where t is expressed in years. The imposed head difference is reduced by a head loss over the blanket (vertical pipe) due to resistance of the fluidized sediment: $H = h - h_e - 0.3D_{bl}$, where h is outer water level, h_e polder level at the exit point and D_{bl} polder blanket thickness.

The required conditions are that: (1) blanket uplift has occurred previously, either in the current event or in past events; (2) heave is possible at the current time step; (3) flood fighting interventions have not been taken (yet) at the current time step. These conditions are expressed in I_{er} as:

$$I_{er}(t) = \left(\min_{0 \dots t} \{Z_u(t)\} < 0 \cup l_{ini} > 0 \right) \cap (Z_h(t) < 0) \cap (t < t_{uh} + (t_{ff}/I_{ff})) \quad (6.6)$$

where l_{ini} is the initial pipe length at the start of the flood event, t_{uh} is the first time that uplift and heave and erosion ($H > H_{eq}$) occur within the flood event (proxy for sand boil formation), t_{ff} is the time required for successful flood fighting and I_{ff} is an indicator which is 1 in case of successful flood fighting and 0 otherwise. The limit states for uplift (Z_u) and heave (Z_h) are given by:

$$Z_u(t) = (\varphi_{it}(t) - h_e) - D_{bl} \cdot (\gamma_{bl,sat} - \gamma_w) / \gamma_w \quad (6.7)$$

$$Z_h(t) = (\varphi_{it}(t) - h_e) / D_{bl} - i_{c,h} \quad (6.8)$$

$$\varphi_{it}(t) = h_e + r_e \cdot (h(t) - h_e) \quad (6.9)$$

where φ_{it} [m] denotes the aquifer head at the inner levee toe, r_e the head response factor to an increase in water level, $\gamma_{bl,sat}$ saturated blanket weight [kN/m^3], γ_w water weight [kN/m^3] and $i_{c,h}$ the critical heave gradient [-].

Flood fighting interventions are included in the model (Eq. 6.6) in two ways: by the probability of a successful detection (through I_{ff}) and by the time required for successful flood fighting (t_{ff}). In case of failed detection, $I_{ff} = 0$ so $t_{ff}/I_{ff} = \infty$. The time for successful flood fighting is a lumped parameter for all actions since the moment of sand boil formation (initiation), and includes required time for detection, mobilization, and placement. The method assumes binary intervention effects: successful (i.e. completely stops piping) or unsuccessful.

The progression rate $v(t)$ depends on constant levee properties (e.g., C_e , k , d_{70} , L) and time-varying variables (H , H_{eq} and l). The equilibrium curve $H_{eq}(l)$ (see Fig. 2.2 and 5.7) is defined by the following three points, between which we apply linear interpolation:

$$\begin{aligned} H_{eq}(0) &= 0 \\ H_{eq}(l_c) &= H_{c,p} \\ H_{eq}(L) &= 0.9H_{c,p} \end{aligned} \quad (6.10)$$

Here $H_{c,p}$ and l_c are the critical head and critical pipe length for backward erosion, respectively. The linear interpolation to the points (0,0) and $(L, 0.9H_{c,p})$ is a conservative estimate based on the modeled equilibrium curves in Fig. 5.7. We use the critical head $H_{c,p}$ for backward erosion as given by Sellmeijer et al. [2011], see:

$$H_{c,p} = L \cdot F_r \cdot F_s \cdot F_g \quad (6.11)$$

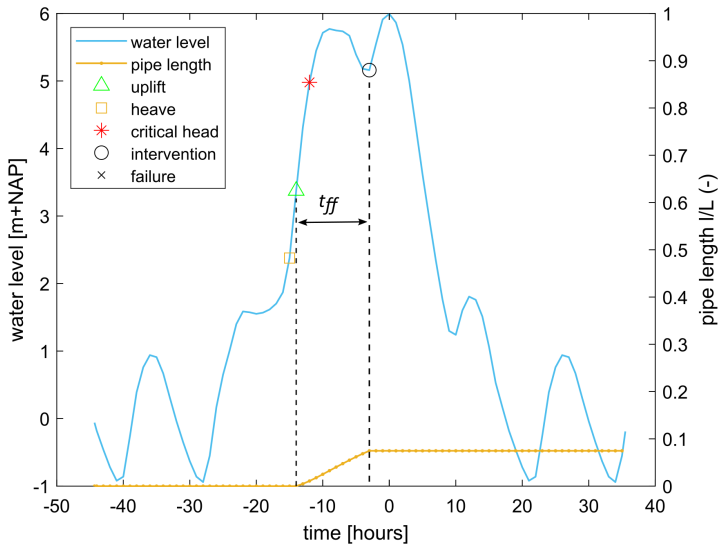


Figure 6.4: Example of pipe development for coastal levee. One realization of the base case as described in section 6.3.1 with $D_p=4$ h, $h_p=6$ m+NAP and $l_{mi}=0$.

in which F_r , F_s and F_g are given in Eq. 2.7. The following function is proposed for the critical pipe length of backward erosion l_c in case of homogeneous aquifers, which agrees with 2D numerical model simulations from DgFlow [Rosenbrand et al., 2022] and MSeep [Sellmeijer, 2006]:

$$\frac{l_c}{L} = \frac{1}{2} \cdot \tanh\left(2\frac{D}{L}\right) \quad (6.12)$$

The set equations 6.5-6.12 provides the pipe growth model. Figure 6.4 shows an example of the pipe length development during a storm surge for a particular case. Pipe growth starts when uplift and heave have occurred, and continues until a flood fighting intervention stops it after some hours (t_{ff}). In this case, no failure occurs as in the end of the event $l/L \approx 0.1 < 1$. In this case the critical water level is approx. 5 m+NAP. Although this level is exceeded by one meter, it is too short to result in failure.

6.2.3 Probabilistic method

To obtain a probabilistic method which describe the dependencies in time and still is efficient, this section describes the modeling of the hydraulic loads and two methods to evaluate the piping failure probability (Eq. 6.4).

Hydraulic loads

The modeling of the hydraulic loads plays a role in each method. Basically, the load (water level) is a stochastic process. In both methods A and B, the variability in water level is simplified. As the piping erosion process is driven by extreme water levels and the probability of multiple independent extreme events in a year is assumed to be negligible,

only the yearly maximum event is considered. The water level variability is simplified to an extreme value distribution of the yearly maximum water level h_p . Hence the time step Δt in the time-dependent reliability analysis is 1 year. Variation of the water level within this annual maximum event is also simplified. The method for modeling the water level variation within the event depends on the source(s) of the extreme event (storm surge or river flood), see section 6.3.1 for more details. For the understanding of the probabilistic methods in this section, it is sufficient to note that the water level variation is described by two random variables: peak water level h_p and peak duration D_p . A more rigorous method would be to base the variability on a large set of hydrographs, either measured or from ensemble simulations. This method is not used in this chapter because of the high computational cost, except in a sensitivity analysis.

Because of the small failure probabilities and extreme value distributions of the hydraulic load (water level), the computation can be more efficient by separating the hydraulic loads and levee properties. For instance, the first is solved by monte carlo (MCS), the second by numerical integration (NI). The following subsections describe two methods with different ways to separate the hydraulic loads and levee properties. The first method (A) is a benchmark method, where there is no separation. This method requires much more computational time for small failure probabilities and therefore only used to validate method B. Method B applies numerical integration for the time-variant parameters (peak water level, peak duration, and pipe length), which allows for smaller sample sizes in the MCS method.

6

Method A: Monte Carlo Simulation (benchmark)

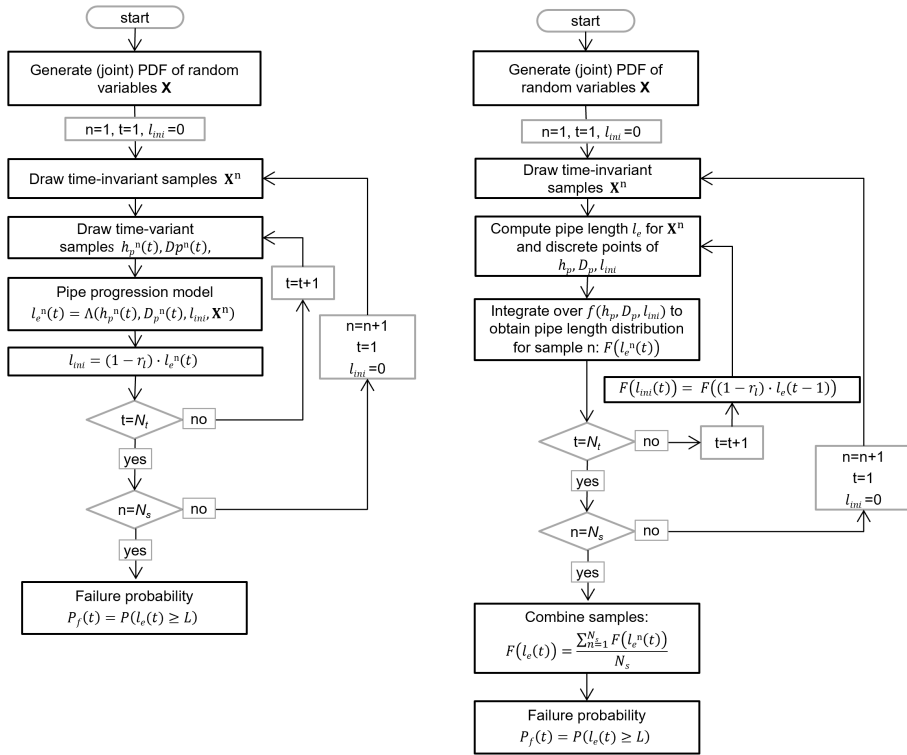
A robust reliability method is Crude Monte Carlo Simulation, which is illustrated in Fig. 6.5a. First, all random variables are sampled from their distributions. Time-invariant parameters \mathbf{X} (levee properties and flood fighting interventions) are sampled only for the first year of the analysis, and remain constant throughout the analysis period. Time-variant parameters (h_p, D_p) are resampled each year from their distribution, assuming independence between years. The initial (pre-storm) pipe length l_{ini} is 0 in the first year of the analysis. Pipe length development over the analysis period $l_e(t)$ is calculated for each sample n separately using the pipe progression model described in section 6.2.2 and the sampled variables $h_p^n(t), D_p^n(t)$ and \mathbf{X}^n . Strength recovery between flood events is included by multiplying l_e with a factor $(1 - r_l)$, where $0 < r_l < 1$ is a pipe length recovery fraction per year. Recovery occurs only when $l_e < L$ (non-failure). In case of failure ($l_e \geq L$), the levee is not repaired, so failed samples stay failed for the rest of the analysis period. The failure probability in each year $P_f(t)$ is obtained by counting the samples where $l_e \geq L$ and dividing by the number of samples N_s :

$$P_f(t) = P(l_e(t) \geq L) = \frac{\sum_{n=1}^{N_s} \mathbf{I}(l_e^n(t) \geq L^n)}{N_s} \quad (6.13)$$

This gives the probability that the levee is in the failed state in year t , so the probability that it failed in the period $0 \dots t$.

Method B: Monte Carlo with Numerical Integration

Also in method B, the pipe development over the analysis period is calculated for each MC sample separately, using three sources of information: (1) the initial pipe length l_{ini} , (2)



(a) Method A: Monte Carlo simulation per sample.

(b) Method B: Monte Carlo + Numerical Integration.

Figure 6.5: Flowchart of probabilistic methods A and B

the (joint) distribution of hydraulic loads $f(h_p, D_p)$, and (3) the relation between the pipe length at the end of a flood event (l_e) and the initial pipe length and hydraulic loads. In method B, the loads are not sampled from their distributions each year, as in method A. Instead, the load variables are discretized and the pipe length development is calculated conditional on these discrete points and then integrated with the load distributions, hence called numerical integration. Fig. 6.5b shows the calculation procedure.

The probability distribution (cdf) of the pipe length l_e in a single MC sample n at the end of year t , $F(l_e^n, t)$, is given by:

$$F(l_e^n, t) = \int_{l_{ini}(t)} \int_{D_p} \int_{h_p(t)} \mathbf{I}(\Lambda(h_p, D_p, l_{ini}, \mathbf{X}^n) < l_e) \cdot f(h_p(t), D_p, l_{ini}(t)) dh_p dD_p dl_{ini} \quad (6.14)$$

Where h_p denotes peak water level, l_{ini} the pipe length prior to an extreme event, D_p peak flood duration, \mathbf{X}^n the time-invariant levee properties of sample n . The indicator function $\mathbf{I}(\cdot)$ equals 1 if true and 0 otherwise. The function $l_e = \Lambda(h_p, D_p, l_{ini}, \mathbf{X}^n)$ is the pipe progression model in section 6.2.2. $f(h_p, D_p, l_{ini})$ is the joint distribution (pdf) of

hydraulic loads and l_{ini} . Depending on the way D_p is defined, these three variables can be assumed independent and the joint pdf can be replaced by the product of marginal pdf's: $f(h_p)f(D_p)f(l_{ini})$.

The initial pipe length distribution in the first year of the analysis, $f(l_{ini}(0))$, needs to be assumed or set to a fixed value. For each year in the analysis period, the distribution of l_e is updated with Eq. 6.14. In the absence of strength recovery between flood events, the end pipe length distribution is taken to the next year, so $F(l_{ini}(t)) = F(l_e(t-1))$. Strength recovery is included by shifting the pipe length distribution so that $F(l_{ini}(t)) = F((1-r_l) \cdot l_e(t-1))$, where $0 < r_l < 1$ is the pipe length recovery fraction per year. The probability $P(l_e \geq L)$ is not changed, as recovery cannot occur after failure. In this way, the pipe length distribution for each sample is updated each year.

Eq. 6.14 gives the numerical integration over the hydraulic loads and initial pipe length for a single MCS sample. Combination of all samples is done through:

$$F(l_e, t) = \frac{\sum_{n=1}^{N_s} F(l_e^n, t)}{N_s} \quad (6.15)$$

Now, the probability of failure $P_f(t) = P(l_e(t) \geq L)$ is easily computed from Eq. 6.15. This gives the probability that the levee is in the failed state in year t , so the probability that it failed in the period $0 \dots t$.

6

6.3 Application to coastal and river levees

This section applies the methods from section 6.2 to assess the influence of time-dependent pipe growth on the reliability of levees. First, a base case illustrates several steps in the method (section 6.3.1 and 6.3.2). Section 6.3.3 verifies whether the trapezoidal storm surge sufficiently represents the variability in storm duration. A few sensitivity analyses are performed on this base case to investigate the influence of uncertainties which are hard to quantify, such as the effectiveness of flood fighting, a pipe being initially present and potential strength recovery between flood events (section 6.3.4). Then, levee properties and hydraulic loads are systematically varied to investigate how significant the contribution of time-dependent pipe growth is for different levee conditions (section 6.3.5).

6.3.1 Random variables in base case

First a base case is analyzed to demonstrate the methods. Table 6.1 contains the distributions of the random variables used for the base case, as illustrated in Fig. 6.2. The choice of random variables aims to give realistic values for the strength and load variables of Dutch levees. However, given the large variation in properties across levees, these values are only indicative. Section 6.3.5 analyzes the effect of time-dependent pipe growth for other conditions. Distributions of $i_{c,h}$, m_u and m_p are based on Schweckendiek et al. [2014]. Most variables are described by a log-normal distribution, or deterministic. The μ and σ in Table 6.1 are the mean and standard deviation of the variable, and are transformed to log-normal distribution parameters m and s using:

$$m = \ln\left(\mu^2 / \sqrt{\sigma^2 + \mu^2}\right), \quad s = \sqrt{\ln(\sigma^2 / \mu^2 + 1)} \quad (6.16)$$

Table 6.1: Distributions of random variables for the base case. μ =mean, σ =standard deviation, Ln=log-normal, Det=deterministic.

Parameter	symp.	unit	μ	σ , CoV	Distr.
Time-invariant:					
Seepage length	L	m	50	$\sigma=5$	Ln
Aquifer depth	D_{aq}	m	20	$\sigma=0.5$	Ln
Blanket thickness	D_{bl}	m	3	$\sigma=0.5$	Ln
Blanket weight	$\gamma_{sat,bl}$	kN/m ³	18	$\sigma=1$	Ln
Critical heave gradient	$i_{c,h}$	-	0.7	$\sigma=0.1$	Ln
Grain size	d_{70}	mm	0.150	CoV=0.1	Ln
Rolling angle	θ	°	37	-	Det
White's coefficient	η	-	0.25	-	Det
Hydr. conductivity	k_{aq}	m/s	$1 \cdot 10^{-4}$	CoV=0.5	Ln
Aquifer response	r_e	-	0.6	-	Det
Polder level	h_e	m+NAP	0	-	Det
Model factor uplift	m_u	-	1	$\sigma=0.1$	Ln
Model factor crit. head	m_p	-	1	$\sigma=0.12$	Ln
Pipe length at t_0	l_0	m	0	-	Det
Erosion coefficient	C_e	-	0.044	$\sigma=0.048$	Ln
Detection probability	P_{ff}	-	0.9	-	Det
Time flood fighting	t_{ff}	hours	10	$\sigma=0.6$	Ln
Recovery rate	r_l	fraction/year	0	-	Det
Time-varying:					
Peak water level	h_p	m+NAP	Gumbel(loc=4, scale=0.25)		
Peak duration (coast)	D_p	hours	4	$\sigma=1$	Ln
Peak duration (river)	D_p	hours	48	$\sigma=24$	Ln

Flood fighting interventions

Timely flood fighting interventions (emergency measures) may stop the erosion process and avoid failure because BEP is a relatively slow failure process which is observable by sand boils. Common interventions create counter-pressure by locally raising the polder head [Nagy, 2014] or block the sand transport using filters [Montalvo-Bartolomei and Robbins, 2020]. The likelihood of a timely, successful flood fighting intervention depends on factors such as detection error, placement error, structural failure and the required time for these actions [Barendregt et al., 2005; Jonkman et al., 2012; Lendering et al., 2016]. These will depend in turn on organizational and logistical factors and will be site-specific. Furthermore, the probability of a successful intervention will likely decrease with increasing water level, as both the number and severity of sand boils will increase but the organization's capacity is limited. To include all these aspects is beyond the scope of this study. For the base case, we assume that the probability of successful detection P_{ff} is 0.9 and the required time for successful flood fighting t_{ff} has a mean of 10 and standard deviation of 0.6 hours. These estimates are based on experiences from flood fighting exercises [Jonkman et al., 2012; Lendering et al., 2014; van Rinsum, 2018; USBR and USACE, 2019]. It is noted that in coastal areas, extreme water levels occur during extreme storms in which

detection and emergency operations may be more difficult.

Hydraulic loads

The base case is analyzed with two extremes in terms of hydraulic load duration: a relatively short coastal storm surge and a long-lasting riverine flood. The method for modeling the water level variation within this annual maximum event depends on the source(s) of the extreme event (storm surge or river flood), see Fig. 6.6.

For levees loaded only by storm surge, the total water level is the sum of tidal variation and storm surge: $h(t) = h_{tide}(t) + h_{surge}(t)$. The tidal amplitude is 1 m and the tidal period 12 hours in the base case. The storm surge is modeled as trapezoidal shape with a peak duration which is defined by the random variable D_p and a base duration D_0 . The peak duration D_p is assumed to have a mean value of 4 hours and standard deviation of 1 hour [Asselman et al., 2010; de Moel et al., 2012], and follows a log-normal distribution. The base duration D_0 is approximately ten times D_p . To avoid unrealistically short base durations in case of small values for D_p , we assume $D_0 = 20 + 5D_p$. The phase difference between storm surge peak and the maximum tide is assumed to be 6 hours (half tidal period), so that the surge peak occurs at low tide. So, for a given case, the water level variation is described by two random variables: h_p and D_p .

Figure 6.6c compares the resulting normalized median trapezoidal storm surge, and the 5th and 95th percentiles of the duration, to a set of 100 synthetic storm surges from the ECMWFs4/DCSMv5 ensemble model [Van den Brink, 2020; Vuik et al., 2018]. To obtain the time-varying water level, the normalized surge trapezium is scaled to the required peak level.

In case of levees loaded by high river discharges, the total water level is the sum of mean water level h_0 and a trapezoidal shape with a peak duration D_p and a base duration D_0 . For the Rhine river, the peak duration D_p is assumed to have a mean value of 48 hours and standard deviation of 24 hours, and follows a log-normal distribution. The base duration D_0 is taken as $D_0 = 240 + 3D_p$ [hours]. Figure 6.6d compares the resulting median trapezoidal hydrograph and 90% confidence interval to a set of synthetic hydrographs from the GRADE-Rhine ensemble model [Hegnauer et al., 2014].

Correlation

The time-invariant levee properties in Table 6.1 are considered fully correlated in time, whereas peak water level and peak duration are considered uncorrelated in time. Some levee properties may be correlated due to physical relations (e.g., grain size and hydraulic conductivity), but these correlations between variables are neglected in this analysis. Spatial correlation is not considered, as this analysis is limited to single levee cross-sections. Cross-section results can be combined to a system level failure probability with the same methods as time-invariant analyses [Steenbergen et al., 2004].

6.3.2 Base case results

The base case illustrates several steps in the reliability computations. To allow for a comparison with the full Monte Carlo method (A), the hydraulic loads in the base case are chosen relatively high to obtain high failure probabilities (order of 10^{-4} for time-dependent and 10^{-1} for instantaneous erosion). In later cases we will apply method B, which allows for smaller (and more realistic) failure probabilities and hence lower hydraulic loads.

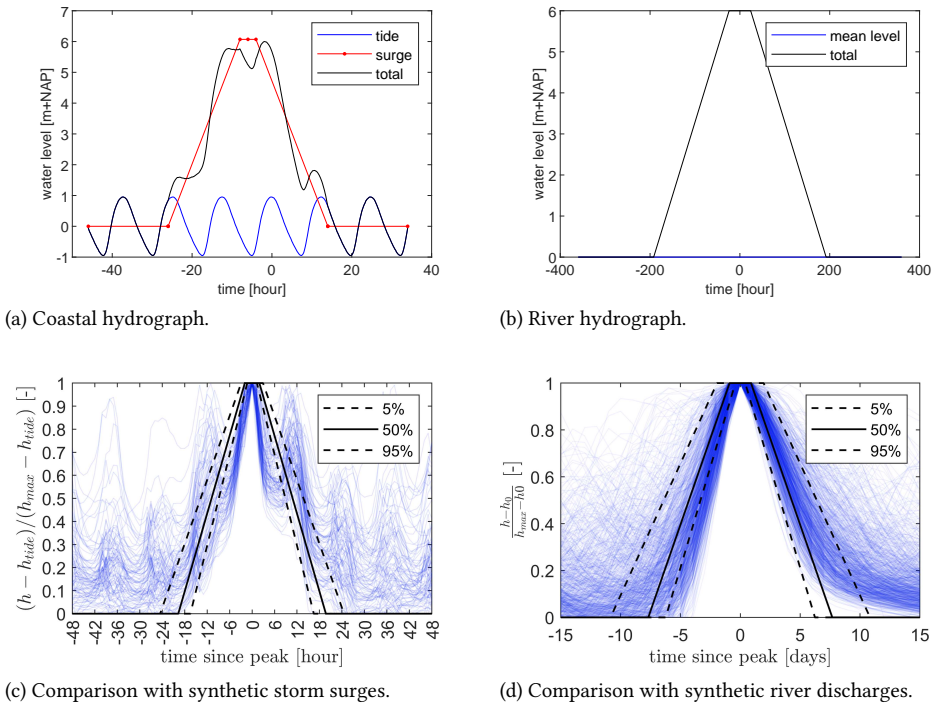


Figure 6.6: Modeling of coastal (a) and riverine (b) water level variation within extreme event as a trapezoidal water level setup. Synthetic storm surge data: Van den Brink [2020]. Synthetic river discharge data: Hegnauer et al. [2014].

Figure 6.7 shows the pipe length development over time and the annual maximum peak water levels and peak durations for only one MC sample of the base case. This is the same sample as shown in Fig. 6.4. The critical head for uplift is approximately 3.5 m+NAP. This level is exceeded in most years, so pipe growth starts from the beginning with a few storms around $h_p = 4.5$ m. Then in 2029 a larger storm arrives, which increases the pipe length to $0.3L$. In subsequent years, pipe growth is almost absent, even in years with $h_p = 4.5$ m. This is due to the fact that the equilibrium head H_{eq} for backward erosion is higher at $l = 0.3L$ than at $l = 0$, see for instance Fig. 5.7. The critical head for backward erosion H_c is around 5 m which is not exceeded after 2029. Although the pipe often develops in shocks in a single realization, the development averaged over all realizations is gradual, as seen in the percentiles in Fig. 6.8a). This figure shows for instance that the failure probability in 2035 is around 2% (0.98 percentile line reaches $l/L = 1$). Figure 6.8b shows the cumulative distribution (CDF) of the pipe length in several years.

Failure probabilities conditional on the main hydraulic load (fragility curves) are an intuitive way to interpret reliability analysis results. Figure 6.9 shows the fragility curves of different components of the failure process, for the coastal base case. Given a hydraulic load of $h_p = 5$ m and $D_p = 4$ h and $l_{ini} = 0$, the conditional failure probability without time-

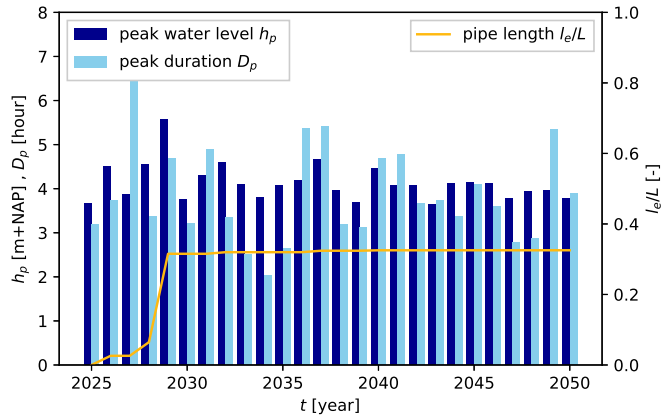
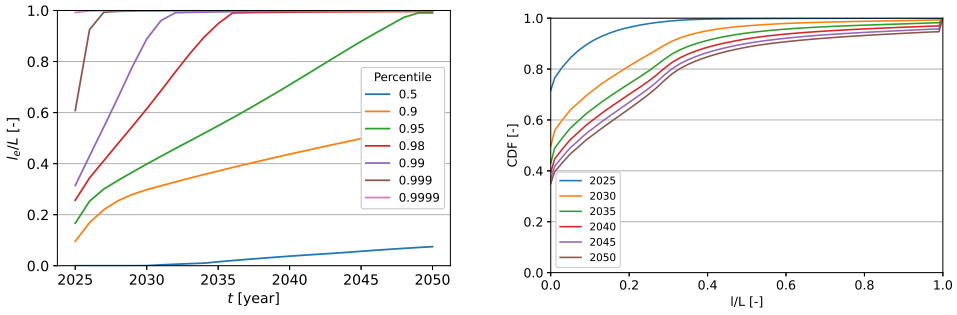


Figure 6.7: Pipe length development and yearly hydraulic loads for one sample of the coastal base case (method A).



(a) Percentiles of pipe length distribution l_e/L .

(b) CDF of pipe length in several years.

Figure 6.8: Pipe length development over the analysis period for the coastal base case.

dependence ($v = \infty$) equals 0.6. The resistance is dominated by the critical head H_c , as uplift and heave probabilities are close to 1. Adding the time-dependent pipe growth reduces $P_f|_{h, D_p, l_{ini}}$ to 0.002. Apparently it is highly unlikely that the pipe progresses under the entire levee in one such storm, despite the critical head H_c being exceeded. If there is an initial pipe length present of $l_{ini} = 0.5L$, this conditional failure probability increases to 0.004 but still is far below the stationary case.

After including the probabilities of the hydraulic load with probabilistic methods A and B, the resulting (cumulative) failure probabilities for the coastal base case are given in Figure 6.10. It appears that methods A and B give similar results. In the first analysis year (2025), the failure probability with instantaneous pipe growth equals 0.1 and with time-dependent pipe growth equals 0.0001; a factor 1000 difference. This $P_f(2025)$ is the probability of complete pipe development from 0 to L within a single flood event. In subsequent years, the difference becomes smaller as the pipe length increases in the time-

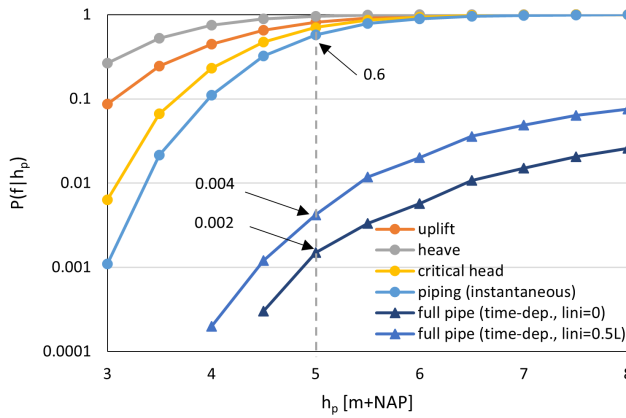
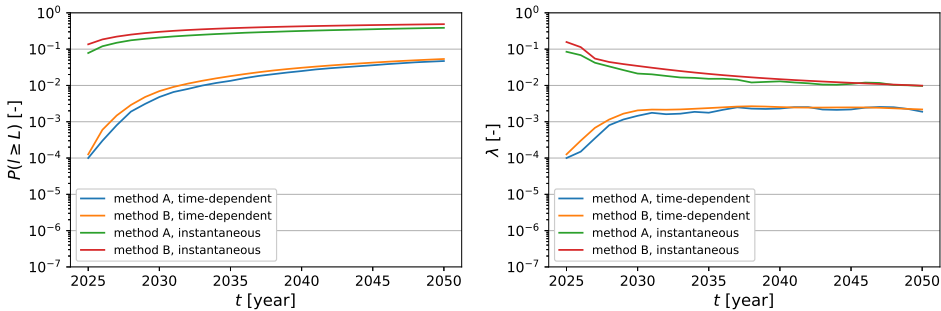


Figure 6.9: Conditional failure probabilities (fragility curves) for coastal base case with $D_p=4$ h, and $l_{ini}/L=0.5$.

dependent case, with finally a factor 10 in 2050. The trend in the conditional failure rate (Fig. 6.10b) is a combination of two effects: an increasing λ over time due to increasing pipe length (degradation; only present in the time-dependent erosion case) and a decreasing λ as the strongest samples survive over time. In case of small failure probabilities, λ of the instantaneous case will be almost constant over time as the probability of survival approximates 1.



(a) Cumulative failure probability $P(l \geq L)$.

(b) Conditional failure rate λ .

Figure 6.10: Cumulative and conditional failure probability over time for the coastal base case, computed with method A and B, with time-dependent and instantaneous pipe growth.

6.3.3 Variability in load duration

To assess how accurate the representation of the load duration by a trapezoidal shape with h_p and D_p is, this section compares this approach to a computation with a set of ensemble floods. Therefore, 25 random ensemble members are taken from the GRADE synthetic river flood dataset (Fig. 6.6d) or the ECMWF synthetic storm surge datasets

(Fig. 6.6c). For each ensemble member, the conditional failure probability is computed for $h_p = 5 \text{ m+NAP}$, $l_{ini} = 0$, no flood fighting and the other time-invariant variables as in the base case. Subsequently these ensemble probabilities are averaged (assuming equally likely ensemble members). Secondly, this conditional failure probability is also computed assuming the trapezia with peak duration distributed as given in Table 6.1. Thirdly, it is also computed with a deterministic trapezium with the mean value of the peak duration.

The results in Table 6.2 show that for the river floods, the three methods yield almost the same result, indicating that the variability can be sufficiently represented by the trapezium. For the coastal case, representing the storms by this trapezium gives a factor 6 higher failure probability compared to the ensemble approach. Comparison of the hydrograph shapes shows that the ensembles are generally narrower at the peak but wider at the base. Apparently the water level around the peak is most important for the pipe growth. Hence the approximation can be improved by a hydrograph which is narrower around the peak and broader in the base. On the other hand, describing D_p by a distribution or only by the mean value does not make a large difference, indicating that the reliability is relatively insensitive to uncertainty in the duration.

Table 6.2: Conditional failure probability given $h_p = 5 \text{ m+NAP}$ and $l_{ini} = 0$ using different methods to represent the variability in load duration.

Case	Method		
	Trapezia, $D_p = \mu$	Trapezia, $D_p \sim LN(\mu, \sigma)$	Ensemble
Coast	0.0035	0.0034	0.00054
River	0.16	0.16	0.14

6.3.4 Sensitivity analysis on base case

This sensitivity analysis quantifies how the base case failure probabilities and the effect of time-dependence change when different assumptions are used regarding a few large unknowns. Results are summarized in Table 6.3, and the corresponding graphs with development of P_f over time are shown in Fig. F.1 and F.2 in the appendix. The discussion below focuses on the effect of time-dependent pipe growth on the reliability as expressed in F_{td} for the year 2050. This factor is defined as the ratio of cumulative failure probabilities with instantaneous ($P_{f,stat}$) and time-dependent ($P_{f,td}$) pipe growth:

$$F_{td} = \frac{P_{f,stat}}{P_{f,td}} \quad (6.17)$$

Effects of a higher safety level are investigated by lowering the peak water levels by 1 m, i.e. using $h_p \sim \text{Gum}(3, 0.25)$ instead of $h_p \sim \text{Gum}(4, 0.25)$ in the base case. For both the coastal and river case, the difference between time-dependent and instantaneous pipe growth is larger in case of a higher safety level. As extreme events occur less frequently, it takes more years for the pipe length to increase, and the failure probability curve in Fig. F.2a increases more slowly over time.

Effects of flood fighting are studied by increasing the required time for successful flood fighting to $t_{ff} \sim LN(\mu = 24, \sigma = 2)$ hours, and by setting the probability of successful flood

Table 6.3: Results of the reliability analyses, including cases in sensitivity analysis. $P_{f,td}$ denotes (cumulative) failure probability including time-dependence, and $P_{f,stat}$ is without time-dependence (instantaneous). Effect of time-dependence is expressed by $F_{td} = P_{f,stat}/P_{f,td}$. A and B refer to the probabilistic methods.

Case	2025			2050		
	$P_{f,td}$	$P_{f,stat}$	F_{td}	$P_{f,td}$	$P_{f,stat}$	F_{td}
Base case - probabilistic method:						
1a Base case - coast - A	$1.0 \cdot 10^{-4}$	$7.8 \cdot 10^{-2}$	780	$4.7 \cdot 10^{-2}$	$3.9 \cdot 10^{-1}$	8.2
1b Base case - coast - B	$1.3 \cdot 10^{-4}$	$1.4 \cdot 10^{-1}$	1100	$5.3 \cdot 10^{-2}$	$4.9 \cdot 10^{-1}$	9.1
1c Base case - river - A	$2.3 \cdot 10^{-3}$	$5.9 \cdot 10^{-2}$	25	$5.9 \cdot 10^{-2}$	$2.6 \cdot 10^{-1}$	4.5
1d Base case - river - B	$2.8 \cdot 10^{-3}$	$1.0 \cdot 10^{-1}$	35	$6.2 \cdot 10^{-2}$	$3.5 \cdot 10^{-1}$	5.6
Effect of higher safety level:						
2a $h_p \sim \text{Gum}(3, 0.25)$ - coast - B	$2.5 \cdot 10^{-6}$	$7.9 \cdot 10^{-3}$	3200	$1.2 \cdot 10^{-3}$	$9.4 \cdot 10^{-2}$	79
2b $h_p \sim \text{Gum}(3, 0.25)$ - river - B	$1.3 \cdot 10^{-4}$	$6.1 \cdot 10^{-3}$	47	$5.3 \cdot 10^{-3}$	$6.7 \cdot 10^{-2}$	13
Effect of flood fighting:						
all: $h_p \sim \text{Gum}(3, 0.25)$ - method B						
3a $t_{ff} = 24$ - coast	$1.0 \cdot 10^{-5}$	$7.9 \cdot 10^{-3}$	790	$3.2 \cdot 10^{-3}$	$9.4 \cdot 10^{-2}$	30
3b $P_{ff} = 0$ - coast	$1.0 \cdot 10^{-5}$	$7.9 \cdot 10^{-3}$	780	$3.2 \cdot 10^{-3}$	$9.4 \cdot 10^{-2}$	29
3c $t_{ff} = 24$ - river	$2.2 \cdot 10^{-4}$	$6.6 \cdot 10^{-3}$	30	$1.3 \cdot 10^{-2}$	$7.6 \cdot 10^{-2}$	5.8
3d $P_{ff} = 0$ - river	$1.5 \cdot 10^{-3}$	$6.6 \cdot 10^{-3}$	4.0	$4.2 \cdot 10^{-2}$	$7.6 \cdot 10^{-2}$	1.8
Effect of an initial pipe:						
all: $h_p \sim \text{Gum}(3, 0.25)$ - method B						
4a $l_0 = 0.25L$ - coast	$2.4 \cdot 10^{-6}$	$7.9 \cdot 10^{-3}$	3300	$1.4 \cdot 10^{-3}$	$9.4 \cdot 10^{-2}$	68
4b $l_0 = 0.50L$ - coast	$7.1 \cdot 10^{-6}$	$6.1 \cdot 10^{-3}$	870	$2.4 \cdot 10^{-3}$	$6.7 \cdot 10^{-2}$	28
4c $l_0 = 0.75L$ - coast	$5.2 \cdot 10^{-5}$	$7.9 \cdot 10^{-3}$	150	$6.3 \cdot 10^{-3}$	$9.4 \cdot 10^{-2}$	15
4d $l_0 = 0.25L$ - river	$1.2 \cdot 10^{-4}$	$6.1 \cdot 10^{-3}$	51	$5.5 \cdot 10^{-3}$	$6.7 \cdot 10^{-2}$	12
4e $l_0 = 0.50L$ - river	$1.4 \cdot 10^{-4}$	$7.9 \cdot 10^{-3}$	58	$6.9 \cdot 10^{-3}$	$9.4 \cdot 10^{-2}$	14
4f $l_0 = 0.75L$ - river	$4.1 \cdot 10^{-4}$	$6.6 \cdot 10^{-3}$	16	$1.2 \cdot 10^{-2}$	$7.6 \cdot 10^{-2}$	6.3
Effect of recovery rate:						
all: coast - method B						
5a $r_t = 5\%/y, h_p \sim \text{Gum}(4, 0.25)$	$1.3 \cdot 10^{-4}$	$1.4 \cdot 10^{-1}$	1100	$2.2 \cdot 10^{-2}$	$4.9 \cdot 10^{-1}$	22
5b $r_t = 10\%/y, h_p \sim \text{Gum}(4, 0.25)$	$1.3 \cdot 10^{-4}$	$1.4 \cdot 10^{-1}$	1100	$1.1 \cdot 10^{-2}$	$4.9 \cdot 10^{-1}$	45
5c $r_t = 5\%/y, h_p \sim \text{Gum}(3, 0.25)$	$2.5 \cdot 10^{-6}$	$7.9 \cdot 10^{-3}$	3200	$3.4 \cdot 10^{-4}$	$9.4 \cdot 10^{-2}$	270
5d $r_t = 10\%/y, h_p \sim \text{Gum}(3, 0.25)$	$2.5 \cdot 10^{-6}$	$7.9 \cdot 10^{-3}$	3200	$1.8 \cdot 10^{-4}$	$9.4 \cdot 10^{-2}$	520

fighting P_{ff} to 0 (no flood fighting). These results indicate that flood fighting is an important factor in the failure probability for river levees, as it explains the majority of the difference in failure probability between time-dependent and instantaneous pipe growth. On the other hand, for coastal levees this is of minor importance. It has some effect, provided that the time required for interventions (t_{ff}) is short. The case with $t_{ff} \sim \text{LN}(\mu = 24, \sigma = 2)$ yields the same failure probability as the case without any flood fighting (lines collapse), as the storm has usually passed 24 hours after the sand boiling started.

Effects of a potentially present pipe development from historical extreme events are investigated by setting the initial pipe length in the first year equal to $0.25L$, $0.50L$ or $0.75L$. The case with $0.50L$ is already rather extreme because it implies that the critical head for backward erosion has been exceeded. For both the coastal and river case, the effect of an initial pipe length up to $0.50L$ is limited. This can be explained from the shape of the equilibrium curve (Fig. 5.7), which results in more rapid pipe growth in the initial regressive phase ($l < l_c$). Hence, most of the time required for erosion and hence the

contribution to time-dependent reliability is associated with the progressive phase ($l > l_c$).

Effects of strength recovery are studied for three recovery rates (r_l) and two safety levels. Here recovery is represented by reducing the pipe length between two years. Strength recovery can make a difference on the long term, e.g. in the coastal case 10% pipe length reduction per year results in a factor 6 difference in failure probability in 2050 (case 2a and 5d in Table 6.3). This will have a relatively large effect if it takes multiple storms for the pipe to progress through the levee. Therefore the effect is smaller for the river case (Fig. F.1h) where failure more often develops within a single flood event.

6.3.5 Influence of levee characteristics

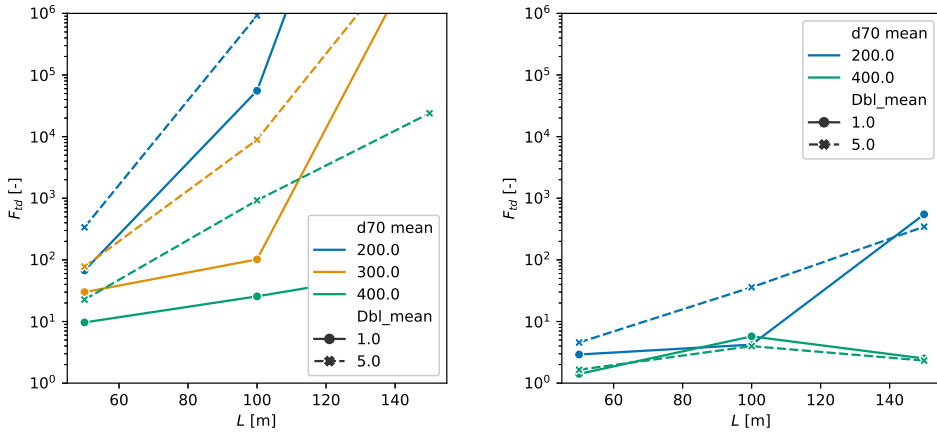
To indicate in which conditions time-dependent pipe growth has a significant effect on the reliability, this section analyzes the influence of several factors which are expected to be important for the time-dependence. The first factor is the relation between the time required for pipe development (seepage length and progression rate) and the flood duration. This is taken into account by varying the seepage length L , grain size d_{70} , and analyzing the extreme scenarios of a short coastal storm surge and a long lasting river flood. Hydraulic conductivity is coupled to grain size as $k_{aq} = -1830 \cdot \ln(C_u) \cdot d_{70}^2$ [Den Rooijen, 1992]. Second, the blanket thickness D_{bl} is varied to obtain different ratios of uplift/heave resistance and backward erosion piping resistance. If the critical head for uplift is higher than the critical head for backward erosion, the erosion starts relatively late in the flood event, but once it occurs it will progress faster because it is more strongly overloaded. Thick blankets also result in a high resistance in the vertical pipe (heave, $0.3D_{bl}$ -reduction), therefore the erosion process stops earlier when the flood level is falling. The analyzed ranges in mean value of each variable are:

- L : 50, 100 and 150 m
- d_{70} : 200, 300 and 400 μm
- k_{aq} : $1 \cdot 10^{-4}$, $2 \cdot 10^{-4}$ and $4 \cdot 10^{-4}$ m/s (coupled to d_{70})
- D_{bl} : 1 and 5 m

The standard deviations or coefficients of variation are equal to the values in Table 6.1. The distribution of peak water levels is coupled to the seepage length, so that wider levees are loaded with higher water levels, to avoid too large differences in instantaneous failure probability between cases with different seepage lengths. For $L = 50$ m, the water level is given by $h_p \sim \text{Gum}(2, 0.25)$. For $L = 100$ m, $h_p \sim \text{Gum}(3, 0.25)$. For $L = 150$ m, $h_p \sim \text{Gum}(4, 0.25)$. Case is without flood fighting. The other variables are copied from the base case in Table 6.1.

All results are expressed as factor F_{td} for the year 2050 (Eq. 6.17), which describes the effect of time-dependent pipe growth on the reliability (Fig. 6.12). Figure 6.11 shows the results for the different levee configurations. Differences in effect between coast and river are clear, as also shown in the base cases. The coastal case shows large differences in effect between levee configurations such as grain size and seepage length, ranging from $F_{td} \approx 10$ to more than 10^6 for large seepage lengths and fine sand. Although effects are smaller for the rivers, it can still be considerable for particular cases such as fine sand combined with a large seepage length and thick blanket (factor 100). For other river cases (coarse sand, thin

blanket) effects are limited ($F_{td} < 5$) and the current assumption of instantaneous failure is considered realistic.



(a) Coast, short duration.

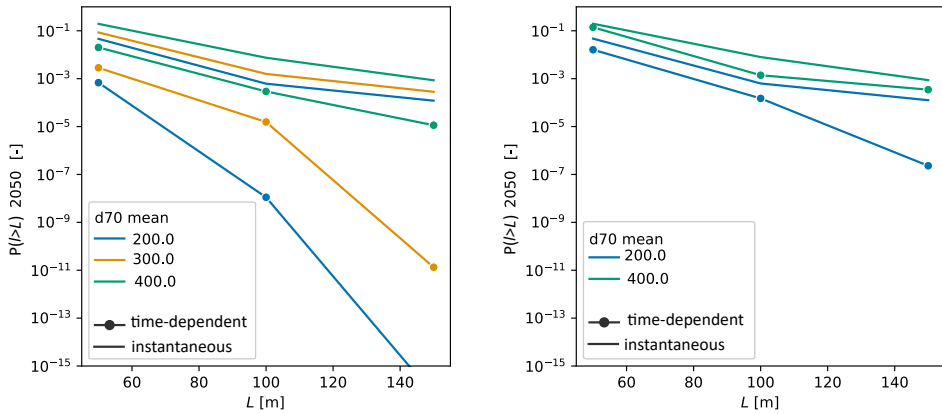
(b) River, long duration.

Figure 6.11: Effect of time-dependent pipe growth on reliability (F_{td}) as function of seepage length L [m], grain size d_{70} [μm] and blanket thickness D_{bl} [m]. Results for initially intact blanket and no flood fighting.

6.3.6 Implications for levees in the Netherlands

The results in Fig. 6.11 show large variations in the effect of time-dependent pipe growth (F_{td}). The two scenarios for the hydraulic loading (coast and Rhine river) are rather extreme. Regions subject to both storm surge and river discharge will fall somewhere in between these extremes. Examples are the Rhine-Meuse Delta and the IJssel-Vecht Delta in the Netherlands (see box in Fig. 6.13). Furthermore, floods in the Meuse river are generally shorter than in the Rhine river. To assess the potential of including time-dependent pipe development in safety assessment and design, this picture of water systems must be combined with the current safety assessment results for the piping failure mechanism (Fig. 6.13). These assessment results are an indicator for future levee reinforcement projects. Levees along the coast or lakes which are assessed as insufficient are expected to benefit strongly from time-dependence. Most levees which are currently assessed as insufficient are located in the upper river areas. Here is some potential in particular cases (fine sand, large L and thick blanket). Also in the delta areas, a substantial part of the levees has insufficient safety against piping. Significant benefits may be expected here as well, due to the compound storm surge and river floods which have a long base duration but short peak. The methods in this chapter also apply to these areas with compound flood events, but there are more load variables which may also be correlated.

The results in Fig. 6.11 give an impression of the potential increase in reliability, but are restricted to the characteristics and assumptions of the base case. The analysis shows that F_{td} is rather sensitive to the levee characteristics, hence the factors should not be applied directly to real cases but determined based on an analysis with local levee char-



(a) Coast, short duration.

(b) River, long duration.

Figure 6.12: Time-dependent ($P_{f,td}$) and instantaneous ($P_{f,stat}$) failure probability in 2050 as function of seepage length L [m] and grain size d_{70} [μm] and blanket thickness D_{bl} [m]. Results for initially intact blanket and no flood fighting.

6

acteristics and load distributions. These results are obtained assuming that no sand boils have occurred. If there has been pipe growth (sand boils) in the past, the failure probability increases slightly (cases 4a-4f in Table 6.3). On the other hand, as the assumed coastal surge duration appeared to be conservative (section 6.3.3), a more accurate representation of the flood duration will probably increase F_{td} in coastal cases. Finally, the results in Fig. 6.11 do not include flood fighting interventions and will increase if this is accounted for.

Currently, the assessment guidelines for levees in the Netherlands contain a criterion for time-dependent pipe growth [IenM, 2019]. It states that the failure probability for piping is negligible when all of the following conditions are met:

- Seepage length $L > 50$ m;
- hydraulic loads are fully governed by storm surge (coast);
- it can be demonstrated that no sand boils have been observed in the past;
- emergency response plans include flood fighting interventions for the occurrence of two successive extreme flood events;
- there is no structure or crossing pipeline present in the levee.

The required seepage length is based on an average progression rate of 2 mm/s (7.2 m/hour), which is considered an upper bound based on experiments, combined with a water level duration of 6 hours [Jongejan and Van Beek, 2015]. So it considers the likelihood of full pipe growth within a single storm event, and neglects resistance of uplift, heave, or critical head. With the methods in this chapter, time-dependence can be analyzed for cases where these conditions are not met (except for levees with structures and pipelines). For instance, the current limitation of this rule to coastal levees can be stretched, so that levees in lake or delta systems can be analyzed as well. If there are emergency response plans, their effectiveness can be quantified. Also the current requirement that no sand boils have

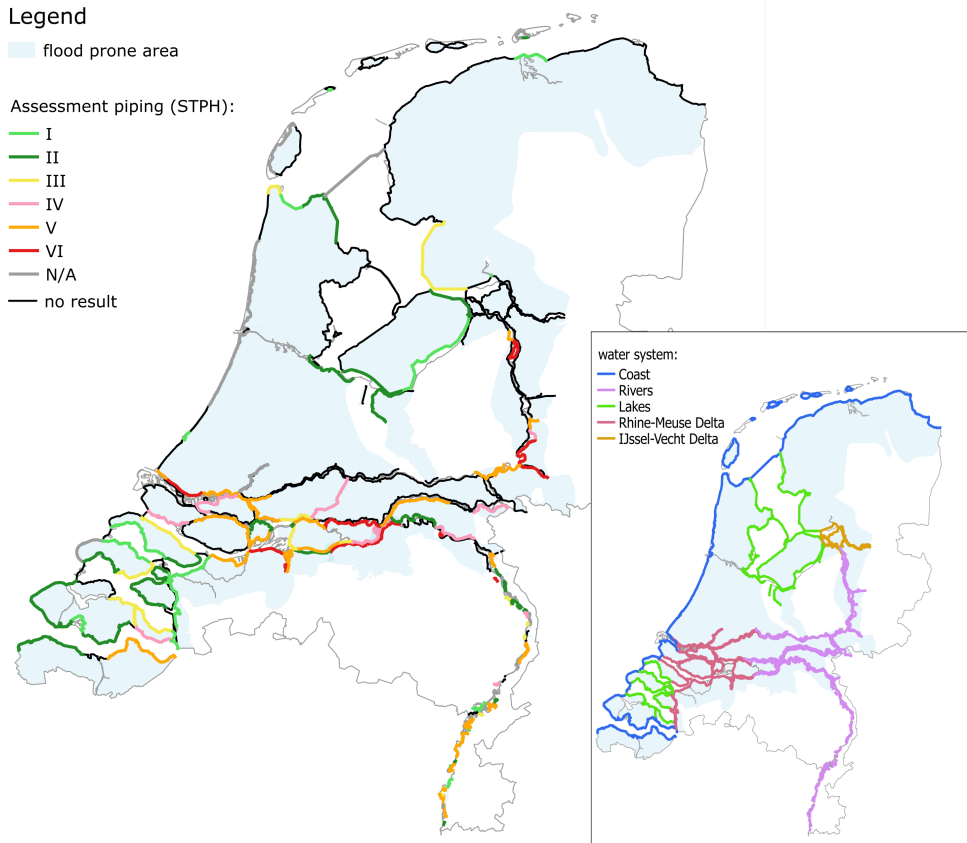


Figure 6.13: National safety assessment results for piping in levees (October 2022, data source: Nationaal Georegister) [Georegister, 2021]. Category I-III comply to the standards, cat. V and VI do not comply.

occurred can be replaced by an estimate of the initial pipe length currently present. Furthermore, the methods can be used to derive such a set of criteria for 'safe' levees which is more broadly applicable and which is based on the additional experiments and model simulations in this thesis.

6.4 Conclusions

The development of backward erosion piping requires time due to limitations in sand transport from the levee foundation. When the flood level falls before the pipe has developed in a hydraulic shortcut, or when timely flood fighting interventions are taken, the piping process stops and failure is prevented. This chapter quantifies how this influences the failure probability of levees. The results presented in this chapter use findings from all previous chapters. The pipe progression model in this chapter is partly based on numerical simulations from chapter 5. The numerical model in turn is partly based on observations from the small-scale and large-scale experiments from chapter 3 and 4.

First, a novel piping failure model is developed which is capable of including pipe growth in reliability analyses. It describes the relevant processes (uplift, heave, backward erosion, flood fighting) in time and in an integrated manner. Limit states for uplift, heave and the critical head for backward erosion are based on the methods as currently applied in the Netherlands. This is extended with the rate of pipe development which is based on the regression functions from chapter 5, combined with an estimate of the shape of the equilibrium curve $H_{eq}(l)$. Flood fighting such as sand bagging is included by a probability of successful intervention and the time required for such an intervention. Second, this model is included in a time-variant reliability analysis framework based on a combination of Monte Carlo Simulation and Numerical Integration to assess the influence of time-dependence on levee failure probability. This relatively computationally expensive method was chosen because of the correlation between years which arises from the degradation character of pipe growth, which is a function of hydraulic loads (uncorrelated), levee properties (fully correlated) and the pipe length itself. Besides computing the current failure probability per year, the method is capable to show how the reliability evolves over the years due to cumulative pipe growth over multiple flood events and strength recovery between flood events.

A series of sensitivity analyses shows the influence of several factors on the time-variant reliability and on the factor F_{td} which gives the ratio of failure probability with and without time-dependent pipe growth. Of course, flood duration is an important factor, where the short coastal storm surge results in a higher F_{td} compared to the longer river floods. For coastal levees it is unlikely that a piping breach will develop in a single extreme event, whereas Rhine river levees without flood fighting are likely to fail in a single event. The results indicate that a higher safety level yields a larger F_{td} . Flood fighting is an important factor in the river cases, where it causes a large part of the effect of time-dependence. In contrast, flood fighting contributes less in the coastal cases, as the flood duration is short already and the required time for flood fighting needs to be very short to be more effective. The analysis showed that a currently present short pipe (i.e., $< 0.25L$) formed during past events does not have a significant impact on the reliability. This can be explained from the relatively rapid erosion in the beginning of the erosion process when pipes are still short, and this contributes little to the time required for erosion.

Hence the progressive erosion phase contributes most to the time required for erosion. Recovery of pipes between flood events has an impact on the long term development of the failure probability. Reliable quantification of this recovery is currently not possible due to a lack of empirical evidence. However, effects of time-dependence can still be analyzed assuming no recovery (conservative).

A parametric study with different levee characteristics and hydraulic loads indicated under which conditions a large effect of time-dependence (F_{td}) may be expected. Influential levee properties are the seepage length and grain size (or permeability). The coastal case shows large effects, ranging from $F_{td} \approx 10$ to more than 10^6 for large seepage lengths and fine sand. Although effects are smaller in the river cases, it can still be considerable (factor 100) for particular cases such as fine sand combined with a large seepage length and thick blanket. For other river cases (coarse sand, very thin blanket) effects are limited ($F_{td} < 5$) and the current assumption of instantaneous failure is considered realistic. Levees along the tidal rivers and delta's fall in between these extremes, and are also expected to have a lower failure probability due to time-dependent pipe development.

Based on these results it is concluded that time-dependent pipe development is important for a realistic reliability estimate, but this is currently not applied in practice. This chapter provides a method for such quantitative probabilistic analyses. The results indicate that a considerable part of the Dutch levees can benefit from including time-dependent pipe development in the BEP failure model, as it can reduce or postpone levee reinforcements. Recommendations for further research include the use of more efficient probabilistic methods such as FORM. It is also required to further validate the prediction model for the progression rate, and reduce the uncertainty in erosion coefficient. Finally, the variability in storm surge duration and representation by a simplified hydrograph needs further study, as well as hydrographs for areas with combined loads from storm surge and river discharge. The main recommendation for practice is to include the effect of time-dependent pipe growth in levee reliability analyses and designs, depending on whether a significant increase can be expected for a given levee (considering coastal or riverine water system, and levee properties). This can be done at different levels of detail, as explained in section 8.3.



7

Levee reliability with physical interactions between failure mechanisms

Vaak wordt gesteld dat het denken aan een bedreiging of een mechanisme belangrijker is dan de gehele analyse die daarop volgt.¹

Calle et al. [1985]

7

Levee reliability analysis often considers failure mechanisms as correlated but non-interacting processes. Interacting failure mechanisms affect each others performance, and thereby the system reliability. We describe such interactions in the context of flood defenses, and analyze under which conditions such interactions have a large impact on reliability using a Monte Carlo-based quantification method. We provide simple examples and an application to levee failure due to landward slope instability and backward erosion piping (BEP). The examples show that the largest interaction effects are expected when the trigger mechanism is relatively likely to occur and the affected mechanism has a relatively large contribution to the system reliability. For the studied levee example, interactions between slope instability and BEP increased the failure probability up to a factor 4 compared to an analysis with correlated but non-interacting failure mechanisms. Implications for the assessment and design of flood defenses are discussed.

This chapter is based on an article submitted for publication, co-authored by Paulina Kindermann, Mark van der Krogt, Vera van Bergeijk, Guido Remmerswaal, Wim Kanning, Bas Jonkman and Matthijs Kok.

¹It is often argued that thinking about a threat or mechanism is more important than the entire analysis that follows

7.1 Introduction

Reliability analysis is a crucial part of the management of infrastructure, in particular when large risks are involved when structures fail. Flood protection infrastructure such as levees, dams and storm surge barriers need to have high levels of reliability to provide sufficient safety against catastrophic flooding. Reliability analysis methods are used to quantify their current performance and expected future performance under changing conditions [Baecher and Christian, 2005; Melchers and Beck, 2017a]. As such, it is an important component of risk-based management of flood protection systems [Jonkman et al., 2009; Vonk et al., 2020]. To quantify flood defense reliability, engineers analyze the likelihood of failure mechanisms such as overtopping erosion or slope instability separately. In a system reliability analysis, these failure mechanisms and different sections are combined considering dependence between random variables in all sections and mechanisms [Steenbergen et al., 2004]. However, such failure processes can also affect each other [Morris et al., 2008], and thereby change the reliability compared to the case of independent failure processes. An example of such a physical interaction in the context of flood defenses is a shallow slope failure in a wide dam or levee during high water, which may not lead to complete instability of the structure, but decreases the erosion resistance of the landward slope against overtopping [Kok et al., 2017].

In line with definitions in the literature [Meango and Ouali, 2019; Murthy and Nguyen, 1985; Sun et al., 2006] interaction is defined here as follows: an interaction occurs if the occurrence of a (influencing) mechanism changes certain system parameters which trigger or prevent failure of other (affected) mechanisms. Although the individual mechanisms alone might not result in system failure due to additional resistance after one of them occurs, the causal dependencies between the two mechanisms can lead to failure [Morris et al., 2008]. The interaction can lead to immediate failure of the affected component, or to an immediate strength reduction which may lead to failure at a later moment. Interactions are defined as positive if they increase the other component's failure probability, and negative if they decrease it [Sun et al., 2006]. These interaction effects on reliability have been described using different terms such as sequential failures [Lee and Song, 2011; Song et al., 2021], failure propagation [Tazi et al., 2018], failure collaboration [Zeng et al., 2016] or trigger effect [Fang et al., 2021].

It is important to note that dependence between failures of different components of a system can take different forms. Well-known dependencies are statistical correlations between the safety margins of components or failure mechanisms, which can arise from correlation between shared variables. For instance, the same parameter can affect multiple mechanisms (e.g., water level) or parameters can be related by nature (e.g., soil grain size and permeability). Similarly, spatial correlations result in correlated elements. Such correlations have been analyzed for flood defense reliability [Roscoe et al., 2015; Steenbergen et al., 2004]. The physical interactions between failure mechanisms studied in this chapter are a different form of dependence, which arises from causal relationships between failure processes, but not from statistical correlation.

Figure 7.1 shows an illustrative example of interaction, which is elaborated further in section 7.3.2. Consider a parallel system of two failure mechanisms A and B depending on the variables $X_1 \dots X_3$ (Fig. 7.1a). Due to the interaction IC, X_3 is affected by a given degree when A fails. The effect of the interaction appears as a change in Z_B if $Z_A < 0$ (Fig.

7.1b). This changes the probability that the system is in the failure domain, indicated by the shaded area. The difference between statistical correlation and physical interaction becomes clear from Fig. 7.1b. In the scatterplot of the safety margins Z_A and Z_B , an interaction shows a discontinuity (at $Z_A = 0$ if A is the trigger), whereas statistical correlations do not. Statistical correlations are not the focus of this chapter, but play a role as they affect the impact of interactions.

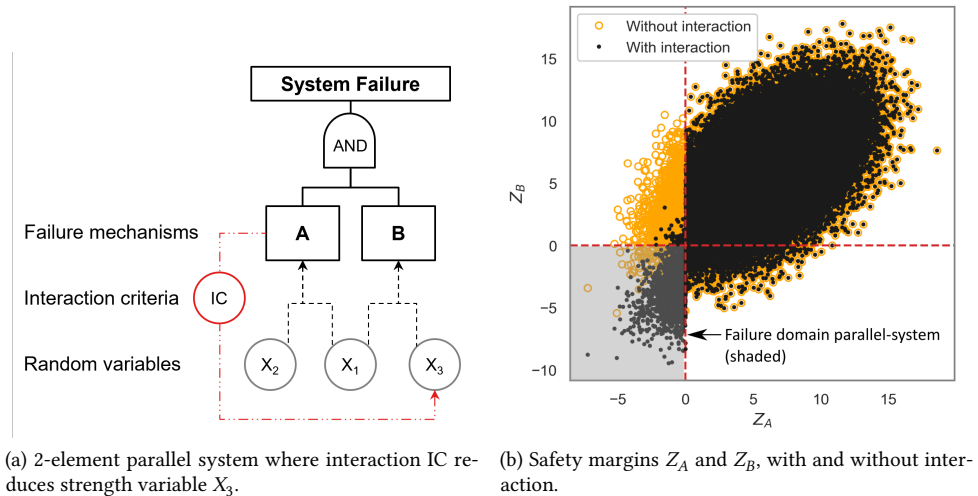


Figure 7.1: Example of an interaction in a correlated 2-element parallel system, such that the resistance of B decreases through X_3 if A fails.

Such physical interactions are not considered in flood defense reliability, but have been analyzed in the context of reliability and degradation of mechanical systems [Fang et al., 2021; Jia and Gardoni, 2018; Meango and Ouali, 2019, 2020; Murthy and Nguyen, 1985; Sun et al., 2006; Tazi et al., 2018; Zeng et al., 2016] and load redistribution after local failures in complex structures [Karamchandani et al., 1992; Lee and Song, 2011; Song et al., 2021]. In these studies on mechanical systems, the failure interaction is mostly caused by gradual or shock degradation of a component, and component performance data is available to calibrate degradation models. In contrast, failure of levees and dams is mostly driven by extreme events (shocks exceeding the strength capacity) instead of gradual degradation, and usually no data on degradation rates is available. Dams and offshore structures have similar failure characteristics as levees and were considered in some recent studies [Adumene et al., 2021; Andreini et al., 2016; Pei et al., 2022]. Pei et al. [2022] analyzed the system reliability of a gravity dam with multiple sections and two failure mechanisms using Bayesian Networks, a failure path search and Monte Carlo Simulation. However, no physical interactions are considered between the two failure paths (strength and instability) for each dam section. Andreini et al. [2016] analyzed the reliability of a dam subject to concentrated leak erosion with two events (erosion initiation and failed interventions) in one failure path, but no physical interaction between failure mechanisms. Adumene et al. [2021] described interactions between environmental factors influencing corrosion

rates of offshore structures using Bayesian Networks. They used Monte Carlo Simulation to quantify the failure probability, in which only statistical dependence between failure mechanisms is modeled but no physical interactions. Others quantified interactions based on expert judgment [Wang et al., 2021].

The main reason why interactions have been neglected in levee reliability analysis, is because levees are often considered as series systems which fail if one of their failure mechanisms occur. In that case, failure paths consist of single failure mechanisms. Interactions are irrelevant in such a system definition because when the trigger mechanism occurs, the levee is assumed to fail anyway. However, there is an increasing interest in methods to make levee reliability assessments less conservative and aim more for best estimates. One way is to distinguish different subsequent processes within a failure path [Van et al., 2022]. Instead of assuming failure when a failure path initiates, one also quantifies the residual resistance after this initiating failure mechanism [van Bergeijk et al., 2021; Calle, 2002; van der Krogt et al., 2019; Remmerswaal et al., 2021; USBR and USACE, 2019]. Accounting for these additional processes within a failure path can introduce physical interactions between these processes.

Currently, it is unclear under which conditions physical interactions between failure mechanisms can have a significant impact on the reliability of flood defenses. Therefore, this chapter presents an application of reliability methods to flood defense infrastructure where different failure mechanisms interact with each other. Interacting failures in flood defenses have not been studied before and are currently neglected in assessment and design. The main contributions are that the chapter addresses the relevance of interacting failures for flood defense reliability, it shows what kind of interactions may occur in levees and how these physical interactions affect levee safety. In addition, it provides a flexible and robust Monte Carlo based method to quantify effects on reliability. We analyze two conceptual examples and an example of a levee considering the failure mechanisms of landward slope instability and backward erosion piping. Although the chapter focuses on flood defenses, the methods apply to a broader range of structures.

The remainder of the chapter is organized as follows. Section 2 describes interactions between failure mechanisms in the context of flood defense reliability, including examples. Section 3 describes the reliability analysis method and the approach for application to the conceptual examples and a levee example. Section 4 presents the results of both examples, focusing on the conditions in which interactions are important. Section 5 discusses implications for application to flood defenses, and section 6 presents the conclusions.

7.2 Interactions in levee failure

7.2.1 Levee failure mechanisms and failure paths

As levees fail due to varying causes, engineers distinguish several failure mechanisms or failure modes. Examples are external erosion by overtopping, internal erosion by seepage, or slope instability. However, a levee can also fail by a combination of failure mechanisms occurring during the same event. Therefore, we first clarify some terminology related to failure mechanisms.

In this chapter, we define *levee failure* as the state in which a levee fails to fulfill its primary function (flood prevention), i.e. when flooding occurs. Such a failure can fol-

low from a breach or excessive overflow. We define a *failure path* as a chain of potential events leading to levee failure. These events may be physical processes related to failure of levee elements (e.g., grass cover erosion) or involve human actions (e.g., fail to detect damage and implement remedial action). The physical processes are commonly referred to as *failure mechanisms*, but it must be noted that in the the context of this chapter *failure mechanism* can refer to a part of the failure path, not necessarily to complete levee failure. Failure paths are also referred to as failure scenarios [CIRIA, 2013; Morris et al., 2008].

7.2.2 Physical interactions in levees

Although levee design considers distinct mechanisms, real levee failures can be a combination of different mechanisms. According to Özer et al. [2020], in about 30% of the levee breaches during the 2002 and 2013 Elbe floods in Germany multiple failure mechanisms were observed. Another example is the London Avenue Canal South levee failure during Hurricane Katrina, where tilting of a flood wall seems to have increased underseepage and induced slope instability or backward erosion [Kanning et al., 2008; Sills et al., 2008; Ubilla et al., 2008].

Table 7.1 lists possible interactions for levees grouped by the main failure mechanisms of external erosion (erosion by wave or flow impact on the levee cover), internal erosion (erosion by seepage flow through the levee) and slope instability. Figure 7.2 illustrates the associated damages which may affect other mechanisms. Within the scope of this chapter, we cannot give an exhaustive list of interactions in levees. Which interactions play a role will strongly depend on the levee characteristics. For instance, the presence of structural elements can introduce additional interactions due to unequal deformation of soil and structural elements. A more structured inventory of possible interactions can be obtained using influence diagrams relating the input parameters of failure mechanisms to their effects on levee elements.

7.2.3 Approaches to quantify interactions in levees

We see two main approaches to quantify failure mechanism interactions. Approach (1) couples the interacting processes in a process-based model. In a reliability analysis, this coupled model is then evaluated instead of the separate failure models. A few studies use such coupled models for internal erosion and slope stability [Fu et al., 2018; Mizutani et al., 2013; Rahimi and Shafieezadeh, 2020]. Fu et al. [2018] also applied the coupled model in a reliability analysis using MCS and a response surface. Approach (2) keeps the failure models separate, but incorporates the interactions in the reliability analysis by evaluating the failure models with adapted parameters, depending on the occurrence of a predefined trigger. This approach can be followed when the interactions can be defined as discrete events.

Approach (2) can be implemented in different ways, depending on the complexity of the interactions. The most simple way is scenario-based (2a), where different scenarios are defined for the occurrence of the trigger. Then the failure probability or the stochastic variables of the affected mechanisms are adapted for the scenarios in which the trigger occurs. Examples of this approach are event tree methods for the quantification of backward erosion piping risks [USBR and USACE, 2019] or slope instability [van der Krogt et al., 2019]. Approach 2a requires the analyst to predefine the sequence in which the events are

Nr. in Fig. 7.2	Trigger mechanism (T) & affected mechanism (A)	Interaction description
1	T: external (wave overtopping) A: internal (backward erosion)	scour hole at the levee toe reduces the cover layer thickness, which increases chances of uplift, rupture, heave and backward erosion.
2	T: external (wave overtopping) A: internal (through-seepage)	grass cover erosion induces seepage erosion from a sandy levee core with a high phreatic line, as the natural filter is removed (micro-instability).
3	T: external (wave attack) A: internal (through-seepage) & stability	damage of outer slope low-permeability lining increases infiltration, which affects internal erosion and slope stability through higher phreatic levels.
4	T: internal (through-seepage, animal burrows) A: external (wave overtopping)	seepage through the embankment due to high phreatic line (through-seepage or micro-instability), possibly in combination with animal burrows, leads to particle loss and deformation of the grass cover, which reduces its resistance against wave overtopping.
5	T: internal (blanket rupture) A: stability	a vertical crack in the blanket layer and a horizontal pipe in the foundation reduces the aquifer head.
6	T: internal (backward erosion) A: stability	Erosion lens or horizontal pipes in the foundation reduce aquifer pore pressures. It also reduces the shear strength at the interface of the aquifer and the blanket, although this occurs locally while slope failure occurs over a larger width (3D effects). [Rahimi and Shafieezadeh, 2020]
7	T: stability A: external (wave overtopping)	shallow slope failure damages the grass cover and creates a cliff, which reduces the resistance against wave overtopping [van Bergeijk et al., 2021].
8	T: stability A: internal (through-seepage)	shallow slope failure induces seepage through the embankment (micro-instability) by removing the cover which acts as a filter against sand transport.
9	T: stability A: internal (backward erosion)	deeper slope failure or deformation of a rigid structure induces a hydraulic shortcut through the blanket, which may change the seepage length. [Ubilla et al., 2008]

Table 7.1: Examples of interactions in earthen flood defenses (levees), grouped by external erosion, internal erosion and slope instability.

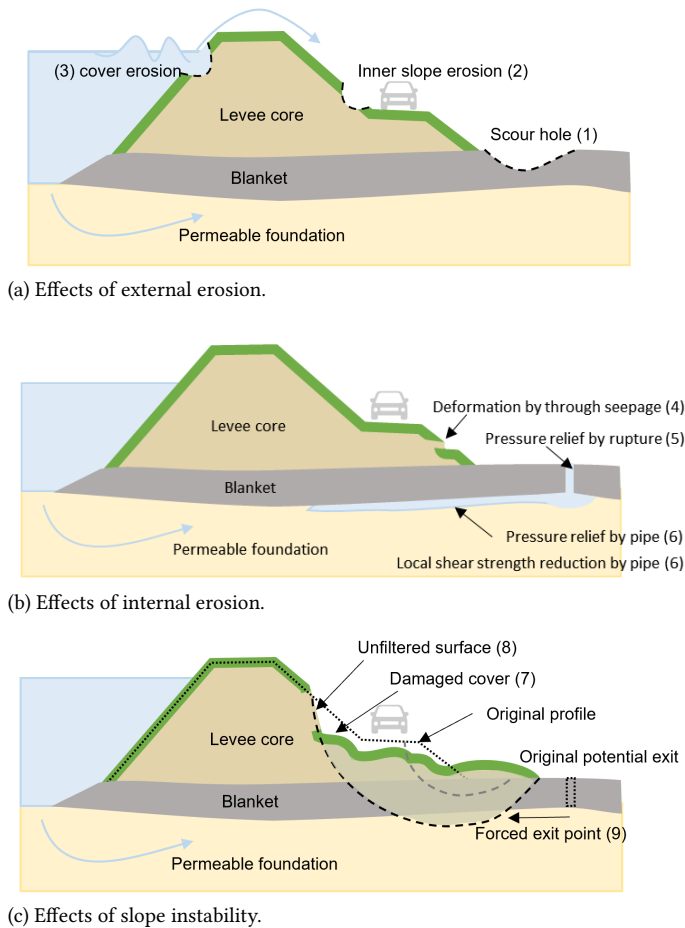


Figure 7.2: Illustration of interaction effects initiated by external erosion, internal erosion and slope instability. Numbers refer to interactions in Table 7.1.

ordered and analyzed. In case of interactions, one would place the trigger event first to be able to include the probability of other events given the trigger. However, the timing or sequence of events may be unknown and can have an important effect on the outcome. Consider the combination of grass cover erosion and slope instability. If the slope failure occurs before wave overtopping, it reduces the erosion-resistance of the grass cover. If overtopping occurs first, this strength reduction by slope failure is irrelevant. When this sequence of events is unknown, or when the interaction cannot be expressed by changing the distribution of a variable, a more flexible approach (2b) is needed, which is described in the next section.

7.3 Quantification method

7.3.1 Reliability method

Structural reliability analysis or probabilistic safety analysis aims to quantify the probability of failure P_F of a structure or system of structures [Baecher and Christian, 2005; Melchers and Beck, 2017b; Song et al., 2021]. The basic components for such a quantitative analysis are failure models, probability distributions of model parameters, and a reliability method to quantify the probability that the model parameters are in the failure domain. The general formulation of this problem is:

$$P_F = P(Z_{sys} \leq 0) = \int_{Z_{sys} \leq 0} f_{\mathbf{X}}(\mathbf{x}) d\mathbf{x} \quad (7.1)$$

Where the system safety margin $Z_{sys} = g(\mathbf{X})$, $Z_{sys} < 0$ defines failure, $g(\cdot)$ denotes a failure model or limit state function (LSF), \mathbf{X} is a vector of random variables, and $f_{\mathbf{X}}(\mathbf{x})$ is the joint probability density of the random variables. Classical methods to solve this problem are Monte Carlo Simulation (MCS) [Rubinstein and Kroese, 2008] and the First Order Reliability Method (FORM) [Hasofer and Lind, 1974].

The reliability method used to quantify the effect of interactions, is based on Monte Carlo Simulation (MCS) because of its flexibility and robustness. The flow chart in Fig. 7.3 presents the MCS framework, which is explained below. First, N_s random samples are generated for all stochastic variables \mathbf{X} , considering their marginal probability density functions (PDF) and the correlation between the variables. Variables which vary randomly in time during an extreme event (e.g., wind speed), need to be re-sampled for different time steps. Although the examples in this chapter are limited to one element (e.g., levee cross section), the method is suitable for systems of multiple elements (N_e , see Fig. 7.3) with correlated variables. Stochastic variables $\mathbf{X}^{i,j,t}$ are drawn for each realization i , element j and time step t . Subsequently, the failure mechanism models $g(\mathbf{X})$ and the system (levee) safety margin $Z_{sys}^{i,j,t}$ are evaluated. The interactions are included in the definition of the failure models, as is explained in more detail in the examples (section 7.3.2 and 7.3.3). Finally, the failure probability P_F is given by the fraction of samples in which system failure occurs ($Z_{sys}^{i,j,t} < 0$) over the total number of samples N_s .

7.3.2 Methods for conceptual examples

Failure models and failure definition

The conceptual analysis is performed for two simple systems: (1) a 2-element parallel system and (2) a series system of two 2-element parallel systems (Fig. 7.4). These examples are sufficiently simple to analyze analytically [Phoon, 2008], yet can illustrate the effects of interactions. Note that for the other simple case of a pure series system, interactions are not relevant as the system is assumed to fail if one of the potential triggers occurs.

In these examples, the failure mechanisms without interaction are described by simple limit state functions (LSF) of two normally distributed variables:

$$Z_A = X_2 - X_1 \quad (7.2)$$

$$Z_B = X_3 - X_1 \quad (7.3)$$

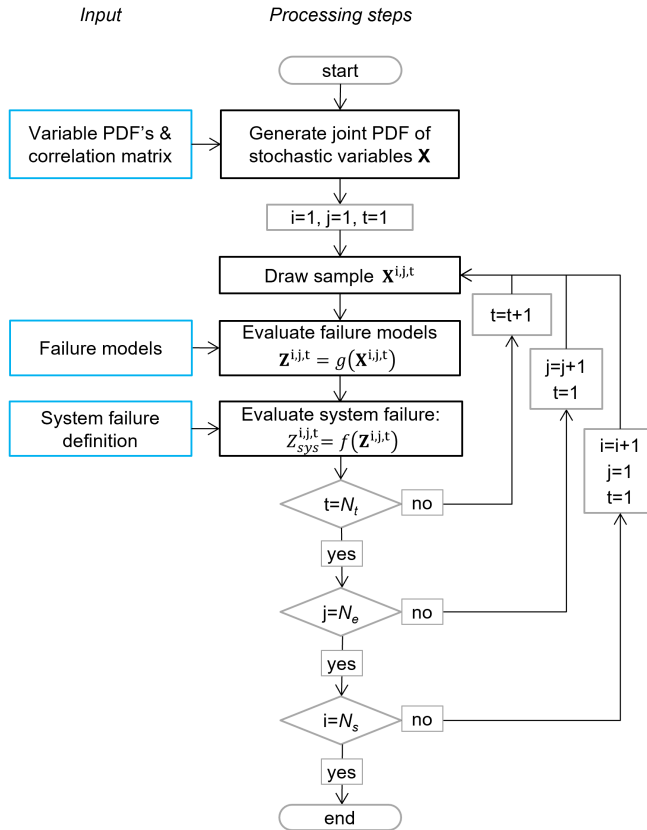


Figure 7.3: Reliability method for interactions based on Monte Carlo Simulation.

$$Z_C = X_4 - X_1 \quad (7.4)$$

$$Z_D = X_5 - X_1 \quad (7.5)$$

In this example, X_1 acts as load, $X_2 \dots X_5$ as resistance, so the load is identical for each component. In the context of flood defenses, X_1 can be interpreted as water level and $X_2 \dots X_5$ as the critical water level of each mechanism. All variables are time-invariant.

The interaction assumed in this example is a reduction (r_{int}) of the strength variable X_3 (for system 1) or X_5 (for system 2) which occurs if sub-mechanism A fails. The limit state functions including interactions are denoted by \hat{Z} and are written as:

$$\hat{Z}_B = X_3(1 - r_{int} \cdot H(X_1 - X_2)) - X_1 \quad (7.6)$$

$$\hat{Z}_D = X_5(1 - r_{int} \cdot H(X_1 - X_2)) - X_1 \quad (7.7)$$

Here $H(\cdot)$ denotes the Heaviside unit step function, which returns 0 when the argument is negative and 1 when positive.

System failure depends on the mechanism failures as defined by Eq. 7.8 (system 1) and Eq. 7.9 (system 2). In case of interactions, Z_B and Z_D are replaced by \hat{Z}_B and \hat{Z}_D .

$$F_{sys1} = [Z_A < 0 \cap Z_B < 0] \quad (7.8)$$

$$F_{sys2} = [(Z_A < 0 \cap Z_B < 0) \cup (Z_C < 0 \cap Z_D < 0)] \quad (7.9)$$

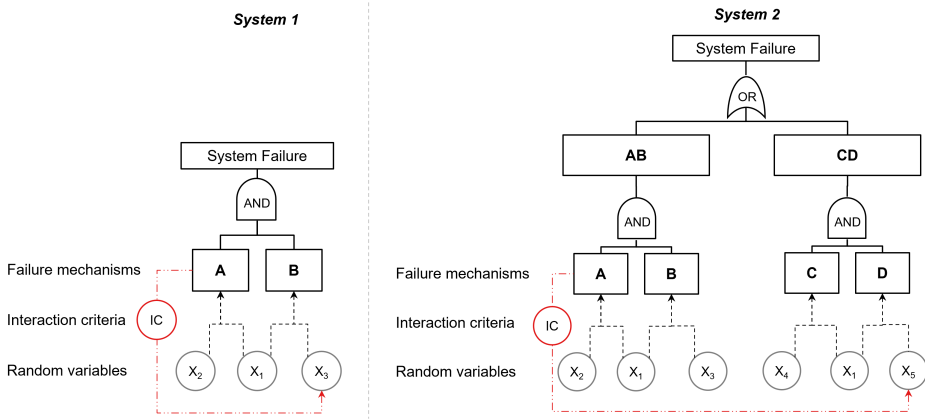


Figure 7.4: Considered systems for conceptual examples. System 1: 2-element parallel system. System 2: Series system of 2 parallel systems.

7

Analyzed cases

The distributions of and correlation between variables are varied to obtain different degrees of correlation between the trigger and affected mechanism ($\rho_{(Z_A, Z_B)}$ for system 1) and different ratios of the failure probability of the trigger and affected mechanism (P_A/P_B). Section 7.4.1 analyzes these variations. All cases have $N_s = 10^5$ samples, $N_e = 1$ element, and $N_t = 1$ timestep.

System 1. The base case of system 1 is characterized by the following variables with mean μ and standard deviation σ : $X_1 \sim \mathcal{N}(\mu = 6, \sigma = 2)$ and $X_2 = X_3 \sim \mathcal{N}(12, 2)$, which are uncorrelated. Subsequently, cases are computed with different means and correlations compared to the base case. The correlation between the strength of the two mechanisms $\rho_{(X_2, X_3)}$ varies between 0, 0.5, 0.8 and 1. To obtain a factor 10 smaller and larger ratio P_A/P_B , μ_{X_3} respectively μ_{X_2} are set to 8.7 instead of 12. System 1 is analyzed with a strength reduction $r_{int} = 0.1$ (10%) and $r_{int} = 0.5$ (50%).

System 2. The base case of system 2 is characterized by the following variables: $X_1 \sim \mathcal{N}(6, 2)$ and $X_2 \dots X_5 \sim \mathcal{N}(12, 2)$, which are uncorrelated. So, the base case has four failure mechanisms which have equal but uncorrelated strength distributions. Again, cases are computed with different means and correlations compared to the base case. The correlation within a subsystem ($\rho_{(X_2, X_3)} = \rho_{(X_4, X_5)}$) varies between 0, 0.5, 0.8 and 1. The correlation across subsystems ($\rho_{(X_2, X_4)} = \rho_{(X_3, X_5)}$) varies between 0, 0.5 and 1. Like for system 1, to obtain a factor 10 smaller and larger ratio P_A/P_D , the mean values $\mu_{X_3} = \mu_{X_5}$ respectively $\mu_{X_2} = \mu_{X_4}$ are set to 8.7 instead of 12. System 2 is analyzed with $r_{int} = 0.5$.

7.3.3 Methods for levee example

This section describes the methods used to analyze a simplified levee example, considering two failure paths: (1) a large slope instability and (2) blanket uplift and backward erosion piping. The considered interaction is number 9 in Table 7.1: initiation of blanket rupture by slope instability. Slope instability may occur at several positions in the levee, ranging from shallow slope failures near the landward toe to deep slope failures cutting through the waterside slope (Fig. 7.5). If the levee remains stable after an initial slope failure near the landward toe, no flooding occurs, but the blanket is still affected which may have an influence on the resistance against backward erosion piping. This influence takes two forms in this example. First, a sufficiently deep slip plane which cuts through the blanket creates a direct hydraulic shortcut through the blanket, so that uplift and rupture are not required anymore to initiate backward erosion. Second, the seepage length for BEP may change depending on the location where the slip plane intersects the blanket bottom. The modeling of the levee example follows the general framework in Figure 7.3. The sections below explain specific modeling choices regarding (stochastic) variables, failure mechanism models and how interactions are included in these models.

Levee characteristics and Hydraulic loads

The impact of the interactions will strongly depend on the specific conditions, as will be shown in the conceptual examples (section 7.4.1). To clearly illustrate the effect of interactions, the levee characteristics used in this levee example are realistic but are chosen in such a way that the impacts of interactions are relatively large. The levee has a sandy core which rests on a clay blanket layer with thickness D_{bl} on top of a homogeneous sandy aquifer with thickness D_{aq} . It has a landward slope of 1:2.5, riverside slope of 1:3, crest height $z_{crest}=5$ m, and a crest width of $L_{crest}=12.5$ m (Fig. 7.5). Table 7.2 shows the stochastic and deterministic variables used in the example. The uncertainties in these variables are similar to values used in other studies on levee reliability in the Netherlands [van der Krogt et al., 2019; Schweckendiek et al., 2014]. Some variables related to slope stability are modeled as deterministic to limit the number of random variables in this example. We assume that k_{aq} and d_{70} are correlated by a Gaussian copula with $\rho = 0.8$, and other variables are uncorrelated.

The failure analysis is conditioned on a range of peak water levels h_{max} between 3 and 5 m above reference level $z = 0$. The flood duration is also uncertain but in this example simplified to either a constant water level (case 1; see section 7.3.3) or a deterministic trapezoidal hydrograph shape with base duration of 30 days at $h = 0$ and peak duration of 1 day at $h = h_{max}$ [Geerse, 2011]. The 30 day flood event is discretized in timesteps of 12 hours around the peak, and the failure processes are evaluated and updated in each time step. All variables are assumed to be constant within a time step. Strength variables are fully dependent between timesteps, and changes in water level are fully determined by the trapezoidal hydrograph shape.

Failure models: slope instability

Slope failure is assumed to occur if the stability factor F_S is smaller than 1. F_S is defined as the ratio of resisting forces and driving forces along the failure plane and is computed with a stability model as function of levee geometry, soil parameters and pore pressures.

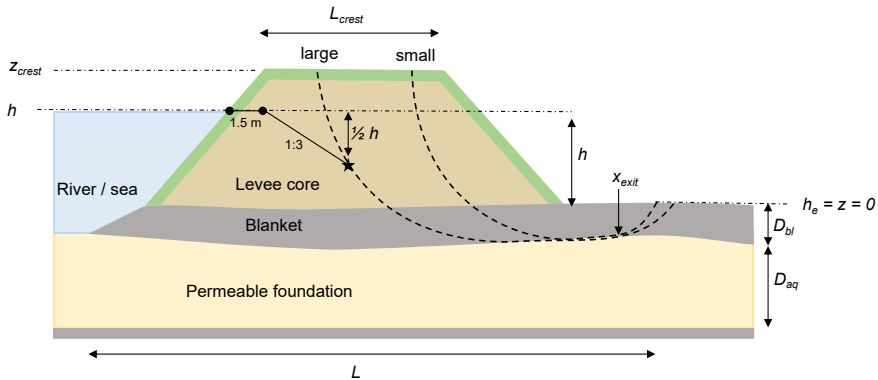


Figure 7.5: Levee example: geometrical parameter definitions and slip plane scenarios (large, small).

Then the limit state function for slope stability is defined as:

$$Z(t) = m_{sl} \cdot F_S(t) - 1 \quad (7.10)$$

where m_{sl} denotes the model uncertainty of the slope stability model, as given in Table 7.2.

Scenarios. Slope failure can occur along a large number of potential slip planes, which are a-priori unknown and depend on the specific combination of parameters. Therefore we use scenarios for the slip plane location. In this example there are only two scenarios: a large slip plane (SIL; Slope Instability Large) which leads to flooding, and a small slip plane (SIS) which does not lead to flooding because of a stable remaining profile but does cut through the blanket layer. A slip plane is assumed to lead to flooding if the location indicated by the star in Fig. 7.5 is part of it. This point is based on a minimal remaining width at the water line of 1.5 m to account for model uncertainty in the slip plane position, and a stable slope of 1:3 between the water level and the assumed height of the residual profile ($1/2h$). Note that failure along the small slip plane may also affect the stability of the large slip plane when water levels increase further during a high-water event. For instance because of a redistribution of weight, a reduction in soil strength at the slip surface or changes in pore water pressure. These effects on secondary slope failures are neglected in this example.

Stability model. We use the D-Stability (version 2021.02) Limit Equilibrium Model [Deltares, 2019] to determine the stability factor for a given input parameter combination. As uplift plays an important role in the interaction, we use the Uplift-Van slip plane model, of which the slip plane has a horizontal part bounded by two circular parts [Van et al., 2005]. Soil strength in sandy layers is modeled with Mohr-Coulomb and in clay layers with SHANSEP [Ladd and Foott, 1974]. For the large slip plane scenario, we force the slip plane position sufficiently close to the water side using a forbidden line between the star in Fig. 7.5 and the landward slope. The small slip plane is forced to cut the blanket using the tangent lines option in D-Stability.

Surrogate model. The large number of D-Stability model evaluations in a MCS analysis requires long computation times. A surrogate model replaces a complex process model

Table 7.2: Stochastic variables for levee example.

variable	symbol	unit	distr.	μ	σ
<i>Hydraulic loads:</i>					
base duration		days	Det.	30	
peak duration		days	Det.	1	
<i>Seepage and Uplift:</i>					
Seepage length	L	m	Logn.	60	5
aquifer thickness	D_{aq}	m	Logn.	25	5
blanket thickness	D_{bl}	m	Logn.	5	0.25
conductivity aquifer	k_{aq}	m/s	Logn.	$1 \cdot 10^{-4}$	$0.5 \cdot 10^{-4}$
conductivity blanket	k_{bl}	m/s	Logn.	$1 \cdot 10^{-6}$	$0.5 \cdot 10^{-6}$
model error uplift	m_u	-	Logn.	1	0.05
<i>Backward Erosion Piping:</i>					
grain size	d_{70}	mm	Logn.	0.180	0.036
angle of repose	θ	°	Det.	37	
constant White	η	-	Det.	0.25	
particle density	ρ_s	kg/m ³	Det.	2650	
model error BEP	m_p	-	Logn.	1	0.12
<i>Slope instability:</i>					
sand, friction angle	ϕ'_s	°	Det.	27	
sand, cohesion	c'_s	kPa	Det.	0	
sand, sat. weight	$\gamma_{sat,s}$	kN/m ³	Det.	20	
sand, unsat. weight	$\gamma_{u,s}$	kN/m ³	Det.	18	
clay, shear strength ratio	S	-	Logn.	0.25	0.03
clay, strength exponent	m_{cl}	-	Det.	0.8	
clay, pre-overburden pressure	POP	kPa	Det.	21.85	
clay, sat. weight	$\gamma_{sat,cl}$	kN/m ³	Logn.	18	1
model error Uplift-Van	m_{sl}	-	Logn.	1.005	0.033

(here: D-Stability) by a simpler model which can be quickly evaluated [Li et al., 2016; Sudret, 2012]. This allows to maintain the robust MCS approach while reducing the computation time. In this example we use multivariate linear interpolation as a very simple surrogate model to obtain stability factors for each realization. More advanced methods were also tested (Lasso Regression and Gaussian Process Regression) but linear interpolation is sufficient for this example. Predictor variables used in the stability surrogate model are: water level h , soil strength of blanket S , leakage length λ , blanket weight $\gamma_{sat,bl}$ and blanket thickness D_{bl} . λ includes the combined effect of k_{aq} , k_{bl} , D_{aq} and D_{bl} on the aquifer head: $\lambda = \sqrt{k_{aq}D_{aq}D_{bl}/k_{bl}}$. In cases with a time varying water level $h(t)$ in combination with a delay dt in slope failure with respect to the water level (see section 7.3.3), the stability factor at time t is computed with the water level at time $t - dt$. Then, the stability factor for each slip plane given a sample of the stochastic variables is:

$$F_{s,i}(t) = \mathcal{M}_i(h(t-dt), S, \gamma_{sat,bl}, D_{bl}, \lambda) \quad (7.11)$$

where i denotes the slip plane scenario (SIS for small and SIL for large) and \mathcal{M} denotes the surrogate model for the stability factor. Apart from the stability factor, the position where

the slip plane cuts the blanket bottom is of interest for the interaction with piping, as it changes the seepage length. This position depends on the slip plane position and blanket-aquifer interface, and is only computed for the small slip plane. Similar to Eq. 7.11, the change in exit location Δx_{exit} is expressed as function of blanket thickness and the water level corresponding to the occurrence of the small slope failure $h(t_{SIS} - dt)$ where t_{SIS} is the time at which the small slope failure occurs:

$$\Delta x_{exit} = \mathcal{M}_{exit}(h(t_{SIS} - dt), D_{bl}) \quad (7.12)$$

The training dataset is composed of all combinations spanning the entire parameter space, with the following ranges of each predictor: $h = \{2, 3, 4, 5\}$ m, $S = \{0.18, 0.20, \dots, 0.30\}$, $\lambda = \{50, 100, \dots, 250\}$ m, $\gamma_{sat,bl} = \{13, 14, \dots, 19\}$ kN/m³, $D_{bl} = \{4.0, 4.5, 5, 5.5\}$ m. This gives 3920 combinations to evaluate in D-Stability.

Failure models: uplift and BEP

The response of the aquifer head to an increased water level is modeled according to Eq. 7.13, which is equivalent to case 7a from the USACE blanket theory [USACE, 2000] or model 4A from Dutch guidelines [TAW, 2004]. This solution is based on horizontal flow in a leaky aquifer, vertical flow (leakage) through the blanket, an infinitely long polder blanket and no riverside blanket:

$$\varphi(x) = \varphi_{polder} + (h - \varphi_{polder}) \frac{\lambda}{L + \lambda} e^{-x/\lambda} \quad (7.13)$$

where φ denotes the aquifer head, x the distance from the landward toe, L the seepage length, and $\lambda = \sqrt{k_{aq} D_{aq} D_{bl} / k_{bl}}$ the polder side leakage length. In our example, $\varphi_{polder} = 0$ m.

Rupture of the blanket is assumed to occur if the aquifer head is larger than the blanket weight (uplift). This model is simply a vertical equilibrium and neglects additional resistance of the soil against tension or shear:

$$Z_{UPL}(t) = m_u \cdot I_u(t) \cdot D_{bl} \cdot (\gamma_{sat,bl} - \gamma_{water}) / \gamma_{water} - (\varphi_{it}(t) - h_e) \quad (7.14)$$

In which m_u denotes the uplift model uncertainty factor [-], D_{bl} the blanket thickness [m], $\gamma_{sat,bl}$ and γ_{water} the weight of the blanket and water [kN/m³], and h_e the polder water level [m]. $I_u(t) = H(\min_{0 \dots t} [Z_{SIS}(t)])$ is an indicator based on the Heaviside unit step function and equals 1 if the blanket is intact and 0 if ruptured by the interaction with the small slope failure which cuts through the blanket layer. It considers the minimum of Z_{SIS} over the interval $0 \dots t$ because the effects of a slope failure will remain in later time steps.

The backward erosion piping (BEP) limit state is the difference between critical head difference H_c and applied head difference $h - h_e$:

$$Z_{BEP}(t) = H_c(t) - (h(t) - h_e) \quad (7.15)$$

where H_c is modeled with the revised Sellmeijer model [Sellmeijer et al., 2011]:

$$H_c(t) = m_s \cdot \hat{L}(t) \cdot \eta \frac{\rho_s - \rho_w}{\rho_w} \tan \theta \frac{d_{70}}{\sqrt[3]{\kappa \hat{L}(t)}} \left(\frac{d_{70,m}}{d_{70}} \right)^{0.6} 0.91 \left(\frac{D_{aq}}{\hat{L}(t)} \right)^{\frac{0.28}{\sqrt[3]{\hat{L}(t)}} - 1} + 0.04 \quad (7.16)$$

In which ρ_s and ρ_w denote the sediment and water density [kg/m^3], η the coefficient of White [-], θ the angle of repose [deg], d_{70} the grain size [m], κ intrinsic permeability [m^2], D_{aq} aquifer thickness [m]. $d_{70,m} = 2.08 \cdot 10^{-4}$ m and m_s is the model uncertainty factor of the Sellmeijer model. \hat{L} is the seepage length including a possible shift Δx_{exit} in exit location due to the interaction with a small slope instability which cuts through the blanket:

$$\hat{L}(t) = L + \Delta x_{exit} \cdot \text{H}(\min_{0 \dots t}(-Z_{SIS}(t))) \quad (7.17)$$

Δx_{exit} is given by Eq. 7.12 and Z_{SIS} by Eqs. 7.10 and 7.11.

System failure definition

In this example, there are two failure paths: either a large slope failure (SIL) or the joint occurrence of uplift (UPL) and backward erosion piping (BEP). Therefore, system failure F_{levee} is defined as the event when:

$$F_{levee} = [Z_{SIL} < 0 \cup (Z_{UPL} < 0 \cap Z_{BEP} < 0)] \quad (7.18)$$

When considering a time-varying water level this becomes:

$$F_{levee} = \left[\min_{0 \dots t}(Z_{SIL}) < 0 \cup \left(\min_{0 \dots t}(Z_{UPL}) < 0 \cap \min_{0 \dots t}(Z_{BEP}) < 0 \right) \right] \quad (7.19)$$

Analyzed cases

Four sub-cases of this levee example are considered, which differ with respect to the timing of slope failures. Levee case 1 is the base case and has a constant water level. Levee case 2 has a time-varying water level as described in section 7.3.3. Levee cases 3 and 4 have a time-varying water level and uncertainty in the timing of the small slope failure, represented by a failure delay dt_{SIS} . In levee case 3, $dt_{SIS} \sim \mathcal{N}(0, 48)$ hours. So on average, the SIS failure occurs at the same water level as in case 1. In levee case 4, $dt_{SIS} \sim \mathcal{N}(96, 48)$ hours, so the SIS failure is on average 96 hours later than in the instantaneous case 1.

7.4 Results

7.4.1 Results of conceptual examples

The conceptual examples aim to investigate under which conditions interactions may have a significant influence on the system failure probability. For instance, the degree of correlation between the components, and the ratio between the component probabilities may influence the effect of the interaction. These examples follow the quantification method of section 7.3.1, with the simplification of only one system-element and one time step.

We express the effect of interactions as the factor $f_{int} = P_{F,int}/P_{F,org}$, where $P_{F,int}$ and $P_{F,org}$ are the system failure probabilities with and without considering interactions, respectively. Furthermore, P_A is used as shorthand for the probability $P(Z_A < 0)$, and likewise P_B , P_C and P_D .

Results system 1 (2-element parallel)

The 2-element parallel system illustrates some basic probabilistic aspects regarding the contribution of interactions in the total failure probability. Of course, the magnitude of the interaction effect is an important determinant for the effect of interactions on the failure probability. In this example we use a 10% and 50% reduction on strength variable X_3 . This analysis focuses on the probabilistic aspects, which determine how frequent this strength reduction occurs and to which extent that affects the total failure probability. As described in section 7.3.2, the variable means and correlations were varied to illustrate how these variations influence the interaction effect f_{int} .

The results of the base case of system 1 are illustrated in Figure 7.6a, which shows the component Z -values with (black) and without (orange) interaction. The weakening due to the interaction appears as a shift in the point cloud. Without interaction, the component probabilities are $P_A = P_B = 0.017$ and the system failure probability $P_{F,org} = P(A \cap B) = 0.0026$ (portion of realizations in the bottom-left quadrant). The interaction triggered by $Z_A < 0$ (with a 50% strength reduction of X_3) decreases the safety margin Z_B , so that P_B increases to 0.031 and $P_{F,int} = 0.016$. Consequently, the interaction effect $f_{int} = 6.3$ for the base case. Now, the ratio between component reliability P_A/P_B and the correlation between the two strength variables $\rho_{(X_2, X_3)}$ are varied. Table 7.3 presents the resulting interaction effects f_{int} . Some of these cases are illustrated in Figure 7.6.

First we discuss the influence of correlation between the strength of the two elements $\rho_{(X_2, X_3)}$. Table 7.3 shows that the stronger this correlation, the smaller the effect of an interaction. This is illustrated in comparing Figure 7.6a and 7.6b. The smaller the correlation $\rho_{(X_2, X_3)}$, the less samples fail both on mechanism A and B, and therefore more samples can be moved to the failure domain by the interaction. In the fully correlated case with equal component probabilities ($P_A = P_B$, Fig. 7.6b), P_F is not affected by the interaction. This is because all samples with $Z_A < 0$, which triggers the interaction, are already in the failure domain. The same holds when $P_A < P_B$ in the fully correlated case. However, if $P_A > P_B$, there is an effect of interaction in the fully correlated case. This is caused by the samples with $Z_A < 0$ and $Z_B > 0$ without interaction, which fail due to the weakening by the interaction ($Z_B < 0$ with interaction).

Second, we discuss the influence of the ratio P_A/P_B . Table 7.3, Figure 7.6c and Figure 7.6d show that the smaller the failure probability of B (the affected) compared to A (the trigger), the larger the interaction effect. If B is already relatively weak without interaction ($P_B \gg P_A$), the conditional probability $P(B|A)$ is close to 1, and further weakening by the interaction will not affect the system probability (Fig. 7.6c). Furthermore, the influence of correlation depends on P_A/P_B . In case of $P_A/P_B = 1$ this influence is relatively large, whereas for $P_A/P_B = 1/10$ and $P_A/P_B = 10$ one needs a very low correlation (< 0.5) to observe a significant change in f_{int} (Table 7.3).

P_A/P_B	50% reduction of X_3				10% reduction of X_3			
	$\rho_{(X_2, X_3)}$				$\rho_{(X_2, X_3)}$			
	0	0.5	0.8	1.0	0	0.5	0.8	1.0
1/10	1.6	1.1	1	1	1.2	1.1	1	1
1	<u>6.3</u>	2.8	1.7	1	1.7	1.6	1.4	1
10	14	11	10	10	2.1	2.0	2.1	2.1

Table 7.3: Results of conceptual analysis system 1 (2-element parallel). Interaction effect f_{int} for different values of P_A/P_B and $\rho_{(X_2, X_3)}$. Base case result underlined.

Results system 2 (series system of two parallel sub-systems)

Compared to system 1, system 2 is more realistic for levee cross sections. The two sub-systems of system 2 can be seen as failure paths which each consist of two failure mechanisms. For instance that a levee fails if either rupture and backward erosion both occur, or slope failure and overtopping erosion both occur. Unlike in system 1, system failure is not only the result of the trigger mechanism and affected mechanism (A and D), but additional mechanisms (B and C) play a role too. Also for system 2 the impact of the interaction on the system reliability is calculated with different values of the variable means and correlations.

The results of the base case of system 2 are illustrated in Figure 7.7. Without interaction, all component probabilities are 0.017 and the system failure probability $P_{F,org} = 0.0051$. The interaction triggered by $Z_A < 0$ decreases the safety margin Z_D (shift in Fig. 7.7a), so that P_D increases to 0.03 and $P_{F,int} = 0.0064$. Consequently, the interaction effect $f_{int} = 1.25$ for the base case of system 2. This interaction effect is considerably smaller than in the base case of system 1 ($f_{int} = 6.3$). The shifted points also appear in Fig. 7.7b, but here show no discontinuity as the change is independent of the occurrence of C. This is due to the system architecture where the interaction affects only one of the parallel mechanisms (D) of the subsystem CD (Fig. 7.4). For low correlations between AB and CD (i.e., small $\rho_{(X_2, X_4)}$), the probability is small that A and C fail together, so in most cases that the interaction from A to D occurs, $Z_C > 0$ so C will be strong enough to prevent the failure path CD (Fig. 7.7b).

The results of the variations in P_A/P_D and the correlations between strength variables are shown in Table 7.4, and some are illustrated in Figure 7.8. Comparing Table 7.3 and Table 7.4 shows that also in system 2, the effects of interaction f_{int} are higher for lower correlation within a subsystem ($\rho_{(X_2, X_3)}$), and for larger ratios between the probability of the trigger and affected mechanism (P_A/P_D). The effect of correlation within a subsystem ($\rho_{(X_2, X_3)}$) is illustrated in comparing Figures 7.7b and 7.8a. Regarding the influence of P_A/P_D , compare Figures 7.8c and 7.8d. In case of $P_A/P_D = 10$ the trigger occurs more often than when $P_A/P_D = 1/10$, resulting in larger effects of interaction on the system reliability.

The effect of correlation between the two subsystems AB and CD is indicated by varying $\rho_{(X_2, X_4)}$. If AB and CD are strongly correlated (i.e. large $\rho_{(X_2, X_4)}$), failure of C is more likely in case of failure A. This results in more interactions occurring in the failure domain of C and D (compare Figs. 7.7b and 7.8b). Therefore, f_{int} is larger when AB and CD are correlated. In practice, AB and CD will often represent different failure paths with different processes and variables involved, so correlation between those subsystems is expected

P_A/P_D	$\rho_{(X_2, X_3)}$ and $\rho_{(X_4, X_5)}$			
	0	0.5	0.8	1.0
	AB and CD uncorrelated: $\rho_{(X_2, X_4)} = 0$			
1/10	1.0	1.0	1.0	1.0
1	<u>1.25</u>	1.05	1.02	1.0
10	3.7	2.8	2.6	2.6
	AB and CD correlated: $\rho_{(X_2, X_4)} = 0.5$			
1/10	1.06	1.0	1.0	1.0
1	1.8	1.2	1.0	1.0
10	5.6	4.0	3.7	3.6
	AB and CD correlated: $\rho_{(X_2, X_4)} = 1$			
1/10	3.4	1.1	1.0	1.0
1	3.2	2.8	1.7	1.0
10	15	11	9.3	9.4

Table 7.4: Results of conceptual analysis system 2. Table shows interaction effect f_{int} for different ratios of component probabilities P_A/P_D and different values of $\rho_{(X_2, X_3)} = \rho_{(X_4, X_5)}$ (correlation within subsystems) and $\rho_{(X_2, X_4)} = \rho_{(X_3, X_5)}$ (correlation between subsystems). Base case result underlined.

to be limited.

7.4.2 Levee example results

To demonstrate the effects of interactions for a realistic case, we analyzed the reliability of a levee with properties as shown in Table 7.2. Levee failure depends on four failure mechanisms: slope instability small (SIS) which cuts through the blanket but does not lead to levee failure, slope instability large (SIL) which directly leads to levee failure, blanket uplift (UPL) and backward erosion piping (BEP) which in combination lead to levee failure. The effect of interaction on the failure probability is illustrated for case 1 (constant water level) and a relatively high water level $h_{max}=4$ m (Table 7.5 and Fig. 7.9).

Table 7.5 show that without interaction, the levee failure probability P_F is dominated by the large slope failure ($P_F \approx P_{SIL}$). The failure path of joint occurrence of uplift and BEP has a much lower probability and contributes only marginally to P_F . After including the interaction triggered by SIS, the uplift probability increases strongly ($P_{UPL} \approx P_{SIS}$). The BEP probability decreases due to the changing L , but this effect is minor. The increased uplift probability increases the system failure probability P_F by a factor 2.6.

Table 7.5: Failure probabilities for levee example case 1 (constant water level), conditional on water level $h_{max}=4$ m.

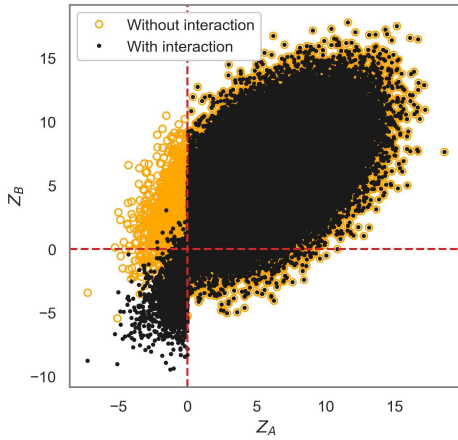
	P_{SIS}	P_{SIL}	P_{UPL}	P_{BEP}	$P_{UPL\&BEP}$	$P_{Failure}$
without interaction	0.24	0.020	0.0039	0.18	0.0014	0.021
with interaction	0.24	0.020	0.24	0.17	0.038	0.054
ratio	1	1	62	0.94	27	2.6

Figure 7.9 visualizes the realizations Z of combinations of failure mechanisms, and how these change due to the interaction. The small and large slope failures (Fig. 7.9a) are

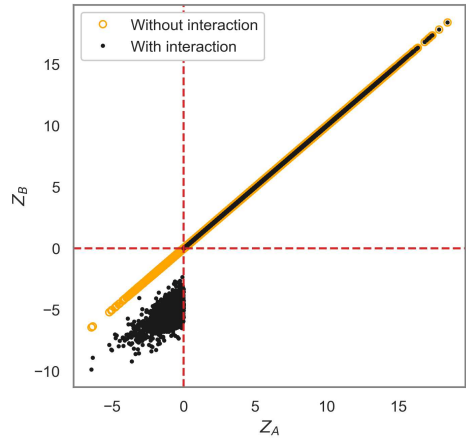
not affected by the interaction, so the Z -values and mechanism probabilities do not change. The interaction triggered by SIS is clearly visible in the decreased uplift resistance Z_{UPL} for all realizations where $Z_{SIS} < 0$ (Fig. 7.9b), which increases the uplift probability from 0.0039 to 0.24. Similarly, the interaction changes the BEP resistance Z_{BEP} by changing the seepage length L but the effect is hardly visible (Fig. 7.9c). The decrease in uplift resistance in part of the samples also appears in Figure 7.9d. Because this decrease is not related to Z_{BEP} , it appears as a shifted point cloud. Levee failure occurs if both UPL and BEP fail, so the bottom left quadrant of Figure 7.9d. Figure 7.9d shows that the number of samples in this failure domain strongly increases due to the interaction.

Figure 7.10 shows the resulting failure probabilities of case 1 conditional on a range of water levels (fragility curves). The magnitude of the interaction effect f_{int} varies with water level (Fig. 7.11) because the ratios of mechanism probabilities vary. In this example, the effect of interaction is significant (up to a factor 4 increase in failure probability), which is in line with the findings from the conceptual examples: the trigger (SIS) has a relatively high probability and the affected mechanism (UPL) is the strongest link in the failure path of uplift & BEP. Note that a similar levee case with a much lower SIS or BEP probability may show no significant interaction effect.

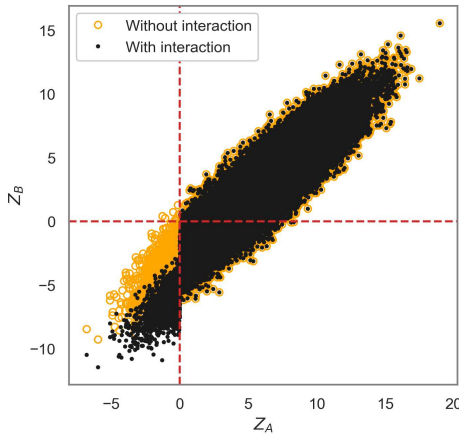
The effect of timing is shown by the cases 1-4 in Figure 7.11. A time-varying water level (case 2) gives a slightly higher interaction effect (f_{int}) than a constant water level (case 1). Although the failure processes respond instantly to the water level, the small slope failure in case 2 can occur at lower levels than h_{max} . And the lower the water level at SIS failure, the closer to the levee will be the slip plane position. Hence the effect of interaction is larger. Adding uncertainty to the timing of the small slope instability (case 3) hardly affect the results. An additional delay in the timing of SIS by 96 hours (case 4) results in lower interaction effects, up to a factor 3.4 instead of 4.2. This lower f_{int} is expected, as more SIS failures occur after the flood peak. In these post-peak failures, the maximum water level applied to BEP is lower than h_{max} , and hence P_{BEP} increases less due to the blanket rupture triggered by SIS. These results show that timing aspects can influence the interactions effect.



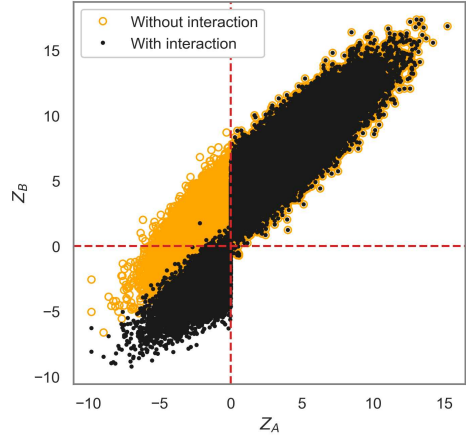
(a) $\rho_{(X_2, X_3)} = 0, P_A/P_B = 1$ (base case).



(b) $\rho_{(X_2, X_3)} = 1.0, P_A/P_B = 1$.



(c) $\rho_{(X_2, X_3)} = 0.8, P_A/P_B = 1/10$.



(d) $\rho_{(X_2, X_3)} = 0.8, P_A/P_B = 10$.

Figure 7.6: Z-Z plots for system 1 with 50% reduction of X_3 ; plots show examples for different correlations $\rho_{(X_2, X_3)}$ and ratios of component probabilities P_A/P_B . Interactions occur where black points deviate from the original yellow points. The failure domains are the bottom-left quadrants, where both $Z_A < 0$ and $Z_B < 0$.

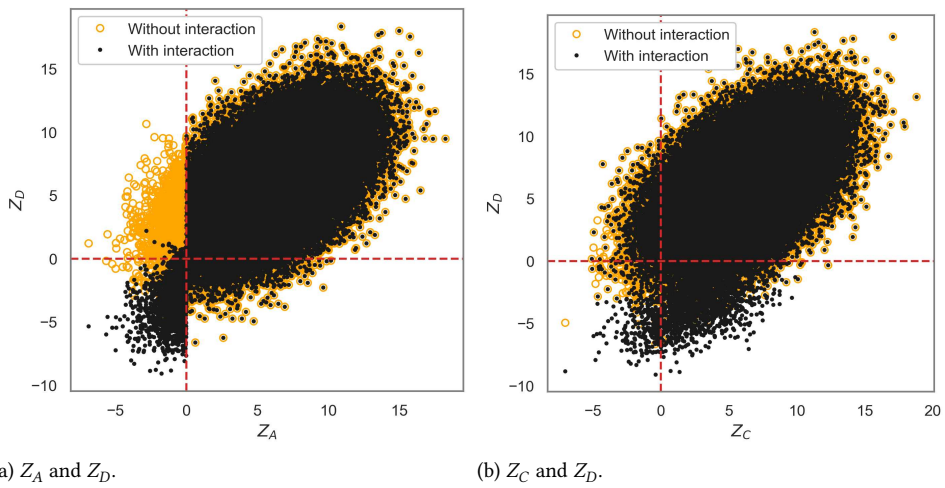
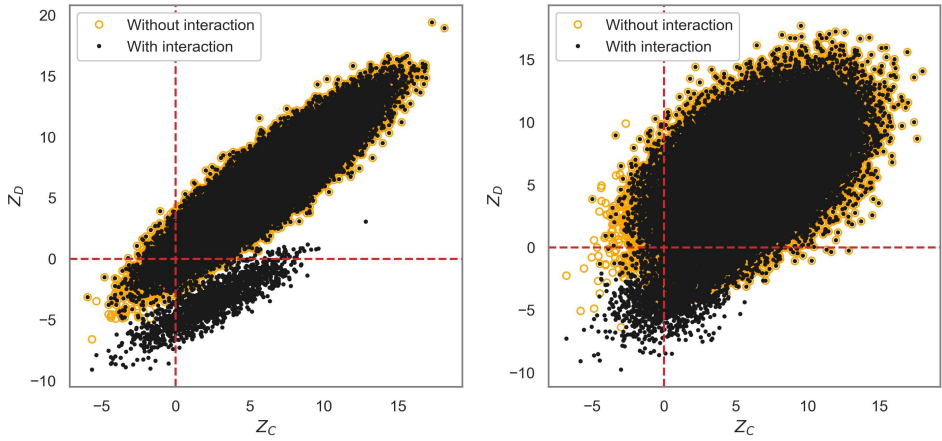
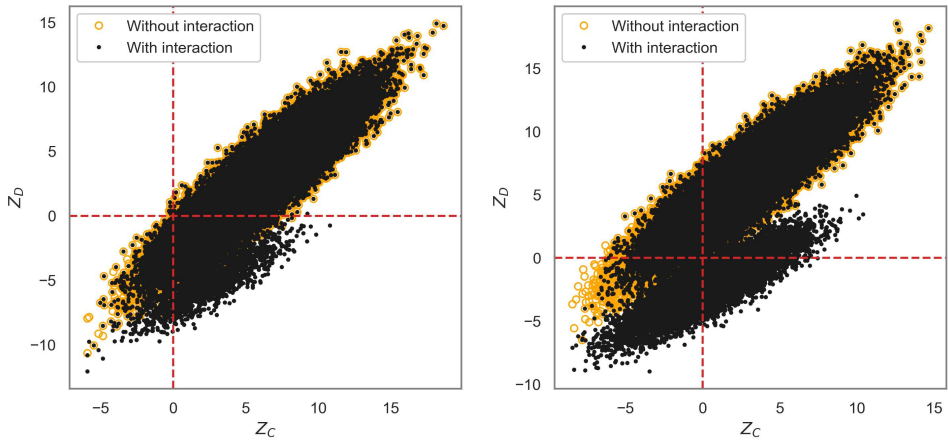
(a) Z_A and Z_D .(b) Z_C and Z_D .

Figure 7.7: Z-Z plots for system 2 base case with $\rho_{(x_2, x_3)} = 0$, $\rho_{(x_2, x_4)} = 0$ and $P_A = P_B = P_C = P_D$. Influencing mechanism is A, affected mechanism is D. Interactions occur where black points deviate from the original yellow circles.



(a) $\rho_{X_2, X_3} = 0.8, \rho_{(X_2, X_4)} = 0, P_A/P_B = 1.$

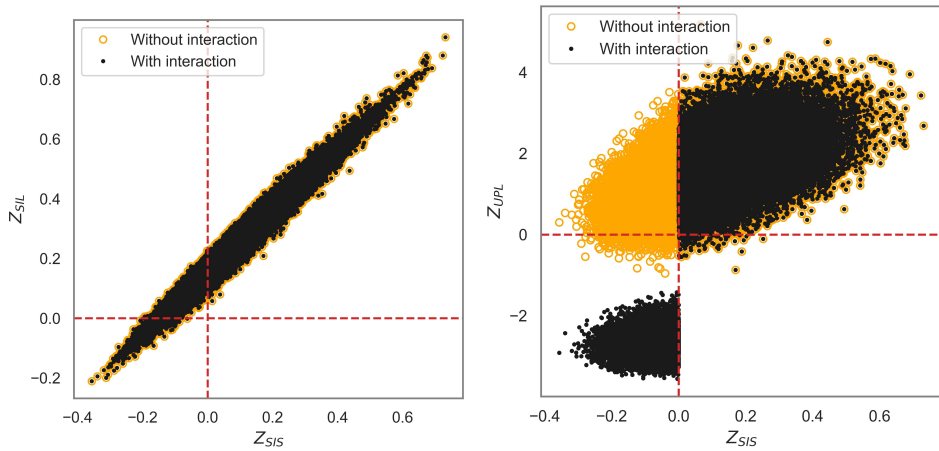
(b) $\rho_{X_2, X_3} = 0, \rho_{(X_2, X_4)} = 0.5, P_A/P_B = 1.$



(c) $\rho_{X_2, X_3} = 0.8, \rho_{(X_2, X_4)} = 0, P_A/P_B = 0.1.$

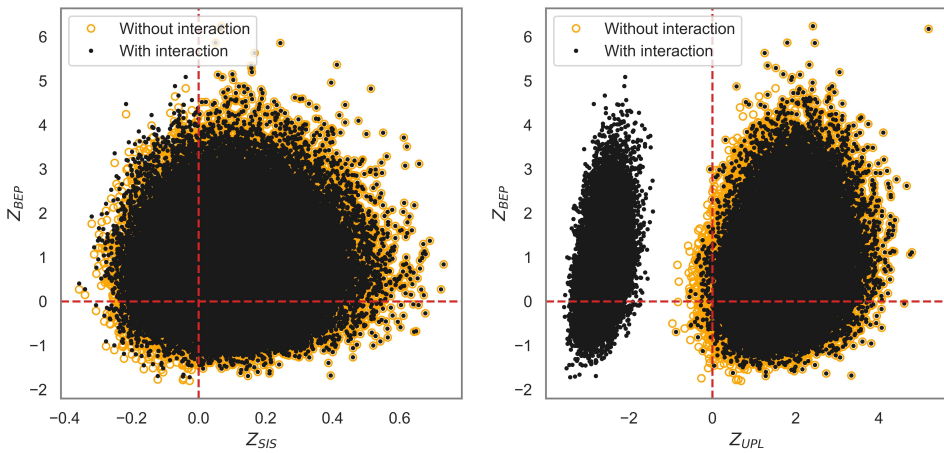
(d) $\rho_{X_2, X_3} = 0.8, \rho_{(X_2, X_4)} = 0, P_A/P_B = 10.$

Figure 7.8: $Z_C - Z_D$ plots for system 2 with 50% strength reduction of X_5 , for different combinations of $\rho_{(X_2, X_3)}$ (correlation within subsystems), $\rho_{(X_2, X_4)}$ (correlation between subsystems) and $P_A/P_B = P_C/P_D$. Interactions occur where black points deviate from the original yellow circles. The failure domains where $Z_C < 0$ and $Z_D < 0$ are the bottom-left quadrants.



(a) Slope instability small (SIS) and large (SIL).

(b) Slope instability small (SIS) and Uplift (UPL).



(c) Slope instability small (SIS) and Backward erosion (BEP). (d) Uplift (UPL) and Backward erosion (BEP).

Figure 7.9: Z-Z plots of different levee failure mechanisms for case 1 (constant water level) and $h=4$ m. Interactions occur where black points deviate from the original yellow circles.

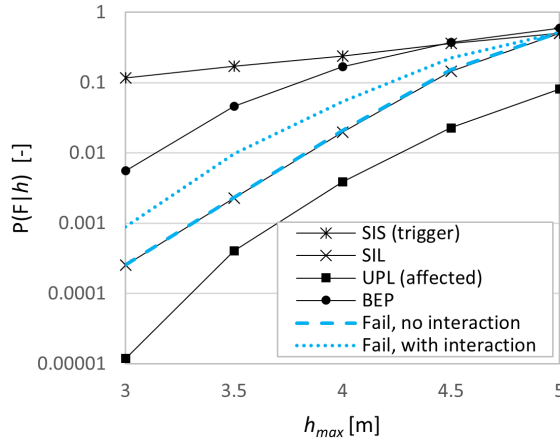


Figure 7.10: Failure probabilities conditional on water level (fragility curve) per mechanism for levee case 1, including the combined levee failure probability ('Fail') with and without interaction. Slope instability small (SIS) and large (SIL), uplift (UPL) and backward erosion piping (BEP). Interaction effect f_{int} is the ratio between the dotted and dashed blue lines, see Fig. 7.11.

7

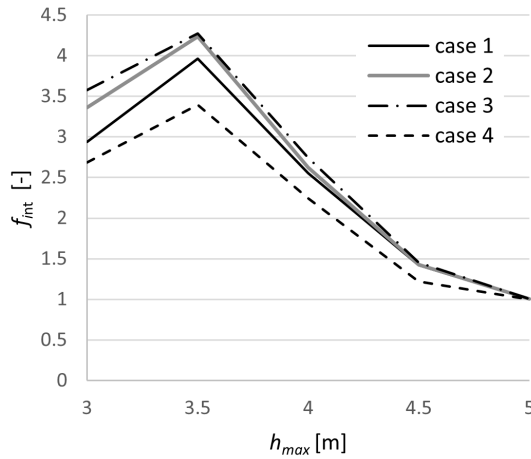


Figure 7.11: Interaction effect f_{int} as function of peak water level h_{max} for case 1 (constant water level), and for time-varying water level with different degrees of delay in SIS failure (cases 2-4).

7.5 Discussion

7.5.1 When are interactions relevant?

For practical applications it may be useful to estimate in an early stage whether interactions are important for the system failure probability, before doing extensive simulations. The conceptual analysis shows that many factors affect the degree to which interactions matter. Three main factors are: (1) the criticality or importance of the affected component (mechanism) to the system reliability, (2) the degree to which this mechanism is affected by interactions, and (3) the probability that the trigger occurs.

These main factors depend on other factors. For instance, the importance of the affected mechanism depends on the system configuration, ratio of mechanism probabilities and correlation between mechanisms. This also holds for different elements in the system: interactions will only matter if they occur in a element (levee section) which has a large influence on the system failure probability. The second factor depends on the degree of strength reduction, but also on the importance of the affected variable in the mechanism performance. In the conceptual examples, the strength was represented in only one variable which was weakened by the interaction. In reality, the strength is generally a combination of variables; if only one of those is weakened, the effect on the mechanism can be smaller.

To estimate the importance of interactions, a conventional reliability analysis (i.e. without interactions) can be used to map the (joint) reliability of all mechanisms and elements. This allows to identify critical elements and mechanisms. Secondly, it requires expert knowledge to identify which interactions are likely to occur and whether these interactions weaken critical mechanisms or elements.

7.5.2 Limitations of the quantification method

Here we discuss two limitations of the applied method, computational cost and time-dependent processes, for which other approaches (section 7.2.3) may be more suitable.

First, the crude MCS method is computationally inefficient. In some cases, the effect of interactions can also be incorporated in a scenario-based approach using event trees, in combination with more efficient techniques such as FORM. For each failure path in the event tree that includes both the trigger mechanism and affected mechanism, the effect of the interaction is then incorporated by an adapted distribution of the affected variable. For this approach it is required that the sequence of events is known (or time is no variable at all) and that the effect of the interaction can be expressed as an adapted distribution of a variable \hat{X} . This requirement is met in the conceptual examples, and for the effect on uplift in levee example case 1, but not for the other levee cases and the effect on BEP through the changing seepage length.

For example, the failure probability of system 2 is the sum of the three failure path probabilities indicated by the black circles in the event tree in Fig. 7.12a:

$$P_F = P(A \cap B) + P(A \cap \bar{B} \cap C \cap \hat{D}) + P(\bar{A} \cap C \cap D) \quad (7.20)$$

Here the overbar denotes non-occurrence, and \hat{D} is mechanism D being evaluated with weakened \hat{X}_5 due to the interaction triggered by A . The individual event probabilities can be evaluated efficiently with FORM, and combined into path probabilities using their

statistical correlation [Roscoe et al., 2015]. A similar approach can be followed for the levee example, as long as the aforementioned requirements are met (Fig. 7.12b).

When using simulation-based methods to evaluate the set of failure models, the efficiency can be improved using variance reduction techniques such as importance sampling, directional sampling and subset simulation. Applying FORM to the set of failure models may give convergence problems with the discontinuities introduced by the step function. This can be avoided by using continuous approximations of the step function.

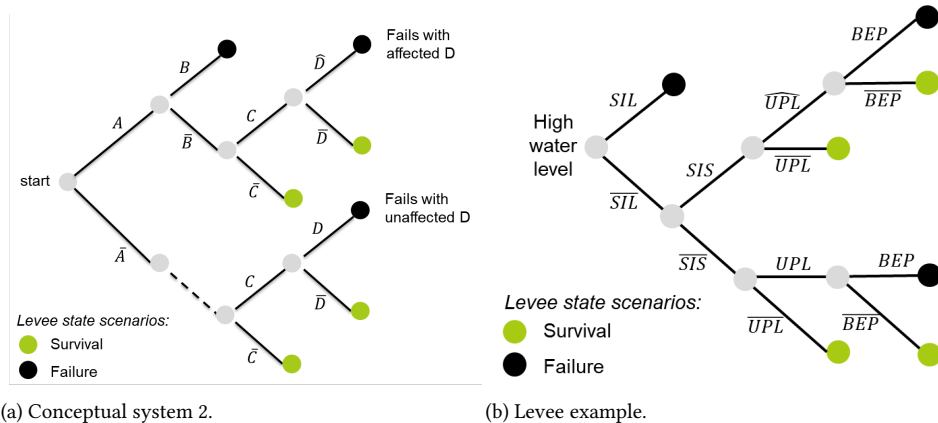


Figure 7.12: Event trees of (a) the conceptual example and (b) the levee example. Branches represent (non-)occurrence of failure mechanisms: slope instability small (SIS) and large (SIL), blanket uplift (UPL) and backward erosion piping (BEP).

The second limitation of the applied method is related to the time-dependence of failure processes within a flood event. When interaction does not only depend on the random variables in the same time step but also on previous time steps, it can become complicated to describe the failure model including interaction. For instance in the levee example the effect of interaction depends on previous time steps and not only on the current (e.g., Eq. 7.12, 7.14 and 7.17). Examples where this becomes more complicated are interactions driven by damages that accumulate each time step. In such cases it may become more practical to evaluate the limit states of each individual mechanism (so without step function describing the interaction) in two steps. After the first LSF evaluation, variables are updated based on the outcomes of the first LSF evaluation. Then, the mechanisms and system failure definition are re-evaluated using the updated variables. The updated variables are then taken to the next time step, which makes sure that the interaction effects propagate in time. For other examples such as interactions between transient groundwater flow and soil erosion, this approach cannot describe the processes and coupled modeling [Rahimi and Shafieezadeh, 2020] may be more suitable. The levee example in this chapter focuses on water level as driving load. Wind- and wave-driven failure processes also fit in the proposed method, but because these are more variable, the temporal correlation between those load variables should be considered in relation to the computational time step.

7.6 Conclusions

Physical interactions between failure mechanisms occur when a trigger mechanism changes physical properties of the system and thereby induce or prevent failure of other (affected) mechanisms. Unlike statistical correlation between mechanism performance, this type of dependence involves a physical change. We discussed different approaches to account for interactions in a reliability analysis, including coupled modeling of the physical processes and scenario-based reliability analysis using event trees. We applied an alternative quantification method based on Monte Carlo simulation. The interactions are included in the limit state functions using step functions. This allows for more flexibility compared to the scenario-based approach in event tree analyses. For instance, the analyst does not need to predefine the sequence in which mechanisms occur and affect other mechanisms. This method is applied to conceptual examples and to a levee subject to failure by landward slope instability and backward erosion piping. The conceptual examples show that the largest interaction effects are expected when the trigger mechanism is relatively likely and the affected mechanism has a relatively large contribution to the system reliability. The levee case study shows that minor slope instabilities which are too small to induce levee failure directly, can lead to levee failure by triggering another failure process (backward erosion through reduction of uplift resistance). In this case, the interaction increased the levee failure probability up to a factor 4 compared to an analysis with correlated but non-interacting failure mechanisms. Although current practice is conservative with respect to several aspects (neglecting correlation between mechanisms, neglecting residual resistance), it is non-conservative with respect to neglecting these interactions. This interaction effect will be strongly case-dependent, for instance depending on the relative contribution of the trigger and affected mechanisms in the system reliability. Based on the findings from this research, further guidelines for practice can be developed that indicate under which conditions interactions need to be accounted for.



8

Conclusions and recommendations

We should not neglect the aspects for which we have no theory while we over emphasize the significance of those for which we do.

Ralph Peck

The aim of this thesis is to improve levee reliability estimates by quantifying the time-dependence of the backward erosion piping (BEP) failure process and its impact on failure probabilities. This problem was studied with a combination of literature review, analysis of previous experiments, additional experiments on different scales, numerical modeling and probabilistic modeling.

8.1 Conclusions

This thesis shows how time-dependent development of backward erosion piping can be quantified and included in levee reliability analyses. Although some parts of the topic have been explored in the past, an important contribution of this thesis is the coherent and connected approach. This is achieved through a combination of experimental research, numerical modeling, a simplified time-dependent piping model, and time-variant reliability analysis. The key findings, which are further elaborated in the next paragraphs, are:

- Analysis of historical levee failures due to BEP and previous experiments indicates that there can be significant time between pipe initiation and breach, highlighting the importance of time-dependence for piping.
- The rate of pipe progression in experiments can be explained by the sediment transport rate, which is shown to depend on the pipe flow conditions. A numerical groundwater flow model which includes this sediment transport process can predict the pipe development in small-scale experiments.
- Relations between the progression rate and levee properties and hydraulic loads as derived with this numerical model can be used in reliability analyses. These analyses

show that including time-dependent pipe development in BEP analyses has a significant positive impact on the levee failure probability, both in coastal and riverine water systems.

Findings from literature and field cases

Time-dependence in piping failure occurs at two distinct time scales: pipe development during an extreme high-water event (hours to days), and long-term development of the reliability over multiple years due to cumulative erosion and strength recovery. Furthermore, time-dependence is present in different parts of the failure process, such as hydraulic loads, groundwater response and pipe growth. This research focuses on the latter, in particular the rate of pipe progression. Estimates of the time scale of pipe progression in historical levee failures (§ 2.2.2) range from 0.1 to 100 m/hour, based on the time between first observation and breach. The vast majority of cases failed around the flood peak water level (+/- one day), on average 4 hours after the peak. Pipe progression rates in previous experiments range from 0.2-8 m/hour. Analysis of these data resulted in a regression model to estimate pipe progression rates based on soil and loading parameters (§ 2.2.4).

Processes determining progression rate

A series of small-scale experiments was used to study the processes determining the rate of pipe development (chapter 3). An array of pressure sensors in the pipe combined with measurements of the pipe geometry provide detailed information on the flow conditions during equilibrium and pipe progression. The observations indicate that pipe progression occurs as rather sudden micro-scale slope failures followed by gradual sediment transport. For uniform sands, the time between these sudden failures, and thus the progression rate, is strongly related to the sediment transport capacity of pipe. An empirical equation for the sediment transport rate in laminar flow (Eq. 3.12) has been derived based on previous experiments with laminar sediment transport in rectangular flumes. This equation is in line with the sediment transport relations during piping erosion obtained from the small-scale experiments in this thesis, although the erosion coefficient is lower for the piping experiments. Finally, the experiments confirm the expected positive relation between progression rate and grain size and overloading.

Large-scale experiments (chapter 4) were conducted to provide a validation test on a realistic levee with a seepage length of 7.2 m and maximum head difference of 1.8 m, a fine sandy aquifer and a clay cover. Furthermore, the setup has a concentrated outflow (hole-exit) which is often present in the field but not in previous experiments. Pipe development could be clearly identified from pressure transducers, and the average progression rate of 0.3 m/hour is in line with the regression model derived in § 2.2.4 based on previous piping experiments. A unique strength recovery experiment (§ 4.4.4) showed that when the levee was re-loaded after nine months, the levee strength had partially recovered. The erosion process started all over again, albeit with 20% lower critical head and 140% higher progression rate. These recovery processes may be caused by factors like levee settlement or siltation, and require further research to quantify any effects on levee reliability against piping.

Modeling time-dependent pipe development

A time-dependent numerical BEP model was developed in chapter 5 to predict pipe progression rates for conditions outside the experimental range. Therefore, a sediment mass balance is implemented in the existing DgFlow 3D finite element equilibrium model, including a sediment transport relation for laminar flow. Model predictions of the critical head were compared to several small-scale experiments and the large-scale experiment, and the model's erosion coefficient C_e was calibrated on these experiments. The critical head in the small-scale experiments is predicted well but challenges remain for modeling the critical head in 3D conditions on larger scales. The critical head in these cases seems to be underpredicted by the model, but rigorous validation is difficult due to a lack of large-scale experiments with local pipe flow measurements. This also results in a relatively low simulated critical head at field scales (scale effects), and therefore is an important topic for further investigation. Regarding the time-dependent pipe development in the regressive and progressive phase, it is encouraging that the model can predict this in the small-scale and large-scale experiments with the same calibrated erosion coefficient $C_e = 0.016$ [-]. When other piping experiments from the literature are included, C_e is described by a log-normal distribution with mean of 0.055 and standard deviation of 0.043. A series of simulations with the model confirms the empirical findings that the progression rates increases with grain size and degree of overloading, and decreases with seepage length. Based on these simulations, regression models are provided to estimate the average (Eq. 5.15) or instantaneous (Eq. 5.18) progression rate in progression-dominated configurations as function of applied head, critical head, seepage length and grain size or hydraulic conductivity. These regression models can be used to estimate the time-dependent pipe development in levees, instead of using the more complex numerical model. Furthermore, it can be used to inform emergency interventions about the order of magnitude of the time to breaching, but it should be recognized that local factors and anomalies can lead to strongly different breaching times for a specific location.

Reliability with time-dependent pipe development

Time-variant reliability analyses were used in chapter 6 to quantify how these time-dependent processes affect the failure probability of levees. Therefore, a time-dependent piping failure model is developed including effects of a varying water level, blanket uplift, heave, backward erosion and flood fighting interventions. Subsequently, a time-variant reliability method is developed to quantify how the failure probability evolves over the years due to cumulative pipe growth over multiple flood events and strength recovery between flood events. Results of a parametric study (§ 6.3.5) indicate the importance of the characteristic flood duration, which depends on the type of water system, seepage length, grain size and blanket thickness. The coastal cases show large reductions in failure probability due to the short flood duration, ranging from a factor 10 to more than a factor 10^6 for large seepage lengths and fine sand. Reductions are smaller for the river cases due to the longer flood duration, but can still be considerable (factor 100) for particular cases such as a long seepage length with fine sand and a thick blanket. For rivers, the effectiveness of flood fighting has an important contribution. The analysis shows that a short pipe (i.e. $< 0.25L$) formed during past events does not have a significant impact on the reliability. Based on the results of the parametric study it is concluded that a considerable part of the Dutch

levees can benefit from including time-dependent pipe development in the BEP failure model. Hence such analyses contribute to reducing or postponing reinforcements.

Interactions between failure mechanisms

Interactions between failure mechanisms occur if a failure process in one failure mechanism affects the failure probability of another failure mechanism through a physical change in levee characteristics. This can become relevant when residual resistance after failure initiation is included in a reliability analysis. Chapter 7 investigates in which situations such interactions may have an effect on the reliability, using conceptual examples and a levee example with an interaction between slope instability and piping. The conceptual examples show that the impact of interactions on the system reliability depends on the importance of the affected failure mechanism, the degree of strength reduction by the trigger and the likelihood of the trigger. Interactions have most impact when the probability of the trigger is large, and the affected mechanism has a large residual resistance (i.e. it is the strongest link in a failure path). The levee example shows that small slope failures, which do not lead to levee failure, can have a negative impact on failure due to blanket uplift and backward erosion piping. For instance, this levee case study showed a factor 4 increase in cross-sectional failure probability due to the small slope failure interaction, compared to an analysis with correlated but non-interacting mechanisms (§ 7.4.2). However, these results are highly case-specific and interactions may have a smaller effect in many other situations. Furthermore, other conservative assumptions may compensate for the non-conservatism from this interaction. Hence interactions may not be relevant for the majority of levee safety assessments, but analysts should be aware that they are potentially important in particular cases.

8.2 Recommendations for research

The following topics require further work to advance the understanding and prediction of backward erosion piping:

8

1. The detailed measurements of pipe flow conditions, pipe geometry and sediment transport rates in the small-scale experiments provide valuable information on the piping process. Not only for time-dependence but also for critical conditions. Such experiments are not available on larger scales. Systematic series of experiments on multiple scales (e.g., 0.3 to 10 m seepage length) with detailed measurements of pipe geometry and pipe flow conditions are needed. These would allow for a validation of the predicted progression rates and reduce the uncertainty about how the critical head depends on the seepage length (scale effect) for 3D situations in case of a concentrated outflow.
2. All experiments and analyses in this thesis assume that the pipe develops in a homogeneous sand layer. It is expected that some aspects of heterogeneity increase the progression rate (overloading after passing a barrier), while other aspects decrease it (meandering path). Therefore it is recommended to investigate the effects of heterogeneity on the progression rate and on the contribution of time-dependence to levee reliability.
3. It is recommended to further validate the regression functions for the progression

rate (Eq. 5.15, Eq. 5.18) with additional simulations considering the effects of parameters such as aquifer geometry, leakage length, soil grading and sediment transport model.

4. Measurements of the critical shear stress in partially formed pipes in the small-scale experiments suggest an effect of upward seepage on grain stability, which is neglected in current BEP models. It is suggested to repeat these measurements in partially developed pipes with the method that was used to measure shear stress in fully developed pipes. When upward seepage has indeed a significant effect, the process can be studied in more detail with a CFD-DEM model.
5. Modeling of the piping process in DgFlow or other 3D numerical BEP models would be improved by integrating the flow resistance of fluidized sediment in the vertical exit channel, as well as implementing a searching pipe path to simulate heterogeneous sands. Following the recommendation on multi-scale experiments, 3D models need to be validated on these sets of experiments to increase the confidence in their extrapolation to field scales. This also includes studying the suitability of modeling the pipe using 1D line elements, and whether this can explain the relatively low critical head as predicted with the 3D model.
6. Alternative piping prevention measures such as sheet piles, geotextiles or relief wells are being implemented more and more. Current (numerical) BEP models are focused on situations without such measures, and often do not contain the relevant (erosion) processes around such measures. Model developments should aim to be sufficiently flexible to simulate such protection measures as well.
7. The time-variant reliability method in this thesis is based on the Monte Carlo method, because the cumulative erosion process introduces dependence between years. As this method is computationally demanding, it is recommended to combine the time-dependent piping process with more efficient reliability methods.

8.3 Recommendations for practice

Although further research is recommended on some aspects (section 8.2), several findings can be readily used in levee management, assessment and design.

1. The main recommendation is to include the effect of time-dependent pipe growth in levee reliability analyses and designs, depending on the water system (coast/river) and levee properties. The findings of chapter 6 indicate in which conditions a significant reduction of the failure probability is expected. In addition to storm-dominated systems, failure probabilities of river levees may be significantly reduced too in case of fine sands, thick blankets and effective flood fighting. Including time-dependent pipe growth can be done with different levels of complexity:
 - (a) Derive a conservative decision rule which indicates whether piping is a potential safety issue given the time-dependence, to be used in screening analyses ("eenvoudige toets" in the current legal safety assessment). And identify under which conditions this can be applied. The current limitation of this rule to coastal levees can be stretched, and the current requirement that no sand boils have occurred can be eliminated when considering a conservative estimate for the initial pipe length.

- (b) A more advanced approach is to use the developed probabilistic time-dependent piping model to derive simplified rules to include the effects of time explicitly in reliability estimates, for instance by a correction factor on the failure probability or critical head. This factor should depend on factors such as the governing high water duration, seepage length and foundation soil.
 - (c) For locations where the above two approaches are insufficient, a more detailed analysis can be done with the time-dependent pipe progression model in a fully probabilistic analysis like in chapter 6.
2. Sand boil detection, flood fighting and monitoring are important. Effective flood fighting increases the positive effect of time-dependent pipe development, and can affect the safety significantly in case of a longer flood duration (river levees).
 - (a) Further consideration is needed on the question whether effectiveness of such interventions should be included in levee safety assessment or designs.
 - (b) If this is desired, perform additional flood fighting exercises to determine the probability of successful intervention (detection, placement, etc.) and required time, and how these effectiveness metrics depend on the flood magnitude.
 - (c) Implement a long-term monitoring program for significant sand boils (also when mitigated), measuring at least flow rate, eroded volume and the head at which erosion starts and stops. This may give useful information on cumulative or accelerated erosion, and reveal urgent safety problems.
 - (d) To benefit more from flood fighting interventions against piping, it is recommended to develop more efficient methods to mitigate sand boils (e.g., sand boil filters) combined with real-time monitoring.
 - (e) Continue inspections for at least a day after the flood peak, as historical failures indicate that piping failure can occur well after the peak.
3. The current safety standard sets a maximum to probability of flooding, regardless of how or how quick a breach occurs. Flood risk can be further reduced by designing levees that do not fail suddenly but more gradually, also called robust or resilient levees. For piping, this would mean for instance a preference for seepage berms over hard barriers such as sheet piles. This reduces damage as a breach likely occurs after the peak when water levels are lower and there is more time for interventions or evacuation. It is recommended to explore the benefits and feasibility of such solutions (technically, economically and legally).
4. Interactions between failure mechanisms can affect the reliability in specific cases (e.g., when the probability of the trigger mechanism is relatively large, and the affected mechanism is the strongest link in a failure path), but are not always recognized because mechanisms are often analyzed separately. Therefore it is recommended to mention this in guidelines for safety assessments. Interactions can generally be included in failure path analyses.

Bibliography

- Abramian, A., Devauchelle, O., Seizilles, G., and Lajeunesse, E. [2019]. Boltzmann distribution of sediment transport. *Physical review letters*, 123(1):014501.
- Adumene, S., Khan, F., Adedigba, S., and Zendehboudi, S. [2021]. Offshore system safety and reliability considering microbial influenced multiple failure modes and their interdependencies. *Reliability Engineering & System Safety*, 215:107862.
- Aielli, S., Pavan, S., Parodi, S., Rosso, A., Tanda, M.G., Marchi, M., Vezzoli, G., Pantano, A., Losa, D., and Sirtori, M. [2018]. Collection and analysis of the reactivation data of the historical sand boils in the Po river levees. In: *European Working Group on Internal Erosion*, pp. 327–335. Springer.
- Akrami, S., Bezuijen, A., van Beek, V., Rosenbrand, E., Terwindt, J., and Förster, U. [2020]. Analysis of development and depth of backward erosion pipes in the presence of a coarse sand barrier. *Acta Geotechnica*, pp. 1–17.
- Allan, R. [2018]. *Backward Erosion Piping*. Phd. thesis, University of New South Wales.
- Andreini, M., Gardoni, P., Pagliara, S., and Sassu, M. [2016]. Probabilistic Models for Erosion Parameters and Reliability Analysis of Earth Dams and Levees. *ASCE-ASME Journal of Risk and Uncertainty in Engineering Systems, Part A: Civil Engineering*, 2(4):04016006.
- Asselman, N.E.M., Peeters, P., and Coen, L. [2010]. *LTV-OM thema Veiligheid, deelrapport 2: Analyse verloop van de maatgevende waterstand en bresgroei*. Technical report, Deltares.
- Baecher, G.B. and Christian, J.T. [2005]. *Reliability and statistics in geotechnical engineering*. John Wiley Sons.
- Barendregt, A., van Noortwijk, J., van der Doef, M., and Holterman, S. [2005]. Determining the time available for evacuation of a dike-ring area by expert judgement. In: *ISSH - Stochastic Hydraulics*. Nijmegen, The Netherlands.
- Barends, F.B.J. [1982]. Transient flow in leaky aquifers. In: *Int. Conf. Modern Approach to Groundwater Resources Management*, volume 1982, pp. 152–161. Capri.
- van Bergeijk, V.M., Verdonk, V.A., Warmink, J.J., and Hulscher, S.J.M.H. [2021]. The Cross-Dike Failure Probability by Wave Overtopping over Grass-Covered and Damaged Dikes. *Water*, 13(5):690.
- Bezuijen, A. and Steedman, R. [2010]. Scaling of hydraulic processes. In: *Physical Modelling in Geotechnics: Proceedings, 7th ICPMG 2010*, pp. 93–98.
- Bligh, W. [1910]. Dams, barrages and weirs on porous foundations. *Engineering News*, 64(26):708–710.
- Bonelli, S. and Benahmed, N. [2010]. Piping flow erosion in water retaining structures: inferring erosion rates from hole erosion tests and quantifying the failure time. In: *IECS 2010, 8th ICOLD European Club Symposium Dam Safety*. ATCOLD, Innsbruck, Austria.
- Botterhuis, T., Waterman, R., and Geerse, C. [2017]. *Gebruikershandleiding Waterstandsverloop: versie 3.0*. Technical report.
- Van den Brink, H.W. [2020]. *Het gebruik van de ECMWF seizoenverwachtingen voor het berekenen van de klimatologie van extreme waterstanden langs de Nederlandse kust*. Technical Report TR-385, KNMI.

- Brown, A.J. and Aspinall, W.P. [2004]. Use of expert opinion elicitation to quantify the internal erosion process in dams. In: *Long-term benefits and performance of dams. 13th Conference of the British Dam Society and the ICOLD European Club*, pp. 282–297. Canterbury, UK.
- Buijs, F.A. [2008]. *Time-dependent reliability analysis of flood defences*. Ph.D. thesis, Newcastle University.
- Buijs, F.A., Hall, J.W., Sayers, P.B., and Van Gelder, P.H.A.J.M. [2009]. Time-dependent reliability analysis of flood defences. *Reliability Engineering and System Safety*, 94(12):1942–1953.
- Buijs, M. [2013]. *Validating a piping model by using field data and historical data of dike failure events*. Msc, VU University Amsterdam.
- Calle, E.O.F. [2002]. *Dijkdoorbraakprocessen*. Technical report, GeoDelft.
- Calle, E.O.F., Dillingh, D., Meermans, W., Vrouwenfelder, A.W.C.M., Vrijling, J.K., De Quellerij, L., and Wubs, A.J. [1985]. *Probabilistisch ontwerpen van waterkeringen*. Technical report.
- Charru, F., Mouilleron, H., and Eiff, O. [2004]. Erosion and deposition of particles on a bed sheared by a viscous flow. *Journal of Fluid Mechanics*, 519:55–80.
- Chen, H.P. and Mehrabani, M.B. [2019]. Reliability analysis and optimum maintenance of coastal flood defences using probabilistic deterioration modelling. *Reliability Engineering and System Safety*, 185:163–174.
- Cheng, N.S. [2004]. Analysis of bedload transport in laminar flows. *Advances in Water Resources*, 27(9):937–942.
- Cheng, N.S. and Chiew, Y.M. [1999]. Incipient sediment motion with upward seepage. *Journal of Hydraulic Research*, 37(5):665–681.
- Chu-Agor, M., Fox, G., and Wilson, G. [2009]. Empirical sediment transport function predicting seepage erosion undercutting for cohesive bank failure prediction. *Journal of hydrology*, 377(1-2):155–164.
- CIRIA [2013]. *The international levee handbook*. Ciria, London, UK.
- van Dam, P. and Beijersbergen, J. [1981]. *Dijkdoorbraak Zalk: 8 januari 1926*. Technical Report S-80.056, Centrum voor Onderzoek Waterkeringen (COW).
- Danka, J. and Zhang, L. [2015]. Dike failure mechanisms and breaching parameters. *J. Geotech. Geoenviron. Eng.*, 141(9):04015039.
- De Rijke, W. [1991]. *Verificatie pipingmodel: Proeven in de deltagoot. Meetverslag*. Technical Report BB91.25, Deltares (WL).
- De Wit, J., Sellmeijer, J., and Penning, A. [1981]. Laboratory testing on piping. In: *Proceedings of the 10th International Conference on Soil Mechanics and Foundation Engineering, Stockholm, Sweden*, pp. 15–19.
- De Wit, J.M. [1984]. *Onderzoek zandmeevoerende wellen Rapportage Modelproeven*. Technical Report CO220887/10, Grondmechanica Delft.
- Delorme, P., Devauchelle, O., Barrier, L., and Metivier, F. [2018]. Growth and shape of a laboratory alluvial fan. *Phys Rev E*, 98(1).
- Delorme, P., Voller, V., Paola, C., Devauchelle, O., Lajeunesse, ., Barrier, L., and Métivier, F. [2017]. Self-similar growth of a bimodal laboratory fan. *Earth Surf. Dynam.*, 5(2):239–252.
- Deltares [2008]. *SBW Hervalidatie Piping - Inventarisatie gegevens zandmeevoerende wellen in de praktijk*. Technical Report 427070-0034, Deltares.
- Deltares [2019]. *D-Stability 20.1 User Manual*. Technical report, Deltares.
- Deltares [2020]. *D-GeoFlow User Manual*. Technical report, Deltares.
- Den Rooijen, H. [1992]. *Literatuuronderzoek doorlatendheid-korrelkarakteristieken*. Technical Report CO-317710/7, Grondmechanica Delft.
- Ding, L.q., Yao, Q.l., Sun, D.y., and Liu, C.j. [2007]. Experimental studies on piping development in three-stratum dike foundations. *Water Resources and Hydropower Engineering*, 2.

- Dirkx, W.J., Beek, R.v., and Bierkens, M. [2020]. The Influence of Grain Size Distribution on the Hydraulic Gradient for Initiating Backward Erosion. *Water*, 12(9):2644.
- El Shamy, U. and Aydin, F. [2008]. Multiscale modeling of flood-induced piping in river levees. *Journal of Geotechnical and Geoenvironmental Engineering*, 134(9):1385–1398.
- van Esch, J.M. [2015]. *WTI 2017: Toetsregel piping. Validation piping module DgFlow (report including primary erosion)*. Technical report, Deltares.
- van Esch, J.M., Sellmeijer, J.B., and Stolle, D. [2013]. Modeling transient groundwater flow and piping under dikes and dams. In: S. Pietruszczak and G. Pande, eds., *3rd International Symposium on Computational Geomechanics (ComGeo III)*, volume 9. Taylor I& Francis, Krakow, Poland.
- Fang, J., Kang, R., and Chen, Y. [2021]. Reliability evaluation of non-repairable systems with failure mechanism trigger effect. *Reliability Engineering and System Safety*, 210:107454.
- Fell, R., Wan, C.F., Cyganiewicz, J., and Foster, M. [2003]. Time for development of internal erosion and piping in embankment dams. *J. Geotech. Geoenviron. Eng.*, 129(4):307–314.
- Foster, M., Fell, R., and Spannagle, M. [2000]. The statistics of embankment dam failures and accidents. *Canadian Geotechnical Journal*, 37(5):1000–1024.
- Fox, G.A., Wilson, G.V., Simon, A., Langendoen, E.J., Akay, O., and Fuchs, J.W. [2007]. Measuring streambank erosion due to ground water seepage: correlation to bank pore water pressure, precipitation and stream stage. *Earth Surface Processes and Landforms*, 32(10):1558–1573.
- Francalanci, S., Parker, G., and Solari, L. [2008]. Effect of Seepage-Induced Nonhydrostatic Pressure Distribution on Bed-Load Transport and Bed Morphodynamics. *Journal of Hydraulic Engineering*, 134(4):378–389.
- Froio, F., Callari, C., Rotunno, A.F., Guidobaldi, A., and Tran, D.K. [2017]. A discrete numerical model of the front region in piping erosion. *Proc. 25th EWG-IE, Delft, Abstract*.
- Fry, J. [2016]. Lessons on internal erosion in embankment dams from failures and physical models. In: *Scour and Erosion: Proceedings of the 8th International Conference on Scour and Erosion (Oxford, UK, 12-15 September 2016)*, p. 41. CRC Press.
- Fu, Z., Su, H., Han, Z., and Wen, Z. [2018]. Multiple failure modes-based practical calculation model on comprehensive risk for levee structure. *Stochastic Environmental Research and Risk Assessment*, 32(4):1051–1064.
- Fujisawa, K., Murakami, A., and Nishimura, S.I. [2010]. Numerical analysis of the erosion and the transport of fine particles within soils leading to the piping phenomenon. *Soils and foundations*, 50(4):471–482.
- Geerse, C.P.M. [2011]. *Hydra-Zoet for the fresh water systems in the Netherlands. Probabilistic model for the assessment of dike heights*. Technical Report PR2168, HKV.
- Georegister [2017]. Nationale Basisbestanden Primaire Waterkeringen. <https://www.nationaalgeoregister.nl/geonetwork/srv/api/records/fa4cc54e-26b3-4f25-b643-59458622901c>.
- Georegister [2021]. Toets- en veiligheidsordelen primaire waterkeringen (WBI). <https://www.nationaalgeoregister.nl/geonetwork/srv/dut/catalog.search#/metadata/bf447383-f2ae-47b0-b124-6c4db12ce689?tab=relations>.
- Ghilardi, T., Franca, M., and Schleiss, A. [2014]. Bulk velocity measurements by video analysis of dye tracer in a macro-rough channel. *Measurement Science and Technology*, 25(3):035003.
- Glynn, M.E. and Kuzmaul, J. [2004]. *Prediction of piping erosion along middle Mississippi river levees - An empirical model*. Technical Report ERDC/GSL TR-04-12.
- Glynn, M.E., Quinn, M.C., and Kuzmaul, J. [2012]. Predicting Piping Potential Along Middle Mississippi River Levees. Société Hydrotechnique de France.
- Govers, G. [1987]. Initiation of motion in overland flow. *Sedimentology*, 34(6):1157–1164.
- Grass, A.J. and Ayoub, R.N. [1982]. Bed load transport of fine sand by laminar and turbulent flow. *Coastal Engineering Proceedings*, 1(18).

- Green, C.H., Parker, D.J., and Tunstall, S.M. [2000]. *Assessment of flood control and management options*. Technical report.
- Griffith, W. [1914]. THE STABILITY OF WEIR FOUNDATIONS ON SAND AND SOIL SUBJECT TO HYDROSTATIC PRESSURE. (ABRIDGED). In: *Institution of Civil Engineers*, volume 197, pp. 221–232. Thomas Telford-ICE Virtual Library.
- Guha-Sapir, D. [2016]. EM-DAT: the CRED/OFDA international disaster database. <https://public.emdat.be/>.
- van den Ham, G. [2019]. *Ijzendoorn summer levee excavation November 2018*. Technical report, Deltares.
- Hanses, U.K. [1985]. *Zur Mechanik der Entwicklung von Erosionskanälen in geschichtetem Untergrund unter Stauanlagen*. Universitätsbibliothek der TU Berlin, Berlin.
- t Hart, R., De Bruijn, H., and De Vries, G. [2016]. *Fenomenologische beschrijving Faalmechanismen WTI*. Technical report, Technical report.
- Hasofer, A.M. and Lind, N.C. [1974]. Exact and invariant second-moment code format. *Journal of the Engineering Mechanics division*, 100(1):111–121.
- Hegnauer, M., Beersma, J., Van den Boogaard, H., Buishand, T., and Passchier, R. [2014]. *Generator of rainfall and discharge extremes (GRADE) for the Rhine and Meuse basins*. Technical report.
- Hoffmans, G. and Van Rijn, L. [2017]. Hydraulic approach for predicting piping in dikes. *Journal of Hydraulic Research*, 56(2):268–281.
- Howard, A.D. and McLane, C.F. [1988]. Erosion of cohesionless sediment by groundwater seepage. *Water Resources Research*, 24(10):1659–1674.
- ICOLD [2017]. *Bulletin 164. Internal erosion of existing dams, levees and dikes, and their foundations*. Technical report, ICOLD-CIGB.
- IenM [2019]. *Bijlage III Voorschriften bepaling sterkte en veiligheid primaire waterkeringen*. Technical report, Ministerie van Infrastructuur en Milieu.
- IPET [2007]. *Performance Evaluation of the New Orleans and Southeast Louisiana Hurricane Protection System. Final Report of the Interagency Performance Evaluation Task Force. Volume IV – The Storm*. Technical report, US Army Corps of Engineers, Washington, DC.
- IRPI [2021]. Database sulle rotte nell'aginataura maestra del Po. <http://geoclimalp.to.cnr.it/Rotte/rotte.php>.
- JCSS [2001]. Probabilistic Model Code - Part 1 - Basis of design. <https://www.jcss-lc.org/jcss-probabilistic-model-code/>.
- Jia, G. and Gardoni, P. [2018]. State-dependent stochastic models: A general stochastic framework for modeling deteriorating engineering systems considering multiple deterioration processes and their interactions. *Structural Safety*, 72:99–110.
- Johanson, J. [1981]. *Dijkdoorbraak van de Heidijk te Nieuwkuyk op 30 december 1880*. Technical report.
- Jongejan, R. and Van Beek, V.M. [2015]. Voorstel voor eenvoudige toetsregel o.b.v. tijd tot falen. Discussienotitie voor WTI2017.
- Jongman, B., Ward, P.J., and Aerts, J.C. [2012]. Global exposure to river and coastal flooding: Long term trends and changes. *Global Environmental Change*, 22(4):823–835.
- Jonkman, S.N. [2005]. Global perspectives on loss of human life caused by floods. *Natural hazards*, 34(2):151–175.
- Jonkman, S.N., Dupuits, E.J.C., and Havinga, F. [2012]. The effects of flood fighting and emergency measures on the reliability of flood defences. *Comprehensive Flood Risk Management, Proceedings of Flood Risk*, pp. 19–23.
- Jonkman, S.N., Kok, M., Van Ledden, M.K., and Vrijling, J.K. [2009]. Risk-based design of flood defence systems: a preliminary analysis of the optimal protection level for the New Orleans metropolitan area. *Journal of Flood Risk Management*, 2(3):170–181.

- Jorissen, R., Kraaij, E., and Tromp, E. [2016]. Dutch flood protection policy and measures based on risk assessment. In: *E3S Web of Conferences*, volume 7, p. 20016. EDP Sciences.
- Kanning, W. [2012]. *The weakest link*. Ph.d. thesis, Delft Technical University.
- Kanning, W., Van Baars, S., and Vrijling, J.K. [2008]. The stability of flood defenses on permeable soils: the London Avenue canal failures in New Orleans. In: *6Th Int. Conference on Case Histories in Geotechnical Engineering, Arlington, VA*, p. 2.72.
- Karamchandani, A., Dalane, J.I., and Bjerager, P. [1992]. Systems Reliability Approach to Fatigue of Structures. *Journal of Structural Engineering*, 118(3):684–700.
- Kenney, T.C. and Lau, D. [1985]. Internal stability of granular filters. *Canadian Geotechnical Journal*, 22(2):215–225.
- Kiureghian, A.D. and Ditlevsen, O. [2009]. Aleatory or epistemic? Does it matter? *Structural Safety*, 31(2):105–112.
- Kok, M., Arevalo, V.J.C., and Vos, M. [2022]. *Towards Improved Flood Defences: Five Years of All-Risk Research into the New Safety Standards*. TU Delft Open, Delft.
- Kok, M., Jongejan, R., Nieuwjaar, M., and Tanczos, I. [2017]. *Fundamentals of flood protection*. Ministry of Infrastructure and the Environment and the Expertise Network for Flood Protection, The Hague, The Netherlands.
- Kovács, G. [1981]. *Seepage Hydraulics*. Elsevier, Amsterdam.
- Kramer, R. [2014]. *Piping under transient conditions: investigation of time-dependent erosion under dikes*. Msc. thesis, University of Twente.
- Kreijns, M., Gerardts, R., and Rutten, M. [2018]. Demonstration sites to speed up innovations in delta technology. *Journal of Cleaner Production*, 171:144–146.
- van der Krogt, M.G., Schweckendiek, T., and Kok, M. [2019]. Do all dike instabilities cause flooding? In: *13th International Conference on Applications of Statistics and Probability in Civil Engineering (ICASP13)*.
- Kuipers, S.F. [1960]. *Een bijdrage tot de kennis van de bodem van Schouwen-Duiveland en Tholen naar de toestand voor 1953*. Ph.D. thesis, Centrum voor Landbouwpublikaties en Landbouwdocumentatie (PUDOC).
- Kézdi, A. [1979]. *Soil physics: selected topics*, volume 25 of *Developments in geotechnical engineering*. Elsevier, Amsterdam.
- Ladd, C.C. and Foott, R. [1974]. New design procedure for stability of soft clays. *Journal of the Geotechnical Engineering Division*, 100(7):763–786.
- Lane, E.W. [1935]. Security from under-seepage-masonry dams on earth foundations. *Transactions of the American Society of Civil Engineers*, 100(1):1235–1272.
- Lee, Y.J. and Song, J. [2011]. Risk Analysis of Fatigue-Induced Sequential Failures by Branch-and-Bound Method Employing System Reliability Bounds. *Journal of Engineering Mechanics*, 137(12):807–821.
- Lendering, K., Jonkman, S., and Kok, M. [2016]. Effectiveness of emergency measures for flood prevention. *Journal of Flood Risk Management*, 9(4):320–334.
- Lendering, K.T., Jonkman, S.N., and Kok, M. [2014]. *Effectiveness and reliability of emergency measures for flood prevention*. Technical report, Delft University of Technology.
- Li, D.Q., Zheng, D., Cao, Z.J., Tang, X.S., and Phoon, K.K. [2016]. Response surface methods for slope reliability analysis: Review and comparison. *Engineering Geology*, 203:3–14.
- Li, G.X., Jie, Y.X., and Li, Q.Y. [2003]. Yangtze dyke and its strengthening. *Lowland Technology International*, 5(2):39–46.
- Liu, X.X. and Chiew, Y.M. [2012]. Effect of seepage on initiation of cohesionless sediment transport. *Acta Geophysica*, 60(6):1778–1796.
- Lobkovsky, A.E., Orpe, A.V., Molloy, R., Kudrolli, A., and Rothman, D.H. [2008]. Erosion of a granular bed driven by laminar fluid flow. *Journal of Fluid Mechanics*, 605:47–58.

- Loiseleux, T., Gondret, P., Rabaud, M., and Doppler, D. [2005]. Onset of erosion and avalanche for an inclined granular bed sheared by a continuous laminar flow. *Physics of fluids*, 17(10):103304.
- Lu, Y., Chiew, Y.M., and Cheng, N.S. [2008]. Review of seepage effects on turbulent open-channel flow and sediment entrainment. *Journal of Hydraulic Research*, 46(4):476–488.
- Malverti, L., Lajeunesse, E., and Métivier, F. [2008]. Small is beautiful: Upscaling from microscale laminar to natural turbulent rivers. *Journal of Geophysical Research: Earth Surface*, 113(F4).
- Mantz, P.A. [1977]. Incipient transport of fine grains and flakes by fluids-extended shield diagram. *Journal of the Hydraulics division*, 103(ASCE 12992).
- Marchi, M., Martínez, M.F.G., Gottardi, G., and Tonni, L. [2021]. Field measurements on a large natural sand boil along the river Po, Italy. *Quarterly Journal of Engineering Geology and Hydrogeology*, 54(4):qjegh2020–097.
- Martínez, M.F.G., Tonni, L., Marchi, M., Tozzi, S., and Gottardi, G. [2020]. Numerical Tool for Prediction of Sand Boil Reactivations near River Embankments. *Journal of Geotechnical and Geoenvironmental Engineering*, 146(12):06020023.
- Meango, T.J.M. and Ouali, M.S. [2019]. Failure interaction models for multicomponent systems: a comparative study. *SN Applied Sciences*, 1(66).
- Meango, T.J.M. and Ouali, M.S. [2020]. Failure interaction model based on extreme shock and Markov processes. *Reliability Engineering and System Safety*, 197:106827.
- Meehan [2018]. Feather River Hydrographs at Levee Breaks. <https://web.stanford.edu/~meehan/flood/peak.html>.
- Melchers, R.E. and Beck, A.T. [2017a]. *Structural Reliability Analysis and Prediction*. John Wiley Sons Ltd.
- Melchers, R.E. and Beck, A.T. [2017b]. Time-Dependent Reliability. In: *Structural Reliability Analysis and Prediction*, pp. 179–245.
- Merz, B., Blöschl, G., Vorogushyn, S., Dottori, F., Aerts, J.C., Bates, P., Bertola, M., Kemter, M., Kreibich, H., and Lall, U. [2021]. Causes, impacts and patterns of disastrous river floods. *Nature Reviews Earth and Environment*, pp. 1–18.
- Miesel, D. [1977]. Untersuchungen zum Problem der rückschreitenden Erosion als Ursache des hydraulischen Grundbruches in Böden mit inhomogener Schichtfolge. In: *Veröffentlichungen des Grundbauinstitutes der Technischen Universität Berlin*, volume 1, pp. 56–71. Technischen Universität Berlin, Berlin.
- Miesel, D. [1978]. Rückschreitende erosion unter bindiger Deckschicht. In: *Baugrundtagung 1978*, pp. 599–626. DGGT, Berlin.
- Mizutani, H., Nakagawa, H., Yoden, T., Kawaike, K., and Zhang, H. [2013]. Numerical modelling of river embankment failure due to overtopping flow considering infiltration effects. *Journal of Hydraulic Research*, 51(6):681–695.
- de Moel, H., Asselman, N.E.M., and Aerts, J.C.J.H. [2012]. Uncertainty and sensitivity analysis of coastal flood damage estimates in the west of the Netherlands. *Nat. Hazards Earth Syst. Sci.*, 12(4):1045–1058.
- Moench, A.F. and Barlow, P.M. [2000]. Aquifer response to stream-stage and recharge variations. I. Analytical step-response functions. *Journal of Hydrology*, 230(3):192–210.
- Montalvo-Bartolomei, A. and Robbins, B. [2020]. Laboratory Evaluation of Lightweight Sand Boil Filters. In: *ASDSO Dam Safety 2019*. Association of State Dam Safety Officials, Orlando, Florida.
- Montalvo-Bartolomei, A.K., Robbins, B.A., and Murphy, J.W. [2018]. *Experimental Evaluation of Kovács' Equations for Estimating Critical Gradients*. Technical report.
- Morris, M.W., Allsop, W., Buijs, F., Kortenhaus, A., Doorn, N., and Lesniewska, D. [2008]. Failure modes and mechanisms for flood defence structures. In: P. Samuels, S. Huntington, W. Allsop, and J. Harrop, eds., *FloodRisk2008*, pp. 693–701. Taylor and Francis, Oxford, UK.

- Muller-Kirchenbauer, H. [1980]. Zum zeitlichen Verlauf der ruckschreitenden erosion in geschichtetem Untergrund unter Dammen und Stauanlagen. In: DVWK, ed., *Talsperrenbau und bauliche Probleme der Pumpspeicherwerke*, volume 43, pp. 1–25. Verlag Paul Parey, Hamburg, Germany.
- Murthy, D.N.P. and Nguyen, D.G. [1985]. Study of a multi-component system with failure interaction. *European Journal of Operational Research*, 21(3):330–338.
- Nagy, L. [2014]. *Buzgárok az árvízvédelemben*. OVF Országos Vízügyi Főigazgatóság, Budapest.
- Nagy, L. and Toth, S. [2005]. *Detailed Technical Report on the collation and analysis of dike breach data with regards to formation process and location factors*. Technical report.
- Ouriemi, M., Aussillous, P., and Guazzelli, E. [2009]. Sediment dynamics. Part 1. Bed-load transport by laminar shearing flows. *Journal of Fluid Mechanics*, 636:295–319.
- Ouriemi, M., Aussillous, P., Medale, M., Peysson, Y., and Guazzelli, I. [2007]. Determination of the critical Shields number for particle erosion in laminar flow. *Physics of Fluids*, 19(6):061706.
- Ozkan, S., Adrian, D.D., Sills, G.L., and Singh, V.P. [2008]. Transient head development due to flood induced seepage under levees. *Journal of geotechnical and geoenvironmental engineering*, 134(6):781–789.
- Paprotny, D., Sebastian, A., Morales-Nápoles, O., and Jonkman, S.N. [2018]. Trends in flood losses in Europe over the past 150 years. *Nature Communications*, 9(1):1985.
- Parekh, M.L., Kanning, W., Bocovich, C., Mooney, M.A., and Koelewijn, A.R. [2016]. Backward Erosion Monitored by Spatial–Temporal Pore Pressure Changes during Field Experiments. *J. Geotech. Geoenviron. Eng.*, 142(10):04016050.
- Parhizkar, M.H. [1993]. *Verification of Piping Rules*. Ph.D. thesis, IHE Delft.
- Paté-Cornell, M.E. [1996]. Uncertainties in risk analysis: Six levels of treatment. *Reliability Engineering and System Safety*, 54(2):95–111.
- Pei, L., Chen, C., He, K., and Lu, X. [2022]. System reliability of a gravity dam-foundation system using Bayesian networks. *Reliability Engineering & System Safety*, 218:108178.
- Peng, M. and Zhang, L. [2011]. Breaching of Changkai Levee in June 2010 in Jiangxi Province, China. *Geotechnical special publication*, p. 476.
- Phoon, K.K. [2008]. Numerical recipes for reliability analysis—a primer. In: *Reliability-Based Design in Geotechnical Engineering*, pp. 13–87. CRC Press.
- Pietrus, T.J. [1981]. *An experimental investigation of hydraulic piping in sand*. Ph.D. thesis, University of Florida.
- Pilotti, M. and Menduni, G. [2001]. Beginning of sediment transport of incoherent grains in shallow shear flows. *Journal of Hydraulic Research*, 39(2):115–124.
- Pol, J. [2020]. *Shields-Darcy piping model. Verschilanalyse met Sellmeijer en D-GeoFlow*. Technical report, Delft University of Technology.
- Pol, J., Kanning, W., and Jonkman, S. [2020]. FPH piping experiment December 2018. <https://doi.org/10.4121/uuid:3b44f87b-cc0f-4c03-a192-e81078dec53d>.
- Pol, J., Kok, M., Barneveld, H., Morales-Napoles, O., and Schielen, R. [2015]. Evaluation of design hydrograph methods and probabilistic methods for estimating design water levels on the river Meuse. In: *E-proceedings of the 36th IAHR World Congress, The Hague, the Netherlands, 28 June-3 July 2015*.
- Pol, J., Van Beek, V.M., Kanning, W., and Jonkman, S.N. [2019]. Progression rate of backward erosion piping in laboratory experiments and reliability analysis. In: J. Ching, D. Li, and J. Zhang, eds., *7th International Symposium on Geotechnical Safety and Risk (ISGSR)*, pp. 764–769. Research Publishing, Tapei.
- Pol, J.C. [2022]. Discussion of ‘Influence of erosion on piping in terms of field conditions’ by G. Hoffmans. *Journal of Hydraulic Research*.

- Pol, J.C., Kanning, W., van Beek, V.M., Robbins, B.A., and Jonkman, S.N. [2022a]. Temporal evolution of backward erosion piping in small-scale experiments. *Acta Geotechnica*.
- Pol, J.C., Kanning, W., and Jonkman, S.N. [2021a]. Temporal Development of Backward Erosion Piping in a Large-Scale Experiment. *Journal of Geotechnical and Geoenvironmental Engineering*, 147(2):04020168.
- Pol, J.C., Kanning, W., and Jonkman, S.N. [2022b]. Strength Recovery in a Large-Scale Backward Erosion Piping Experiment. In: *28th Annual Meeting of the European Working Group on Internal Erosion*. Sheffield, UK.
- Pol, J.C., Van Klaveren, W., Kanning, W., Van Beek, V.M., Robbins, B.A., and Jonkman, S.N. [2021b]. Progression Rate of Backward Erosion Piping: Small Scale Experiments. In: J. Rice, X. Liu, M. McIlroy, I. Sasanakul, and M. Xiao, eds., *10th international conference on scour and erosion (ICSE-10)*, pp. 93–102. International Society of Soil Mechanics and Geotechnical Engineering (ISSMGE), Arlington, Virginia, USA.
- Poussin, J., Bubeck, P., Aerts, J., and Ward, P. [2012]. Potential of semi-structural and non-structural adaptation strategies to reduce future flood risk: case study for the Meuse. *Natural Hazards and Earth System Sciences*, 12(11):3455–3471.
- Rahimi, M. and Shafieezadeh, A. [2020]. Coupled backward erosion piping and slope instability performance model for levees. *Transportation Geotechnics*, 24:100394.
- Rahimi, M., Shafieezadeh, A., Wood, D., and Kubatko, E. [2020]. A physics-based approach for predicting time-dependent progression length of backward erosion piping. *Canadian Geotechnical Journal*, 0(ja):null.
- Remmerswaal, G., Vardon, P.J., and Hicks, M.A. [2021]. Evaluating residual dyke resistance using the Random Material Point Method. *Computers and Geotechnics*, 133:104034.
- van Rhee, C. [2015]. Slope failure by unstable breaching. *Proceedings of the Institution of Civil Engineers - Maritime Engineering*, 168(2):84–92.
- Rice, J., van Beek, V., and Bezuijen, A. [2021]. History and Future of Backward Erosion Research. In: *Proceedings of the 10th International Conference on Scour and Erosion (ICSE-10)*, pp. 1–24.
- Rice, J.D. and Polanco, L. [2012]. Reliability-based underseepage analysis in levees using a response surface–Monte Carlo simulation method. *Journal of geotechnical and geoenvironmental engineering*, 138(7):821–830.
- Richards, K.S. and Reddy, K.R. [2007]. Critical appraisal of piping phenomena in earth dams. *Bulletin of Engineering Geology and the Environment*, 66(4):381–402.
- Rijkswaterstaat [1895]. *Verslag over den stormvloed van 22/23 December 1894*. Technical report.
- van Rinsum, G. [2018]. *Grass revetment reinforcements: A study into the effectiveness of measures applied during critical conditions*. Technical report.
- Risher, P. and Gibson, S. [2016]. Applying Mechanistic Dam Breach Models to Historic Levee Breaches. In: *FLOODrisk 2016 - 3rd European Conference on Flood Risk Management*.
- Robbins, B. [2016]. Numerical modeling of backward erosion piping. *Applied Numerical Modeling in Geomechanics*, pp. 551–558.
- Robbins, B., Montalvo-Bartolomei, A., and Griffiths, D. [2020a]. Analyses of Backward Erosion Progression Rates from Small-Scale Flume Experiments. *Journal of Geotechnical and Geoenvironmental Engineering*, 146(9):04020093.
- Robbins, B.A. [2022]. *Finite Element Modeling of Backward Erosion Piping*. Phd, Colorado School of Mines.
- Robbins, B.A., van Beek, V.M., Pol, J.C., and Griffiths, D.V. [2022]. Errors in finite element analysis of backward erosion piping. *Geomechanics for Energy and the Environment*, p. 100331.
- Robbins, B.A. and Griffiths, D.V. [2021]. A two-dimensional, adaptive finite element approach for simulation of backward erosion piping. *Computers and Geotechnics*, 129:103820.

- Robbins, B.A., Sharp, M.K., and Corcoran, M.K. [2015]. Laboratory Tests for Backward Erosion Piping. In: *Geotechnical Safety and Risk V*, pp. 849–854. IOS Press.
- Robbins, B.A., Stephens, I.J., Beek, V.M.V., Koelewijn, A.R., and Bezuijen, A. [2020b]. Field measurements of sand boil hydraulics. *Géotechnique*, 70(2):153–160.
- Robbins, B.A., Stephens, I.J., Leavell, D.A., López-Soto, J.F., and Montalvo-Bartolomei, A.M. [2018]. Laboratory piping tests on fine gravel. *Canadian Geotechnical Journal*, 55(11):1552–1563.
- Robbins, B.A., Van Beek, V.M., Lopez-Soto, J.F., Montalvo-Bartolomei, A.M., and Murphy, J. [2017]. A novel laboratory test for backward erosion piping. *International Journal of Physical Modelling in Geotechnics*, 18(5):266–279.
- Roscoe, K., Diermanse, F., and Vrouwenvelder, T. [2015]. System reliability with correlated components: Accuracy of the Equivalent Planes method. *Structural Safety*, 57(Supplement C):53–64.
- Rosenbrand, E., van Beek, V., and Bezuijen, A. [2021]. Numerical modelling of the resistance of the coarse sand barrier against backward erosion piping. *Géotechnique*, pp. 1–29.
- Rosenbrand, E., van Beek, V., Bezuijen, A., Akrami, S., Terwindt, J., Koelewijn, A., and Förster, U. [2020]. Multi-scale experiments for a coarse sand barrier against backward erosion piping. *Géotechnique*, pp. 1–11.
- Rosenbrand, E., Wopereis, L., Wiersma, A., Kanning, W., Bezuijen, A., and Blinde, J. [2022]. *Kennis voor Keringen 2021: Achtergrondrapport Voorlanden*. Technical report, Deltares.
- Rotunno, A.F., Callari, C., and Froiio, F. [2017]. Computational Modeling of Backward Erosion Piping. In: *Models, Simulation, and Experimental Issues in Structural Mechanics*, pp. 225–234. Springer.
- Rotunno, A.F., Callari, C., and Froiio, F. [2019]. A finite element method for localized erosion in porous media with applications to backward piping in levees. *International Journal for Numerical and Analytical Methods in Geomechanics*, 43(1):293–316.
- Rubinstein, R.Y. and Kroese, D.P. [2008]. *Simulation and the Monte Carlo method*. John Wiley and Sons.
- Schmertmann, J. [2000]. 'No-filter factor of safety against piping through sands'. In: F. Silva and E. Kavazanjian, eds., *Judgment and Innovation*, pp. 65–105. ASCE, Reston, VA, USA.
- Schweckendiek, T., Vrouwenvelder, A.C.W.M., and Calle, E.O.F. [2014]. Updating piping reliability with field performance observations. *Structural Safety*, 47:13–23.
- Seizilles, G., Lajeunesse, E., Devauchelle, O., and Bak, M. [2014]. Cross-stream diffusion in bedload transport. *Physics of Fluids*, 26(1):013302.
- Sellmeijer, H., de la Cruz, J.L., van Beek, V.M., and Knoeff, H. [2011]. Fine-tuning of the backward erosion piping model through small-scale, medium-scale and IJkdijk experiments. *European Journal of Environmental and Civil Engineering*, 15(8):1139–1154.
- Sellmeijer, J. [1988]. *On the mechanism of piping under impervious structures*. Ph.d. thesis, Delft University of Technology.
- Sellmeijer, J. [2006]. Numerical computation of seepage erosion below dams (piping). In: H. Verheij and G. Hoffmans, eds., *3rd International Conference on Scour and Erosion (ICSE-3)*, pp. 596–601. CURNET, Amsterdam, The Netherlands.
- Sellmeijer, J. and Koenders, M. [1991]. A mathematical model for piping. *Applied Mathematical Modelling*, 15(11):646–651.
- Shen, J. [1981]. *Discharge characteristics of triangular-notch thin-plate weirs*. United States Department of the Interior, Geological Survey.
- Sills, G., Vroman, N., Wahl, R., and Schwanz, N. [2008]. Overview of New Orleans levee failures: lessons learned and their impact on national levee design and assessment. *Journal of Geotechnical and Geoenvironmental Engineering*, 134(5):556–565.
- Silvis, F. [1991]. *Verificatie piping model: proeven in de deltagoot*. Technical report, Grondmechanica Delft.

- Slijkhuis, K.A.H., Van Gelder, P.H.A.J.M., Vrijling, J.K., and Vrouwenvelder, A.C.W.M. [1999]. On the lack of information in hydraulic engineering models. In: *Safety and Reliability, Proceedings of ESREL '99-The Tenth European Conference on Safety and Reliability, Munich-Garching, Germany*, pp. 713–718.
- Song, J., Kang, W.H., Lee, Y.J., and Chun, J. [2021]. Structural System Reliability: Overview of Theories and Applications to Optimization. *ASCE-ASME Journal of Risk and Uncertainty in Engineering Systems, Part A: Civil Engineering*, 7(2):03121001.
- Spiga, M. and Morino, G. [1994]. A symmetric solution for velocity profile in laminar flow through rectangular ducts. *International communications in heat and mass transfer*, 21(4):469–475.
- Stafleu, J., Maljers, D., Busschers, F., Gunnink, J., Schokker, J., Dambrink, R., Hummelman, H., and Schijf, M. [2012]. *GeoTop modelling*. Technical report, TNO.
- Steenbergen, H.M.G.M., Lassing, B., Vrouwenvelder, A.C.W.M., and Waarts, P.H. [2004]. Reliability analysis of flood defence systems. *Heron*, 49(1):51–73.
- Sudret, B. [2012]. Meta-models for structural reliability and uncertainty quantification. In: *Asian-Pacific Symposium on Structural Reliability and its Applications*, pp. 1–24. Research Publishing.
- Sun, Y., Ma, L., Mathew, J., and Zhang, S. [2006]. An analytical model for interactive failures. *Reliability Engineering and System Safety*, 91(5):495–504.
- TAW [2004]. *Technisch Rapport Waterspanningen bij Dijken*. Technical Report DWW-2004-057.
- Tazi, N., Châtelet, E., and Bouzidi, Y. [2018]. How combined performance and propagation of failure dependencies affect the reliability of a MSS. *Reliability Engineering and System Safety*, 169:531–541.
- Terzaghi, K. [1922]. Der grundbruch an stauwerken und seine verhutung. *Wasserkraft*, 17:445–449.
- Townsend, F., Schmertmann, J., Logan, T., Pietrus, T., and Wong, Y. [1981]. *An analytical and experimental investigation of a quantitative theory for piping in sand*. Technical report, University of Florida.
- Tran, D.K., Froiio, F., Vincens, E., Prime, N., and Callari, C. [2017]. Numerical modelling of backward front propagation in piping erosion by DEM-LBM coupling. *European Journal of Environmental and Civil Engineering*, 21(7-8):960–987.
- Tóth, S. [2004]. Case Study on Failure Mechanism of Flood Embankments Due to Rapid Sand Boiling on Alluvial Flood Plains and the Identification of Vulnerable Levee Sections.
- Tóth, S. and Nagy, L. [2006]. Dyke failures in Hungary of the past 220 years. In: J. Marsalek, G. Stancalie, and G. Balint, eds., *Transboundary Floods: Reducing Risks Through Flood Management*, pp. 247–258. Springer, Dordrecht.
- Tu, P.Q. [2014]. Reliability analysis of the Red River dikes system in Viet Nam. ItemResolutionURL<http://resolver.tudelft.nl/uuid:852175ad-bcdc-4fe4-ae01-271f2405fd91>.
- Ubilla, J., Abdoun, T., Sasanakul, I., Sharp, M., Steedman, S., Vanadit-Ellis, W., and Zimmie, T. [2008]. New Orleans levee system performance during hurricane Katrina: London Avenue and Orleans canal south. *Journal of Geotechnical and Geoenvironmental Engineering*, 134(5):668–680.
- USACE [2000]. *Design and Construction of Levees. Engineer Manual*. Technical Report EM 1110-2-1913.
- USBR and USACE [2019]. *Best Practices in Dam and Levee Safety Risk Analysis*. Technical report.
- Van, M., Koelewijn, A.R., and Barends, F. [2005]. Uplift phenomenon: Model, validation, and design. *International Journal of Geomechanics*, 5(2):98–106.
- Van, M.A., Rosenbrand, E., Tourment, R., Smith, P., and Zwanenburg, C. [2022]. *Failure paths for levees*. Technical report, International Society of Soil mechanics and Geotechnical Engineering (ISSMGE) – Technical Committee TC201 ‘Geotechnical aspects of dikes and levees’.
- Van Beek, V., Robbins, B., Rosenbrand, E., and van Esch, J. [2022]. 3D modelling of backward erosion piping experiments. *Geomechanics for Energy and the Environment*, p. 100375.

- Van Beek, V.M. [2015]. *Backward erosion piping: Initiation and progression*. Ph.d. thesis, Delft University of Technology.
- Van Beek, V.M., Bezuijen, A., Sellmeijer, J.B., and Barends, F.B.J. [2014]. Initiation of backward erosion piping in uniform sands. *Géotechnique*, 64(12):927–941.
- Van Beek, V.M., De Bruijn, H.T.J., Knoeff, J.G., Bezuijen, A., and Förster, U. [2010]. Levee failure due to piping: A full-scale experiment. In: *5th International Conference on Scour and Erosion (ICSE-5)*, pp. 283–292. ASCE, San Francisco, USA.
- Van Beek, V.M., van Essen, H.M., Vandenboer, K., and Bezuijen, A. [2015]. Developments in modelling of backward erosion piping. *Géotechnique*, 65(9):740–754.
- Van Beek, V.M. and Hoffmans, G.J.C.M. [2017]. Evaluation of Dutch backward erosion piping models and a future perspective. In: *Proceedings 25th Meeting European Working Group on Internal Erosion in Embankment Dams and their Foundations*, pp. 97–113.
- Van Beek, V.M., Knoeff, H., and Sellmeijer, H. [2011]. Observations on the process of backward erosion piping in small-, medium-and full-scale experiments. *European Journal of Environmental and Civil Engineering*, 15(8):1115–1137.
- Van Beek, V.M., Koelewijn, A., Kruse, G., Sellmeijer, H., and Barends, F.B.J. [2008]. Piping phenomena in heterogeneous sands-experiments and simulations. In: *4th International Conference on Scour and Erosion (ICSE-4)*, pp. 453–459. Tokyo, Japan.
- Van Beek, V.M., Robbins, B.A., Hoffmans, G.J.C.M., Bezuijen, A., and van Rijn, L.C. [2019]. Use of incipient motion data for backward erosion piping models. *International Journal of Sediment Research*.
- Van Beek, V.M., Wiersma, A., van Egdome, M., and Robbins, B.A. [2018]. Databases for Backward Erosion Piping Laboratory Experiments and Field Observations. In: *European Working Group on Internal Erosion*, pp. 336–346. Springer.
- Van Beek, V.M., Yao, Q.L., and Van, M.A. [2013]. Backward erosion piping model verification using cases in China and the Netherlands. In: *International Conference on Case Histories in Geotechnical Engineering*.
- Vandenboer, K. [2019]. *A study on the mechanisms of backward erosion piping*. Ph.D. thesis, Ghent University.
- Vandenboer, K., van Beek, V., and Bezuijen, A. [2014]. 3D finite element method (FEM) simulation of groundwater flow during backward erosion piping. *Frontiers of Structural and Civil Engineering*, 8(2):160–166.
- Vandenboer, K., van Beek, V., and Bezuijen, A. [2018a]. 3D character of backward erosion piping. *Géotechnique*, 68(1):86–90.
- Vandenboer, K., van Beek, V.M., and Bezuijen, A. [2018b]. Analysis of the pipe depth development in small-scale backward erosion piping experiments. *Acta Geotechnica*, 14(2):477–486.
- Vandenboer, K., Celette, F., and Bezuijen, A. [2019]. The effect of sudden critical and supercritical hydraulic loads on backward erosion piping: small-scale experiments. *Acta Geotechnica*, 14(3):783–794.
- Vergouwe, R. [2016]. *The National Flood Risk Analysis for the Netherlands. Final Report*. Technical report.
- Vonk, B., Klerk, W.J., Fröhle, P., Gersonius, B., Den Heijer, F., Jordan, P., Radu Ciocan, U., Rijke, J., Sayers, P., and Ashley, R. [2020]. Adaptive asset management for flood protection: The FAIR framework in action. *Infrastructures*, 5(12):109.
- Vorogushyn, S., Merz, B., and Apel, H. [2009]. Development of dike fragility curves for piping and micro-instability breach mechanisms. *Natural Hazards and Earth System Sciences*, 9(4):1383–1401.
- Vorogushyn, S., Merz, B., Lindenschmidt, K.E., and Apel, H. [2010]. A new methodology for flood hazard assessment considering dike breaches. *Water Resources Research*, 46(8):n/a–n/a.

- Vrijling, J. [2001]. Probabilistic design of water defense systems in The Netherlands. *Reliability engineering and system safety*, 74(3):337–344.
- Vuik, V., Geerse, C., and Rongen, G. [2018]. *Vergelijking ECMWF windvelden met uitgangspunten WBI*. Technical Report PR3714.20, HKV.
- Waarsenburg, F. and Van Dam, P. [1980]. *Dijkdoorbraak Tholen: december 1894*. Technical report, Rijkswaterstaat, DWW.
- Wang, D.y., Fu, X.d., Jie, Y.x., Dong, W.j., and Hu, D. [2014]. Simulation of pipe progression in a levee foundation with coupled seepage and pipe flow domains. *Soils and Foundations*, 54(5):974–984.
- Wang, Q., Jia, G., Jia, Y., and Song, W. [2021]. A new approach for risk assessment of failure modes considering risk interaction and propagation effects. *Reliability Engineering & System Safety*, 216:108044.
- Ward, B.D. [1968]. *Surface shear at incipient motion of uniform sands*. Phd thesis, University of Arizona.
- Weijers, J.B.A. and Sellmeijer, J.B. [1993]. A new model to deal with the piping mechanism. In: *International conference Geo-filters*, pp. 349–355. Balkema.
- Wesselink, A., Warner, J., Syed, M.A., Chan, F., Tran, D.D., Huq, H., Huthoff, F., Le Thuy, N., Pinter, N., and Van Staveren, M. [2015]. Trends in flood risk management in deltas around the world: Are we going ‘soft’? *International Journal of Water Governance*, 3(4):25–46.
- Wewer, M., Aguilar-López, J.P., Kok, M., and Bogaard, T. [2021]. A transient backward erosion piping model based on laminar flow transport equations. *Computers and Geotechnics*, 132:103992.
- White, C. [1940]. The equilibrium of grains on the bed of a stream. *Proceedings of the Royal Society of London. Series A. Mathematical and Physical Sciences*, 174(958):322–338.
- White, S. [1970]. Plane bed thresholds of fine grained sediments. *Nature*, 228(5267):152–153.
- Wilderom, M.H. [1964]. *Tussen afsluitdammen en deltadijken, II Noord-Zeeland*. Technical report.
- Wilson, G.V., Wells, R., Kuhnle, R., Fox, G., and Nieber, J. [2018]. Sediment detachment and transport processes associated with internal erosion of soil pipes. *Earth Surface Processes and Landforms*, 43(1):45–63.
- Wolff, D. [2008]. Reliability of levee systems. *Reliability-based design in geotechnical engineering*, pp. 448–496.
- Wong, M. and Parker, G. [2006]. Reanalysis and correction of bed-load relation of Meyer-Peter and Müller using their own database. *Journal of Hydraulic Engineering*, 132(11):1159–1168.
- Xiao, Y., Cao, H., and Luo, G. [2019a]. Experimental investigation of the backward erosion mechanism near the pipe tip. *Acta Geotechnica*, 14(3):767–781.
- Xiao, Y., Cao, H., Luo, G., and Zhai, C. [2019b]. Modelling seepage flow near the pipe tip. *Acta Geotechnica*.
- Xiao, Y.P., Cao, H., and Zhai, C. [2018]. Analytical and experimental investigation of a disturbed zone around a pipe in sand. *Journal of the Brazilian Society of Mechanical Sciences and Engineering*, 40(4):238.
- Yagisawa, J., van Damme, M., Pol, J., and Bricker, J. [2019]. Verification of a Predictive Formula for Critical Shear Stress with Large Scale Levee Erosion Experiment. In: *11th ICOLD European Club Symposium*. Chania, Crete.
- Yalin, M.S. [1963]. An Expression for Bed-Load Transportation. *Journal of the Hydraulics Division*, 89(3):221–250.
- Yalin, M.S. and Karahan, E. [1979]. Inception of sediment transport. *Journal of the hydraulics division*, 105(11):1433–1443.
- Yao, Q. [2014]. *Multi-size Experiments and Numerical Simulation for Backward Erosion Piping in Dike Foundations*. Ph.D. thesis, China Institute of Water Resources and Hydropower Research (IWHR).
- Yao, Q., Van Beek, V., Van, M., and Ding, L. [2013]. Backward Piping in Multi-layer Dike Foundations: Experiments and Model Validation. In: *2013 IAHR World Congress*.

- Yao, Q.l., Ding, L.q., Sun, D.y., Liu, C.j., and Zhang, Q.y. [2007]. Experimental studies on piping in single-and two-stratum dike foundations [J]. *Water Resources and Hydropower Engineering*, 2:003.
- Zeng, Z., Kang, R., and Chen, Y. [2016]. Using PoF models to predict system reliability considering failure collaboration. *Chinese Journal of Aeronautics*, 29(5):1294–1301.
- Özer, I.E., van Damme, M., and Jonkman, S.N. [2020]. Towards an International Levee Performance Database (ILPD) and its use for macro-scale analysis of levee breaches and failures. *Water*, 12(1):119.
- Zhou, X., Ding, L., Yao, Q., and Li, G. [2007]. Laboratory model test for evolution of seepage deformation controlled by means of suspended cut-off wall in foundation of dike. *Shuili Fadian Xuebao/Journal of Hydroelectric Engineering*, 26(2):54–59.
- Zhou, X.j., Jie, Y.x., and Li, G.x. [2012]. Numerical simulation of the developing course of piping. *Computers and Geotechnics*, 44(Supplement C):104–108.





Failure case Strijenham

Introduction

Most field observations of BEP, such as sand boils and levee failures, are concentrated in river systems [Van Beek et al., 2018; Özer et al., 2020]. The subsoil composition is an important factor in explaining this difference. Meandering rivers resulted in an abundance of sandy channels and a relatively thin cohesive blanket. Blankets are generally thicker in the coastal systems and tidal deposits have more resistance to piping due to their layered structure and high fines content. Flood duration is another factor: floods in the Rhine and Meuse rivers are driven by snowmelt and extensive rainfall and result in high stages for weeks, while coastal floods are driven by storm surge with a duration of one or two days. Despite these favorable conditions, failures such as in New Orleans [IPET, 2007] show that the risk of BEP is not negligible in coastal areas.

This appendix describes a late 19th century case study from The Netherlands. Although sand boils occur almost yearly in The Netherlands, failures have rarely been associated with piping. The breach occurred in December 1894 near the village of Strijenham along the Eastern Scheldt estuary. This case helps to better understand the temporal dimension of piping failures since it occurred in a coastal area with a short flood durations and since the levee failed during a moderate storm after it survived an extreme storm. Therefore this appendix pays special attention to the flood duration and the likely development of the failure process over time.

Strijenham levee and subsoil

Study area

The breach occurred near the hamlet ‘Strijenham’ on the (former) island of Tholen in the south-western delta area in The Netherlands (Fig. A.1). Currently, the estuary is protected by the Eastern Scheldt storm surge barrier, but back in 1894 the estuary was in open connection with the North Sea. Polder Nieuw Strijen was developed around the year 1310, by closing the tidal channel ‘Striene’ from the Eastern Scheldt. The levee from 1310 was relocated after a breach in 1531 and did not breach until 1894.

Historical maps from 1730, 1864, 1910 and 1930 (Fig. A.2) show that an area of ap-

A

proximately 50 m just behind the levee was not in use as farmland, perhaps because of significant seepage. According to the province, the area behind the levee was excavated [Waarsenburg and Van Dam, 1980]. Kuipers [1960] notes that there was a freshwater well present. The map from 1730 confirms this, as it shows a pond right at the breach location, with a ditch running towards the village and sluice. Several reports of the disaster mention that the heavy seepage prior to the failure was observed in or close to an oyster pit just behind the levee [Waarsenburg and Van Dam, 1980]. Oyster pits are not indicated explicitly on the maps, but it is plausible that the pond or the entire wet area was used for this purpose.

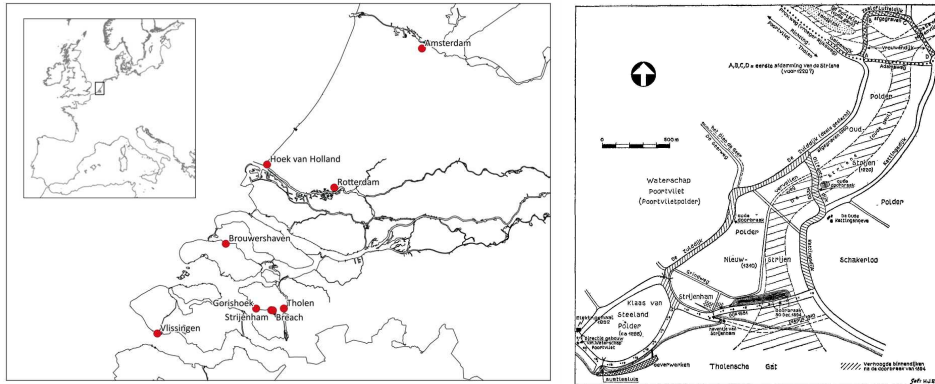
Levee cross-section

The reconstructed levee cross section is based on sketches of the pre-failure levee by Waarsenburg and Van Dam [1980], the restored levee by Wilderom [1964] and the current digital elevation model AHN3. From the sketches of the pre-failure levee [Waarsenburg and Van Dam, 1980], we derived a levee base width of 45-55 m. The crest height after restoration was +5.5 m NAP (NAP=Dutch Datum). Since the government knew that the cause of failure was not the height, it was probably similar before the failure. Currently there is only a ditch at 40 m from the inner toe. The detailed map from 1730 and the sketch by Kuipers [1960] indicate that in the 19th century there was a ditch present directly at the inner toe. Currently, the distance from inner toe to the outer toe (base of revetment) is approximately 60 m, and there is no foreshore. The drawing by Waarsenburg and Van Dam [1980] and Buijs [2013] indicate a similar levee base width. Reports describe the levee material as rather sandy with a clay cover.

Subsoil

Susceptibility to BEP depends heavily on the subsoil characteristics. An important feature in the subsoil at this site is the former tidal channel. Wilderom [1964] and Buijs [2013] locate the breach in the middle of this channel. The Dutch geological model GeoTOP [Stafleu et al., 2012] locates the channel slightly more to the west; the breach location is then at the eastern side of the channel.

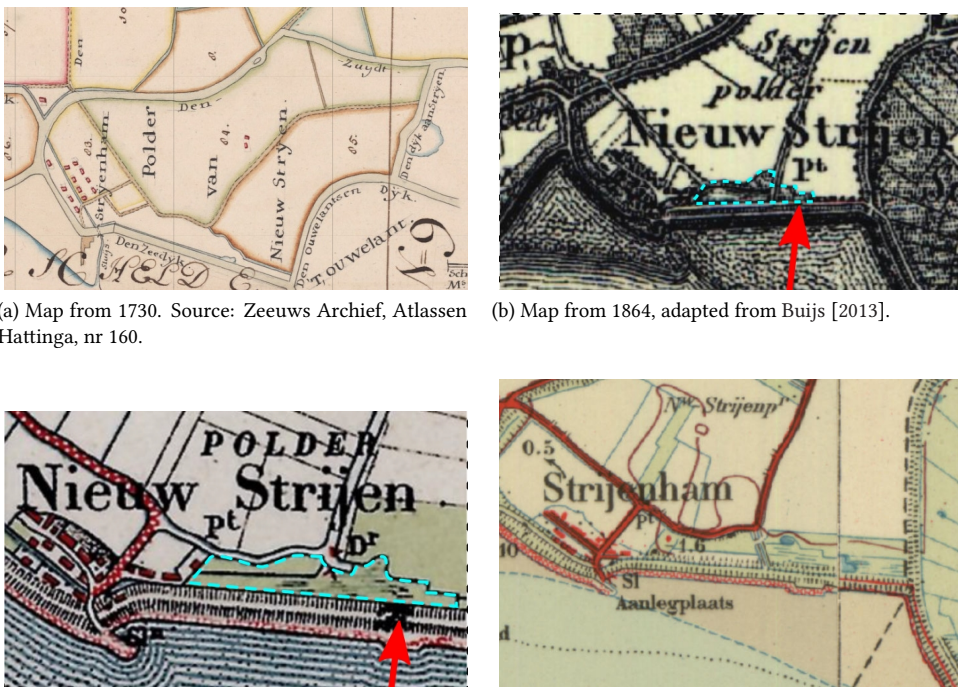
Buijs [2013] took five corings up to 4 m depth at the location of the tidal channel approximately 1 km behind the levee. Here, the clay cover is 2-3 m deep (bottom at -1.7 to -2.5 m NAP), with fine sand below. The grain size d_{70} equals 0.160 to 0.170 mm, with one sample of 0.122 mm. The sand is relatively uniform (uniformity coefficient of 2). CPT's from <https://www.dinoloket.nl/> at the levee crest and levee toe show the transition from cohesive to sandy layer is around -6 to -7 m NAP (40 m west of breach), -6.5 m NAP (at breach location) and -0.5 to -1 m NAP (40 m east of breach). This makes it plausible that at the east end, the ditch was nearly or completely in contact with the aquifer.



(a) Location in South-Western Delta.

(b) Map of the area by Wilderom [1964].

Figure A.1: Overview of the study area.



(a) Map from 1730. Source: Zeeuws Archief, Atlassen Hattinga, nr 160.

(b) Map from 1864, adapted from Buijs [2013].

(c) Map from 1910, adapted from Buijs [2013].

(d) Map from 1950. Source: TopoTijdReis.

Figure A.2: Historical maps of the area around the breach location, showing an unused land or a pond behind the levee at the breach location (red arrow).

A

The flood events of 1894 and breach

In December 1894, the Dutch coast was hit by two consecutive storms. The first one on December 22/23 was the most severe and well documented. A state Flood Report describes both the storm characteristics and resulting damage [Rijkswaterstaat, 1895]. Starting as a south-westerly storm, it changed towards north-westerly in the afternoon of December 22, resulting in a severe surge over the North Sea. The storm duration was relatively short. One week later on December 29/30, a second north-westerly storm hit the coast. This second storm was not exceptional and no official Flood Report was produced, but the Strijenham levee failed during this event.

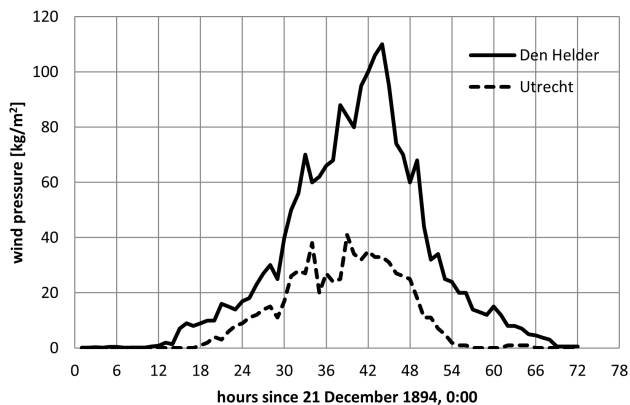


Figure A.3: Development of the storm on 22/23 December, based on data from Rijkswaterstaat [1895].

Water levels

Water level data are retrieved from Rijkswaterstaat [1895] and supplemented by an additional archive study, here indicated as [NationaalArchief]¹. Table A.1 summarizes the available peak water levels. Peak water levels are available from the Flood Report for the 22/23 December storm, and for storms in previous years [Rijkswaterstaat, 1895]. Peak water levels for the 29/30 December storm at the main gauge stations (Hoek van Holland, Vlissingen and Brouwershaven) are retrieved from [NationaalArchief].

Information about the surge duration is limited. The main gauge stations (Hoek van Holland, Vlissingen and Brouwershaven) have water levels four times per day, during high and low tides. These data are available for both storms [NationaalArchief]. The same archive also contains 30-minute measurements during the first part of the 22 December surge at Hoek van Holland.

Assuming linear interpolation between Gorishoek and Tholen, the water level at Strijenham is on average 6 cm higher than at Gorishoek (based on 11 storms). Table A.1 shows

¹full citation: Nationaal Archief, Den Haag, Staatscommissie inzake Buitengewoon Hoge Waterstanden op de Rotterdamse Waterweg, nummer toegang 2.16.124, inventarisnummer 4. "Tabel I", tabellen van de waterstanden in de Nieuwe Waterweg, de Scheur, de Nieuwe Maas en Lek, de Nederrijn, de Hollandse IJssel en de Noord in de periode 1887-1916.

Table A.1: Peak water levels [m+NAP] during the two storms, based on Rijkswaterstaat [1895].

Station	22/23 Dec. 1894	29/30 Dec. 1894
Hoek van Holland	3.28	2.17
Brouwershaven	>3.59	2.56
Vlissingen	3.67 at 10.10 PM	3.02
Tholen	4.20 at 12.00 PM	
Gorishoek	4.04 at 11.45 PM	3.37 [Wilderom, 1964]
Strijenham (own estimate)	4.10	3.43

that the 23 December storm was significantly higher than the 29 December storm at the location of the breach.

The maximum water level in previous years gives information about the survived loads. Figure A.4 shows that the maximum water level at Gorishoek between 1853 and 1894 was 3.86 m+NAP (floods of 1863 and 1883). In 1825, there had been an extreme flood (45-75 cm above 1863 level), but for this event water levels are unknown at Gorishoek. So, the dike had not breached in previous floods which were only 18 cm lower than the 22/23 December flood. Note that the 29 December flood was still a relatively high one, with a return period of approximately 6 years.

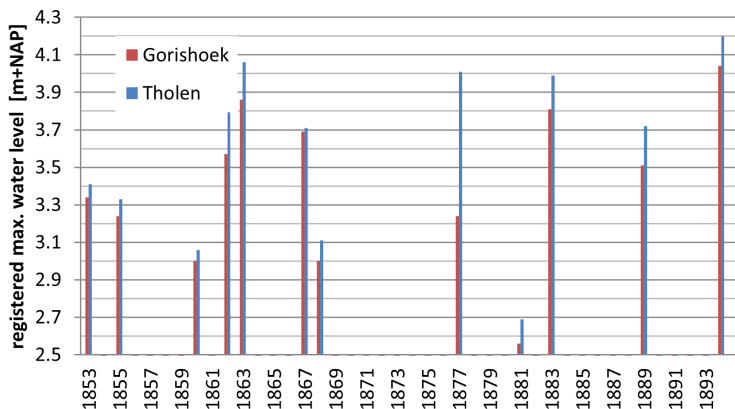
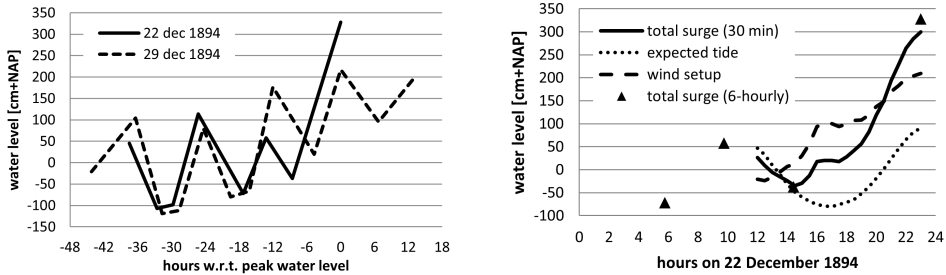


Figure A.4: Yearly maximum water levels for gage stations close to Strijenham.

Figure A.5a shows the surge duration of both storms at Hoek van Holland based on the measurements during high- and low tide. More than 24 hours before the peaks it shows the tidal fluctuation (+/- 1 m). On 22 December, the surge develops in about 10 hours. For more details, see the 30-minute measurements in Figure A.5b. This sharp increase may be caused by a drawdown during the first hours of the storm, turning into surge when the wind direction changed from south-westerly towards north-westerly. On 29 December, the surge development takes about 20 hours. The surge duration is not known for stations in the vicinity of the breach, but the pattern at Brouwershaven is very similar to Hoek van Holland, so we assume it is representative for the duration.



(a) Comparison of water levels in storms of 22/23 December and on 29/30 December.

(b) 30-minute water level measurements (22 December only).

Figure A.5: Water level measurements at gauge station Hoek van Holland. Data from [NationaalArchief].

Levee breach

Several sources dated between 1895 and 1927 shortly describe the breaching and an interpretation of the cause, see the original references in Wilderom [1964] and Waarsenburg and Van Dam [1980]. All five sources mention seepage, two mention the observation of strong seepage by the dike inspector, and one gives the specific times of observation and breaching. Three of them mention the oyster pit behind the dike (and one lowly excavated land, which could be the same). These reports result in the following timeline:

- 22 December 1894, 11 P.M.: peak water level of first (extreme) storm, no significant damage observed at Strijenham levee.
- Saturday 29 December 1894, 4 P.M.: peak water level of second (lower) storm.
- 30 December 1894, 3 P.M.: strong seepage observed, after some time the crest starts sinking slowly.
- 30 December 1894, evening: polder inundates.
- 31 December 1894: levee breach is 54-60 m wide.

Reports do not describe a sand boil or where the eroded sand settled.

Effective head difference

For model validation of the critical head H_c , it is relevant at which head difference the levee failed. From a stationary point of view, the effective head difference which led to the failure is given by: $H = H_c = (h - h_p) - 0.3D_{bl}$, in which h =water level, h_p =polder water level, D_{bl} =blanket thickness. The $0.3D_{bl}$ correction for exit hole resistance is used in current levee safety assessments in the Netherlands.

An upper limit for h is the peak level of 22/23 Dec (4.10 m+NAP). A lower limit is hard to determine but a first estimate is the peak level of 1863 (3.92 m+NAP), as the levee survived several storms afterwards. An upper limit for h_p is -0.7 m NAP, which is based on the polder surface level of -0.8 mNAP between 1967-1985 (www.topotijdreis.nl) plus 10 cm subsidence. A lower limit is -1.17 m NAP, the polder water level before 1953 [Kuipers, 1960] plus 10 cm subsidence. Given the polder level and locally very shallow clay-sand interface, it is most likely that there was no clay cover present at the breach location.

Table A.2: Dutch failure cases as described in Parhizkar [1993].

Case	Material	C_{Bligh} [-]	C_{Lane} [-]	D [m]	L [m]	d_{10} [mm]	d_{60} [mm]	d_{70} [mm]	H_c [m]
Nieuwkuijk (1880)	fine sand, med. dense	15	7	20	37	0.125	0.160	0.180	3.0
Zalk (1926)	fine sand, med. dense	15	7	15	30	0.165	0.212	0.240	2.5
Nieuw-Strijen polder (1894)	fine sand, med. dense	15	7	20	60	0.125	0.160	0.170	6.3

However, we use 1 m as an upper limit of the cover thickness. Then the critical effective head difference is estimated between 4.32 (3.92+0.7-0.3) and 5.27 m (4.1+1.17).

Buijs [2013] found significantly lower values of 0.56 to 3.42 m, because (1) she did not use the water level of the previous 22/23 Dec storm, (2) she uses higher polder levels and (3) she based the cover thickness on core samples at some distance of the breach and not on the CPT near the levee that indicates the locally shallow clay-sand interface. The MSc thesis of Parhizkar [1993] gives a critical head difference of 6.3 m (Nieuw-Strijen polder), but the basis of this value is unclear. It is noted that later reports [Deltares, 2008; Kanning, 2012] contain the same data as Parhizkar [1993], but the values of D , L and H_c for the Strijenharn-Tholen case and the Zalk case have been mixed up. The original values from Parhizkar [1993] are given in table A.2.

Predictions

Model parameters

For each model parameter, three values are given in Table A.3: an unfavorable bound, a best estimate and a favorable bound. The aquifer depth varies between 60 m [Buijs, 2013], 20 m [Parhizkar, 1993] and 10 m (if the clay layer at 13-15 m depth in DINO dataset is confining). The seepage length is estimated as 60 m +/-5 m based on the information mentioned above. Hydraulic conductivity is computed with Den Rooijen and Blake-Kozeny correlations from d_{10} ranges (60-80 μm) from corings by Buijs [2013]. The upper limit is set to 10 m/day based on estimates for the entire 60 m aquifer by Buijs [2013]. The range in d_{70} is based on the corings by Buijs [2013]. Values for d_{15} and d_{50} are estimated based on the finding by Buijs [2013] that the uniformity coefficient is approximately 2. Other constants are: $\rho_s=2650 \text{ kg/m}^3$, $\rho_w=1025 \text{ kg/m}^3$, and porosity $n=0.38$.

Model prediction

Table A.4 shows the results of the model predictions of the critical head by:

1. Bligh [1910] with creep factor of 15
2. Sellmeijer et al. [2011]
3. Hoffmans and Van Rijn [2017]

The predicted critical head ranges between 2.87 and 7.9 m. The results show that the Sellmeijer model is most sensitive to the uncertainties in input parameters, and Bligh is

Table A.3: Ranges of levee characteristics and model parameters for Strijenham failure case.

Parameter	Symb.	Unit	Unfavorable bound	Best estimate	Favorable bound
Aquifer depth	D	m	60	20	10
Seepage length	L	m	55	60	65
Hydr. conductivity	k	m/d	10	4	3
Grain size	d_{15}	mm	0.06	0.08	0.085
Grain size	d_{50}	mm	0.11	0.14	0.15
Grain size	d_{70}	mm	0.12	0.16	0.17
Coefficient in Eq. 2.19	c	-	1.99	1.6	1.28
Coefficient in Eq. 5.15	C_e	-	0.1	0.05	0.016
Acting head diff. in Eq. 5.15	H	m	5.27	5.0	4.32

the least sensitive as it only depends on L . In the 40 years before failure, the levee has survived several events where the effective head was at least 4 m. And it did not survive a head difference of 5.27 m. These values fall within the uncertainty range of each of the models. Hence the large uncertainty in model input parameters does not allow for a judgment of which prediction model performs better on this case.

The progression rate is predicted with:

1. the calibrated Kezdi model (Eq. 2.19)
2. the average progression rate fitted on the DgFlow simulations (Eq. 5.15)

The acting head difference H is assumed to vary between 4.32 and 5.27 m, with 5 m as best estimate. Predicted progression rates are typically a few meters per day, and vary by about a factor 10 between lower and upper bound (Table A.4). Even in the scenario with the fastest progression (13.8 m/day), full pipe development would require 4 full days of storm surge. Hence, if the failure is due to backward erosion piping, it is likely that the pipe has developed over several storms.

Table A.4: Ranges of model predictions for Strijenham failure case.

Model	Unfavorable bound	Best estimate	Favorable bound
Effective critical head difference [m]:			
Bligh [1910]	3.67	4.0	4.33
Sellmeijer et al. [2011]	2.87	5.59	7.90
Hoffmans and Van Rijn [2017]	2.99	4.40	5.01
Average progression rate [m/d]:			
Eq. 2.19	5.0	1.4	0.7
Eq. 5.15, assuming $H_c = H - 0.2$ m	6.3	2.6	0.5
Eq. 5.15, assuming $H_c = H - 0.5$ m	9.9	4.1	0.7
Eq. 5.15, assuming $H_c = H - 1.0$ m	13.8	5.6	1.0

B

B

Progression rates from previous
laboratory experiments

Table B.1: Progression rates in previous experiments [Pol et al., 2019]. Sources: [1]=Van Beek et al. [2011], [2]=Sellmeijer et al. [2011], [3]=Vandenboer et al. [2019], [4]=Robbins et al. [2017], [5]=Yao [2014]. Setup: ss=small scale, ms=medium scale. [‡]the d_{60} is used for tests by Robbins. [§]overloading at $1.4 \cdot H_c$. *multi-layered sample.

Test	Source	Setup	Exit	L [m]	n [-]	d_{70} [‡] [mm]	k [m/s]	H_c [m]	$v_{c,avg}$ [m/s]
B35	[1]	SS box	slope	0.34	0.386	0.154	$1.3 \cdot 10^{-4}$	0.14	$3.0 \cdot 10^{-4}$
B36	[1]	SS box	slope	0.33	0.387	0.154	$1.1 \cdot 10^{-4}$	0.14	$3.1 \cdot 10^{-4}$
B40	[1]	SS box	slope	0.33	0.356	0.154	$5.3 \cdot 10^{-5}$	0.15	$4.2 \cdot 10^{-4}$
B41	[1]	SS box	slope	0.33	0.355	0.154	$7.3 \cdot 10^{-5}$	0.15	$4.4 \cdot 10^{-4}$
I46	[1]	SS box	slope	0.34	0.364	0.202	$1.1 \cdot 10^{-4}$	0.16	$8.3 \cdot 10^{-4}$
I47	[1]	SS box	slope	0.34	0.343	0.431	$7.3 \cdot 10^{-4}$	0.087	$9.3 \cdot 10^{-4}$
I48	[1]	SS box	slope	0.34	0.342	0.431	$1.1 \cdot 10^{-3}$	0.079	$7.9 \cdot 10^{-4}$
I49	[1]	SS box	slope	0.34	0.374	0.400	$8.0 \cdot 10^{-4}$	0.069	$1.4 \cdot 10^{-3}$
B54	[1]	SS box	slope	0.33	0.370	0.154	$7.4 \cdot 10^{-5}$	0.18	$7.3 \cdot 10^{-4}$
B55	[1]	SS box	slope	0.33	0.378	0.154	$8.8 \cdot 10^{-5}$	0.14	$6.6 \cdot 10^{-4}$
B82	[1]	SS box	slope	0.34	0.363	0.154	$5.9 \cdot 10^{-5}$	0.14	$5.9 \cdot 10^{-4}$
B84	[1]	SS box	slope	0.33	0.399	0.154	$6.0 \cdot 10^{-5}$	0.10	$2.4 \cdot 10^{-4}$
Bms1	[1]	MS box	slope	1.37	0.391	0.154	$1.2 \cdot 10^{-4}$	0.28	$4.1 \cdot 10^{-4}$
Bms2	[1]	MS box	slope	1.45	0.402	0.154	$1.4 \cdot 10^{-4}$	0.37	$1.6 \cdot 10^{-4}$
Ims3	[1]	MS box	slope	1.46	0.388	0.210	$2.0 \cdot 10^{-4}$	0.26	$4.0 \cdot 10^{-4}$
Ims4	[1]	MS box	slope	1.46	0.404	0.210	$3.7 \cdot 10^{-4}$	0.20	$1.7 \cdot 10^{-4}$
Ims5	[1]	MS box	slope	1.42	0.375	0.210	$2.2 \cdot 10^{-4}$	0.29	$1.2 \cdot 10^{-4}$
Bms7	[1]	MS box	slope	1.30	0.386	0.154	$1.5 \cdot 10^{-4}$	0.29	$3.8 \cdot 10^{-4}$
Bms8	[1]	MS box	slope	1.33	0.402	0.154	$2.6 \cdot 10^{-4}$	0.19	$4.0 \cdot 10^{-4}$
ijkdijk1	[2]	levee	area	15	0.398	0.180	$8.0 \cdot 10^{-5}$	2.30	$5.1 \cdot 10^{-5}$
ijkdijk2	[2]	levee	area	15	0.371	0.260	$1.4 \cdot 10^{-4}$	1.75	$1.2 \cdot 10^{-4}$
ijkdijk3	[2]	levee	area	15	0.398	0.180	$8.0 \cdot 10^{-5}$	2.10	$6.7 \cdot 10^{-5}$
Vdb_f1	[3]	SS box	hole	0.30	0.402	0.190	$1.0 \cdot 10^{-4}$	0.060	$7.7 \cdot 10^{-5}$
Vdb_f1.4 [§]	[3]	SS box	hole	0.30	0.402	0.190	$1.0 \cdot 10^{-4}$	0.080	$2.9 \cdot 10^{-4}$
2B	[4]	cylinder	slope	0.95	0.390	0.332	$6.5 \cdot 10^{-4}$	0.43	$5.1 \cdot 10^{-4}$
3B	[4]	cylinder	slope	0.97	0.408	0.332	$1.2 \cdot 10^{-3}$	0.27	$7.4 \cdot 10^{-4}$
4B	[4]	cylinder	slope	0.98	0.390	0.332	$6.5 \cdot 10^{-4}$	0.39	$1.8 \cdot 10^{-3}$
4B	[4]	cylinder	slope	0.98	0.390	0.332	$6.5 \cdot 10^{-4}$	0.21	$8.5 \cdot 10^{-4}$
4B	[4]	cylinder	slope	0.98	0.390	0.332	$6.5 \cdot 10^{-4}$	0.18	$1.2 \cdot 10^{-3}$
4B	[4]	cylinder	slope	0.98	0.390	0.332	$6.5 \cdot 10^{-4}$	0.20	$8.9 \cdot 10^{-4}$
4B	[4]	cylinder	slope	0.98	0.390	0.332	$6.5 \cdot 10^{-4}$	0.22	$8.8 \cdot 10^{-4}$
6B	[4]	cylinder	slope	0.96	0.379	0.332	$6.4 \cdot 10^{-4}$	0.36	$1.8 \cdot 10^{-3}$
7B	[4]	cylinder	slope	0.96	0.379	0.332	$6.2 \cdot 10^{-4}$	0.39	$2.1 \cdot 10^{-3}$
1C	[4]	cylinder	slope	0.94	0.419	0.332	$8.0 \cdot 10^{-4}$	0.19	$4.3 \cdot 10^{-4}$
2C	[4]	cylinder	slope	0.92	0.401	0.332	$6.6 \cdot 10^{-4}$	0.23	$1.1 \cdot 10^{-3}$
3C	[4]	cylinder	slope	0.93	0.379	0.332	$4.8 \cdot 10^{-4}$	0.33	$2.0 \cdot 10^{-3}$
4C	[4]	cylinder	slope	0.92	0.394	0.332	$6.1 \cdot 10^{-4}$	0.24	$7.3 \cdot 10^{-4}$
B_C109 *	[5]	SS box	slope	0.34	0.360	0.154	$5.6 \cdot 10^{-5}$	0.13	$8.3 \cdot 10^{-4}$
B_C110 *	[5]	SS box	slope	0.34	0.357	0.154	$5.6 \cdot 10^{-5}$	0.12	$7.5 \cdot 10^{-4}$
B_C111 *	[5]	SS box	slope	0.36	0.363	0.154	$5.6 \cdot 10^{-5}$	0.11	$3.3 \cdot 10^{-4}$
B_115	[5]	SS box	hole	0.35	0.357	0.154	$5.6 \cdot 10^{-5}$	0.080	$1.4 \cdot 10^{-4}$
B_118	[5]	SS box	hole	0.35	0.357	0.154	$5.6 \cdot 10^{-5}$	0.080	$1.7 \cdot 10^{-4}$
B_C116 *	[5]	SS box	hole	0.35	0.348	0.154	$5.6 \cdot 10^{-5}$	0.070	$3.0 \cdot 10^{-4}$
B_C117 *	[5]	SS box	hole	0.35	0.348	0.154	$5.6 \cdot 10^{-5}$	0.060	$1.3 \cdot 10^{-4}$

C

C

Data of sediment transport in laminar flow

This appendix describes how the sediment transport data in laminar flow from the different sources are interpreted and expressed in the same parameters, so that the datasets can be merged. Most recent sources express sediment transport relations based on three variables: a dimensionless sediment transport rate q_{*v} , the Shields number Θ and a critical Shields number Θ_c :

$$q_{*v} = \frac{q_v}{(\rho_s - \rho_w)g d^3 / \mu} \quad (\text{C.1})$$

$$\Theta = \frac{\tau}{(\rho_s - \rho_w)g d} \quad (\text{C.2})$$

Where q_v is a volumetric transport rate [$\text{m}^3/\text{m/s}$], μ is the dynamic viscosity [$\text{Pa}\cdot\text{s}$] and τ is the bed shear stress [Pa]. The following sections describe how these properties are obtained from each study in Table 3.4 in Chapter 3.

Grass and Ayoub [1982] plotted a dimensionless sediment transport rate $q_{s,m}/(u_* d(\rho_s - \rho_w))$ as function of $\Theta(\text{Re}_*)^{0.64}$. Here $q_{s,m}$ is a mass transport rate per unit flow width [kg/s/m], $u_* = \sqrt{\tau/\rho}$ is the bed shear velocity, $\text{Re}_* = u_* d/\nu$ is the particle Reynolds number. The value on the horizontal axis can be written as

$$\frac{\tau}{(\rho_s - \rho_w)g d} (d \sqrt{\tau/\rho/\nu})^{-0.64} \quad (\text{C.3})$$

and τ can be calculated for each data point using grain and fluid properties and Eq. C.3. We assume a particle density of 2650 kg/m^3 as this is not specified in Grass and Ayoub [1982]. Then, Θ and u_* are calculated from τ . Regarding the vertical axis, $q_{s,m}$ [kg/s/m] follows from the data point values and u_* . This is finally translated into a volumetric transport rate and q_{*v} . As Grass and Ayoub [1982] do not provide a critical Shields number, we assumed a critical Shields number based on the Calibrated White approach in Van Beek [2015]. This

results in a Θ_c of 0.11 for tests in a water temperature of 4° C, 0.1 for 17° C and 0.09 for 30° C.

Charru et al. [2004] plotted a dimensionless sediment transport rate $Q_{sat}d^2/V_s$ [-] as function of Shields number Θ (Fig. C.2). Here V_s is the Stokes velocity ($(\rho_s - \rho)gd^2/18\mu$) and Q_{sat} is expressed in grains/s/m. We translated the value of Q_{sat} to a volumetric transport rate q_v assuming spherical particles ($q_v = \frac{\pi}{6}d^3Q_{sat}$), and then calculated q_{*v} . The authors report a critical Shields number $\Theta_c = 0.12$.

C

Malverti et al. [2008] plot the Einstein number q_{*E} (dimensionless sediment transport rate by inertial scaling) as function of the Shields number (Fig. C.3). The dimensionless sediment transport rate q_{*E} was translated from inertial scaling to viscous scaling to obtain q_{*v} . We assume $\rho_w = 1000$ kg/m³ and $\nu = 10^{-6}$ m²/s. The authors report a critical Shields number $\Theta_c = 0.12$.

Lobkovsky et al. [2008] present sediment transport relations expressed as Einstein number q_{*E} vs. excess Shields number $\Theta - \Theta_c$. They report $\Theta_c = 0.3$. This Θ_c is large compared to the other experiments, and Ouriemi et al. [2009] argue that it can be explained by the choice of Lobkovsky et al. [2008] to neglect side wall effects on the flow. Therefore, data from Lobkovsky is not used in the chapter on small-scale experiments. If one would multiply the Shields numbers by a factor 0.12/0.30 (Ouriemi et al. [2009] finds $\Theta_c = 0.12$), the sediment transport relations are in line with the other data.

Seizilles et al. [2014] plotted a dimensional sediment transport rate q_x [grains/mm/s] as function of shields number Θ . Like for Charru et al. [2004], we translated the value of q_x to a volumetric transport rate assuming spherical particles, and then calculated q_{*v} . We assume $\rho_w = 1000$ kg/m³ and $\nu = 10^{-6}$ m²/s. The authors report a critical Shields number $\Theta_c = 0.125$.

Delorme et al. [2017] plotted a volumetric sediment transport rate q_v [mm²/s] as function of shear stress τ . We translated the value of q_v to the dimensionless transport rate q_{*v} . The authors report a critical Shields number of 0.19 for coal and 0.25 for silica.

We note that these values appear very high compared to critical Shields numbers obtained in the literature (see Fig. 2.4 in Chapter 2). For the silica, $D^* = 3.3$, where Θ_c is in the range of 0.10-0.15. For coal, $D^* = 6.8$, where Θ_c is in the range of 0.07-0.12.

Delorme et al. [2018] plotted a mass sediment transport rate $q_{s,m}$ [g/m/s] as function of Shields number Θ . We translated the value of $q_{s,m}$ to a volumetric transport rate assuming spherical particles, and then calculated q_{*v} . They report a critical Shields number of 0.14.

Abramian et al. [2019] plotted a sediment transport rate expressed in [grains/cm/s] as function of the Shields number. Like for Charru et al. [2004] and Seizilles et al. [2014], we translated the sediment rate to a volumetric transport rate assuming spherical particles, and then calculated q_{*v} . The authors report a critical Shields number of 0.17.

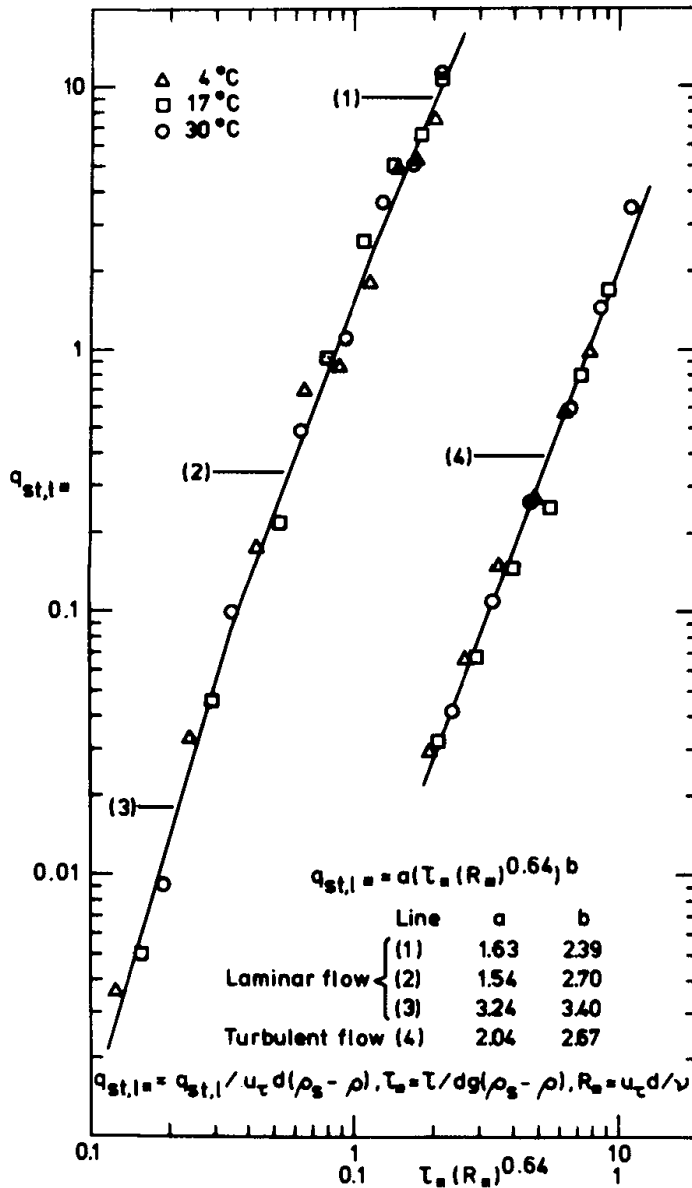


FIGURE 3. Optimized correlation of measured bed load sediment transport rates induced by laminar and turbulent flows.

Figure C.1: Measured and fitted sediment transport relations from Grass and Ayoub [1982]

F. Charru, H. Mouilleron and O. Eiff

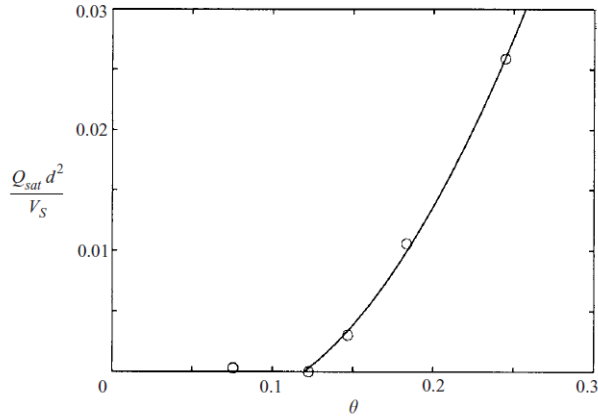


FIGURE 14. Saturated flow rate Q_{sat} versus Shields number θ : \circ , experiments; solid line, parabolic fit given by equation (9).

Figure C.2: Measured and fitted sediment transport relations from Charru et al. [2004]

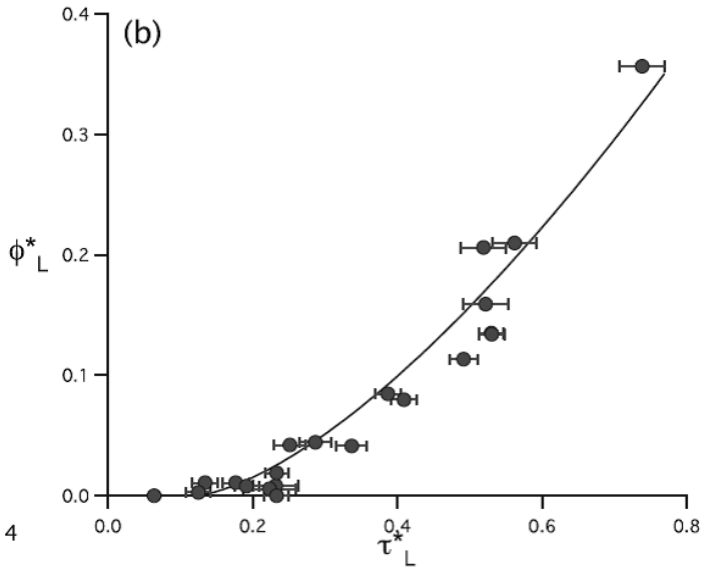


Figure C.3: Measured and fitted sediment transport relations from Malverti et al. [2008]

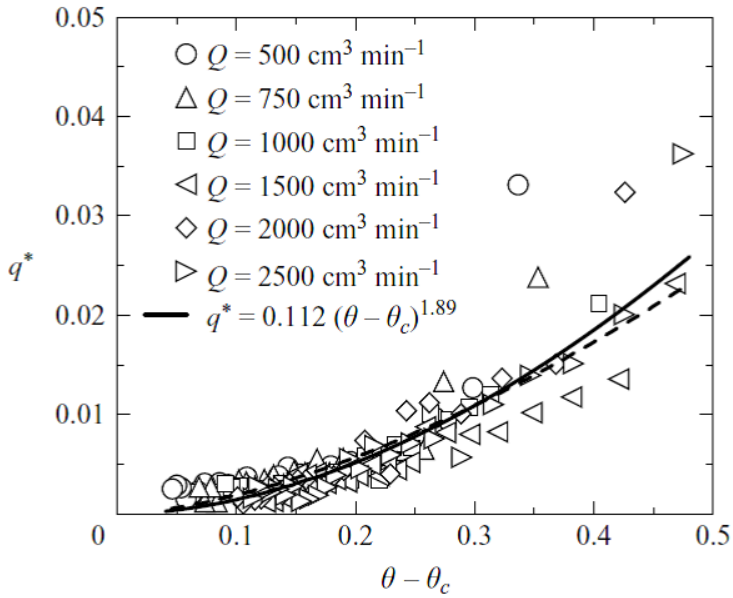


Figure C.4: Measured and fitted sediment transport relations from Lobkovsky et al. [2008]

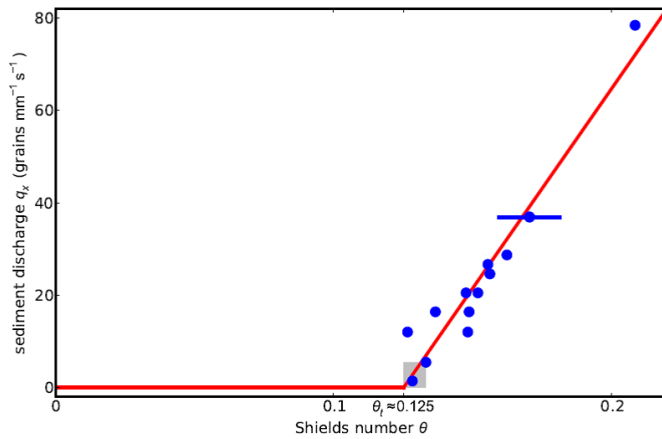
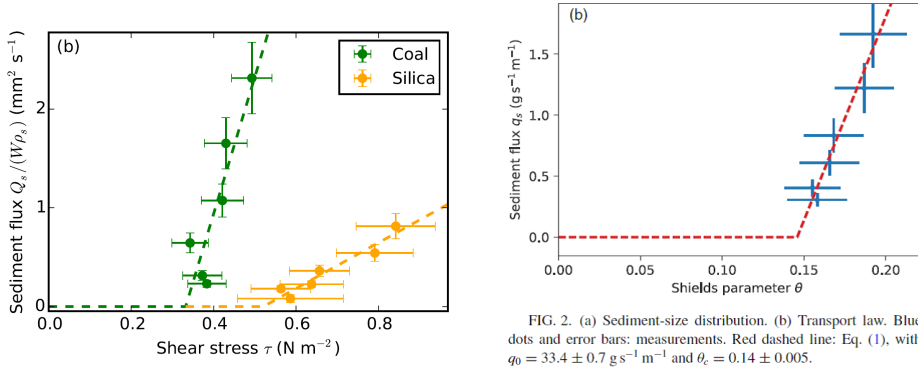


FIG. 2. Imposed bedload flux q_x as a function of the measured Shields parameter θ (blue dots). The transport law (14) is fitted to the data (red line, $q_x = \alpha V_* \theta_i (\theta - \theta_c) / d_s^2$ with $\alpha = 0.025$ and $\theta_c = 0.125$). The particle tracking experiments are limited to the shaded area.

Figure C.5: Measured and fitted sediment transport relations from Seizilles et al. [2014]



(a) sediment transport relations from Delorme et al. [2017].

(b) sediment transport relations from Delorme et al. [2018].

Figure C.6: Measured and fitted sediment transport relations from Delorme et al. [2017] and Delorme et al. [2018].

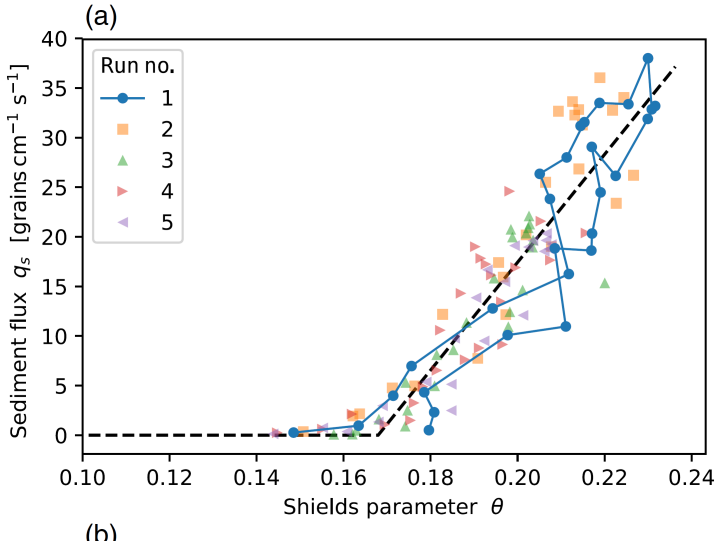


Figure C.7: Measured and fitted sediment transport relations from Abramian et al. [2019]

D

DgFlow simulation results

D

Table D.1: DgFlow simulations for critical conditions.

L [m]	sand	exit	w/a	$i_{tip,c}$	H_c [m]
0.9	S22	hole	20	0.7	0.084
0.9	S22	plane	20	0.7	0.158
3	S22	hole	20	0.7	0.144
3	S22	hole	20	0.7	0.182
3	S22	hole	30	0.7	0.157
3	S22	hole	67	0.7	0.182
3	S23	hole	20	0.7	0.170
3	S32	hole	20	0.7	0.151
3	S33	hole	20	0.7	0.178
3	S42	hole	20	0.7	0.153
3	S43	hole	20	0.7	0.184
3	S22	plane	20	0.7	0.284
9	S22	hole	20	0.2	0.254
9	S22	hole	200	0.2	0.424
9	S22	hole	43	0.2	0.304
9	S22	plane	20	0.2	0.376
30	S22	hole	20	0.2	0.470
30	S22	hole	115	0.2	0.693
30	S22	hole	64	0.2	0.607
30	S22	hole	667	0.2	1.047
30	S32	hole	20	0.2	0.501
30	S42	hole	20	0.2	0.501
30	S22	plane	20	0.2	0.764
90	S22	hole	20	0.15	0.864
90	S22	hole	2000	0.15	2.457
90	S22	hole	93	0.15	1.188
90	S22	plane	20	0.15	1.294

Table D.2: DgFlow simulations for time-dependent pipe progression.

L [m]	sand	exit	w/a [-]	$i_{lip,c}$ [-]	C_e [-]	overload [%]	H_c [m]	dl/dt [m/s]
0.9	S22	hole	20	0.7	0.080	5	0.084	$1.05 \cdot 10^{-4}$
0.9	S22	hole	20	0.7	0.080	10	0.084	$1.54 \cdot 10^{-4}$
0.9	S22	hole	20	0.7	0.080	20	0.084	$2.28 \cdot 10^{-4}$
0.9	S22	hole	20	0.7	0.080	30	0.084	$2.94 \cdot 10^{-4}$
0.9	S22	hole	20	0.7	0.080	40	0.084	$3.62 \cdot 10^{-4}$
0.9	S22	plane	20	0.7	0.080	10	0.158	$7.64 \cdot 10^{-4}$
3	S22	hole	20	1.4	0.080	10	0.182	$1.63 \cdot 10^{-4}$
3	S22	hole	20	0.7	0.008	10	0.144	$7.10 \cdot 10^{-6}$
3	S22	hole	20	0.7	0.040	10	0.144	$3.54 \cdot 10^{-5}$
3	S22	hole	20	0.7	0.080	5	0.144	$5.65 \cdot 10^{-5}$
3	S22	hole	20	0.7	0.080	10	0.144	$7.08 \cdot 10^{-5}$
3	S22	hole	20	0.7	0.080	10	0.144	$7.38 \cdot 10^{-5}$
3	S22	hole	20	0.7	0.080	10	0.144	$6.93 \cdot 10^{-5}$
3	S22	hole	20	0.7	0.080	10	0.144	$7.15 \cdot 10^{-5}$
3	S22	hole	20	0.7	0.080	10	0.144	$7.10 \cdot 10^{-5}$
3	S22	hole	20	0.7	0.080	10	0.144	$7.16 \cdot 10^{-5}$
3	S22	hole	20	0.7	0.080	10	0.144	$7.06 \cdot 10^{-5}$
3	S22	hole	20	0.7	0.080	10	0.144	$7.16 \cdot 10^{-5}$
3	S22	hole	20	0.7	0.080	20	0.144	$1.02 \cdot 10^{-4}$
3	S22	hole	20	0.7	0.080	30	0.144	$1.31 \cdot 10^{-4}$
3	S22	hole	20	0.7	0.080	40	0.144	$1.62 \cdot 10^{-4}$
3	S22	hole	20	0.7	0.159	10	0.144	$1.46 \cdot 10^{-4}$
3	S22	hole	30	0.7	0.080	10	0.157	$7.95 \cdot 10^{-5}$
3	S23	hole	20	0.7	0.080	10	0.170	$8.48 \cdot 10^{-5}$
3	S32	hole	20	0.7	0.079	10	0.151	$1.52 \cdot 10^{-4}$
3	S33	hole	20	0.7	0.079	10	0.178	$1.69 \cdot 10^{-4}$
3	S42	hole	20	0.7	0.008	10	0.153	$2.11 \cdot 10^{-5}$
3	S42	hole	20	0.7	0.040	10	0.153	$1.22 \cdot 10^{-4}$
3	S42	hole	20	0.7	0.081	5	0.153	$1.82 \cdot 10^{-4}$
3	S42	hole	20	0.7	0.081	10	0.153	$2.64 \cdot 10^{-4}$
3	S42	hole	20	0.7	0.081	20	0.153	$3.86 \cdot 10^{-4}$
3	S42	hole	20	0.7	0.081	30	0.153	$5.21 \cdot 10^{-4}$
3	S42	hole	20	0.7	0.081	40	0.153	$9.67 \cdot 10^{-4}$
3	S43	hole	20	0.7	0.081	10	0.184	$3.04 \cdot 10^{-4}$
3	S22	plane	20	0.7	0.080	10	0.284	$3.61 \cdot 10^{-4}$
3	S22	hole	20	0.7	0.008	40	0.144	$1.64 \cdot 10^{-5}$
3	S22	hole	20	0.7	0.040	40	0.144	$8.10 \cdot 10^{-5}$
3	S22	hole	20	0.7	0.159	40	0.144	$3.36 \cdot 10^{-4}$
3	S42	hole	20	0.7	0.008	40	0.153	$5.42 \cdot 10^{-5}$
3	S42	hole	20	0.7	0.040	40	0.153	$2.81 \cdot 10^{-4}$
3	S22	plane	20	0.7	0.080	40	0.284	$8.20 \cdot 10^{-4}$
9	S22	hole	20	0.2	0.080	5	0.254	$4.62 \cdot 10^{-5}$
9	S22	hole	20	0.2	0.080	10	0.254	$5.47 \cdot 10^{-5}$
9	S22	hole	20	0.2	0.080	20	0.254	$7.24 \cdot 10^{-5}$
9	S22	hole	20	0.2	0.080	30	0.254	$9.19 \cdot 10^{-5}$

Continued on next page

Table D.2 – continued from previous page

L [m]	sand	exit	w/a [-]	$i_{tip,c}$ [-]	C_e [-]	overload [%]	H_c [m]	dl/dt [m/s]
9	S22	hole	20	0.2	0.080	40	0.254	$1.11 \cdot 10^{-4}$
9	S22	hole	43	0.2	0.080	10	0.304	$6.80 \cdot 10^{-5}$
9	S22	plane	20	0.2	0.080	10	0.376	$1.21 \cdot 10^{-4}$
30	S22	hole	20	0.2	0.080	5	0.470	$2.43 \cdot 10^{-5}$
30	S22	hole	20	0.2	0.080	10	0.470	$2.91 \cdot 10^{-5}$
30	S22	hole	20	0.2	0.080	20	0.470	$3.83 \cdot 10^{-5}$
30	S22	hole	20	0.2	0.080	30	0.470	$4.78 \cdot 10^{-5}$
30	S22	hole	20	0.2	0.080	40	0.470	$5.78 \cdot 10^{-5}$
30	S22	hole	20	0.2	0.159	10	0.470	$5.98 \cdot 10^{-5}$
30	S22	hole	20	0.2	0.159	40	0.470	$1.24 \cdot 10^{-4}$
30	S22	hole	115	0.2	0.080	10	0.693	$3.91 \cdot 10^{-5}$
30	S22	hole	64	0.2	0.080	10	0.607	$3.54 \cdot 10^{-5}$
30	S22	hole	667	0.2	0.080	10	1.047	$5.59 \cdot 10^{-5}$
30	S32	hole	20	0.2	0.079	10	0.501	$6.06 \cdot 10^{-5}$
30	S42	hole	20	0.2	0.008	10	0.501	$8.79 \cdot 10^{-6}$
30	S42	hole	20	0.2	0.040	10	0.501	$4.54 \cdot 10^{-5}$
30	S42	hole	20	0.2	0.081	10	0.501	$1.01 \cdot 10^{-4}$
30	S42	hole	20	0.2	0.081	40	0.501	$3.85 \cdot 10^{-4}$
30	S22	plane	20	0.2	0.080	10	0.764	$7.61 \cdot 10^{-5}$
30	S42	hole	20	0.2	0.008	40	0.501	$1.85 \cdot 10^{-5}$
30	S42	hole	20	0.2	0.040	40	0.501	$9.49 \cdot 10^{-5}$
30	S22	plane	20	0.2	0.080	40	0.764	$1.26 \cdot 10^{-4}$
90	S22	hole	20	0.15	0.080	5	0.864	$1.72 \cdot 10^{-5}$
90	S22	hole	20	0.15	0.080	10	0.864	$2.01 \cdot 10^{-5}$
90	S22	hole	20	0.15	0.080	20	0.864	$2.60 \cdot 10^{-5}$
90	S22	hole	20	0.15	0.080	30	0.864	$3.23 \cdot 10^{-5}$
90	S22	hole	20	0.15	0.080	40	0.864	$3.88 \cdot 10^{-5}$
90	S22	hole	93	0.15	0.080	10	1.188	$2.52 \cdot 10^{-5}$
90	S22	plane	20	0.15	0.080	10	1.294	$4.14 \cdot 10^{-5}$



E

Sensitivity analysis: C_e based on additional tests

E

The reliability analysis in chapter 6 uses Eq. 6.5 to predict the progression rate. This equation is a curve-fit on numerical simulations in chapter 5, and includes the erosion coefficient C_e as calibration factor. The distribution of C_e (lognormal with mean 0.044 and standard deviation 0.048), was derived from the C_e values required to predict the average progression rate in 7 progression-dominated experiments [Sellmeijer et al., 2011; Vandenboer et al., 2019; Yao, 2014] plus the C_e values obtained by calibration of the 7 small-scale and large-scale tests in table 5.1.

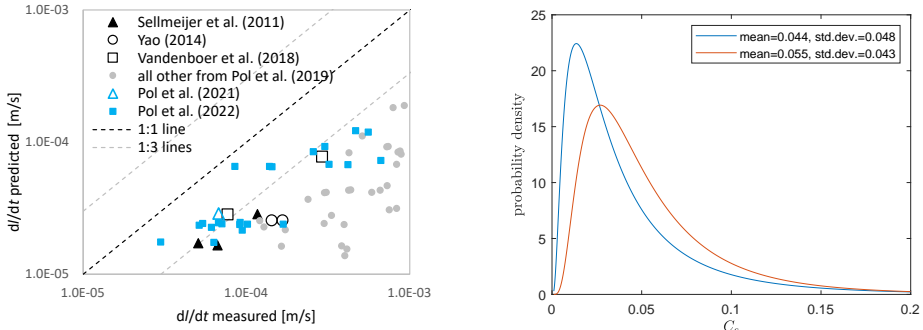
An additional validation can be done by predicting the average progression rate for all suitable experiments from chapter 3 and 4. This appendix investigates (1) how that would affect the distribution of C_e , and (2) how this different distribution affects the time-dependent reliability of the base case in chapter 6.

Distribution of C_e

The additional experiments are the 22 small-scale tests in Table 3.2 except for tests 218, 219 and 244, and the large-scale test from chapter 4. Figure E.1a shows that the measured average progression rate is around a factor 3 higher than predicted with $C_e = 0.016$, similar to the experiments by Yao [2014], Vandenboer et al. [2019] and Sellmeijer et al. [2011]. The C_e values required for a perfect prediction were determined also for these 23 experiments. Adding these 23 values to the 14 values mentioned above, the distribution for C_e changes to a lognormal distribution with mean 0.055 and standard deviation 0.043. This updated distribution is considered more representative than the original one.

Reliability of base case

The effect of this updated distribution on the results is assessed for the coastal and riverine base cases (2a and 2b in Table 6.3). The results in Table E.1 and Figure E.2 show that the time-dependent failure probabilities increase by about 30%, hence $F_{t,d}$ decreases.



(a) Predicted average progression rate with Eq. 5.15 and $C_e = 0.016$ compared to experimental results. (b) PDF's of C_e before and after update.

Figure E.1: Change of C_e distribution with additional experiments.

E

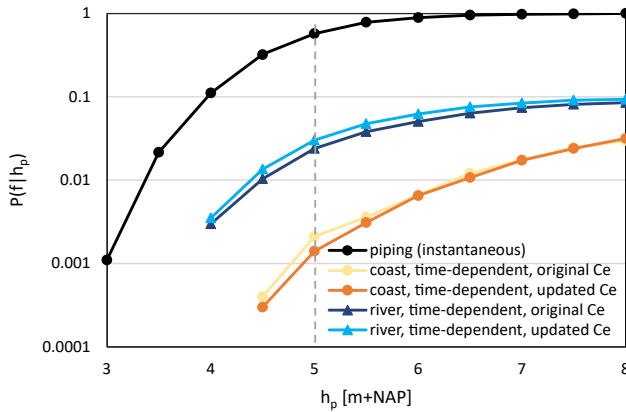


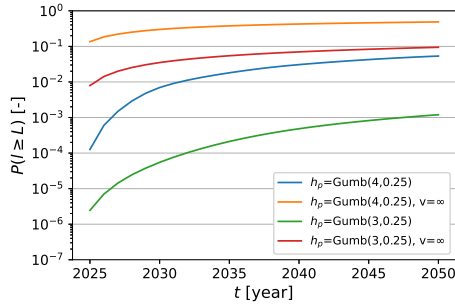
Figure E.2: Fragility curves for coastal and riverine base cases with $l_{ini} = 0$, for original and updated distribution of C_e .

Table E.1: Results of the reliability analyses with original (2a-2b) and updated (6a-6b) distribution of C_e . All cases are computed with probabilistic method B and $h_p \sim \text{Gum}(3,0.25)$. $P_{f,td}$ denotes (cumulative) failure probability including time-dependence, and $P_{f,stat}$ is without time-dependence (instantaneous). Effect of time-dependence is expressed by $F_{td} = P_{f,stat}/P_{f,td}$.

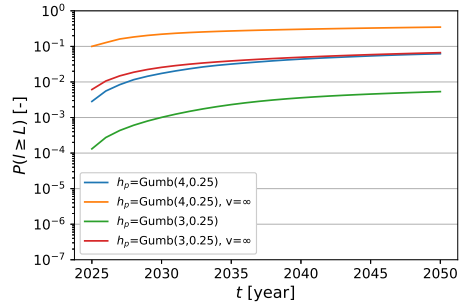
Case		2025			2050		
		$P_{f,td}$	$P_{f,stat}$	F_{td}	$P_{f,td}$	$P_{f,stat}$	F_{td}
2a	coast - original C_e	$2.5 \cdot 10^{-6}$	$7.9 \cdot 10^{-3}$	3200	$1.2 \cdot 10^{-3}$	$9.4 \cdot 10^{-2}$	79
2b	river - original C_e	$1.3 \cdot 10^{-4}$	$6.1 \cdot 10^{-3}$	47	$5.3 \cdot 10^{-3}$	$6.7 \cdot 10^{-2}$	13
6a	coast - updated C_e	$3.9 \cdot 10^{-6}$	$7.9 \cdot 10^{-3}$	2000	$1.6 \cdot 10^{-3}$	$9.4 \cdot 10^{-2}$	61
6b	river - updated C_e	$1.7 \cdot 10^{-4}$	$6.1 \cdot 10^{-3}$	37	$6.5 \cdot 10^{-3}$	$6.7 \cdot 10^{-2}$	10

F

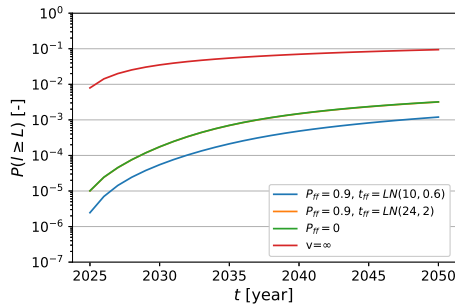
Time-variant reliability: results sensitivity analysis



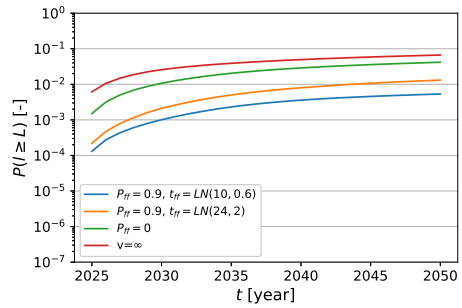
(a) Safety level - coast.



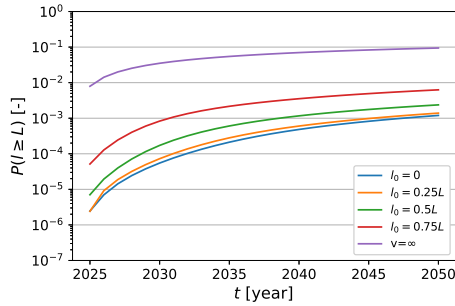
(b) Safety level - river.



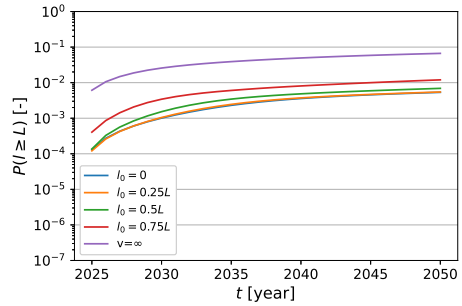
(c) Flood fighting - coast.



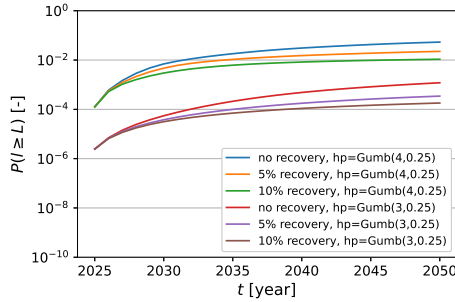
(d) Flood fighting - river.



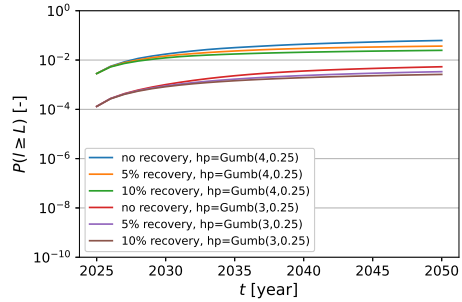
(e) Initial pipe length - coast.



(f) Initial pipe length - river.

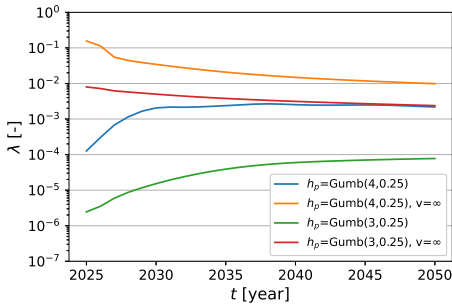


(g) Strength recovery - coast.

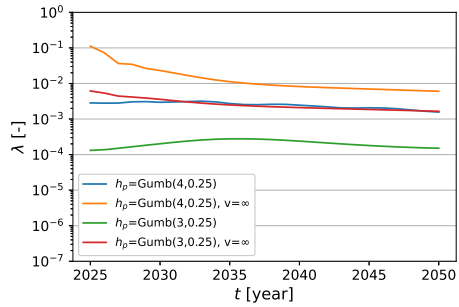


(h) Strength recovery - river.

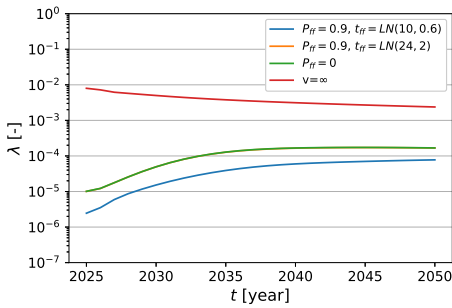
Figure F.1: Results of sensitivity analysis, presented in terms of $P(l \geq L)$ showing the influence of different factors. $v = \infty$ indicates instantaneous erosion (infinite progression rate). Left column: coast. Right column: river.



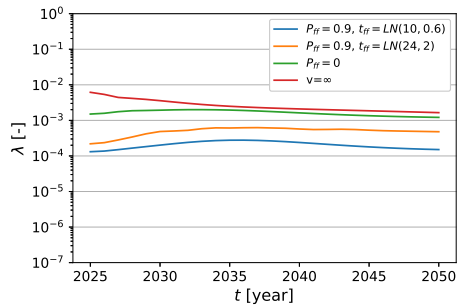
(a) Safety level - coast.



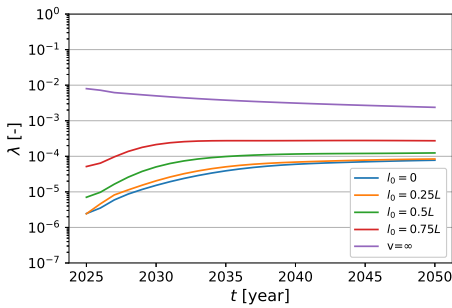
(b) Safety level - river.



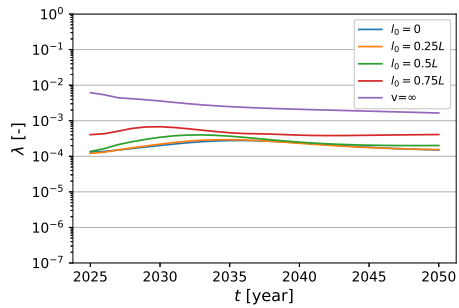
(c) Flood fighting - coast.



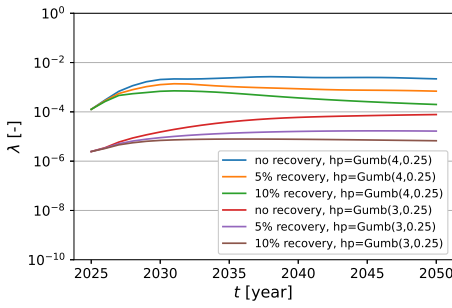
(d) Flood fighting - river.



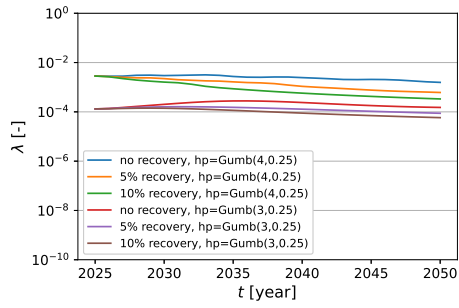
(e) Initial pipe length - coast.



(f) Initial pipe length - river.



(g) Strength recovery - coast.



(h) Strength recovery - river.

Figure F.2: Results of sensitivity analysis, presented in terms of conditional failure rate λ , showing the influence of different factors. $v = \infty$ indicates instantaneous erosion (infinite progression rate). Left column: coast. Right column: river.





List of Symbols

Roman letters

a	m	pipe depth
A	m ²	pipe cross sectional area
C_u	-	coefficient of uniformity ($=d_{60}/d_{10}$)
C_e	-	dimensionless erosion coefficient in Eq. 5.12
$C_{e,\tau}$	m ² Pa ⁻² s ⁻¹	erosion coefficient in Eq. 5.11
C_k	-	coefficient in Kézdi formula (Eq. 2.18)
d_x	m	particle diameter (x^{th} quantile)
D, D_{aq}	m	aquifer thickness
D_{bl}	m	blanket layer thickness
D^*	-	dimensionless particle diameter
D_r	-	relative density ($\frac{e_{max}-e}{e_{max}-e_{min}}$)
D_p	hour	peak duration of high water
e	-	void ratio ($n/(1-n)$)
f_{DW}	-	Darcy-Weisbach friction factor
f_{int}	-	effect of interaction ($P_{f_{int}}/P_{f_{org}}$)
F_{td}	-	effect of time-dependence ($P_{f,stat}/P_{f,td}$)
$g(.)$		limit state function
g	m/s ²	gravitational acceleration
h	m+NAP	hydraulic head or water level
h_p, h_{max}	m+NAP	peak level of high water
h_e	m+NAP	water level at exit point
$H(.)$		Heaviside unit step function
H	m	head difference
H_c	m	critical head difference
H_{eq}	m	equilibrium head difference
i	-	hydraulic gradient (dh/dx)
$i_{c,h}$	-	critical heave gradient
k	m/s	hydraulic conductivity
k_{aq}	m/s	hydraulic conductivity of aquifer
L	m	seepage length
L_s	m	total length of sand sample
l	m	pipe length
l_c	m	critical pipe length
l_{ini}	m	initial pipe length at the start of a flood event
l_e	m	pipe length at the end of a flood event
m_v	-	model uncertainty on progression rate

m_u	-	model uncertainty for uplift
m_p	-	model uncertainty for backward erosion
n	-	soil porosity
p	Pa	pipe pressure
$P()$	-	probability
$P_{f,stat}$	-	failure probability (stationary, instantaneous)
$P_{f,td}$	-	failure probability (time-dependent)
$P_{f,int}$	-	failure probability with interaction
$P_{f,org}$	-	failure probability without interaction
Q_w	m^3/s	water flow rate
Q_s	m^3/s	volumetric sediment discharge
q_v	m^2/s	volumetric sediment discharge per unit width
q_{*E}	-	dimensionless sediment discharge, Einstein number
q_{*v}	-	dimensionless sediment discharge, viscous scaling
R	m	hydraulic radius
Re	-	Reynolds number
Re^*	-	particle Reynolds number
r_e	-	aquifer response factor at exit hole (Ch. 6)
r_l	-	pipe length recovery fraction per year
t	s	time
t_{ff}	s	time required for successful flood fighting
u_p	m/s	pore flow velocity
u_{max}	m/s	maximum pipe flow velocity in cross section
u^*	m/s	bed shear velocity
U	m/s	average pipe flow velocity in cross section
v	m/s	progression rate (dl/dt)
$v_{c,avg}$	m/s	average progression rate in progressive phase
V_p	m^3	pipe volume
V_{sb}	m^3	sand boil volume
W	m	width of aquifer / sand bed
w	m	pipe width
x	m	longitudinal position in sand sample
y	m	transverse position in sand sample
z	m	vertical position in sand sample
\mathbf{X}		vector of random variables
Z		limit state, safety margin

Greek letters

β	-	reliability index
γ	kN/m^3	unit weight (water/soil/particles)
Δ	-	specific particle density ($\rho_s/\rho_w - 1$)
η	-	White's constant
θ	°	bedding angle
θ_{sb}	°	slope angle of sand boil
θ_w	°	weir angle
Θ	-	dimensionless bed shear stress (Shields number)
κ	m^2/s	intrinsic permeability
λ	m	leakage length (Ch. 7)
λ	-	conditional failure rate (Ch. 6)
μ	$\text{Pa} \cdot \text{s}$	dynamic viscosity of water
ν	m^2/s	kinematic viscosity of water
ρ_p	-	Pearson correlation coefficient
ρ_s	kg/m^3	particle density
ρ_w	kg/m^3	water density
τ	Pa	bed shear stress
τ_c	Pa	critical bed shear stress (initiation of motion)
ϕ	°	friction angle
φ	m	aquifer head

Abbreviations

BEP	Backward Erosion Piping
FPH	Flood Proof Holland
FEM	Finite Element Model
DEM	Discrete Element Model
LSF	Limit State Function
MCS	Monte Carlo Simulation
NAP	Normaal Amsterdams Peil (Dutch datum)



Curriculum Vitæ

12 December 1990 Born in Rijssen, The Netherlands

Education

2012 - 2014 MSc. Hydraulic Engineering
(specialization Water Management & Engineering)
Delft University of Technology

2009 - 2012 BSc. Civil Engineering
Delft University of Technology

2003 - 2009 Pre-university secondary education (VWO)
Fruytier Scholengemeenschap, Apeldoorn, The Netherlands

Employment

2017 - present PhD researcher
Hydraulic Structures & Flood Risk
Delft University of Technology
Research on improving reliability estimates of flood defenses by including time-dependent piping erosion processes.

2014 - present Consultant Rivers, Coasts & Deltas
HKV, Lelystad, The Netherlands
Technical advisor on flood risk and river management: flood defenses, water system analyses, hydraulic loads, river interventions, sediment transport, dam and levee reliability, backward erosion piping, monitoring, data analysis.

2014 Graduate Internship
HKV, Lelystad, The Netherlands
Thesis on hydrograph shape variability on the river Meuse: evaluation of design hydrograph methods and probabilistic methods to estimate design water levels on the river Meuse.

2013 Internship
RPS, Delft, The Netherlands
Projects on levee reinforcements, flood risk analysis and ground-water monitoring.



List of Publications

Peer-reviewed journal papers

1. **Pol**, J.C. (2022). Discussion of ‘Influence of erosion on piping in terms of field conditions’ by G. Hoffmans. *Journal of Hydraulic Research*, (accepted for publication).
2. Callari, C. and **Pol**, J.C. (2022). Numerical interpretation of regressive localized internal erosion in a real-scale levee physical model. *Geomechanics for Energy and the Environment*. <https://doi.org/10.1016/j.gete.2022.100395>
3. **Pol**, J.C., Kanning, W., van Beek, V.M., Robbins, B.A. & Jonkman, S.N. (2022). Temporal evolution of backward erosion piping in small-scale experiments. *Acta Geotechnica*, <https://doi.org/10.1007/s11440-022-01545-1>
4. B.A. Robbins, V.M. van Beek, J.C. **Pol**, D.V. Griffiths (2022). Errors in finite element analysis of backward erosion piping. *Geomechanics for Energy and the Environment*, 100331, <https://doi.org/10.1016/j.gete.2022.100331>
5. **Pol**, J.C., Kanning, W., & Jonkman, S.N. (2021). Temporal Development of Backward Erosion Piping in a Large-Scale Experiment. *Journal of Geotechnical and Geoenvironmental Engineering*, 147(2), 04020168, [https://doi.org/10.1061/\(ASCE\)GT.1943-5606.0002415](https://doi.org/10.1061/(ASCE)GT.1943-5606.0002415).

Conference contributions

1. **Pol**, J.C. & Noordam, A. (2022). Time-dependent 3D numerical modeling of backward erosion piping. Abstract from the 28th meeting of the European Working Group on Internal Erosion, 18-21 July 2022, Sheffield, UK.
2. **Pol**, J.C., Kanning, W. & Jonkman, S.N. (2022). Strength Recovery in a Large-Scale Backward Erosion Piping Experiment. Abstract from the 28th meeting of the European Working Group on Internal Erosion, 18-21 July 2022, Sheffield, UK.
3. **Pol**, J.C., van Klaveren, W., Kanning, W., van Beek, V.M., Robbins, B.A., and Jonkman, S.N. (2020). Progression Rate of Backward Erosion Piping: Small Scale Experiments. Proceedings of the 10th International Conference on Scour and Erosion (ICSE-10), Arlington, USA. 18-21 October, 2021. Rice, J., Liu, X., McIlroy, M., Sasanakul, I., and Xiao, M. (Eds), pp 93-102. [\[link\]](#)
4. **Pol**, J.C., Van Beek, V.M., Kanning, W., and Jonkman, S.N. (2019). Progression rate of backward erosion piping in laboratory experiments and reliability analysis. Proceedings of the 7th international symposium on geotechnical safety and risk, Tapei, Taiwan. [\[link\]](#)
5. Yagisawa, J., van Damme, M., **Pol**, J., and Bricker, J. (2019). Verification of a predictive formula for critical shear stress with large scale levee erosion experiment. Proceedings of the 11th ICOLD European Club Symposium, 2-4 October 2019, Chania, Crete. [\[link\]](#)

Professional journals and reports

1. Barendsen, L., Bartels, W., and **Pol**, J.C. (2021). Pipingrisico bij dijken met lek naar het achterland. *Land + Water* October 2021, pp31-33.
2. **Pol**, J.C. (2020). Shields-Darcy pipingmodel. Verschilanalyse met Sellmeijer en D-GeoFlow. Technical report commissioned by Expertise Netwerk Waterveiligheid. 19 oktober 2020.